Assessment of the gold exploration potential of northern Portugal: a new research approach

Sara Manuela Ferreira Leal

Programa Doutoral em Geociências
Especialidade em Recursos Geológicos e Geomateriais

Departamento de Geociências, Ambiente e Ordenamento do Território
2021

Orientador
Alexandre Martins Campos de Lima, Professor Associado, FCUP

Coorientador
Fernando Manuel Pereira de Noronha, Professor Emérito, FCUP

This work was financially supported by SFRH/BD/114693/2016 (FCT Portugal).

This work was partially funded by the COMPETE 2020 through the ICT (Institute of Earth Sciences) project (UIDB/GEO/04683/2020) with POCI-01-0145-FEDER-007690.

Citation

"*Discovery consists of seeing what everybody has seen and thinking what nobody has thought.*"

Albert Szent-Gyorgyi in Irving Good, The Scientist Speculates (1962)

Acknowledgments

Nothing of any significant value is accomplished in isolation or alone, and so it is with the greatest sincerity and self-effacement that I wish to thank those who have seen me through this journey. Doctoral research is a collaborative effort in which several people and institutions knowingly and unknowingly contribute to the thesis's production and the development of the research project.

First and foremost, I want to extend my gratitude to my supervisor, Alexandre Lima, who encouraging me to embark on this research. I would thank his unfailing support and guidance, for his patience and trust, and for creating the intellectual space for exploring the issues, I dealt with in this study. His kind help and support have made my study during PhD a wonderful time, with good conversations about the topic (or not!) and fantastic fieldwork days. Their knowledge and experience have encouraged me throughout my academic research and future professional life.

I gratefully acknowledge the support of Fernando Noronha as co-supervisor. He has been generous and continually steering me in the right direction and asking all the right questions to provoke thoughts. His solid advice and guidance through this challenging path have been substantial.

I would especially like to thank Jim Mortensen and Rob Chapman for their unwavering support, advice, and friendship. Professor Jim Mortensen has a contagious enthusiasm for all aspects of the gold mineralization in Iberia and has largely contributed to my understanding of the region and provided valuable discussions throughout the research.

Thanks to Miguel Fernández and the University of Oviedo for sharing their lab and equipment with me and being friendly and welcoming. Thanks to Mercedes Fuertes-Fuente for helping me with the microprobe analysis and many valuable discussions about gold mineralizations.

I would especially like to thank Roberto Matias for his infectious passion for all aspects of Roman gold mineralization and for helping me with the sampling of the gold detrital particles.

Thanks to MINAPORT company for allowing me access to their drill-cores and underground mining works. A special thanks to John Morris and Nataniel Bernardo.

I would like to express gratitude to the co-authors of the papers in this thesis for sharing their knowledge and experience with me and their valuable contributions.

My sincere gratitude to the Department of Geosciences, Environment and Spatial Plannings, in particular to Maria dos Anjos Ribeiro, Helena Brites, Rui Moura, António

Guerner, Alexandra Guedes, Helena Sant'Ovaia, Angela Almeida, and Deolinda Flores for their kindness and for always being available when it was necessary.

I thank the staff at the Department of Geosciences, Environment, and Spatial Plannings. Thank you, Paulo Ferreira, Cândida Neto, Irene Costa, Mónica Alves, Isabel Sá, Cristina Vilas Boas, Joana Damásio, for the help and availability during all these years and the good conversations.

I want to thank all my colleagues from the Geoscience Doctoral Program for a cherished time spent together in the office, lab, and social settings. Particularly to Cláudia Cruz, António Oliveira and Ana Marta.

To complete a PhD takes more than intellectual curiosity, persistence, and resilience. The support of solid friendships and family is equally important.

Special thanks go to Joana Ribeiro, Ana Cláudia Santos, and Luís Lima for all friendship and support, scientific discussions, fieldwork days, lunches, dinners, and other occasions! I would like to thank you to those who helped me maintain good mental health!

It is a pleasure to thank all my geologist friends, but especially Ana Moreira, Filipa Pinheiro, Joana Ferreira, and Marieta Freitas, for the countless good times and laughter.

In addition, I would like to thank all my non-geologist friends from my hometown Paredes who gave me the necessary social distractions from my research and made my PhD journey a wonderful time. Thank you for listening to me talk about gold mineralization (even though not understanding one word!), accompanying me in the fieldwork during hot and raining days, and constantly reminding me of what matters.

Finally, my deep and sincere gratitude to my family and Miguel for their continuous and unparalleled love, help, and emotional support. They selflessly encouraged me to explore new directions in life and seek my destiny. This journey would not have been possible if not for them. I would not have made it without your love and kindness. Your belief in me, your encouragement when the times got tough, and your assistance through this process gave me the strength to succeed. Constantly reminding me of what matters at the end of this journey. To them, my most resounding thank you.

Content

Abstract

The Bigorne and Numão deposits, located in the Iberian Variscan belt, northern Portugal, are an example of structurally controlled, gold-only mineralization. Establishing the controls on mineralization distribution improves the exploration potential and provides implications for the tectonic and metallogenic evolution of the northern Portugal and Iberian Variscan belt. The mineralization controls in the two case studies (Bigorne and Numão areas) were identified by field mapping, drill-core logging, petrography, and analytical techniques that included whole-rock geochemistry, stable isotopes, and mineral chemistry.

Bigorne deposit is hosted in late- and late-to post-D3 variscan granites with ca. 309.6 ± 1 Ma to 303.3 ± 8.1 Ma age. Numão deposit is hosted in metamorphic sequences of the Schist Greywacke Complex of pre-Ordovician age. As a whole, the gold mineralized bodies in both cases are structurally controlled, associated with the two main large-scale regional faults systems, which are related to the late Variscan deformation events. Textural and mineralogical analysis of the gold-bearing veins has revealed that gold is (i) paragenetically late, (ii) infilling intergranular spaces or cavities/cracks within pre-existing sulfides (mostly arsenopyrite and pyrite); and (iii) occurring as the native metal, generally in alloy with silver (electrum), or less commonly with bismuth, copper and other trace elements.

The regional framework of the Bigorne and Numão deposits, the mineralized bodies' relationship with the host rocks, and the gold mineral assemblage allowed us to infer a relative timing for gold mineralization of nearly ~300 Ma.

Arsenopyrite and chlorite geothermometers, mineral phase stabilities, stable isotope data, and published fluid inclusion studies were used to reconstruct the temperature and compositional evolution of the gold mineralization systems at local and regional scales. The role of the liquid bismuth collector model was discussed as an alternative deposition mechanism for gold in the Bigorne deposit. The $\delta^{34}S$ values range from -2.8 to -7.5‰ whereas the $\delta^{18}O$ values have a narrow range (12 to 13.5‰). These data, interpreted in the regional and local geology context, suggested a decoupled metal source, a similarly modified mineralizing fluid, and a low temperature for gold deposition (~300ºC). The gold-bearing fluids source was assigned to a regionally significant gold mineralizing event, generated from deep-crustal rocks during decompression uplift in an extensional tectonic regime, related to the late orogenic evolution of the area.

The research, discussions, and conclusions culminated through this PhD thesis, intend to provide novel and valuable data regarding both the Bigorne and Numão deposits. The

main PhD achievements have implications for the understanding of the metallogeny of gold mineralizations in the NW of the Iberian Variscan belt and globally, providing new pathfinders that can be applied to gold exploration.

Keywords

Gold mineralizations

Mineral exploration

Metallogenic province

Iberian Variscan belt

Resumo

Os depósitos de Bigorne e Numão, localizam-se no Maciço Ibérico, a norte de Portugal, sendo um exemplo de mineralizações de ouro, estruturalmente controladas. A definição dos fatores que controlam a distribuição da mineralização contribui para a definição do potencial de prospeção, contribuindo também para o entendimento da evolução tectónica e metalogénica do norte de Portugal, e do Maciço Ibérico. Os fatores que controlam a mineralização nas áreas de Bigorne e Numão foram identificados pela cartografia geológica, elaboração de logs geológicos, petrografia e por técnicas analíticas que incluíram, geoquímica de rocha total, isótopos estáveis e química mineral.

As estruturas mineralizadas do depósito de Bigorne cortam os granitos variscos, tardi- a tardi- a pós-C3 (ca. 309.6 ± 1 Ma a 303.3 ± 8.1 Ma). O depósito de Numão está encaixado em sequências metamórficas do Complexo Xisto-Grauváquico. As mineralizações de ouro nestes dois depósitos são estruturalmente controladas. Observando-se uma relação espacial com o sistema tardio de falhas regionais variscas. A análise textural e mineralógica das estruturas mineralizadas revelou que o ouro é tardio na paragénese mineral, encontrando-se a preencher espaços intergranulares ou cavidades em sulfuretos precoces (arsenopirite e pirite). O ouro ocorre como metal nativo, geralmente numa liga com a prata (*eletrum*), ou menos comummente com bismuto, cobre e outros elementos traço.

O contexto geológico regional dos depósitos, a relação das estruturas mineralizadas com as rochas encaixantes e a sequência paragenética permitem inferir uma idade relativa de aproximadamente ~ 300 Ma para a deposição da mineralização de ouro.

Os geotermómetros da arsenopirite e da clorite, a estabilidade das fases minerais, os dados de isótopos estáveis, bem como estudos de inclusões fluídas publicados anteriormente ajudaram a reconstruir a temperatura e a evolução composicional das mineralizações de ouro no norte de Portugal. O papel do modelo *liquid bismuth collector* como mecanismo alternativo à deposição do ouro também é discutido para o depósito de Bigorne. Os valores de $\delta^{34}S$ variam entre -2.8 e -7.5‰, enquanto que os valores de $\delta^{18}O$ variam numa faixa mais restrita, entre 12 e 13.5‰. Os dados de isótopos estáveis, interpretados no contexto da geologia regional e local, sugerem fontes de metal diferentes, mas fluidos mineralizantes similares e de baixa temperatura (~ 300°C).

Os fluidos mineralizantes estão relacionados com um regime tectónico extensional, gerado em rochas da crosta profunda durante o *uplift*, nos estádios finais da orogenia varisca. Esta interpretação tem implicações na metalogenia do ouro do norte de Portugal e do Maciço Ibérico, bem como a nível global. Os resultados obtidos ao longo desta

investigação contribuem com novos guias que poderão ser aplicados na prospeção de mineralizações auríferas.

Palavras-chave

Mineralizações de ouro

Prospeção mineral

Província metalogénica

Maciço Ibérico

List of Abbreviations and acronyms

All the abbreviations and acronyms are defined the first time they are used. Furthermore, all of them are listed below.

VCDT: Vienna Canon Diablo Troilite

SMOW: Standard Mean Ocean Water

OGD: Orogenic Gold Deposit

IRGD: Intrusion Related Gold deposits

RIGS: Reduced Intrusion Gold System

OIGS: Oxidized Intrusion Gold System

IOCG: Oxide Copper Gold deposits

VMS: volcanogenic massive sulfide

GIS: Geographic Information Systems

CPL: Crossed Polarized Light

PPL: Plane Polarized Light

BSE: Back-scattered electron images

SEM: scanning electron microscope

p-XRF: Portable X-ray Fluorescence

ICP-MS: Inductively Coupled Plasma Mass Spectrometer

ICP-OE: Inductively Coupled Plasma Optical Emission

EMPA: Electron Probe Micro Analyzer

REE: Rare Earth Element

HREE: Heavy Rare Earth Element

LREE: Light Rare Earth Element

ppm: parts per million

apfu: Atoms per formula unit

kbar: Kilobar

P: pressure

T: temperature

wt.%: weight percentage

at. %: atomic percentage

Ma: millions of years ago

ca.: circa

e.g.,: “for example.”

USGS: United States Geological Survey

EDM: Empresa de Desenvolvimento Mineiro

CZ: Cantabrian Zone

WALZ: West Asturian-Leonese Zone

GTMZ: Galiza-Trás-os-Montes Zone

CIZ: Central Iberian Zone

OMZ: Ossa-Morena Zone

SPZ: South Portuguese Zone

VMF: Vilariça-Manteigas fault

PRVF: Penacova-Régua-Verín fault

DBSZ: Douro Beira shear zone

VLSZ: Vigo-Lamego shear zone

SIORMINP: Sistema de Informação de Ocorrências e Recursos Minerais Portugueses

IGME: Instituto Geológico y Minero de España

List of figures

List of tables

CHAPTER 1 | Introduction

1.1 Scope and relevance

Gold mining is a significant economic driver metal for the global economic cycle of many countries worldwide, being considered one of the most *widespread* commodities for thousands of years. Naturally, gold is never a pure mineral phase forming alloys with silver, copper, mercury, and tellurium; less commonly with titanium, bismuth, palladium, lead, and zinc (Boyle, 1979; Macdonald, 2007). In the Earth's crust, gold is a relatively rare element (0.0015 ppm (parts per million); Rudnick and Gao, 2014), irregularly distributed with a low degree of element concentration, supporting the importance of discovering enriched sources and the required efficiency of the gold ore-forming process (Macdonald, 2007).

Currently, most of the produced gold came from active mines and goes into the manufacturing of jewelry. Until recent times, it was considered a monetary metal, and most of the gold bars produced each year went into the vaults of government treasuries or central banks (Fig. 1-A-B: World Gold Council, 2021; United States Geological Survey (USGS), 2021). However, because of its superior electrical conductivity and resistance to corrosion and other desirable combinations of physical and chemical properties, gold also emerged in the late 20th century in the field of high-tech development and industrial applications (*e.g.,* manufacture of connectors, printed circuits, semiconductors, and a host of other electronic products) (Macdonald, 2007; Politano et al., 2014; Zemskov et al., 2014; Goldfarb et al., 2017; European Commission, 2014, 2017; USGS, 2021). Furthermore, this precious metal is of great interest because it is associated in various geological environments with significant critical metals such as antimony, tellurium, selenium, and bismuth (European Commission, 2014, 2017). Some minerals associations can also be used as indicators of the conditions of ore deposit formation (as discussed in chapter 4).

Available data from World Gold Council, 2021, report increased prices for precious metals, such as gold, which reached a high price record of 56€ per gram in August 2020, contributing to the increased metal production value (Fig. 1-D). As stated by USGS, 2021, the principal contributors to the total gold mine production in 2020 were China, Australia, and Russia (Fig. 1-C). China currently produces about 13% of the world's gold. Currently, gold is produced in European countries in Finland, Sweden, Bulgaria, Spain, Turkey, Poland, Romania, Serbia, Slovakia, Russia, and Greece. In addition, gold mining projects are in permitting stage across, *e.g.*, the United Kingdom and Portugal. Exploration is also underway in other countries like France, Italy, and Austria (Lima et al., 2018).

Nonetheless, discovery rates for all metallic ores, including gold, are decreasing. The cost per significant discovery is increasing abruptly (Groves and Santosh, 2015). Thus, the global trend in the mining industry, particularly in gold mining, is that metal demand and production are permanently growing (Fig. 1-E), but the ore grades and resource availability are progressively declining (Calvo et al., 2016; Korolev et al., 2018 and references therein). These issues stimulate an emerging interest in exploring and exploiting gold deposits worldwide, turning the attention to small-scale mining projects (like those in Portugal), which have prompted new scientific research on gold systems, such as the one herein presented.

An analysis of the main exploration methods of ore deposits, including gold, indicates that techniques have evolved mainly throughout the last few years, and current technology is one of the main allies for developing competitive exploration projects. Most of the currently used tools rely on several high-tech types of equipment for obtaining geochemical information (*e.g.*, mineral chemistry, stable isotopes, and whole-rock chemistry), allied with extensive and detailed fieldwork (*e.g.*, Robert et al., 2007). Understanding the geological settings that control mineralization, to which numerical simulations can be applied, can provide robust tools to constrain the sources of the metals and fluids that transport them, which are key elements in discovering new deposits (Carranza, 2012). Consistent with, a key element of success for the geologist is to understand and detect the different types of gold systems, their most favorable geological settings, controls at a regional and local scale, and compare erosion levels with the depth of system formation to assess its degree of preservation (Sillitoe and Thompson, 2006).

Despite its small size, Portugal has huge geological diversity and belongs to one of the various metallogenic provinces in the European Variscan belt (Fig. 2-A). From the 1940s, and with particular emphasis on the 1970s to 1980s, the Portuguese mining industry was booming, beginning with tungsten and tin in northern and central parts of the country and also focusing on precious metals and base metals (Martins, 2012).

In the north of Portugal (Fig. 2-B), numerous hypogene gold deposits have been inspired multidisciplinary studies over the years (*e.g.*, Almeida and Noronha, 1988; Couto et al., 1990; Mateus and Barriga, 1991; Neiva, 1992; Noronha and Ramos, 1993; Cathelineau et al., 1993; Boiron et al., 1996; 2003; Nogueira, 1997; Mateus, 1997; Noronha et al., 2000; Rosa, 2001; Inverno, 2002; Vallance et al., 2003; Fuertes-Fuente et al., 2016; Cruz et al., 2018; Neiva et al., 2008, 2019; Leal et al., 2021) and also have been targets of many exploration companies. Consequently, in Portugal, the exciting potential for the extractive industry and academic research has always been and continues to grow and

enhance significantly. In summary, the motivation for this work comes from the ongoing gold exploration demand worldwide, improvement of knowledge of Portuguese gold mineralization, and, subsequently, the metallogenic evolution of the region.

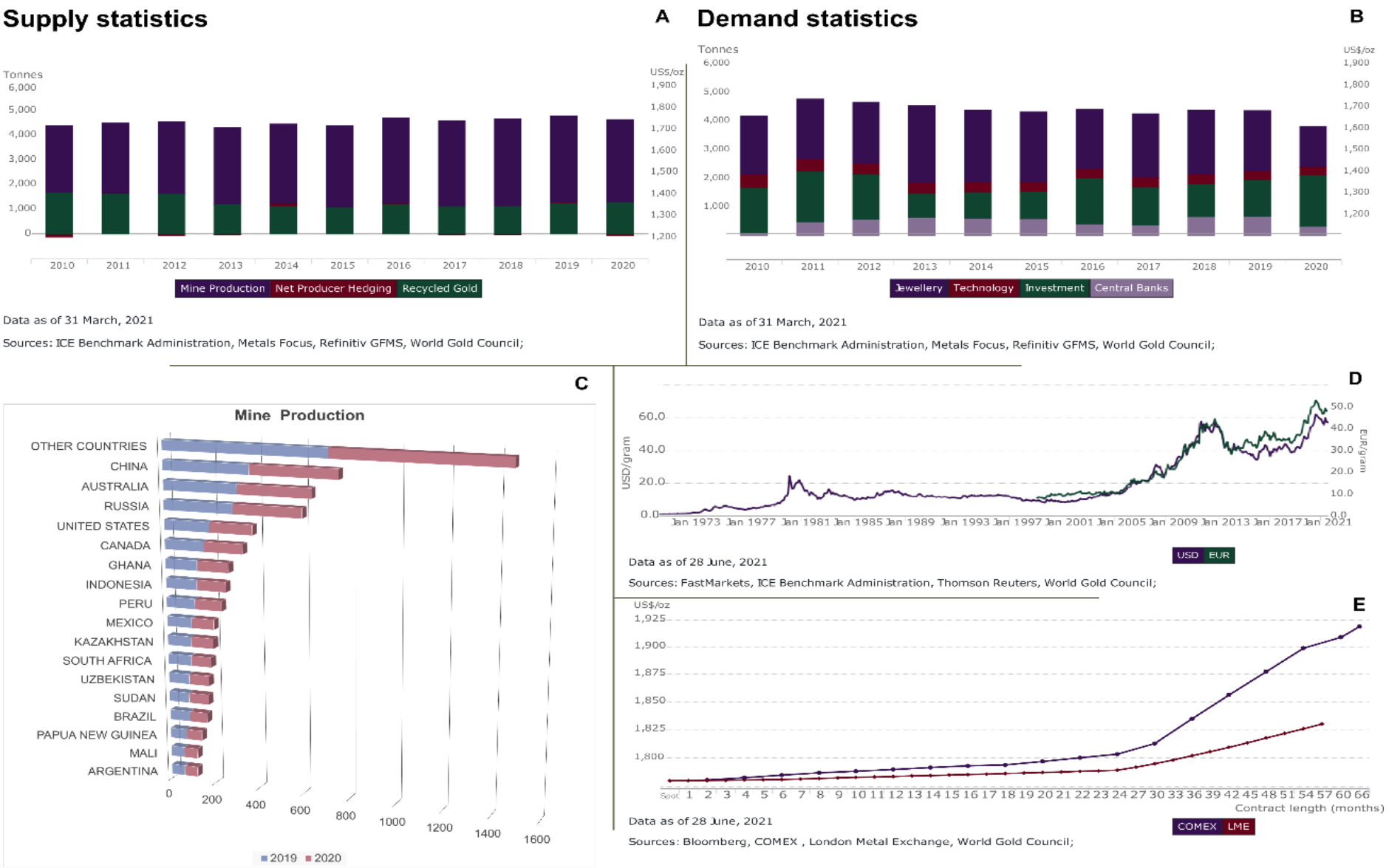

Fig. 1. Gold supply (A) and demand (B) in tonnes and US$ value. Mine production (C) by country during 2019 and 2020. Average annual (1973-2021) gold prices (D) are in US$/oz and €/oz. Curves of the future gold price (E). Data as of 28 June 2021. Sources: World Gold Council.

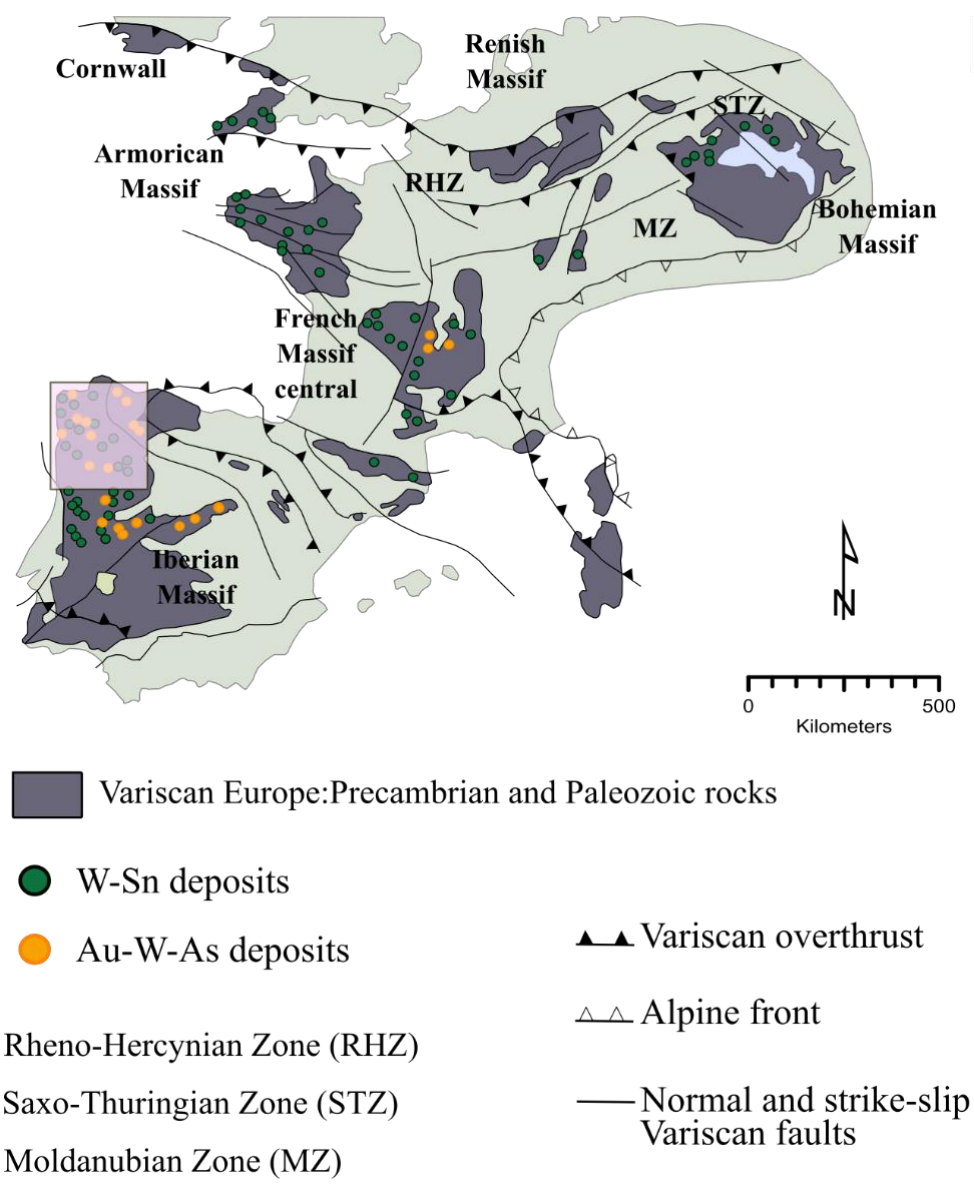

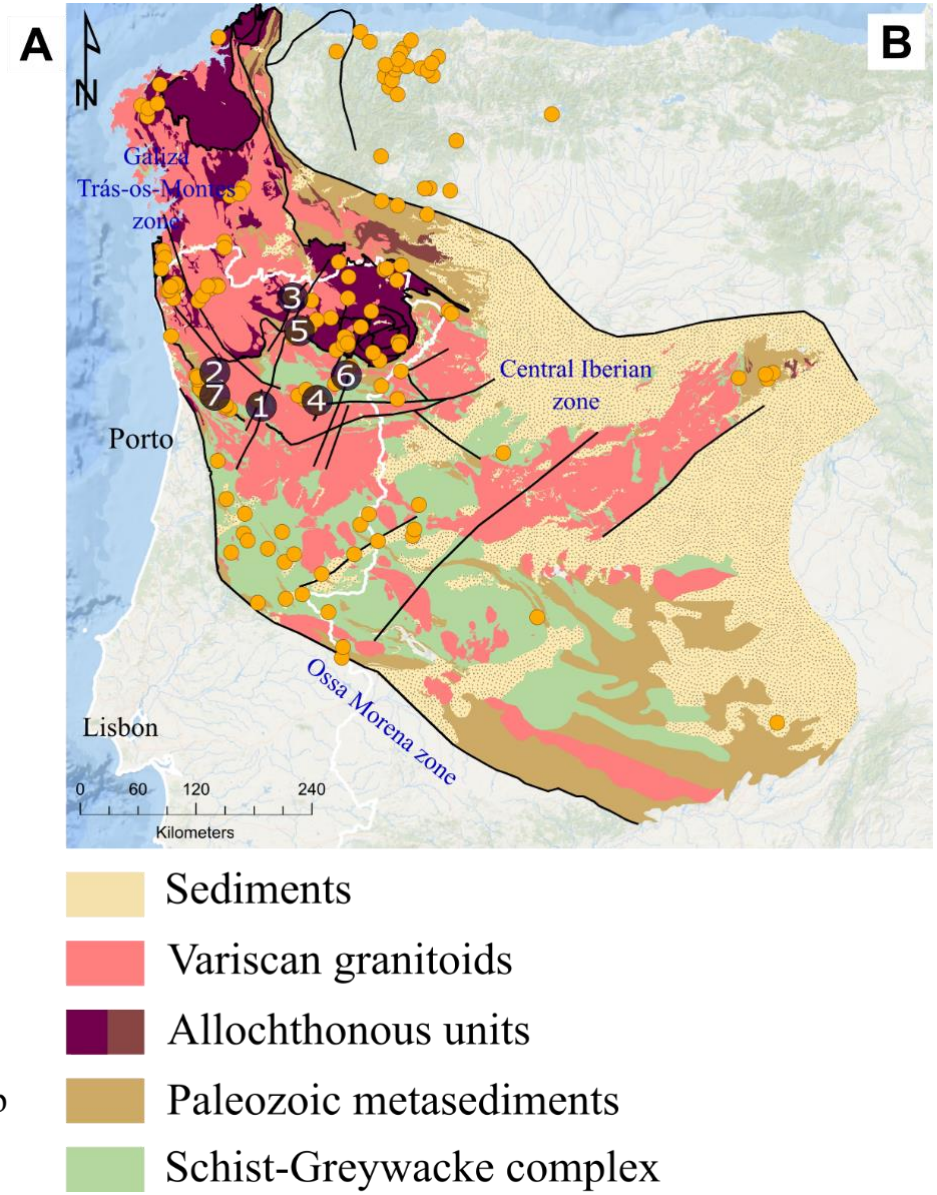

Fig. 2. (A) Map of the Variscan belt in central and western Europe (modified from Díez-Montes, 2007; Timón-Sánchez et al., 2019) and main metallogenic provinces. **(B)** Geological sketch of the Variscan Belt in Western Europe (modified from Martínez-Catalán et al., 2007; Villaseca et al., 2014) and the main gold systems contained within NW Iberia. Numbers 1, 2, 3, 4, 5, 6 and 7 are gold systems in Table 2.

1.2 Research target and key issues

Currently, multidisciplinary studies have become mandatory in successful exploration and exploitation projects for gold mineralization, as they are crucial (i) to understand the ore formation mechanisms, (ii) to the classification of mineral deposits, (iii) to the ore processing techniques, and (iv) geoenvironmental studies (Carranza, 2012).

This project provides an opportunity to dovetail a multidisciplinary and detailed deposit-scale study with new data contributing to the discussion regarding ore-forming processes and gold metallogeny in northern Portugal. Bigorne and Numão areas, located in the north of Portugal, are the case studies (Fig. 4). Additionally, attempt to apply and develop a gold exploration technique that is not recurrently used in exploration projects in Portugal (see chapter 5). The availability of the dataset from Iberian gold systems provides an excellent basis for investigating the geological and metallogenic evolution of the Variscan belt and its relationship to gold mineralization and other metals.

Based on these primary goals, this research project focuses on the following main questions:

(1) What are the nature and sources of mineralizing fluids?
(2) What are the mineral deposition conditions for gold assemblage?
(3) What is the relative age relationship between the host rocks and gold mineralization?
(4) How does it link to the regional tectonic and structural evolution of the belt?
(5) At the metallogenic province scale, what events were likely to explain the metals' origin and concentrations?
(6) How could Portuguese deposits be considered in the context of global gold deposit classifications?

The fundamental milestones of this work are formulated in specific objectives as follows:

1) To recognize the geological characteristics of the gold mineralization and the deposit in terms of fieldwork, host rocks, tectonic setting, mineralization style, mineralogy, and textures, and mineralization controlling factors;
2) To determine mineral paragenetic sequences for the mineralized structures, as well as the hydrothermal alterations associated with the gold mineralization;
3) To characterize the petrographic and geochemical features of the host rocks of the gold mineralized structures;

4) To perform a spatial characterization of the composition of the hypogene and superficial gold particles to identify the potential of the microchemical characterization as an exploration tool in Portugal;
5) To find evidence for the source of gold by analyzing and interpreting the light isotope signatures (S, O, H) of fluids and minerals from the gold mineral assemblage;
6) To determine the relative timing relations between the host rocks and mineralized structures;
7) Compare the studied deposits with others of similar character to genetically classify them and constrain the metallogenic model as a function of their characteristics and origin of mineralization.

1.3 Overview of the thesis structure

The thesis is organized into seven chapters, each divided into several sections. Chapters 1, 2, 3, and 7 are traditional thesis chapters representing original work and figures modified from cited sources. Chapters 4, 5, and 6 are manuscript-based chapters submitted to peer-reviewed journals before the conclusion of this document.

Therefore, some repetition of information between manuscript-based chapters is inevitable. However, to avoid this, the original manuscript was disassembled, and present as; i) **Highlights section** with the research topics and objectives of the manuscript; and then the following section of the original manuscript are present: ii) **Local geological setting**; iii) **Sampling and analytical methods**; iv) **Results**; v) **Discussion**; vi) **Conclusions**. Each manuscript-based chapter focuses on the outcomes from different geological aspects and genesis of the Bigorne and Numão deposits (Chapter 4 and 6) and the development and application of an innovative gold exploration technique applied in the Bigorne area (Chapter 5). Supplementary information for each of these chapters is provided in referenced appendices.

This thesis is based on the following original publications:

Research article 1: Ore Geology Reviews

Geological setting of the Bigorne gold deposit, Iberian Variscan Belt (northern Portugal) and Au-Bi-Te mineral assemblages as indicators of the ore-forming conditions.

Statement of own contribution:

The lead author on this manuscript conducted fieldwork, sampling campaigns and carried out all analytical studies, digital mapping, and manuscript preparation. In addition, co-authors provided sampling support, technical advice, and suggestions in the field and manuscript preparation.

Research article 2: Geological Society of London, Special Publications

Characterization of heavy mineral concentrates and detrital gold particles from the Bigorne granite-hosted gold deposit in the Iberian Variscan Belt.

Statement of own contribution:

The lead author on this manuscript conducted fieldwork, sampling campaigns, preparation samples, carried out all analytical studies, and manuscript preparation. Co-authors provided technical support to the sampling process and suggestions in the field during analysis and manuscript preparation.

Research article 3: Ore Geology Reviews

Numão gold deposit in the Iberian Variscan belt, northern Portugal: ore features and mineralization controls. A gold deposit in a W-Sn metallogenic province.

Statement of own contribution:

The lead author on this manuscript led fieldwork, sampling campaigns, core logging and carried out all analytical studies, digital mapping, and manuscript preparation. Co-authors provided technical advice and suggestions in the field and sampling during analysis and manuscript preparation.

The content of each chapter can be summarized as follow:

Chapter 1 – Introduction

A brief introduction presents the source and relevance of the study. The scientific questions of the thesis are formulated. The general organization of the thesis is detailed there. This chapter includes state-of-the-art on a global and local scale of the gold mineralizations. It presents the different accepted metallogenic models proposed for the formation of gold deposits. A summary of the knowledge of gold metallogeny in Europe and Portugal is addressed.

Chapter 2 – Regional background

This chapter exposes the general organization of the Variscan belt in Western Europe and the geodynamic evolution of Variscan orogeny, emphasizing the Central Iberian Zone, which hosted a significant number of mineral deposits, including those that are the object of study in this project.

Chapter 3 – Research approach

This chapter has provided an overview of the workflow of the research project, including the main steps and the methodology applied in study areas. The detailed sampling techniques, sample processing, and analytical procedures are presented in chapters 4, 5, and 6.

Chapter 4 – Bigorne deposit

This chapter comprises a manuscript titled "*Geological setting of the Bigorne gold deposit, Iberian Variscan Belt (northern Portugal) and Au-Bi-Te mineral assemblages as indicators of the ore-forming conditions*" by Leal, S., Lima., A., Noronha, F., Mortensen, J., MacKenzie, D.

Chapter 5 – Bigorne detrital gold

Chapter 5 presents the manuscript titled "*Characterization of heavy mineral concentrates and detrital gold particles from the Bigorne granite-hosted gold deposit in the Iberian Variscan Belt*" by Leal, S., Lima, A., Noronha, F.

Chapter 6 – Numão deposit

This chapter comprises a manuscript titled "*Numão gold deposit in the Iberian Variscan belt, northern Portugal: ore features and mineralization controls. A gold deposit in a W-Sn metallogenic province*" by Leal, S., Lima., A., Morris, J., Pedro, M., Noronha, F.

Chapter 7 – General Conclusions

A key findings summary of the research is presented with an evaluation of project outcomes concerning the project aims. The implications of the research and future work are also presented.

1.4 Literature Review

Gold occurs as a primary commodity and/or a by-product in various mineral deposit types and geological settings. In the last decade, significant advancement has been made in the concept-based mineral system models, providing essential outlines for designing and evaluating exploration programs, and performing resource assessments of selected areas (Robert et al., 2007). Many debates on gold systems have arisen because of the extensive classification schemes and models proposed to explain several gold deposits that sometimes appear to be based on insufficient or vague definitions with mutually overlapping categories (Phillips and Powell, 2015). The determination standards are very variable between the different authors. Beyond these literature controversies, the critical motivation for deposits classifications is to provide tools that can be easily applied to gold exploration and exploitation different approaches required by each model (Phillips and Powell, 2015).

Since the modern era in gold exploration, there have been major advances in understanding and classifying a wide range of gold deposit types (Hart and Goldfarb, 2005). Lindgren, in 1933 was one of the first authors to observe a relationship between ore deposition in hydrothermal deposits and its physical environment, separating them into three classes: hypothermal, mesothermal, and epithermal. All over the years, several authors proposed a wide range of gold deposit classifications (*e.g.*, Lindgren, 1933; Emmons, 1933; Cox and Singer, 1986; Bache, 1987; Gebre-Mariam et al., 1995; Groves et al., 1998; Thompson et al.,1999; Sillitoe, 2000; Lang et al., 2000; Poulsen et al., 2000; Goldfarb et al., (2001, 2005); Robert et al., 2007; Hart, 2007; Goldfarb and Groves, 2015; Phillips and Powell, 2015; Mortensen et al., 2019; Groves et al., 2020) according to:

a) pressure, temperature, and crustal depth;

b) structural style (shear zone type, breccia pipe, sheeted veins);

c) mineralization types and hydrothermal signatures (ore and alteration mineralogy and chemistry);

d) age (Precambrian and Phanerozoic);

e) host rock-type (turbidite-, slate-, BIF-, magmatic-, intrusion-, greenstone-, or volcanic-hosted);

f) geographical terms (Motherlode-,Bendigo-, Homestake-, Carlin- and Korean-types).

The majority of hypogene gold deposits of the Earth’s crust are generated by fluxes of hot fluids (hydrothermal fluids) that are efficiently focused within relatively small volumes of rock (Garofalo and Ridley, 2014). In more recent times, with advances in analytical

knowledge, there was an increase in the development of new methodologies to find the source and types of the ore-forming metals and fluids (*e.g*., isotope analysis) and the timing of the gold mineralization (Groves et al., 2020). Nevertheless, these efforts intend to achieve the classification, definition, interpretation, and comprehension of the gold deposit types and provide models that can be applied to worldwide gold deposit examples.

Phillips and Powell (2015) highlighted a valuable and practical classification scheme for deposits with economic gold that distinguishes gold-only and gold-plus deposits based on the economic base metals content. A proportion of gold is extracted from gold-plus hydrothermal deposit types such as iron-oxide copper-gold (IOCG) deposits, porphyry deposits, and low- and high-sulfidation epithermal deposits as co-product with other metals, commonly with copper or silver (Phillips and Powell, 2015). However, significant global gold production is from gold-only deposits, with uneconomic concentrations of other base metals such as Cu, Pb, and Zn. This group includes orogenic gold- (OGD), some intrusion-related gold- (IRGD), and Carlin-type gold deposits.

According to the gold deposits literature records from NW of the Iberian Variscan belt, the below brief review only outlines the gold-only deposits due to the exclusive or dominant product being gold in all of them (Table 1). The main gold-only deposits types present in NW of the Iberian Variscan belt are:

- Carlin-type gold deposits commonly correspond to replacement ore bodies primarily described in the Carlin area (Nevada, USA), with irregular discordant breccia bodies and concordant strata-bound disseminated zones. These deposits have enrichment in many chemical elements, like As, Sb, Hg, and Tl. Clastic sedimentary rocks, greenstones, and rarely granitoid stocks hosted the mineralized structures (*e.g*., Cline et al., 2005).

  The deposits formed within a few kilometers of the Earth's surface from fluids at a temperature between ~180° and 240°C. The isotopic studies suggest multiple fluid sources, including meteoric, magmatic, and metamorphic (*e.g*., Saunders et al., 2014 and references therein). Carlin-type deposits formed at a limited time range (~42 to 36 Ma) due to continental rifting and passive margin sediments deposition, followed by the compressional orogenic stage (Cline et al., 2005). These deposits occur in many parts of the world (*e.g*., Yukon, Canada; Carlin, Nevada; Qinling, China; Salamón and El Valle, Spain).

- The IRGD (intrusion-related gold deposits) are the product of local-scale fluid convection that is likely derived from and driven by a cooling magmatic intrusion (*e.g*.,

Lang et al., 2000; Sillitoe and Thompson, 1998; Groves et al., 1998). The model further evolved into RIGS (reduced intrusion-related gold system) and OIGS (oxidized intrusion-related gold system). RIGS lacked proximal base-metal occurrences but links with W-Sn metallogenic provinces. Its low primary oxidation state differentiates this deposits group from IOCG deposits and many of the examples described by Sillitoe, 1991. The OIGS group includes the well-known porphyry, high-sulfidation epithermal gold deposit types, skarn, and mantle type deposits formed in continental and oceanic convergent plate settings (described as *gold-plus* deposits (Phillips and Powell, 2015)).

The RIGS is commonly hosted in metamorphic terranes and has a direct genetic link with felsic intrusions (*e.g.*, Hart, 2007). The deposit structure is zoning and includes: i) sheeted veins (intrusion-hosted deposits); ii) skarns, dissemination, and replacements (pluton-proximal deposits); iii) stockworks and breccias (pluton-distal deposits) (*e.g.*, Newberry, 1995; McCoy et al., 1997; Thompson et al., 1999; Lang and Baker, 2001; Hart and Goldfarb, 2005; Hart, 2007).

Metal zonation includes Au-Bi-Te±W in intrusion-hosted ores, with As-Au, As-Sb-Au, and Ag-Pb-Zn associations becoming apparent distally from causative plutons (Hart and Goldfarb, 2005; Hart, 2007). Vertical crustal-scale zonation is also apparent, with epizonal deposits forming at shallower levels (Hart, 2007).

The ore fluids are similar to those that characterize the OGD (Baker, 2002), making their distinction difficult. The most distinctive feature of RIGS is zoning in deposit type and crustal-scale vertical zonation (Hart, 2007).

- The concept of orogenic-type gold deposit (OGD) was first introduced by Böhlke (1982) and then thoroughly addressed by Gebre-Mariam et al. (1995) and Groves et al. (1998), followed by Goldfarb et al. (2001, 2005). The traditional classification of OGD is based on studies from some of the world's largest deposits, most of them hosted by Precambrian rocks, formed at mid-crustal levels in compressional or transpressional tectonic settings (*e.g.*, syntectonic vein-type deposits). They define a coherent group that formed in broad thermal equilibrium with their wall-rocks from low-salinity $H_2O–CO_2$ ore fluids at a broad spectrum of formation depth and temperature, including epizonal (≤6 km, 150°-300°C), mesozonal (6-12 km, 300°-457°C), and hypozonal (>12 km, >475°C crustal depths from 2 to 15 km, and arguably up to 20 km (Groves, 1993; Kolb and Meyer, 2002; Kolb et al., 2005, 2015).

  OGD group includes Precambrian to Phanerozoic deposits preferentially formed in compressional tectonic regimes that eventually lead to a continent-continent collision and crustal growth (Goldfarb et al., 2001).

However, in recent years the Crustal Continuum model has been thoroughly discussed (*e.g.*, Tomkins and Grundy, 2009; Phillips and Powell, 2009). This model suggests that OGD cannot form at metamorphic conditions beyond mid amphibolite facies due to the inhibited fluid flow at temperatures above approximately 600-650°C. Gold deposits hosted by rocks exposed to higher metamorphic conditions are assumed to have formed pre-peak metamorphism and subsequently overprinted by peak metamorphic conditions (Tomkins and Grundy, 2009) or have formed under retrograde PT conditions (*e.g.*, Kolb et al., 2015). So, OGD in amphibolite and granulite facies (hypozonal group) are, in fact, metamorphically overprinted greenschist deposits (Phillips and Powell, 2009; Kolb et al., 2015 and references therein). More recently, evidence suggests that the hypozonal group is post-peak metamorphic (Kolb et al., 2015; Groves et al., 2020). In addition to the fluid's uncertainty, defining the boundary between the OGD and RIGD models is not easy. Different authors ascribed many deposits to one model or another (*e.g.*, Thompson and Newberry, 2000; Goldfarb et al., 2001).

The Phanerozoic OGD group is anomalous compared to the typical Precambrian OGD, formed in low-grade metamorphic terranes, mostly greenschist, which generally contrast temporal-spatial relationships with regional metamorphism (Goldfarb and Groves, 2015 and references therein). In typical OGD, the ore fluid is considered to have been derived from the transition between low- to high-grade metamorphic rocks (Kerrich et al., 2005; Goldfarb and Groves, 2015; Groves et al., 2020). Nevertheless, the Crustal Continuum model hardly represents the genesis of Phanerozoic OGD. The subcrustal devolatilization model, in which fluid was derived from a metasomatized mantle, was proposed for these deposits (Goldfarb and Santosh, 2014; Zhao et al., 2019; Groves et al., 2020; Wang et al., 2020; Deng et al., 2020 and references therein). Concerning this debate, estimating the timing of mineralization relative to peak metamorphism is vital to understanding the formation of OGD. Goldfarb and Groves (2015) provide an exhaustive review of OGD genetic models, including the various geological, geochemical, isotopic, and fluid inclusion constraints on the component ore fluids and gold-related metals.

The models are developed and applied as a working tool in the mining industry and academy. They provide information about the system's complexity and guidance on the type of future proper measurements or observations. For instance, the improvement of internally consistent databases for gold deposits in a specific region (like North Portugal) allowed refining the modeling of physicochemical conditions of

the ore-forming fluids, contributing to the improvement and validation of the gold deposits models.

Table 1. Deposit-scale mineral system models for OGD, IRGD, Carlin-style deposits showing contrasts in many parameters at this scale (Groves and Santosh, 2015). Legend: Most similar to OGD; Contrast with OGD; Major contrast with OGD.

Parameter	OGS	IRGS	Carlin
Ore fluid	Low salinity H_2O-CO_2-CH_4	Low salinity H_2O-CO_2-CH_4	Low salinity H_2O-(CO_2)
T, P	200-650ºC 0.5-5 kbar	200-600ºC 0.5-1.5 kbar	180-240ºC 0.5-1.0 kbar
Major host rocks	Greenstones, turbidities	Shelf sedimentary	Shelf carbonates
Quartz veins	Abundant	Abundant	Absent
Metal zonation	Weak	Strong	Weak
Ore mineral zonation	Weak	Weak	Strong
Main metals	Au, Ag, As, Te, Sb, W, S	Au, Ag, Bi, Te, W. (Sn)	Au, As, Hg, Sb, Te
Main alteration elements	K(Na), CO_2, SiO_2	K(Na), CO_2, SiO_2	SiO_2 – CO_2
Compressional to extensional	Compressional	Mildly extensional	Mildly extensional

1.5 Gold metallogeny of northwestern Iberia

The Variscan belt in western Europe is a well-known metallogenic province that hosts several types of world-class Au, Cu-Zn, W-Sn, U deposits that have been mined for a very long time and are well documented (*e.g.,* Marignac and Cuney, 1999; Bouchot et al., 2005; Romer and Kroner, 2018; Timón-Sánchez et al., 2019 and references therein). The main gold provinces are located in the Bohemian Massif, the Armorican Massif, the French Massif Central, the Pyrenees and the Central Iberian Massif (Fig. 2-A). These mineral deposits are related to the European Variscan belt, which formed due to the closure of the Rheic Ocean during the Gondwana-Laurussia collision at the final assemblage of Pangea (Timón-Sánchez et al., 2019). As a whole, several authors have been defining three main age groups for Sn(W) mineral deposits in Europe, *e.g.*, 400-360 Ma, 335-310 Ma, and 300-275 Ma (*e.g.*, Romer and Kroner, 2016 and references therein).

However, gold mineralizations were generated during several periods of the geological history of Europe, which can be summarized as follows (Cassard et al., 2015 and references therein):

(1) In eastern Finland, the Ilomantsi region is marked by OGD related to greenstone belts (Neoarchean geologic era) (Vaasjoki et al., 1993). However, these deposits are of limited importance (Eilu et al., 2012) compared to significant gold districts in Australia or Canada (Goldfarb et al., 2001);

(2) the Palaeoproterozoic of the Fennoscandian Shield, and more precisely to the upper part of Palaeoproterozoic, from 1.9 to 1.8 Ga, related to the Svecokarelian orogeny. Gold mineralization can be associated with most volcanogenic massive sulfide (VMS), porphyry, and epithermal types, or with the younger orogenic type (Weihed et al., 2008; Eilu and Weihed, 2005);

(3) The Lower Paleozoic era is marked by a peak centered on the Ordovician, which essentially corresponds to gold-bearing VMS in the Caledonian domain of Scandinavia. They are also associated with a more widespread mineralization event in Great Britain and Portugal;

(4) The Upper Paleozoic is the gold mineralizing period widespread in the Variscan belt. The first mineralized event (upper Devonian and early lower Carboniferous) is related to VMS (*e.g.*, southern Iberian Massif (Iberian Pyrite Belt) or the Châteaulin basin (France)). The second event, traditionally classified as OGD by several authors (*e.g.*, Bouchot et al., 2005; MacKenzie et al., 2019), was related to the late evolution of the Variscan orogeny (late Carboniferous and early Permian times);

(5) Younger gold mineralizing events have been described along the Tethyan margin in the Balkan-Carpathian domain, related to the evolution of Southern Europe. Two events can be identified: an early Upper Cretaceous age corresponds to porphyry-type mineralization (Cu and Au), and the last one, of Cenozoic age, is essentially related to epithermal type mineralization.

Among the main gold metallogenic events recorded in Europe describe above, the period which covers the building of the European belt during Variscan orogeny is the most significant at the scale of the Iberian Variscan belt (Goldfarb et al., 2001; Frimmel, 2008).

Gold mineralizations are a prominent feature of the European Variscan belt, especially in the NW part of the Iberian Massif (Fig. 2-A-B). Most of the Iberian gold deposits were exploited during Roman times. Since then, mining has been intermittent and mainly restricted to the first half of the 20th century. Gold exploitation was revived between 1929-1993 in the Jales mine project, which produced approximately 830,000 ounces of gold with an ore grade of 12.9 g/t (Empresa de Desenvolvimento Mineiro-EDM, 2017). Nowadays, mining exploration continues in some deposits such as Corcoesto, El Valle-Boinás and Salave in Spain, Penedono, Bigorne, and Numão in Portugal (Fig. 2-B). Almost all of Portugal's gold mineralizations, distributed throughout few main deposits (estimated 352.81 tonnes; World Gold Council, 2021) and 216 recorded mineral occurrences (being 124 occurrences are in the north part of the country) (Martins, 2012; SIORMINP, 2021).

Diverse types of *gold-only* hydrothermal deposits have been identified in Iberia; however, several questions remain open, as discuss in the subsequent paragraphs.

These deposits include different types Carlin-like deposits (*e.g.,* Salamón and El Valle-Boinás: Crespo et al., 2000; Cepedal et al., 2008), orogenic gold deposits (*e.g.,* Corcoesto: Boiron et al., 1996, 2003; Tresminas, Noronha et al., 2000; Llamas de Cabrera: Gómez-Fernández et al., 2012; Tomiño: Urbano, 1998; Limarinho: Fuertes-Fuente et al., 2016; Penedono: Neiva et al., 2019; and Castromil: Vallance et al., 2003; Bigorne: Leal et al., 2021) and intrusion-related gold deposits (*e.g.,* Salave: Rodríguez-Terente et al., 2018; Linares: Cepedal et al., 2013; Bigorne: Caessa et al., 1998; Inverno, 2002; Jales: Rosa, 2001). As a whole, the Portuguese deposits have been classified as orogenic gold-type deposits (*e.g.,* Noronha et al., 2000; Boiron et al., 2003; Fuertes-Fuente et al., 2016; Neiva et al., 2019; Mackenzie et al., 2019). However, some authors consider some deposits link better with the intrusion-related gold deposit type (*e.g.,* Neiva,1945; Cerveira, 1952; Neiva et al., 1992; Rosa, 2001; Inverno, 2002). The spatial association of some Portuguese gold deposits with granitic intrusions is evident.

However, the genetic role of these intrusions in the mineralization process is not yet adequately addressed (see Chapters 4 and 5). They are comparable to the other late Paleozoic gold deposits in the Iberian Massif, French Massif Central, and Bohemian Massif (Table 2; Fig. 2). Most of them are considered post-metamorphic peak formed during the basement uplift in the late to- post-orogenic extensional phases of the Variscan orogeny (*e.g.,* Boiron et al., 1996, 2003; Noronha et al., 2000; Gómez-Fernández et al., 2012; Fuertes-Fuente et al., 2016). Paleozoic metamorphic sequences and Variscan granites (related to C3 deformation phase) host the main gold occurrences in northern Portugal, displaying a structural control with regional ductile and brittle shear zones (*e.g.,* Noronha et al., 2000; Mateus and Noronha, 2001).

Despite the issues on the fluid inclusion studies (*e.g.,* Goldfarb and Groves, 2015), this technique has been extensively applied in hydrothermal ore deposits (*e.g.,* Bodnar et al., 2014 and references therein), particularly in gold mineralization. The published fluid inclusion studies of Portuguese gold deposits revealed a dominance of an early-stage with aqueous-carbonic low-salinity fluids and low to moderate salinity aqueous fluids during the middle to late stages of the mineralizing event (Table 2). Assuming that the main period of gold deposition occurs associated with the late influx of superficial fluids, with relatively low temperature (*e.g.*, Noronha et al., 1993; Boiron et al., 1996; 2003; Nogueira, 1997; Noronha et al., 2000; Mateus and Noronha, 2001; Vallance et al., 2003; Fuertes-Fuente et al., 2016, Neiva et al., 2019). The studies mentioned above (Table 2) emphasize the involvement of the two ore-forming fluids for gold mineralizations in Portugal and Spain (*e.g.,* Gómez-Fernández et al., 2012) identical to those found in some deposits in French Massif Central (*e.g.,* Boiron et al., 1990; Bouchot et al., 2005) and Bohemian Massif (*e.g.,* Zachariáš et al., 2013).

The stable isotope ratios of various elements (*e.g.*, H, C, O, S) have numerous uses to improve understanding the genesis and formation of ore deposits and have various applications to mineral exploration (Barker et al., 2013). Ratios of the stable isotopes have been measured and applied to mineral deposit research since the 1950s to make out the origin and evolution of ore-forming fluids and metals (*e.g.,* Engel et al., 1958; Ohmoto and Goldhaber, 1997; Taylor, 1997). However, stable isotope data have not been routinely collected during mineral exploration and scientific researches in Portuguese gold mineralizations (Table 2). Previous studies (Rosa, 2001; Vallance et al., 2003; Fuertes-Fuente et al., 2016; Neiva et al., 2019) of the oxygen isotopes data on quartz from mineralized veins show a narrow range between 11 to 14 ‰, falling in both metamorphic and magmatic waters fields, defined by Taylor, 1974 for the origin of the

fluids. The sulfur isotope's data are variable (-0.1 to -9.2 ‰), alongside H isotopes values (-83.6 to -61 ‰).

The gold mineral assemblage shows a restricted relation with sulfides, mainly arsenopyrite. The arsenopyrite geothermometer data show early As-rich arsenopyrite with high temperatures formation followed by low temperature S-rich arsenopyrite, suggesting a progressive increase in the sulfur content and a decrease in the arsenic content as the temperature drops. These temperatures overlapped the temperatures yielding in the fluid inclusion studies (~400ºC to lower than 200ºC) (*e.g*., Boiron et al., 2003).

The available absolute ages of the gold deposits in northern Portugal are scarce. Dating Portuguese gold deposits is challenging because of the dating minerals' scarceness, such as molybdenites, carbonates, monazites, xenotime. The only absolute age was obtained in the Jales district by Neiva et al. (1992) and Rosa (2001) in muscovite yielding ~300 Ma for gold mineralization. The timing of the mineralization will be discussed in section 7.1 from chapter 7.

Based on mineral assemblage criteria from mineralized veins at the present erosion level, two major groups have been recognized by several authors in many gold deposits (*e.g.,* Couto et al., 1990; Noronha et al., 2000; Vallance et al., 2003; Fuertes-Fuente et al., 2016): Group 1) As-Fe-Au-(Bi); and Group 2) Au-Ag-(Cu)-Bi-Pb-Sb-(S). An early-stage (W-As) have been recognized in several gold deposits in northern Portugal. No clear evidence was found for gold deposition during this stage. This topic will be discussed in chapter 6.

Table 2. Main features of gold mineralizations in Northern Portugal, Northwest Spain, Bohemian Massif and French Massif Central.

Deposit	Bigorne (1)	Castromil (2)	Limarinho (3)	Penedono (4)	Campo/Jales/Tresminas (5)
Host rock	Biotite-rich granites	Biotite-rich granite and aplites	Two mica granites	Two mica and muscovite > biotite granites	Two mica granites and greenschist metasediments
Metamorphic conditions			T=500 to 550 °C P = 300 to 350 MPa	T = 761 ± 50 °C P = 5.0 ± 1.0 kbar	
Age of host rock (Ma)	309.6 to 303±8	305.3 ± 0.8	315 to 310	318 to 317 and 310.1 ± 1.1	311 ± 1 Ma
Mineralized structures geometry	N10º-40ºE	N30º- 80º	N30º - 40ºE; subvertical	N40º - 80°E to N10°E	N30º - 70ºE N120ºE
Mineralization style	Quartz + oxidized veins	Quartz veins + disseminated	Quartz veins	Quartz veins	Quartz veins + disseminated
Ore assemblage	Wf + Sch + Apy + Py + (Ccp) + Bi + Au	Py + Apy + Au + Ag + Pb	Apy + Py + Ccp + Pb + Zn	Po-As-Cu-Au-Ag-Bi-Sch-Pb	Po + Lo + Sch + Apy + Sph + Ccp + Au + Ag + Bi + Pb
Mineralization age	Younger than 303 Ma	Younger than 305 Ma	Younger than 310 Ma	Younger than 310 Ma	300.7 ± 2.8 Ma

Deposit		Bigorne (1)	Castromil (2)	Limarinho (3)	Penedono (4)	Campo/Jales/Tresminas (5)
Au fineness		963 – 770	819 - 654	1000 - 750	953 - 529	940 - 560
Apy geothermometer (TºC)		455 - 354		500 - 355	444 - 300	450 - 300
Chlorite geothermometer (TºC)				380 - 317		300 - 150
Sulfur isotope (‰) in arsenopyrite and mix sulfides		-2.8	-0.1	-9.2 – (-7.1)	-5.3 – (-4.3)	-2 - 2
Oxygen isotope (‰) in quartz		12.3 - 12	15.1 - 11.6	12.7 - 13.7		
Hydrogen isotope (‰)		-64.7 – (-62.5) (qz)		−24.2 – (−23.1) (chl)		
Fluid inclusions	Fluid composition	H_2O-NaCl-CO_2-(CH_4)	H_2O–CO_2–CH_4–NaCl	H_2O–CO_2(CH_4–N_2)–NaCl	H_2O–CO_2–CH_4–N_2–NaCl	H_2O-CO_2-CH_4-N_2
		H_2O-NaCl	H_2O–NaCl	H_2O–NaCl	H_2O–NaCl	H_2O–(NaCl)
	P–T Conditions (ºC)	350- 135	400 - < 200	330 to < 200	380 - 260	400 - 320
		350 - 100 MPa	300 - 100 MPa	200 - 60 MPa	300-150 MPa	
Sources of data		This study Leal et al., under review Leal et al., 2021	Vallance et al., 2003 Cruz et al., 2018 This study	Fuertes-Fuente et al., 2016	Boiron et al., 1996 Cathelineau et al., 1993 Neiva et al., 2019	Rosa, 2001 Neiva et al., 1995 Ribeiro et al., 1999

Table 2 (Cont.). Main features of gold mineralizations in Northern Portugal, Northwest Spain, Bohemian Massif and French Massif Central.

Deposit	Numão (6)	Valongo district (7)	Northwest Spain	Bohemian Massif	French Massif Central
Host rock	Metasediments	Metasediments	Magmatic and metasedimentary rocks	Magmatic and metasedimentary rocks	
Metamorphic conditions	Greenschist facies				
Age of host rock (Ma)	Paleozoic	Precambrian(?)and/or Cambrian to Devonian			
Mineralized structures geometry	N-S – N40º N100º				
Mineralization style	Quartz veins + disseminated	Quartz veins	Quartz veins + disseminated	Quartz veins + disseminated	
Ore assemblage	Sch + Po + Py + Apy + Ccp + Au + Bi + Ag	W-Sn + Au-Sb + Pb-Zn-Ag	W-Mo-Cu-Au–As (Ag–Pb–Zn–Cu–Sb)	Arsenopyrite–Pyrite–Pyrrhotite–Gold (±minor sulfides) -	Arsenopyrite–Pyrite–Gold (±sulfides)- Stibnite±sulfides and sulfosalts
Mineralization age			292.4 ± 1.2 – 270 Ma	340 - 310	340 - 290

Deposit		Numão (6)	Valongo district (7)	Northwest Spain	Bohemian Massif	French Massif Central
Au fineness		841 - 663				
Apy geothermometer (TºC)		502 - 381	400 - 340		395 - 475	
Chlorite geothermometer (TºC)		341 - 264		370 - 355		
Sulfur isotope (‰) in arsenopyrite and mix sulfides		-7.5 – (-7)		6 - 19	0.8 - 4.1	
Oxygen isotope (‰) in quartz		13 – 13.5		11.3 – 16.2	10.1 - 13	-1 - 12
Hydrogen isotope (‰)		-83.6 – (-72) (qz)				
Fluid inclusions	Fluid composition		H_2O–NaCl–CO_2(–CH_4)	CO_2–(CH_4) H_2O–NaCl–CO_2–(CH_4-N_2)	H_2O–NaCl–CO_2–(CH_4–N_2)	H_2O–NaCl–CO_2–(CH_4–N_2)
			H_2O–NaCl	H_2O–NaCl	H_2O–NaCl	H_2O–NaCl
	P–T Conditions (ºC)		340 - 128	390 - 180	450 - 130	550 - 200
				220 - <200 MPa	180 – 20 MPa	120 – 40 MPa
Sources of data		This study Leal et al., under review	Couto et al.,1990	Boiron et al., 1996 Cepedal et al., 2013 Rodríguez-Terente et al., 2018	Boiron et al., 1990 Groves et al., 1998 Zachariáš et al., 2013	Boiron et al., 2003 Bouchot et al., 2005 Cheval-Garabédian et al., 2020

CHAPTER 2 | Regional background

2.1 Geological Overview of the Iberian Variscan belt

The Variscan cycle and the formation of the European Variscan belt are linked throughout Europe to the development of a wide diversity of metallic and nonmetallic mineral resources (Romer and Kroner, 2016, 2018).

The main tectonism within the European Variscan Belt occurred during the amalgamation of Pangea in Upper Carboniferous times when the closing of the Paleozoic Rheic Ocean led to a complex and polycyclic collision between Gondwana and Laurussia (*e.g*., Matte, 2003; Nance et al., 2010; Kroner et al., 2016 and references within). The Variscan Belt is a continental-scale tectonic system (1000 km wide and >8000 km long) and has been subdivided into three main segments: Appalachians (Alleghanian belt), Variscides, and Urals (*e.g*., Matte, 2003; Simancas, 2019). The Variscides refer to the late-Paleozoic belt extending from Morocco to Iberia and Central Europe (Simancas, 2019).

The Iberia (Iberian Variscan belt) contains Gondwana affinity rocks (*e.g*., Murphy et al., 2016; Gutiérrez-Marco et al., 2017) and has been divided into six tectonostratigraphic zones, which reflect variable stratigraphic, structural, petrological features (Fig. 2: Lotze, 1945; Julivert et al., 1974; Farias et al., 1987). Pastor-Galán et al. (2020) make a brief description of each zone based on several authors:

(1) The Cantabrian Zone (CZ) represents a Gondwana thin-skinned foreland fold-and-thrust belt, representing the shortening developed during Mississippian times. It has overall low-grade internal deformation and metamorphism (*e.g*., Marcos and Pulgar, 1982; Pérez Estaún et al., 1988; Gutiérrez-Alonso, 1996; Alonso et al., 2009; Pastor-Galán et al., 2013);

(2) The West Asturian-Leonese Zone (WALZ) represents a metamorphic fold-and-thrust belt with Barrovian metamorphism. The collapse of this belt is coeval with thrust emplacement on top of the CZ (*e.g*., Martínez Catalán et al., 2014 and references therein);

(3) The Galiza-Trás-os-Montes Zone (GTMZ) represents the allochthonous terranes that contains high-pressure units and relicts of oceanic-like crust (*e.g*., Julivert et al., 1974; Farias et al., 1987; López-Carmona et al., 2014; Martínez Catalán et al., 2019);

(4) The Central Iberian Zone (CIZ) represents the Gondwana hinterland with Barrovian and Buchan metamorphisms. This zone is characterized by a significant number and types of magmatic rocks with different ages (*e.g*., Julivert et al., 1974; Farias et al., 1987; Díez Balda et al., 1995; Ribeiro et al., 1990; Gutiérrez-Alonso et al., 2018);

(5) The Ossa-Morena Zone (OMZ) represents the most distal zone of the Gondwana platform and is characterized by a metamorphic fold-and-thrust belt with dominantly sinistral displacement (*e.g.*, Quesada, 2006);

(6) The South Portuguese Zone (SPZ) represents a foreland fold-and-thrust belt with minor internal deformation and metamorphism with Avalonian affinity and a solid sinistral component of shear (*e.g.*, Pereira et al., 2012; Pérez-Cáceres et al., 2016; Oliveira et al., 2019).

These tectonostratigraphic zones are usually continuous in the Iberian Variscan belt, with roughly parallel boundaries separated by low- or high-angle crustal-scale shear zones (*e.g.*, Martínez Catalán et al., 2007; Ribeiro et al., 1990). The boundaries between them are major Variscan thrust- and reverse faults (Fig. 3), which were in some instances reactivated by extensional tectonics in post-Variscan time (Nance et al., 2010).

2.1.1 Deformation events and metamorphism

The Variscan orogeny in Iberia shows multiple deformation, metamorphic, and magmatic events (*e.g.*, Martínez Catalán et al., 2014; Azor et al., 2019; Fig. 2) that evolved diachronous from the suture towards the external zones (Dallmeyer et al., 1997).
Pastor-Galán et al., 2020 describe the following events based on several others research referenced in his paper: (1) an initial continent-continent collision began ca. 370 - 365 Ma, which produced high-pressure metamorphism (*e.g.*, López-Carmona et al., 2014); (2) a protracted shortening phase occurred between 360 and 330 Ma, frequently divided into main phases C1 and C2, that was accompanied by Barrovian-type metamorphism (*e.g.*, Dias da Silva et al., 2020) and magmatism at 340 Ma (*e.g.*, Gutiérrez-Alonso et al., 2018); (3) at 333 - 317 Ma, the development of an extensional collapse event (E1), forming core complexes and granitic domes in the CIZ and WALZ (*e.g.*, Dias da Silva et al., 2020 and references therein). The E1 event is coeval with forming the foreland fold-and-thrust belt formation in the CZ (*e.g.*, Gutiérrez-Alonso, 1996); (4) a late Carboniferous shortening event (C3: 315 - 290 Ma) related to the formation of the Cantabrian Orocline and being accompanied by the emplacement of mantle-derived intrusions (*e.g.*, Gutiérrez- Alonso et al., 2011; Pastor-Galán et al., 2012); (5) the formation of core complexes and regional uplift in the CIZ are related to the final early Permian extensional event (E2) (Dias da Silva et al., 2020); and (6) A final shortening event (C4), possibly coeval with E2, resulted in widespread brittle deformation (*e.g.*, Azor et al., 2019). The compressional Variscan stages are all highly diachronic, with ages getting younger from the CIZ towards the CZ, thus revealing an eastward progression of the orogenic front (Dallmeyer et al., 1997; Martínez Catalán et al., 2014). These

structures were defined in the Autochthon and affected the Allochthon, which was emplaced during C2.

2.1.2 Magmatism

The large production of granitic rocks is an essential fingerprint of magmatism throughout the Variscan cycle in the Iberian Variscan belt, especially in its northern and central domains (GTMZ, CIZ, and WALZ). In the South of Iberia, especially at the border of OMZ, adjacent to the SPZ, the mafic and intermediate rocks are much more abundant (Ribeiro et al., 2019).

The sequence of magmatic events (pre-variscan and Variscan) recorded in the rocks of Iberia (*e.g.*, Gutiérrez-Alonso et al., 2018 and references therein) can be summarized as follows: (1) a subduction-related Cadomian event (ca. 600 Ma) dominated by I-type granitoids and volcanic rocks, which is scarcely represented in NW Iberia; (2) a voluminous extension-related late Cambrian to an early Ordovician event (ca. 490-470 Ma), generally interpreted to be linked with to Rheic Ocean opening; (3) a volcanic event ca. 400–390 Ma scarcely represented; (4) a Carboniferous syn-orogenic (Variscan) event concentrated between ca. 325 and 315; and (5) a post-orogenic event (ca. 305-290 Ma), related to the emplacement of voluminous granitoids and some mafic rocks with their extrusive equivalents in the internal and external zones of the orogen. This post-orogenic magmatism is observed throughout the Variscan belt (*e.g.*, Kroner and Romer, 2013).

The case studies are located in the NW of the Iberian Massif, more precisely in CIZ; therefore, the regional geology of this tectonostratigraphic zone will be described in the next section (2.2).

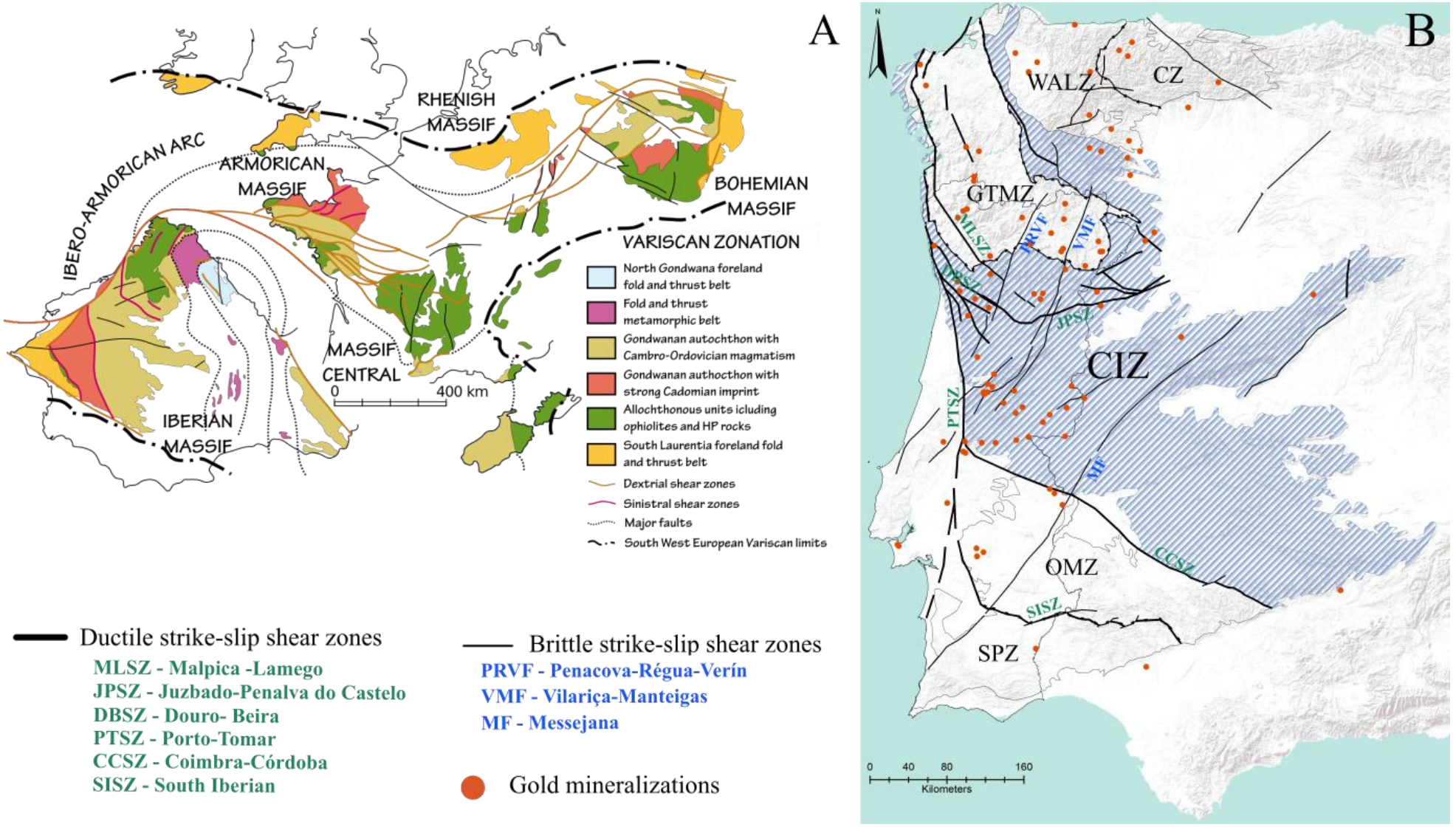

Fig. 3. (A) Schematic map of the different zones in the European Variscan belt (adapted from Pastor-Galán et al., 2012). (B) Map of the Iberian Variscan belt showing major geotectonic zones and main regional structures (adapted from Díez Fernández and Arenas 2015). The main gold occurrences in Iberia (data from SIORMINP and IGME).

2.2 Central Iberian Zone (CIZ)

The CIZ represents the axial zone of the Iberian Variscan belt (Fig. 4) and is limited at north by the Olho-de-Sapo antiform (Julivert et al., 1974). At west and south, the CIZ is limited by the Porto-Tomar-Ferreira do Alentejo and Tomar-Badajoz-Córdoba shear zones, respectively (Fig. 3-B; Dias et al., 2016; and references therein).

The CIZ comprises three different rock types domains: (1) the Ollo de Sapo domain (Paleozoic rocks in Fig. 4); (2) the "Schistose-Greywacke domain," and (3) Variscan magmatic rocks. The Olho de Sapo domain contains abundant lower Ordovician magmatism of calc-alkaline affinity (*e.g.*, Gutiérrez-Marco et al., 2019 and references therein). The autochthonous of the CIZ is marked by the predominance of pre-Ordovician sequences (SGC-Schist Greywacke complex), lower Ordovician quartzites with transgressive character, and the presence of an unconformity separating the lower Ordovician from Precambrian-Cambrian rocks (Martínez Catalán et al., 2014). The Variscan magmatic rocks in CIZ will be described in section 2.2.2.

2.2.1 Deformation events and metamorphism

A deformational sequence has been proposed for the NW of the Iberian Variscan belt, during the early Carboniferous to the early Permian times. This sequence include three major compressional (C1, C2 and C3) and two major extensional (E1 and E2) Variscan events (Martínez Catalán et al., 2014; Dias da Silva et al., 2020). It is important to clarify that D1, D2 and D3 deformation phases (Noronha et al., 1978; Ribeiro et al., 1990) are equivalent to the Martínez Catalán et al., (2014) nomenclature C1, C2 and C3.

Most of the authors considered the extensional events related to the extensional collapse of the orogen (*e.g.*, Martínez Catalán et al., 2014; Ballèvre et al., 2014). Although, for others (*e.g.*, Ribeiro et al., 2007; Dias et al., 2013), these events could result from local compressions related to the allochthonous/autochthonous units.

The C1 deformation phase, which is more widespread at the regional scale (Noronha et al., 1978; Ribeiro et al., 1990), produced overturned to recumbent folds with axial planar cleavage (S1) that assumes an E-W direction at east changing to the NW-SE orientation next to the coast, shaping the south branch of the Ibero-Armorican Arc (Dias et al., 2013; Ribeiro et al., 1990). The C1 took place between ~360–350 Ma (Dallmeyer et al., 1997; Martínez-Catalán et al., 2014; Azor et al., 2019 references therein).

The C2 deformation phase is associated with the emplacement of the allochthonous nappe pile at NW of Iberia. Thus, the D2 (~345-330 Ma; Dallmeyer et al., 1997; Martínez-Catalán et al., 2014; Azor et al., 2019) is well represented at the base of the allochthonous and parautochthonous units in GTMZ. Prograde Barrovian metamorphism

(known as M1) reached its pressure peak at the end of C2 (Rubio Pascual et al., 2013; Pastor-Galán et al., 2020).

After the allochthonous complexes emplacement, a thermal relaxation period occurred with the heated thickened crust, triggering the synorogenic extensional collapse arising from the first extensional event (E1; Alcock et al., 2015; Martínez Catalán et al., 2014). General decompression produced a Buchan-type metamorphic event (M2), characterized by high temperature and low pressure conditions (*e.g*., Rubio Pascual et al., 2016) and widespread anatectic melting (*e.g*., López-Moro et al., 2018; Pereira et al., 2018; Pastor-Galán et al., 2020).

C3 produced vertical folds with subhorizontal axes and subvertical strike-slip shear zones, both right and left lateral (*e.g*., Martínez Catalán et al., 2014). C3 was coeval with regional retrograde metamorphism (M3) and the intrusion of mantle-derived granitoids surrounded by contact metamorphic aureoles. M3 is characterized by a regional decrease of temperature and pressure, simultaneously with the development of C3 structures, associated with late Variscan exhumation (315-300 Ma; Martínez Catalán et al., 2014; Alcock et al., 2015).

The folding and the shear zones associated with the C3 deformation phase contributed to the definition of the Ibero-Armorican Arc (Ribeiro et al., 1990; Dias et al., 2013). The C3 folds occur frequently related to ductile strike-slip shear zones and are coeval with the emplacement of syntectonic granites (~315–305 Ma; (*e.g*., Dias et al., 1998; Valle Aguado et al., 2005). The late stages of crustal extension (E2) continued during and after C3, producing new migmatitic domes with brittle-ductile faults developed at their limits.

2.2.2 Magmatism

Collisional (331-310 Ma) and post-collisional (310-280 Ma) granite magmatism is a prominent feature in the CIZ and GTMZ and displays a wide diversity of Variscan granite types (Fig. 2 and 3). There are S-type peraluminous and I-type granites, including rare metaluminous varieties and granites with transitional features between S and I-type (*e.g*., Dias et al., 1998, 2002; Castro et al., 2002; Bea, 2004; Neiva et al., 2012; Villaseca et al., 2014; Martínez-Catalán et al., 2014; Teixeira et al., 2017; Pereira et al., 2018).

The Variscan magmatic rocks occupy more than 50%, on average, of the CIZ basement. Minor intermediate and mafic rocks, ranging in composition from gabbro to quartz-diorite, monzonite, and tonalite, are also widespread, forming small plutons and complexes (Ribeiro et al., 2019).

The main magmatic events recorded in CIZ are synorogenic magmatism (Syn-C3) and post-orogenic magmatism (post-C3) (*e.g*., Gutiérrez-Alonso et al., 2018; Ribeiro et al., 2019; Hildenbrand et al., 2021).

The synorogenic magmatism comprises:

1) Two-mica synextensional collapse granitoids (ca. 331–310 Ma), mostly crustal (S-type) peraluminous leucogranites. These granites result from the crystallization of wet peraluminous magmas generated by the melting of the aluminous metasedimentary middle/lower-crustal sources, with a significant pelitic contribution related to the orogenic metamorphism (*e.g*., Almeida et al., 1998; Dias et al., 2002; Valle Aguado et al., 2005). These granites formed in the core of thermal domes coincident with late Variscan large-scale antiforms (Hildenbrand et al., 2021 and references therein).

(2) Biotite-rich granites complexes (320-305 Ma: syn-to late-C3 biotite granites). These granite complexes are composed of: (i) biotitic monzogranites, moderately peraluminous, with magnesian and alkali-calcic affinity, and less enriched isotopic signature. They are also S-type, suggesting significant participation of metaigneous protoliths or immature metasedimentary sources. An origin by partial melting metagraywackes and/or felsic metaigneous lower crust materials in the granulitic facies is proposed (Almeida et al., 1998; Dias et al., 1998, 2002; Simões, 2000; Valle Aguado et al., 2005; Costa, 2011; Martins et al., 2013, Ribeiro et al., 2019). (ii) biotitic monzogranites/granodiorites with abundant mafic microgranular enclaves, weak to moderate peraluminous character with alkali-calcic magnesian signature (granitoids syn-D3) or alkali-calcic magnesian-ferroan and more depleted isotopic signature (Ribeiro et al., 2019). Some pre to syn-C3 granodiorites (early granodiorites: 347-337 Ma) were classified based mainly on the visible tectonic foliation and a more mafic composition than the synextensional granitoids and were interpreted as being deeper-seated intrusions than the POS (e.g., Ferreira et al., 1987; Hildenbrand et al., 2021). The biotite-rich granites are distributed parallel to ductile shear zones trending NNW-SSE, ENE-WSW, and NNE-SSW (Ferreira et al., 1987; Dias et al., 2002; Valle Aguado et al., 2005).

The post-orogenic magmatic rocks (ca. 305–280 Ma) intrude all the structural domains of the orogen. They include weakly metaluminous granites with calc-alkaline-K and ferroan affinity and depleted isotopic composition compared to the remaining granitoid groups (Ribeiro et al., 2019). Beyond the granites, the post-C3 suite includes a large number of minor intrusions of mafic and ultramafic rocks (*e.g*., Sant'Ovaia et al., 2000; Martins et al., 2009; Villaseca et al., 2012; Gonçalves et al., 2020; Cruz et al., 2020;

Oliveira et al., 2020). Some authors interpreted this group as generated by lithospheric delamination triggered by the oroclinal bending of the mountain belt in a geodynamic context of extensional processes (*e.g*., Fernández-Suárez et al., 2000; Gutiérrez-Alonso et al., 2011; 2018 and references therein).

2.2.3 Regional structures

Strike-slip shear zones are structures with enhanced permeability and, therefore, a channel fluid flow (*e.g*., McCaig, 1988; López-Moro et al., 2019) that eventually may generate metasomatic processes and occasionally result in the mineral deposits formation (*e.g*., Dipple and Ferry, 1992; González-Clavijo et al., 1993; Pereira et al., 1993; López-Moro et al., 2019 and references therein).

A complex network of major shear zones (ductile and brittle) was developed during the deformation events of the Variscan orogeny. The timing and kinematics of the major ductile shear zones are still under debate. These structures in CIZ have been interpreted as structures developed during the C1 event by several authors (*e.g*., Díez-Balda et al., 1990; Ábalos et al., 1992; Dias and Ribeiro, 1994; Dias et al., 2016) and the C3 event possibly nucleated within existing C1-C2 structures (*e.g*., Dias da Silva et al., 2017).

Dextral strike-slip shear zones are predominantly sub-parallel to the main NW-SE Variscan structures. However, one of the most prominent ones (the N–S trending Porto-Tomar-Ferreira do Alentejo shear zone) is oblique. In contrast, most of the sinistral shear zones are oriented oblique, ENE-WSW. These shear zones have been interpreted as follows: 1) part of a major dextral shear zone between the Appalachians and the Urals (Arthaud and Matte, 1975); 2) result of a curve effect during the continental collision (Brun and Burg, 1982); 3) escape structures around a rigid indenter, which is inferred to form the core of the Cantabrian Arc (Dias and Ribeiro, 1995; Ribeiro et al., 2007); 4) a response to an N-S compressive stress field (Marques et al., 2002); 5) large-scale structures that accommodated oblique (dextral) convergence between Gondwana and Laurussia (Martínez-Catalán, 2011; Shelley and Bossière, 2000); and finally 6) the result of dominantly dextral shear and less pervasive conjugate sinistral shearing attributable to the oroclinal buckling that gave rise to the Cantabrian Arc (Gutiérrez-Alonso et al., 2004, 2008).

The relative timing of major ductile strike-slip shear zones was previously constrained to ca. 315-295 Ma using structural relations with granites of known age that were either deformed by the shear zones or cut cross them (Valle Aguado et al., 2005; Valverde-Vaquero et al., 2007; Martins et al., 2009; Gutiérrez-Alonso et al., 2011; Díez-Fernández et al., 2016). Although Gutiérrez Alonso, 2015 based on direct Ar-Ar dating of the shear

zones and cross-cutting relationships with precisely dated igneous rocks, infer that some of them were active during the period 315-305 Ma. Note that these shear zones show a younger age concerning the sinistral shear zones that bound the OMZ and SPZ (340-330 Ma; *e.g*., Dallmeyer et al., 1993).

The N-S shortening (in present-day coordinates) of C3 deformation structures continued through the early Permian under brittle conditions (so-called C4 event – late Variscan stages) (*e.g*., Marques et al., 2002; Dias da Silva et al., 2020) and overlapped with the formation of E2 extensional faults (Dias and Ribeiro, 1991; Dias da Silva et al., 2020). During the C4 event, an N–S compression produced a series of NNE-SSW and NNW-SSE brittle faults (Arthaud and Matte,1975; Dias and Ribeiro, 1991; Marques et al., 2002).

Major NNE-SSW sinistral strike-slip fault zones are relatively late features that cut across the deformed metasedimentary and intrusive rocks. Locally they appear to be contemporaneous with localized emplacement of some post-tectonic intrusions (Martins et al., 2009). In the Iberian Massif, this late Variscan deformation gave rise to some of the most essential observed basement faults, like Vilariça-Manteigas (VMF) and Penacova-Régua-Verin faults (PRVF) (Ribeiro et al., 1990; Marques et al., 2002; Moreira et al., 2010; Dias et al., 2013).

This geometry and kinematics concluded that an N–S maximum compressive stress was responsible for developing the brittle network in northern Portugal. Ribeiro (1974), Ribeiro et al. (1979), and Pereira et al. (1993) defined two main episodes of Variscan faulting: (1) two conjugate systems, bearing in average N80º (sinistral) and N25º (dextral), contemporaneous with C3 (the last Variscan folding phase with axial planes striking approximately N135º); and (2) late-Variscan strike-slip faulting with a dextral N135º system conjugate to a sinistral N25º family, Permian in age. The argument used for the relative age of both systems was that they cut the C3 structures and post-C3 granites (300-270 Ma). A lower limit to the age of the Late-Variscan wrench-faulting episode is established by K-Ar isotope dating of fault rocks; this age is ca. 312 Ma (Marques et al., 2002). In W Iberia, the upper limit of the late- Variscan strike-slip faulting age must be somewhat younger than 270 Ma because this is the youngest age of post-kinematic granites cut by late-Variscan faulting (Marques et al., 2002).

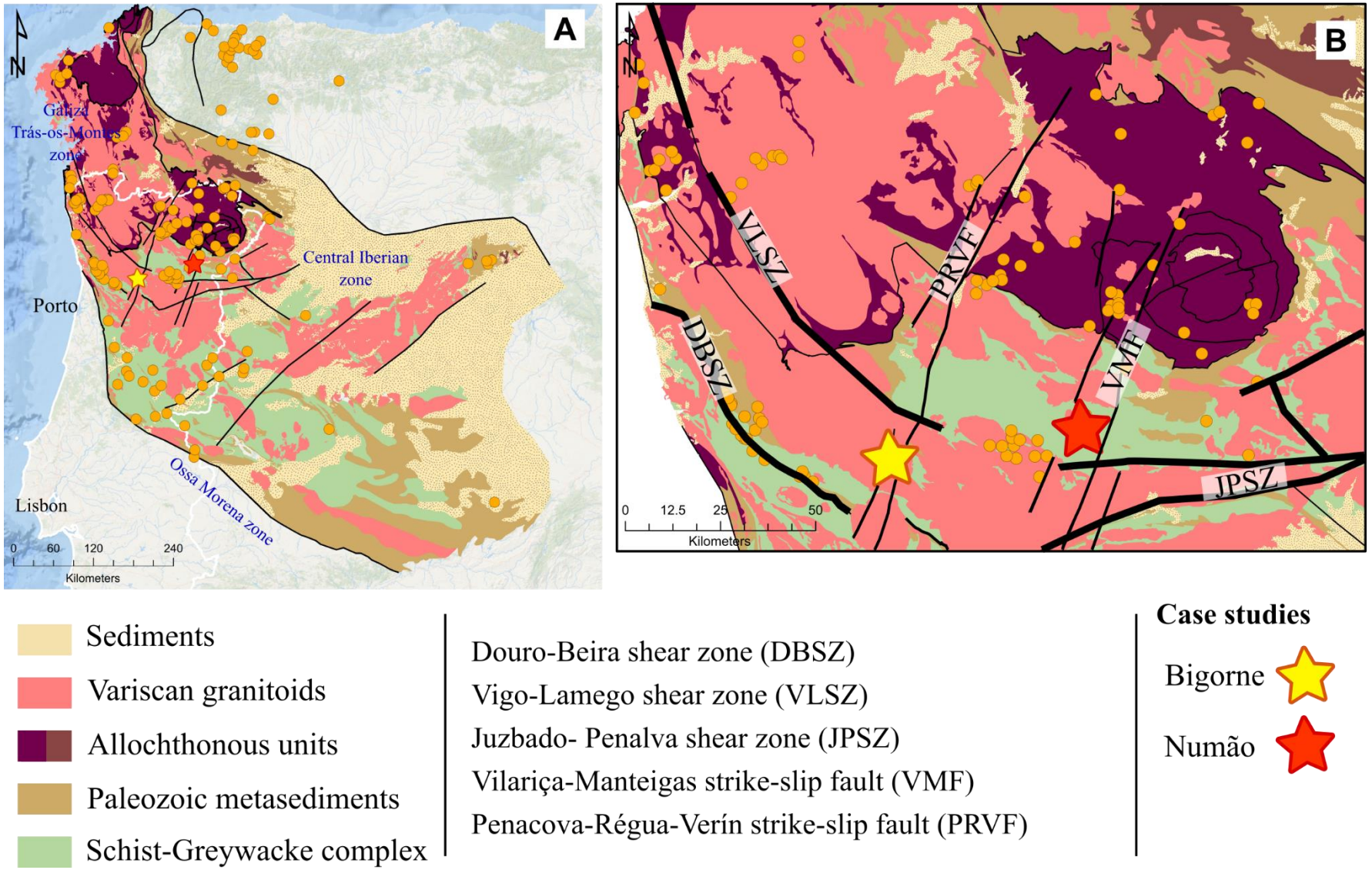

Fig. 4. (A) Geological sketch of the Variscan Belt in western Europe (modified from Martínez-Catalán et al., 2007; Villaseca et al., 2014) and gold deposits within the Central Iberian Zone highlight the case studies. B- Simplified geology of northwestern Portugal highlighting the main regional structures in the Bigorne and Numão area

CHAPTER 3 | Research approach

3.1 Research approach

As previously mentioned, the focus and the central aim of the research was developing and accessing an unusual gold exploration technique in Portugal (Chapter 5), contributing with new data (field and analytical data) for the case studies (Chapters 4 and 6), Bigorne and Numão areas (Fig. 4). The project was focused on the same research methodology for the two case studies (Fig. 5) to answer the thesis's central questions (section 1.2).

Nevertheless, the Numão case study represents a rare opportunity to study a mineralized system in the early stages of mining, contributing with new and supportive data in the gold mineral processing. The sampling and data interpretation strategy workflow included Geographic Information Systems (GIS) software to integrate all data and lithological mapping.

The main steps and strategies applied to develop this work are presented in Fig. 5.

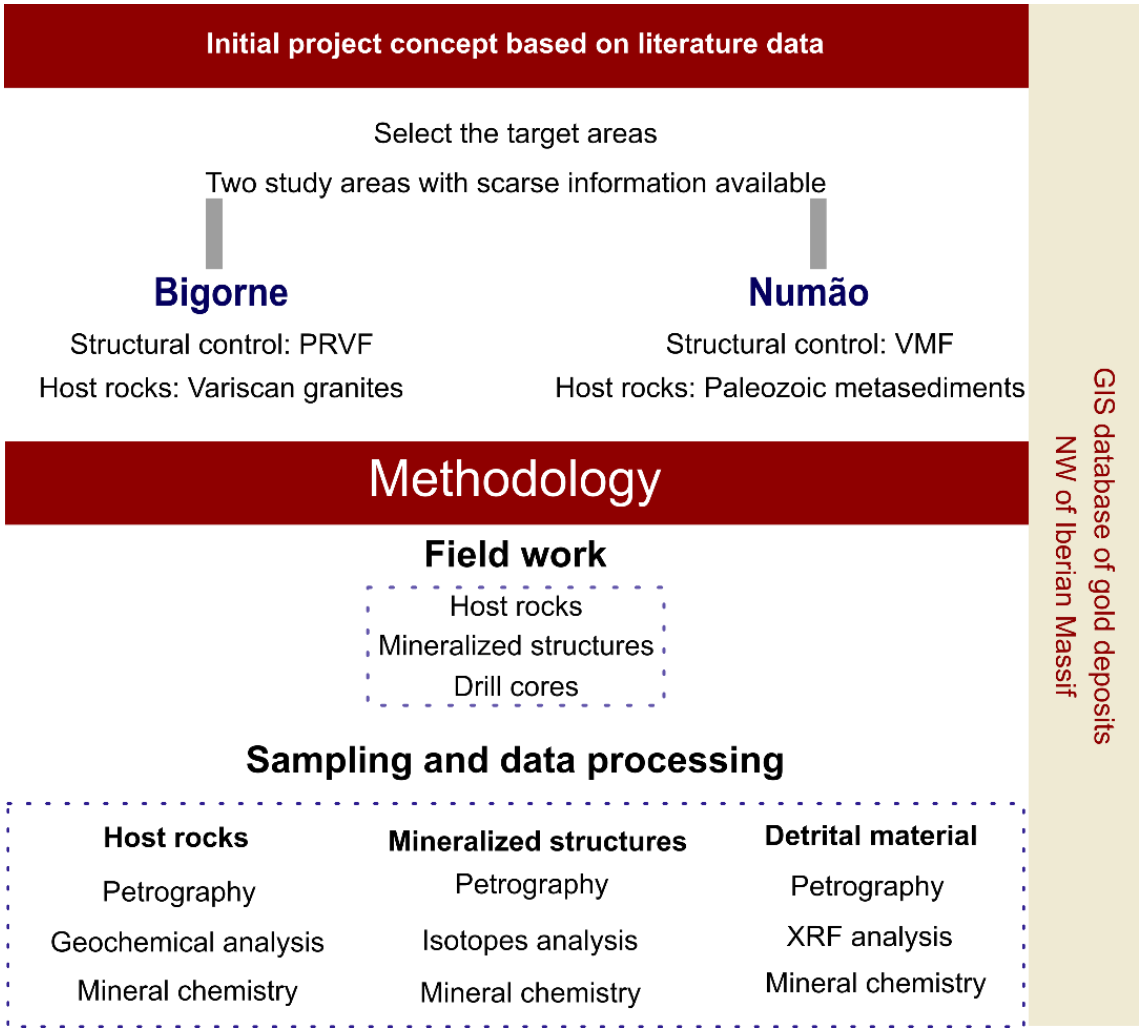

Fig. 5. Description of the working methodology.

CHAPTER 4 | Bigorne deposit

Manuscript 1: Ore Geology reviews (*under review*)

Geological setting of the Bigorne gold deposit, Iberian Variscan Belt (northern Portugal), and Au-Bi-Te mineral assemblages as indicators of the ore-forming conditions (2021)

Sara Leal[1,2*], Alexandre Lima[1,2], Fernando Noronha[1,2], James Mortensen [3], Doug MacKenzie[4]

[1] Institute of Earth Sciences (Pole-Porto), Porto, Portugal

[2] Department of Geosciences, Environment and Spatial Planning, University of Porto, Porto, Portugal

[3] Department of Earth, Ocean and Atmospheric Sciences, University of British Columbia, 2020-2207 Main Mall, Vancouver, British Columbia V6T 1Z4, Canada

[4] Geology Department, University of Otago, PO Box 56, Dunedin, 9054, New Zealand

Highlights:

The spatial association of several important gold deposits in the NW portion of the Iberian Massif (Portugal) with their hosted granitic intrusions is evidently (*e.g.*, Jales, Ponte da Barca, Penedono, Castromil, Bigorne, Limarinho; Fig. 6). The nature and genesis of some granite-hosted gold deposits in the region include the Bigorne deposit (Fig. 6-C), are still not well understood. Previous work on deposit geology and mineralogy interpreted Bigorne as an intrusion-related gold system (Caessa et al., 1998; Inverno, 2002).

The present work describes the ore mineralogy, mineral chemistry, position of gold in the paragenetic sequence, and hydrothermal alteration at the Bigorne deposit, which help define the parameters that have controlled the ore-forming process. In particular, the mineralogical and thermodynamic stabilities of Au-Bi-Te-(S) phases present in the deposit are investigated to constrain the thermal evolution of all mineralization stages. The source of fluid components in the Bigorne deposit are investigated using sulfur, hydrogen, and oxygen isotopic compositions of minerals co-deposited with gold-bearing sulfides. The study's main goals are to constrain the regional-scale metallogenic evolution of the Iberian Massif, comparing the Bigorne deposit with other granite-hosted gold deposits in northwestern Iberia, and evaluate the role of the host intrusions in the mineralization process. Results of the work contribute to the development of genetic and exploration models for Iberian gold deposits.

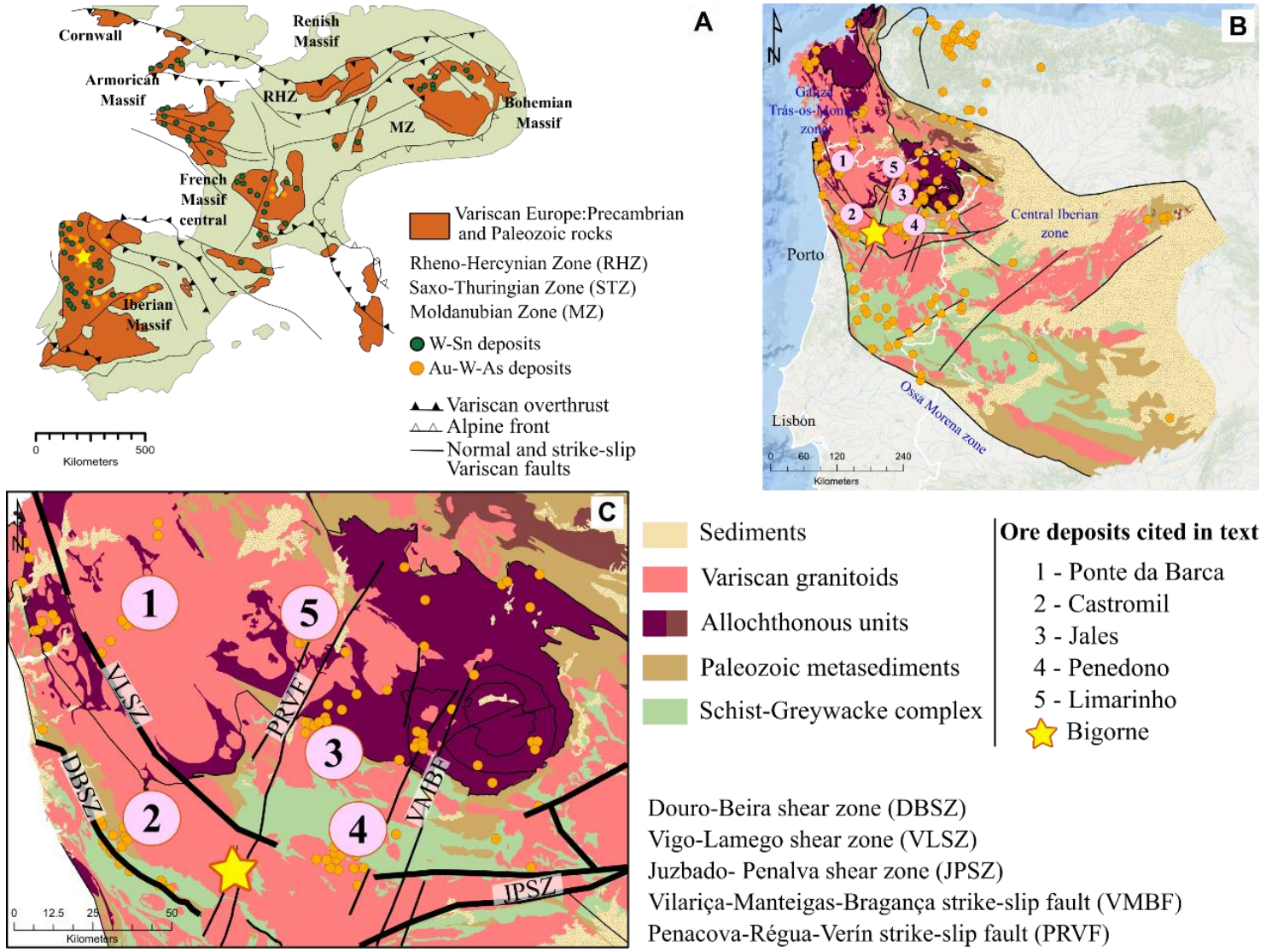

Fig. 6. (A) Map of the Variscan belt in central and western Europe (modified from Díez-Montes, 2007; Timón-Sánchez et al., 2019) and major W-Sn and Au-W-As deposits. (B) Geological sketch of the Variscan Belt in western Europe (modified from Martínez-Catalán et al., 2007; Villaseca et al., 2014) and the main granite-hosted gold deposits contained within the Central Iberian Zone. (C) Simplified geology of northwestern Portugal highlighting the main regional structures in the Bigorne area.

4.1 Local geology setting

The Bigorne deposit is located in the CIZ in northern Portugal (Fig. 1-B, C). The deposit area is underlain by Variscan felsic intrusive rocks and Early Palaeozoic metasedimentary rocks. The metamorphic sequence was variably affected by regional metamorphism and deformation during the Variscan orogeny (Fig. 6-C).

4.1.1 Metasedimentary rocks

Metasedimentary rocks in the Bigorne area are variably metamorphosed and include: i) pre-Ordovician lithologies, which constitute a thick and monotonous sequence of pelites and greywackes, generally referred to as Schist Greywacke Complex (SGC) (Carrington da Costa, 1950); ii) an Ordovician clastic succession of stable marine platform sandstones, and iii) Silurian black schist (Fig. 7-A). The emplacement of voluminous felsic magmas generated low-P-high-T metamorphic contact aureoles in which pelites, sandstones, and greywackes were transformed into slate, quartzite, phyllite, spotted schist, and hornfels.

4.1.2 Intrusive rocks

Variscan granitoids underlie about 90% of the Bigorne area (Fig. 7-A) and include several mappable intrusive phases, each with different mineralogical characteristics. They make up part of an extensive, composite massif termed the Lamego massif by Pereira et al., (2018), consisting mainly of biotite and biotite-muscovite granites (Ferreira et al., 1987; Carvalho et al., 2012). The various intrusive phases form NW-SE elongated bodies corresponding to the main orientation of the NW Iberian Variscan Belt. The Lamego massif that hosts the Bigorne deposit is bounded between two NW-SE-striking ductile shear zones: the Douro Beira shear zone (DBSZ) and the Vigo-Lamego shear zone (VLSZ) (Fig. 6-C). No geochronological data exist for the intrusions in the immediate Bigorne area. However, ages for the local granitoids can be inferred by comparison with similar intrusive phases from elsewhere in the Lamego massif. The intrusive sequence in the Bigorne area (Fig. 7-A) is therefore interpreted as follows: (1) pre-to syn-D3 biotite granite (U-Pb: 319 ± 4 Ma) and (2) volumetrically dominant late-D3 and late- to post-D3 granodiorite-monzogranite and muscovite-biotite granite (U-Pb: age range of 309.6 ± 1 Ma to 303.3 ± 8.1 Ma) (Dias et al., 1998; Costa, 2011; Carvalho et al., 2012).

4.1.3 Structural geology

The overall ductile and brittle structures (dated at ca. 307 Ma; Gutiérrez-Alonso et al., 2015) of the region are mainly related to late Variscan (D3 and post-D3) tectonism. Three

major crustal-scale structures are present in the Bigorne area (Fig. 6-C): (1) the NW-SE striking DBSZ; 2) the NNW-SSE to NW-SE striking VLSZ; and (3) NNE-SSW striking PRVF strike-slip fault. The DBSZ and VLSZ are somewhat older and are generally interpreted to have accommodated mainly dextral deformation (coeval ages cluster around 308 Ma; Gutiérrez-Alonso et al., 2015). The PRVF is thought to have nucleated during D3 as a dextral strike-slip fault and subsequently reactivated as a sinistral structure with a transtensional component in late-Variscan times (Pereira et al., 1993; Marques et al., 2002). Although the PRVF traverses the Bigorne study area, there is only limited evidence for significant strike-slip displacement. Several more minor faults parallel to the PRVF are also present, and many of these show minor (<1-2 km) sinistral displacement of NW-SE trending bands of metasedimentary rocks (Fig. 7-A). An important alluvial deposit along the Balsemão River west of Bigorne corresponds to an NNE-SSW-trending lineament that is tentatively interpreted to mark a fault zone and possibly a small down-dropped graben structure that formed late in the evolution of the PRVF (Fig. 7-A-B).

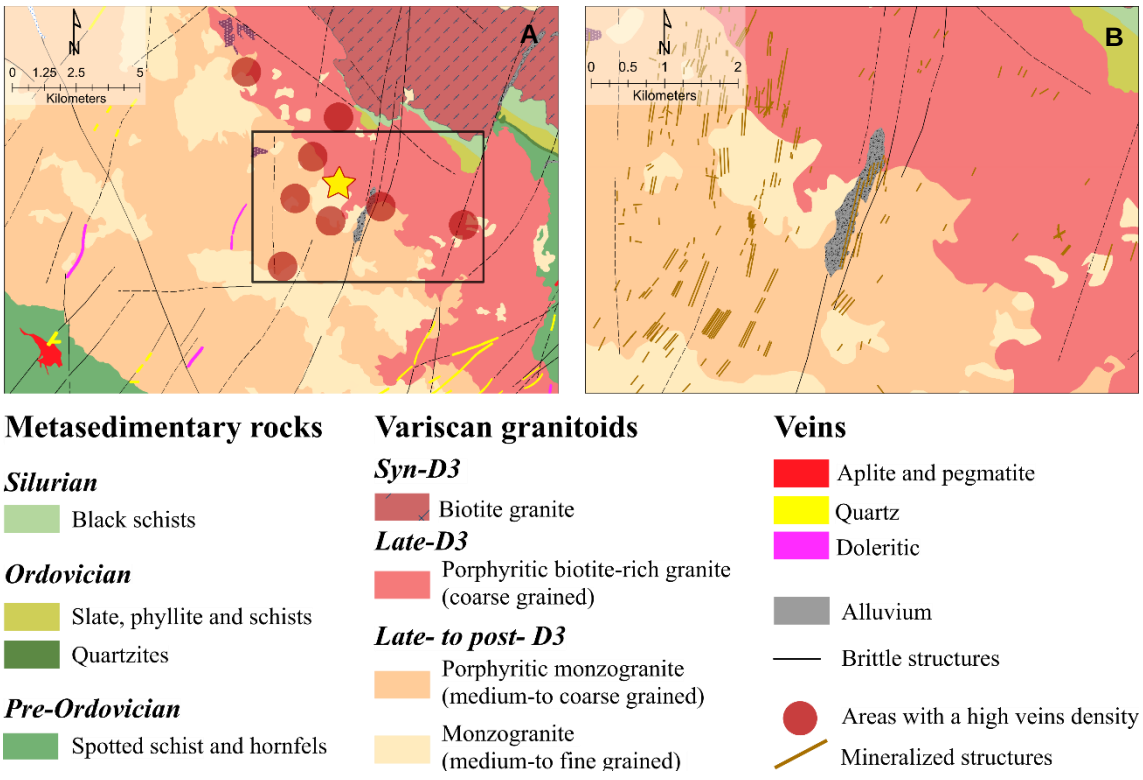

Fig. 7. Geological map showing the location of Bigorne deposit: (A) Geological map of the Bigorne area (adapted from Teixeira et al., 1968). The star shows the location of the Bigorne deposit. (B) Geological map of the area of Bigorne deposit showing the mapped mineralized veins.

4.2 Sampling and analytical methods

Representative rock samples from the Bigorne deposit were collected from surface outcrops during a detailed field mapping and sampling campaign (Fig. 7-B). Studies were carried out on representative samples from the different types of mineralized bodies, altered wall rocks, and intrusive host rocks to identify the mineralogy and investigate the ore paragenesis.

Observations of mineral assemblages were done by transmitted and reflected light microscopy at the Institute of Earth Sciences, University of Porto. Complementary studies for characterization of mineral assemblages were performed at the Materials Centre of the University of Porto (CEMUP) (equipment: FEI Quanta 400 FEG-ESEM/EDAX Genesis X4M) and Oviedo University, Spain (equipment: SEM-EDS (JEOL-6610LV)). Plagioclase compositions were determined by the Michel-Levy method. Abbreviations of minerals were adopted from Kretz (1983) and Whitney and Evans (2010).

4.2.1 Whole-rock geochemistry

Samples from intrusive host rocks were crushed in a jaw crusher and pulverized in an agate mill. Major and trace elements were determined by ICP-OES (Inductively Coupled Plasma Optical Emission) and ICP-MS (Inductively Coupled Plasma Mass Spectrometer), respectively. Detection limits for all elements are given in Table 3. The whole-rock FeO was determined by titration. These analyses were carried out by Activation Laboratories Ltd. (Actlabs), Ontario, Canada (https://actlabs.com/geochemistry/). The analytical package was 4LITHO (FeO) $^{(11+)}$.

4.2.2 Mineral chemistry

Mineral analyses were performed at the Oviedo University (Spain) using an electron microprobe (EPMA), CAMECA SX-100 model. Major elements were determined at 15 kV accelerating voltage, with a 15 nA beam current (2 µm focused beam) an acquisition time between 10 and 20 s for X-ray peak and background. To attain lower detection limits for testing the possible presence of invisible gold in sulfides, approximately 100 analyses of trace elements (Au, Ag, Sb, Pb, Bi, Te, Se, Cu, Zn, Co, Ni, Hg) were performed on arsenopyrite and pyrite and also in other ore minerals. The operating conditions were a 20 keV accelerating voltage, with a 100 nA beam current (5 µm focused beam), and 120–180 s count time. The minimum detection limits were 594 ppm for Au and 228 ppm for Ag, 161 ppm for Sb, 549 ppm for Pb, 455 for Bi ppm, 186 ppm for Te, 161 ppm for Cu, 130 ppm for Zn, 350 ppm for Se, 180 ppm for Co, 275 ppm for S, 108 ppm for Fe

and 270 ppm for As. The acquired X-ray intensities were corrected for atomic number, mass absorption, and secondary fluorescence effects using the CAMECA x-phi program. Natural and synthetic sulfides, oxides, and native elements were used as reference materials.

4.2.3 Isotopic analysis

Isotopic analyses were made on quartz and arsenopyrite that are considered to be associated with the precipitation of gold in the Bigorne deposit. Oxygen, hydrogen, and sulfur isotopic compositions were measured on bulk samples because it was impossible to separate the different generations of quartz and arsenopyrite. Six bulk samples from the different mineralized veins were subjected to hydrogen and oxygen isotope analysis and five bulk samples to sulfur isotope analysis. All samples of mineral separates were hand-picked and checked under a binocular microscope to ensure the purity of > 98%.

Conventional isotope analyses were carried out in the Stable Isotopes Laboratory of Salamanca University, Spain.

4.2.3.1 *Oxygen*

All separates were analyzed using a laser fluorination procedure involving total sample reaction with excess ClF_3 using a CO_2 laser as a heat source. All combustion resulted in 100% release of O_2 from the silica lattice. This O_2 was then converted to CO_2 by reaction with hot graphite, and then analyzed by a VG SIRA II spectrometer. Results are reported in standard notation ($\delta^{18}O$) as per mil (‰) deviations from the Standard Mean Ocean Water (SMOW) standard in Table 8. Reproducibility is better than ± 0.2‰ (1σ).

4.2.3.2 *Hydrogen*

Pure quartz samples were heated to 150°C under a high vacuum to release unstable volatiles. Samples were gradually heated until the sample melted. The released water was then reduced to H_2 and passed slowly through a tube containing a quantity of metallic uranium inside a furnace at 800ºC, with the evolved gas measured quantitatively in a Hg manometer, before collecting using a Toeppler pump. Replicate analyses of water standards (international standards SMOW and GISP, and internal standard Lt Std) gave a reproducibility of ± 2‰. Analytical results are summarized as δD notation as per mil (‰) variations from the international SMOW standard in Table 8.

4.2.3.3 *Sulfur*

Sulfide separates were analyzed by conventional techniques (Robinson and Kusakabe, 1975), in which SO_2 gas was liberated by combusting the sulfides under vacuum with excess Cu_2O at 1075 °C. Liberated gases were analyzed on a VG Isotech SIRA II mass

spectrometer. Reproducibility was better than ± 0.2‰ (1σ). Data are reported in $\delta^{34}S$ notation as permil (‰) variations from the Vienna Cañon Diablo Troilite (VCDT) standard. The analytical results are summarized in Table 8.

4.3 Results

4.3.1 Host rock

4.3.1.1 *Main features*

Gold mineralization in the Bigorne deposit is hosted by late and late to post-D3 granitoids, which occur as three mappable phases within the Lamego massif (Fig. 6-C). Macroscopically, three main intrusive phases can be distinguished: (1) biotite-rich, coarse-grained porphyritic granite corresponding to the regional late-D3 granites; (2) biotite>muscovite, medium-grained porphyritic granite; and (3) biotite=muscovite medium-to fine-grained granite with sparse phenocrysts corresponding to the regional late to post-D3 granites (Fig. 8). Local textural variations are common in the granites, and it is typical to find small enclaves of granodiorite in the late to post-D3 granites. The contacts between granites phases are usually sharp, and no transitional zones are observed. The main petrographic features reveal a wide range of textures but generally have a similar mineralogical composition (Fig. 8). The different petrographic characteristics are summarized in Table 3.

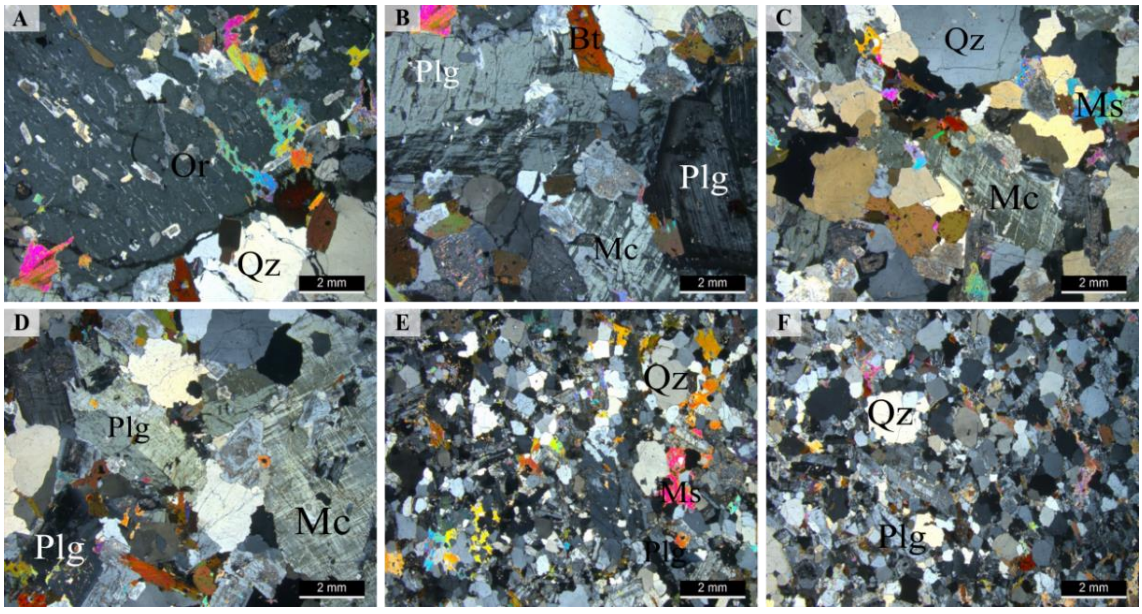

Fig. 8. Petrographic features of Bigorne granites. Late-D3 granites: (A) Phenocrysts of orthoclase (Or). (B) Microcline (Mc) with cross-hatch twinned and zoning plagioclase (Plg). Late-to post-D3 granites: (C) (D) Medium-grained porphyritic granite with microcline phenocrysts and altered plagioclases. (E) (F) General aspect of the fine-grained granite with sparse phenocrysts. All images in CPL (Crossed Polarized Light).

Table 3. Summary of the petrographic features of granites in the Bigorne deposit.

Bigorne granites			
Classification	**Late-D3**	**Late-to post-D3**	
Texture	Biotite-rich, coarse-grained porphyritic granite.	Biotite > muscovite, medium-grained porphyritic granite.	Biotite ≈ muscovite, medium to fine-grained with sparse phenocrysts.
Quartz (Qz)	Anhedral, typically interstitial with inclusions of muscovite, apatite, and rutile. Wavy extinction and sutured borders are frequent.	As anhedral crystals. It occurs as a globular shape in Kfs. Wavy extinction.	Qz as anhedral crystals. Wavy extinction is shown. This occurs as phenocrysts with globular shape.
K-Feldspar (Kfs)	Mostly perthitic microcline and orthoclase. It is a subhedral cross-hatch twinned and contains inclusions of Pl, Qz, Bt, and Ms.	Microline phenocrysts are subhedral cross-hatch. Essentially perthitic microcline.	K-feldspar non-perthitic microcline. Some orthoclase (Mc > Or).
Plagioclase (Pl)	Pl (Oligoclase – andesine) is euhedral to subhedral and shows concentrically chemical zoning, with more calcic composition center. Strong alteration provides epidote and calcite.	Pl (oligoclase) is a subhedral. Chemical zoning (sodic borders). Strong alteration provides epidote and calcite.	Pl (oligoclase) is euhedral to subhedral. Pl is subhedral, polysynthetic twins
Biotite (Bt)	Clusters of crystals without a preferred orientation. Pleochroic halos.	The Bt content and the mode of occurrence is similar to late-D3 granite. Biotite is strongly pleochroic.	Smaller crystal than other phases.
Muscovite (Ms)	Muscovite fill fractures in Pl. Symplectic texture with quartz. Secondary Ms replaces mainly Pl and microcline.	Ms has inclusions of quartz and plagioclase and is locally intergrown with quartz.	Muscovitization of the biotite. Secondary muscovite replaces mainly plagioclase, but also microcline.
Accessory minerals	Apatite, monazite, zircon, ilmenite and rare xenotime.	Apatite, monazite, zircon, ilmenite.	Apatite, monazite, zircon, sphene.
Other observations	Fibrolite needles and a few andalusite grains were found.	Masses of fibrolite needles were found.	The occurrence of calcite from plagioclase alteration.

4.3.1.2 *Whole-rock geochemistry*

Major and trace element data of representative samples of Bigorne intrusive rocks are given in Table 4. Measured SiO_2 contents range from 67.62 to 70.75 wt.%. K_2O contents (3.88-5.34 wt.%) are always higher than Na_2O, corresponding to alkali-calcic and calc-alkalic associations in the discriminant diagram of Frost et al. (2001) (Fig. 9-A). These granitoids show a peraluminous character, with A/CNK index (Shand, 1943) ranging from intermediate (1.09) to high (1.28) values. Compositional variances in major elements between different samples are minor, as shown graphically in the B-A diagram (Fig. 9-B) of Debon and Le Fort (1983) modified by Villaseca et al., 1998. On the total alkali-SiO_2 diagram of Middlemost (1994), the studied samples plot in the granodiorite and granite field *sensu stricto* (Fig. 9-C). The B parameter values (Fe + Mg + Ti in millications) are more dispersed in late to post-D3 granites than in late-D3 granites, higher in samples 5, 6, and 7, which have a granodioritic composition. The chondrite-normalized rare earth element (REE) patterns (normalization values from Boynton, 1984; Fig. 9-D) are analogous for all samples, but with differences in the total abundance: 234-277 ppm in the late-D3 and 167-386 ppm in the late-to post-D3 granites with the higher values in granodiorite samples. All samples show similar REE spectra with enrichment in LREE relatively to heavy rare earth element (HREE) (La/LuN=24.93-49.34) and a similar negative Eu anomaly (Eu/Eu*=0.37-0.58). Multi-elemental diagram normalized to the average bulk continental crust composition of Taylor and McLennan (1995) shows similar patterns for the two granitic phases (Fig. 9-E), with positive anomalies in Cs, Rb, Th, U, La, and Nd (light rare earth element - LREE), and negative ones in Nb, Ta, Sr, Ti, Tm, and Yb (HREE).

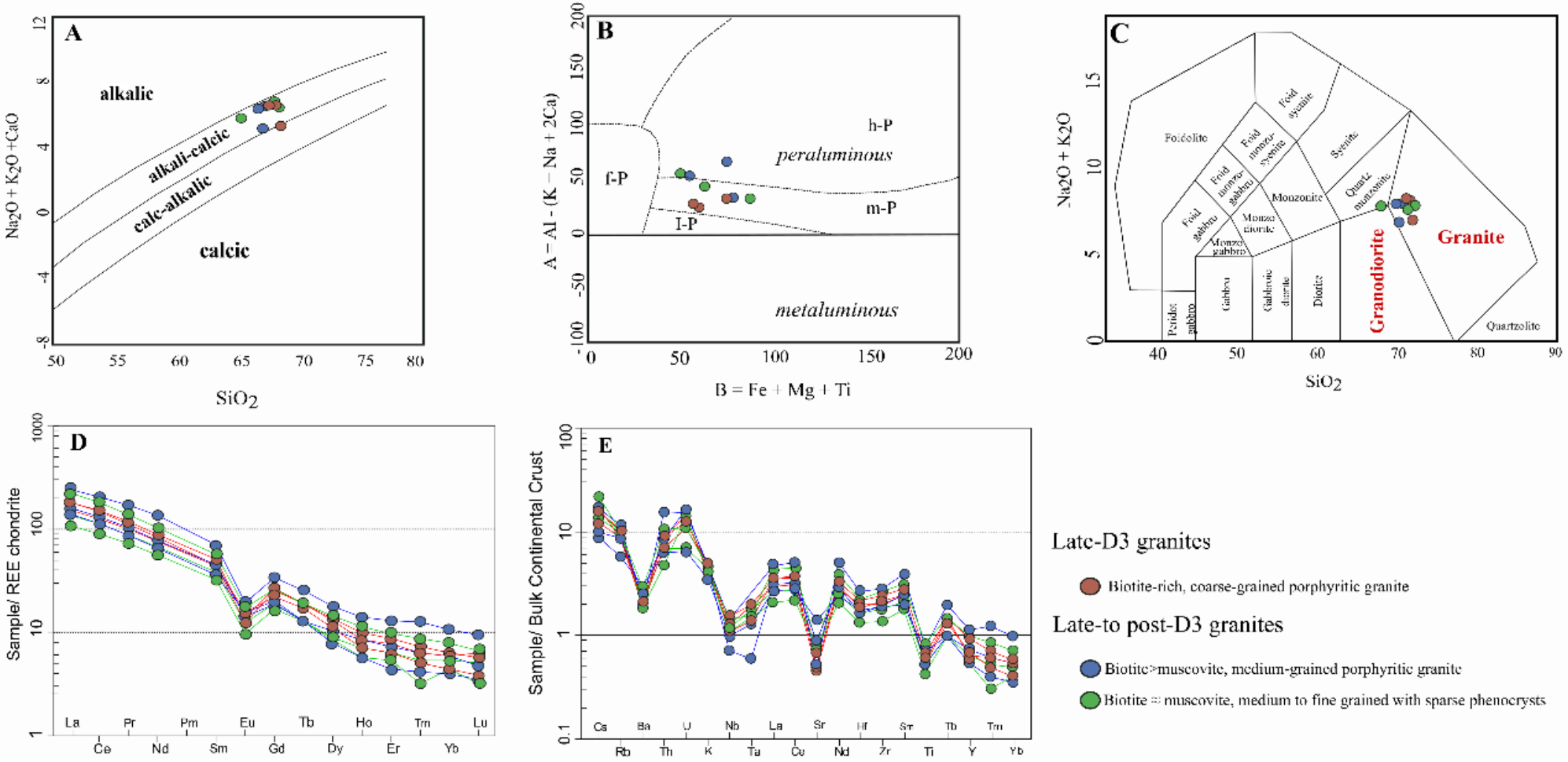

Fig. 9. Whole-rock classification diagrams for intrusive rocks from the Bigorne area. (A) Frost et al., (2001) discrimination diagram; (B) Maficity (B) vs. peraluminosity (A) diagram of Debon and Le Fort (1983) modified by Villaseca et al., (1998); (C) TAS diagram (Middlemost EAK, 1994); (D) Chondrite (Boynton, 1984) normalized REE diagrams; (E) Average Bulk Continental Crust (Taylor and McLennan, 1995) normalized spider plots.

Table 4. Representative major (wt.%) and trace-element (ppm) whole-rock geochemical analyses from the Bigorne granites in the study area. Samples from this study: BIG-1, BIG-4, and BIG-7. Samples and results from Carvalho et al., 2012: 2, 5,8. Samples and results from Oliveira, 2017: 3, 6, and 9. The detection limits from 2, 3, 5, 6, 8, and 9 samples are in Carvalho et al., 2012 and Oliveira, 2017.

		Late-D3			**Late-to post-D3**					
		Coarse-grained porphyritic granite			Medium-grained porphyritic granite			Medium-to fine-grained with sparse phenocrysts		
Samples										
Elements (wt.%)	Detection limit in this study (wt.%)	**BIG-1**	2	3	**BIG-4**	5	6	**BIG-7**	8	9
SiO_2	0.01	70.75	70.42	69.96	70.68	70.39	67.62	69.48	69.1	69.75
TiO_2	0.001	0.61	0.51	0.49	0.48	0.39	0.77	0.64	0.7	0.48
Al_2O_3	0.01	13.7	14.64	14.38	14.78	14.96	15.84	15.76	14.66	15.65
Fe_2O_3	0.01	0.59	0.14	-	1.16	0.17	-	0.22	0.17	-
FeO	0.1	2.6	2.31	-	1.6	1.85	-	2.8	3.1	-
Fe_2O_3t	0.01	3.48	-	3.07	2.93	-	3.94	3.33	-	2.52
MnO	0.001	0.05	0.03	0.04	0.04	0.03	0.05	0.05	0.06	0.03
MgO	0.01	0.94	0.67	0.6	0.82	0.72	1.14	1	0.97	0.68
CaO	0.01	1.63	1.57	1.5	1.33	1.12	2.13	1.73	1.52	1.4
Na_2O	0.01	2.68	2.8	2.89	2.92	3.07	3.01	3.03	2.69	3.09
K_2O	0.01	4.31	5.34	5.25	4.89	4.7	4.94	3.88	5.28	4.9
P_2O_5	0.01	0.36	0.34	0.23	0.31	0.36	0.38	0.26	0.38	0.27
LOI		1.21	-	-	1.01	-	-	1.48	-	-
Total		99.44	99.76	99.06	100	99.06	100.6	100.3	99.76	99.57
(ppm)										
Rb	2	278	336	288	318	324	315	185	369	283
Ba	2	482	500	533	544	472	734	761	510	642
Sr	2	176	120	130	194	198	218	370	133	235
Be	1	7	6	6	6	3	4	4	5	4
Nb	1	17	14	12	13	12	16	11	16	8
Ta	0.1	2	*	1.4	1.8	*	1.6	1.3	*	0.6
Zr	2	244	202	216	182	138	270	192	284	194
Th	0.1	31.6	25	31.9	24.4	17	37.1	22.3	55	30.2
Hf	0.2	6.6	6	5.6	4.9	4	6.8	5.3	8	5
U	0.1	13.3	10	11.4	6.4	13	10.1	6	14	15.1
Y	1	19	13	14	13	11	20	15	23	11
La	0.1	57.4	48	57	42.7	33.8	70.6	43.9	76.5	50.2
Ce	0.1	124	103	121	91.7	73.4	149	92.9	168	108
Pr	0.05	14.6	12.4	13.8	10.8	8.9	17	10.7	21.3	12.7
Nd	0.1	53.3	45.7	50.2	40.8	33.6	62.9	39.2	82.6	47
Sm	0.1	10	8.6	8.7	7.5	6.3	11.1	7	13.8	8.8
Eu	0.05	1	0.9	1.14	0.9	0.7	1.26	1.14	1.4	1.03
Gd	0.1	6.9	6.5	5.7	4.9	4.3	6.7	5.2	8.8	4.8
Tb	0.1	0.9	0.9	0.8	0.6	0.6	0.9	0.6	1.2	0.6
Dy	0.1	4.3	4.1	3.5	2.8	2.7	4.6	3.3	5.7	2.5
Ho	0.1	0.7	0.6	0.5	0.5	0.4	0.8	0.6	1	0.4

Er	0.1	1.8	1.6	1.3	1.3	1.1	2	1.5	2.7	0.9
Tm	0.05	0.23	0.2	0.16	0.17	0.1	0.28	0.2	0.4	0.13
Yb	0.1	1.3	1.2	0.9	1.1	0.9	1.6	1.2	2.2	0.8
Lu	0.01	0.18	0.2	0.12	0.16	0.1	0.21	0.15	0.3	0.11
∑ LREE		267.20	225.10	257.54	199.30	161.00	318.56	200.04	372.40	232.53
∑ HREE		9.41	8.80	7.28	6.63	5.90	10.39	7.55	13.50	5.44
∑ REE		276.61	233.90	264.82	205.93	166.90	328.95	207.59	385.90	237.97
Eu/Eu*		0.37	0.37	0.49	0.45	0.41	0.45	0.58	0.39	0.48
Co	6.00	5	*	5	3	*	5	6	*	*
Zn	80.00	440	70	80	80	90	70	100	80	*
Ga	22.00	25	22	22	25	24	22	26	25	80
Ge	1.00	*	2	2	*	2	1	*	1	25
Sc	6.00	4	4	5	3.7	7	6	7	3	1
V	35.00	28	28	32	23	45	42	38	31	3
Cr	250.00	17	*	230	16	*	210	13	*	31
Pb	26.00	47	37	29	40	32	25	38	31	*
Tl	1.60	*	1.5	1.9	*	1.7	1.2	*	1.6	< 0.4
Sn	9.00	11	7	9	9	8	6	15	4	1.6
Cs	17.30	16	12.4	16.2	22	13.8	9	17	10	4
W	3.00	2	2	2	2	2	1	3	<1	10
As	5.00	14.6	*	6	11.7	*	< 5	45.4	*	*
Ag	0.70	*	0.6	< 0.5	*	0.7	0.5	*	0.6	*
B parameter		56.92	59.48	63.21	50.63	87.28	74.57	78.12	54.45	54.45
A/CNK		1.11	1.09	1.18	1.23	1.12	1.28	1.14	1.21	1.21
Rb/Sr		2.80	2.22	1.64	1.64	1.44	0.50	2.77	1.20	1.20
Ba/Rb		1.49	1.85	1.71	1.46	2.33	4.11	1.38	2.27	2.27

Note: The analyses, which are below the detection limit, are not shown (In, Sb, Ni, Mo, Bi, and Cu). * values below the detection limit.

4.3.2 Deposit-scale structure

4.3.2.1 *Mineralized zones*

The main gold mineralization at Bigorne commonly occurs as sheeted quartz-sulfide vein arrays filling parallel, sub-vertical to steeply dipping, NNE-SSW-trending extensional fractures (Fig. 10-A). The orientations of the main mineralized structures observed in the outcrops are N10º-20ºE/70ºW and N20º-40ºE/60º-80ºW. Sub-horizontal slickenlines have been observed along the margins of some of the quartz-sulfide veins in rare locations, indicating a minor strike-slip shear component of deformation has locally affected the deposit. Another barren, milky quartz system with an E-W trend is observed; the NNE system locally cuts this. These later veins typically do not show marginal hydrothermal alteration zones. The mineralized fractures are of variable length

(centimeter to metric dimension) (Fig. 10-A) and variable width (1 up to 15cm). Interconnected, multidirectional vein stockworks are not observed anywhere in the Bigorne deposit. Vein contacts are typically sharp and planar and display little or no shear-related markers or lineations. The veins crosscut all of the intrusive phases in the Bigorne area (Fig. 10-B). Mineralized portions of the intrusions show differential weathering, with the veins standing out in "positive relief" (Fig. 10-A-D), likely reflecting minor silicification in narrow envelopes surrounding the fractures and veins.

Individual veins may contain up to several g/tonne of gold (Caessa et al., 1998), with rare samples yielding up to 40 g/tonne (Mortensen and Mackenzie, unpublished data). The mineralized zones at Bigorne consist of quartz-sulfide veins (Fig. 10-B-C), simple fractures with oxidized material (Fig. 10-D-E), and disseminated sulfides in the hydrothermal alteration halo of the mineralized veins (Fig. 10-F).

The mineralogy of the oxidized material consists of Fe-hydroxides and dispersed sulfide aggregates (vuggy gossanous veining) (Fig. 10-D-E). The quartz-sulfide veins reveal slight internal textural variation and are associated with major sulfides (arsenopyrite and pyrite) and minor wolframite, scheelite, and tourmaline. The sulfides appear attached to the vein walls or filling fractures in quartz (Fig. 10-C). In the contact of quartz-sulfide veins with the granite is present a hydrothermal alteration halo with low extension (1 to 20cm width) rich on white mica with some disseminated euhedral arsenopyrite crystals (Fig. 10-F). These alteration zones are diffuse, irregular, and restricted to the immediate vicinity of veins.

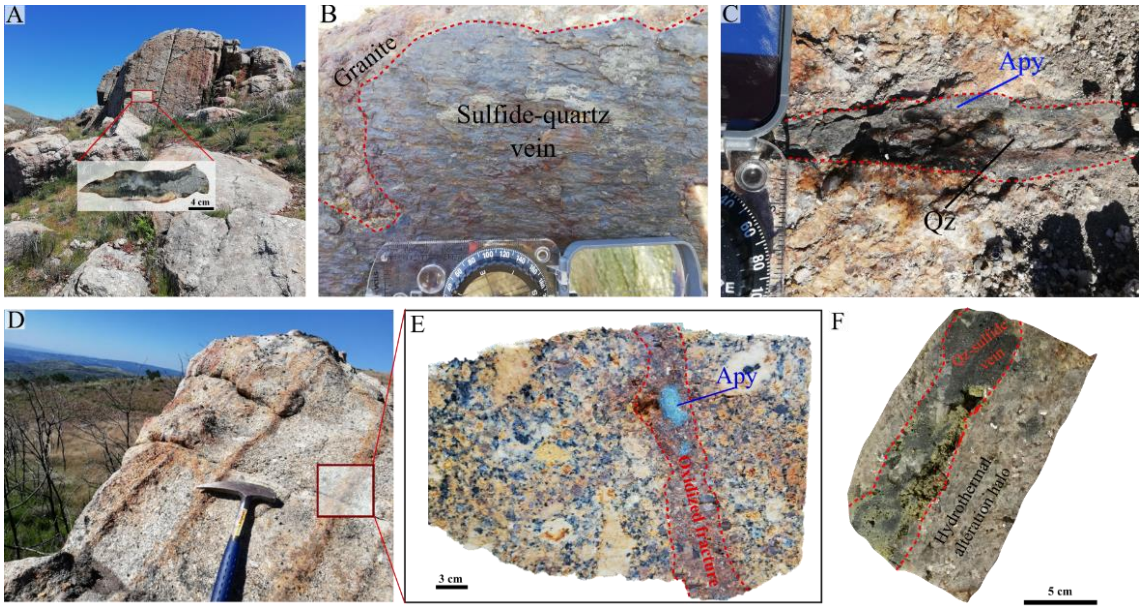

Fig. 10. Representative mineralization in the Bigorne deposit. (A) Outcrop-scale exposure of an array of granite-hosted, sheeted veins. (B) Mineralized quartz-sulfide vein showing slickensides. (C) Mineralized quartz-sulfide vein. (D) Oxidized fracture with arsenopyrite. (F) Quartz-sulfide vein with hydrothermal alteration halo.

4.3.2.2 *Paragenetic sequence*

Petrographic observations from mineralized zones at Bigorne suggest at least three main mineralization stages (Fig. 11), including (i) Stage 1 - an early oxide stage with quartz ± wolframite-scheelite ± arsenopyrite-pyrite, (ii) Stage 2 - a late sulfide stage quartz ± arsenopyrite-pyrite-galena-sphalerite-chalcopyrite ± gold assemblage, and iii) Stage 3 - a supergene stage with scorodite and covellite. The main hydrothermal alteration present comprises a mica selvage enveloping the mineralized quartz veins.

Geochemical analyses of white micas from the hydrothermal alteration halos are given in Table 5, and geochemical analyses of sulfides and bismuth tellurides from Bigorne gold-bearing quartz veins are given in Table 6 and 7.

Stage-1

In the early stages, quartz crystals occur as milky quartz (Qz-1) infilling parallel to the vein walls. Small amounts of wolframite and scheelite are locally observed in the margins of a few mineralized veins associated with Stage 1 quartz (Qz-1) (Fig. 12-A-B). Qz-1 shows wavy extinction and deformation bands, indicating that it underwent brittle deformation after formation (Fig. 12-B). Some sparsely distributed arsenopyrite (Apy-1) is also present. Apy1 is As-rich (32.47 at. % of As; Fig. 13-A) and euhedral to subhedral. Application of the arsenopyrite geothermometer indicates a maximum temperature of 455ºC for arsenopyrite deposition in this stage (Fig. 13-C: Kretschmar and Scott, 1976; Sharp et al., 1985). In this early stage of mineralization, the granite is altered along with the vein walls. Tourmaline occurs in clusters generally normal to the wall-rock contacts (Fig. 12-C). All the analyzed white micas from the hydrothermal alteration halo (Fig. 12-D) have high contents in TiO_2, FeO, and MgO (Table 5), representing solid solution between muscovite and celadonite, and belong to the phengite series (Rieder et al., 1998; Tischendorf et al., 2004).

Stage 2

The later quartz (Qz-2) is clearer than quartz (Qz-1) and cements fractured arsenopyrite along with white micas (± chlorite) (Fig. 12-B). Qz-2 shows a less marked wavy extinction than Qz-1. The white micas are fine-grained, subhedral, and radial with a chemical composition near the celadonite component. Apy-2 is As-poor (30.60 at. % of As; Fig. 13-A) and forms massive aggregates (up to 20 mm in length) that fill quartz-sulfide veinlets and show well-developed faces at the border of massive aggregates. Single crystals of Apy-2 are generally smaller than those in Apy-1. Petrographic observation and microprobe data suggest continuous arsenopyrite deposition from early to late mineralization stages (Fig. 13-A). EPMA data reveal a pure FeAsS phase. The As

content corresponds to minimum formation temperatures of 354°C for this stage (Fig. 13-C; Kretschmar and Scott 1976; Sharp et al., 1985). In most of the analyzed arsenopyrite crystals, the variation in the Fe content is insignificant (33.10 ± 0.3 at. %). Generally, trace elements contents in arsenopyrite are below the detection limit of the Electron Probe Micro Analyzer (EMPA).

Pyrite occurs as aggregated intergrowths with arsenopyrite (Fig. 12-E). The EPMA data show one chemical type of pyrite (Table 6), which is As-poor (As < 1 wt.%) with homogeneous composition. Chalcopyrite is present in fractures that cut the arsenopyrite crystals. In arsenopyrite and pyrite, trace amounts of galena and sphalerite occur as blebs and slight irregular inclusions (< 50µm).

Sulfides from the mineralized bodies and the host rock have been affected by brittle deformation and are moderate to pervasively oxidized (Fig. 12-E-F).

Stage 3

The latest paragenetic stage mainly comprises very clear light grey quartz (Qz-3), which fills cavities. Covellite is rare and partially surrounds arsenopyrite and bismuthinite. Scorodite usually proceeds inward from crystal boundaries or along with fractures. All minerals are anhedral and brecciated.

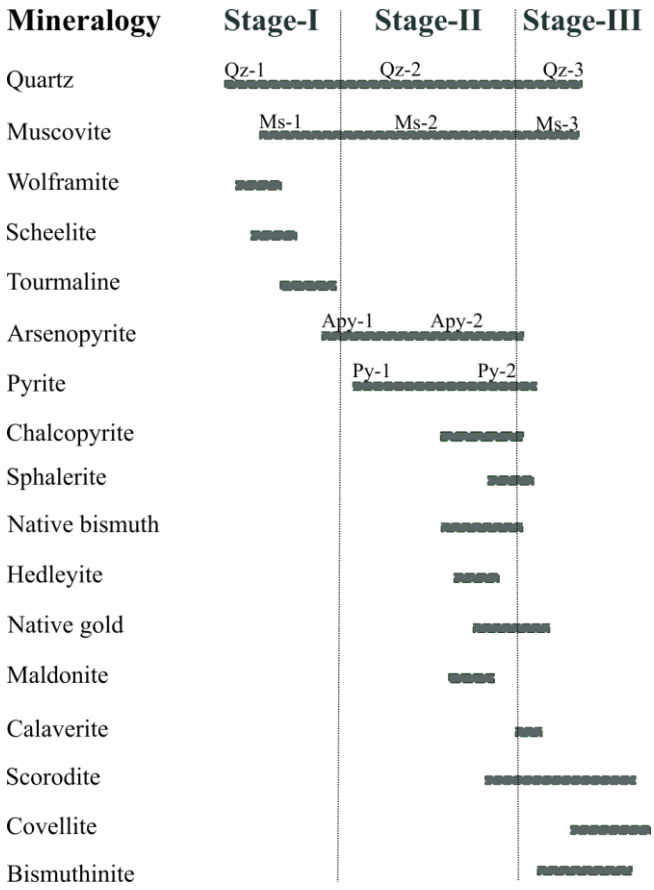

Fig. 11. The paragenetic sequence of gold mineralization from the Bigorne deposit.

4.3.2.3 *Gold mineral assemblages*

Three generations of native gold were distinguished at Bigorne based on textural features. Au-1 forms composite aggregates with Bi-Te ± (S) phases less than 10µm in size and occurs only as irregular inclusions in arsenopyrite (Fig. 14-A). Au-2 comprises small veinlets and individual (30µm-100µm) homogenous particles, and it is the most abundant type of gold in the deposit (Fig. 14-B). Au-2 also occurs in arsenopyrite, pyrite, and scorodite, infilling intergranular spaces between crystals and microfractures. Au-3 comprises low-fineness gold particles associated with later mineral assemblages, including chalcopyrite (less common type) (Fig. 14-C).

Gold compounds such as maldonite (Au_2Bi) (Fig. 14-D) and, to a lesser degree calaverite ($AuTe_2$) (Fig. 14-E) are observed in a few samples from the Bigorne veins. Maldonite appears as small droplets or cavity infillings only within arsenopyrite crystals (2 µm up to 20 µm). Calaverite appears to fill fractures in arsenopyrite and is associated with bismuthinite (Bi_2S_3). These minerals occurred as single grains or as gold intergrowths with Bi-Te±(S) phases and native bismuth, forming composite aggregates with curvilinear boundaries or triple junctions between the phases and textures like droplet-shape inclusions (Fig. 14-F-G-H). There is textural evidence that clusters of Au-Bi-Te droplets predate the fracturing of the host arsenopyrite.

Native bismuth occurs together with native gold, maldonite, and other Bi-Te minerals and as monomineralic veinlets in arsenopyrite. In some cases, thin rims of bismuthinite (Bi_2S_3) overgrow native bismuth in contact with gangue minerals.

EMPA analyses show that gold occurs as a moderate- to high-fineness native gold (typically < 22 wt.% Ag) composition (Leal et al., 2021). Native bismuth is chemically pure. The crystals are commonly tiny, which makes the EMPA analysis difficult. Only a few bismuth-telluride phases have been confidently identified by EPMA analysis (hedleyite (Bi_7Te_3); Table 7). The rest of all are identified by SEM-EDS analysis. Trace admixtures in hedleyite may consist of Sb (up to 0.4 wt.%), Se (up to 0.04 wt.%), and Au (0.61wt.%; one analysis only). Measured Fe, S, and As contents are from the arsenopyrite host. The rest of the analyses have contamination by native gold, and maldonite cannot be ruled out.

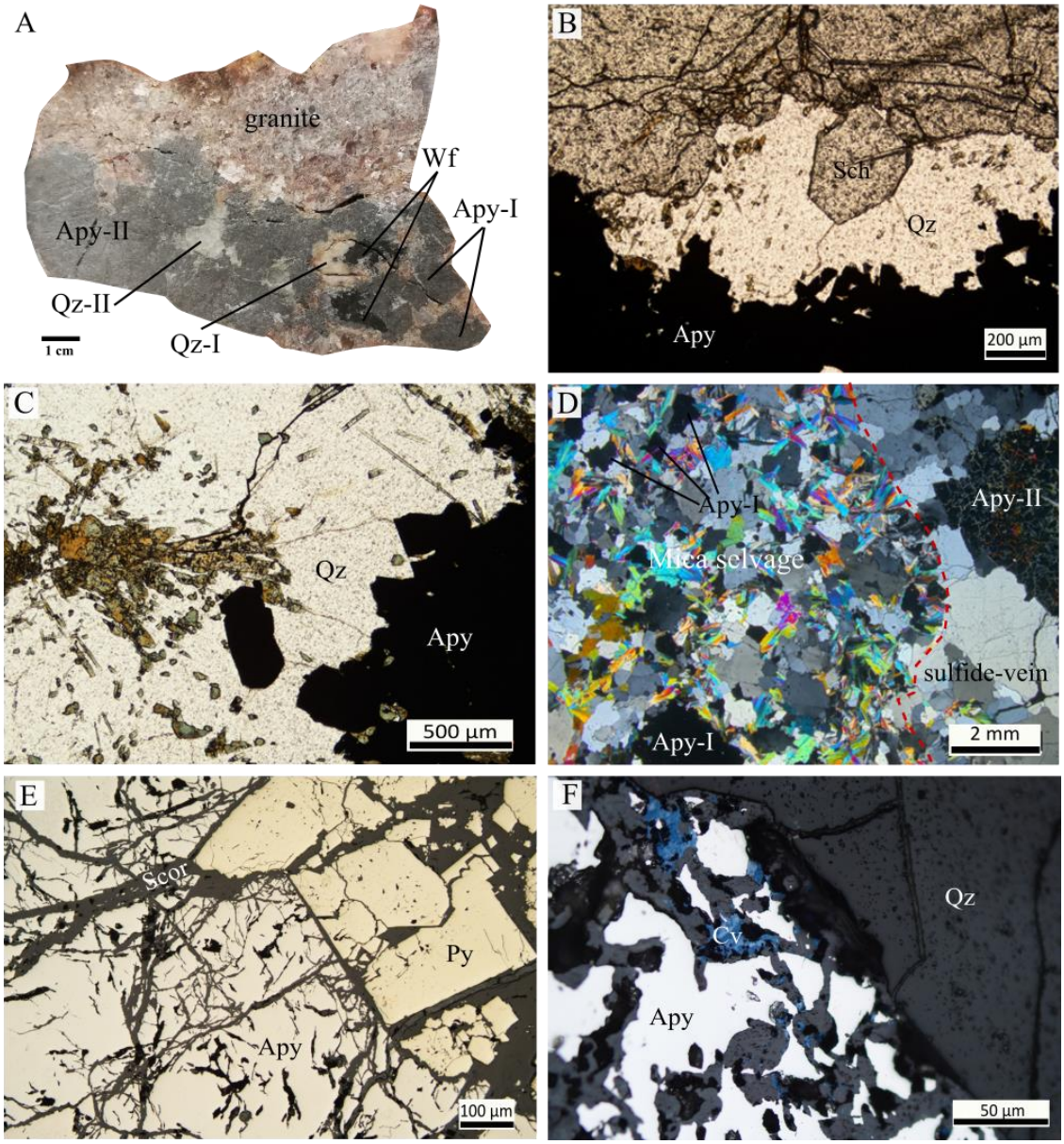

Fig. 12. Example of a representative mineralized vein from Bigorne deposit. (A) Sulfide-vein with wolframite. (B) Scheelite in the margins of mineralized veins. (C)Tourmaline in mineralized veins. (D) Alteration halo - Mica-selvage. (E) Sulfide stage (stage-II). (F) Supergene phases: covellite and scorodite. B, C, E, and F photomicrographs were taken under PPL (Plane Polarized Light), and D were taken under CPL.

Table 5. Representative compositions of white micas in the Bigorne gold deposit by EPMA (in wt.%, structural formulae based on 22 oxygen atoms).

	Muscovite (n=12)	Phengite I (n=82)	Phengite II (n=4)
SiO_2	41.89	44.93	47.07
TiO_2	0.53	0.59	0.82
Al_2O_3	33.84	33.79	27.97
Cr_2O_3	0.01	0.01	0.01
FeO	1.87	1.59	2.45
MnO	0.02	0.02	0.00
NiO	0.01	0.02	0.00
MgO	1.11	1.38	2.83
CaO	0.05	0.05	0.09
Na_2O	0.43	0.42	0.09
K_2O	10.58	10.61	10.63
P_2O_5	0.07	0.02	0.02
Total	94.62	97.82	96.30
Si	5.95	6.13	6.55
Ti	0.06	0.06	0.08
Al^{IV}	2.05	1.87	1.45
Al^{VI}	3.61	3.57	3.14
Fe	0.22	0.18	0.29
Mg	0.24	0.28	0.59
Ca	0.01	0.01	0.01
Na	0.12	0.11	0.03
K	1.92	1.85	1.89

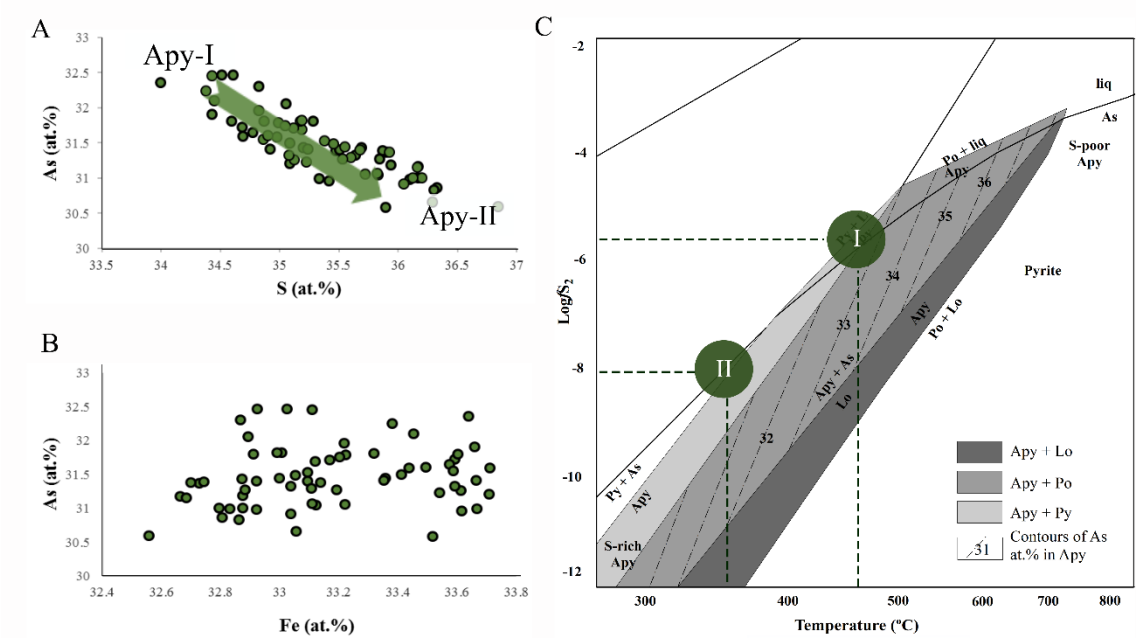

Fig. 13. (A) Variation content between As at. % and S at.%. (B) Variation content between As at. % and Fe at.%. (C)Formation temperature and inferred sulfur fugacity of arsenopyrites formed in the Bigorne gold deposit based on the As at. % of arsenopyrite. Modified after Kretschmar and Scott (1976) and Sharp et al., (1985). I - Arsenopyrite-I and II - Arsenopyrite-II.

Table 6. Electron microprobe data of multiple samples of arsenopyrite and pyrite from representative mineralized bodies at the Bigorne deposit.

	Arsenopyrite		**Pyrite**	
N	65		18	
	Average	*±σ*	*Average*	*±σ*
wt.%				
As	44.1	0.5	0.1	0.3
S	21.2	0.5	53.3	0.5
Fe	34.6	0.3	46.2	0.3
Ag	0.0	0.0	0.0	0.0
Cu	0.0	0.0	0.0	0.0
Se	0.2	0.0	0.0	0.0
Ni	0.0	0.0	0.0	0.0
at.%				
As	31.4	0.4	0.0	0.2
S	35.2	0.6	66.7	0.3
Fe	33.1	0.3	33.3	0.3
Ag	0.0	0.0	0.0	0.0
Cu	0.0	0.0	0.0	0.0
Se	0.1	0.0	0.0	0.0
Ni	0.0	0.0	0.0	0.0

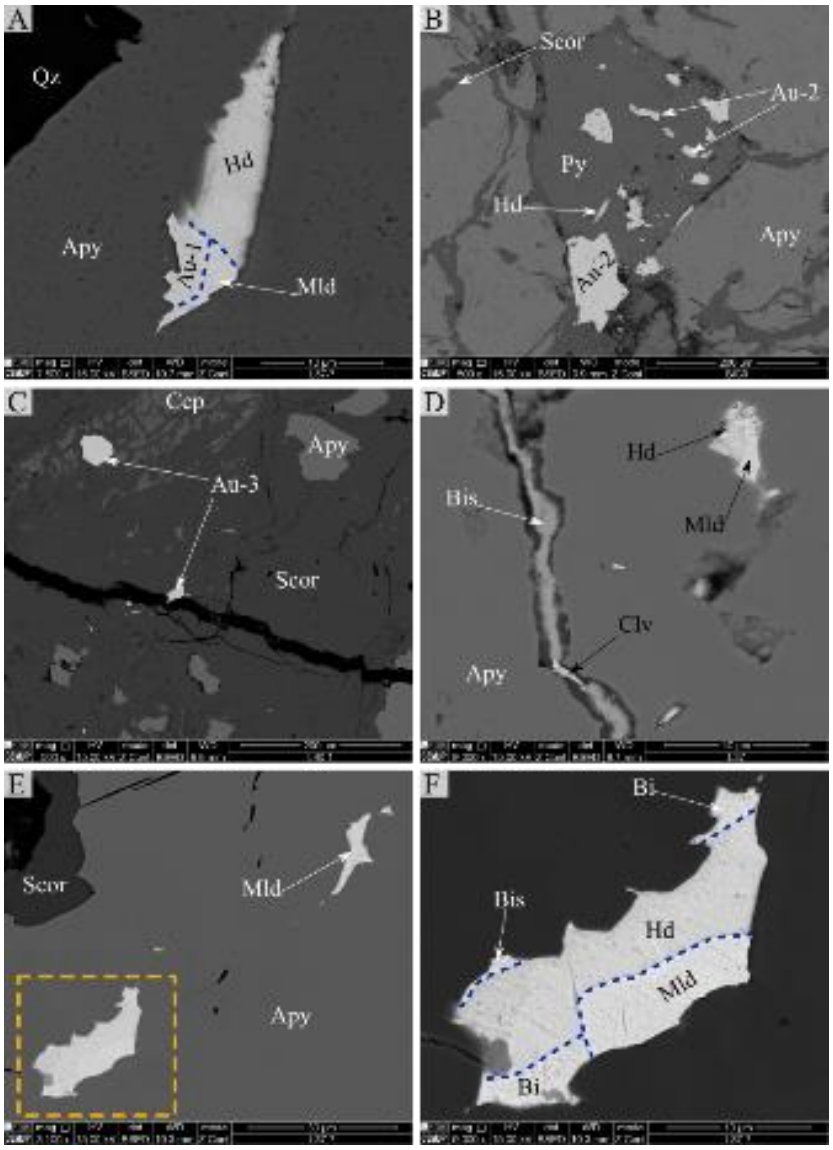

Fig. 14. Back-scattered electron (BSE) images. (A) Native gold (Au-1), maldonite (Mld), and hedleyite (Hd) aggregate in arsenopyrite. (B) Native gold (Au-2) and hedleyite (Hd) in pyrite and grain boundaries. (C) Au-3 in chalcopyrite. (D) Calaverite filling the cavities in bismuthinite. (E) Maldonite occurs isolated in microcavities in arsenopyrite and Au-Bi-Te aggregate. (F) Composite aggregates with maldonite (Mld), hedleyite (Hd), and native bismuth.

Table 7. Representative electron microprobe data (wt.%) of Bi-chalcogenides in the Bigorne deposit.

	Ag	Sb	S	Au	Fe	Cu	Bi	As	Se	Cd	Te	Total
Hedleyite												
1.1	-	0.42	1.53	0.61	4.55	-	73.26	4.48	0.05	0.00	15.35	100.27
2.1	-	0.48	0.14	-	1.17	-	79.42	0.02	0.04	0.00	17.35	98.78
3.1	-	-	0.1	-	2.24	0.06	67.03	0.22	-	0.03	18.36	98.47
4.1	-	-	0.08	-	1.75	0.06	66.90	0.14	0.02	0.03	17.44	96.46
Maldonite												
1.1	0.50	-	-	64.89	0.68	0.1	30.32	0.03	0.01	-	0.06	97.15
2.1	0.24	-	-	64.58	0.70	-	29.5	0.03	-	-	-	99.52
3.1	0.35	-	-	64.97	0.90	-	29.04	0.01	0.01	-	-	99.79

(-) values below the detection limit.

4.3.3 Hydrogen, oxygen, and sulfur isotopes

The hydrogen and oxygen isotopic compositions of quartz from the main mineralization stage are given in Table 8. Measured $\delta^{18}O$ in quartz from mineralized veins at Bigorne shows a restricted range of values around (+12‰ to +12.3‰) (Table 8). Assuming there was equilibrium between fluids and minerals, the isotopic compositions for δD and $\delta^{18}O$ of fluids were calculated based on estimated temperatures from arsenopyrite geothermometer (*e.g.*, Apy-1, 455 °C; Apy-2, 354 °C) (Table 6). The oxygen isotopic compositions of ore-forming fluids ($\delta^{18}O_{fluid}$) have been calculated the oxygen isotopic fractionation equation of the quartz–water system defined by Matsuhisa et al. (1979). The calculated $\delta^{18}O$ fluid values from quartz range between +9.3 and +6.8‰. All the δD_{SMOW} values of quartz can be used to represent δD_{fluid} values. The δD compositions of fluids from quartz are between -62.5 and -64.7‰. Sulfur isotope determinations were carried out on representative arsenopyrites from the mineralized veins in the Bigorne deposit. The $\delta^{34}S$ values clustered around -2.8‰ (Table 8).

Table 8. Isotopes values of representative minerals from mineralized bodies at Bigorne deposit.

Mineral	Sample	$\delta^{18}O_{SMOW}$ (‰)	Estimated T[a]	$\delta^{18}O_{FLUID}$ (‰)	δD_{SMOW} (‰)	$\delta^{34}S_{VCDT}$ (‰)
Quartz	BIG. A	12.0	455-354ºC	9 – 6.8	-64.7	
	BIG. B	12.2	455-354ºC	9.2 - 7	-63.4	
	BIG. C	12.3	455-354ºC	9.3 – 7.1	-62.5	
	BIG. D	12.1				
	BIG. E	12.2				
	BIG. F	12.0				
Arsenopyrite	S. 1					-2.8
	S. 2					-2.7
	S. 3					-2.8
	S. 4					-2.6
	S. 5					-2.7

4.4 Discussion

4.4.1 Timing of mineralization

Most gold mineralization at Bigorne occurs on the west side of the inferred main strand of the PRVF; however, prospecting and sampling have demonstrated that similar mineralization is also present between strands and to the immediate east of the fault zone (Mortensen and MacKenzie, unpublished data). Although the mineralization is probably closely related to displacement on the PRVF, the relatively small amount of

sinistral displacement that appears to have occurred on the fault makes it impossible to establish the exact temporal relationship between mineralization and fault offset. U-Pb dating by Martins et al. (2009) indicates that displacement on the PRVF occurred at 299 ±3 Ma or slightly earlier, and we suggest that the Bigorne deposit likely formed at approximately this same time.

4.4.2 Host rocks

Taking into account the different granites that occur in the study area, its petrological and geochemical characteristics are similar to the other Variscan biotite-rich late- and late-to post-tectonic ilmenite type granites with mafic microgranular enclaves considered as the result of magmas that mainly originated in the lower crust but recorded some mantel influence (Dias et al., 1998; Sant'Ovaia et al., 2010; Costa, 2011; Carvalho et al., 2012).

Inferred crystallization ages of the various intrusive host rocks for Bigorne gold mineralization are considerably older than our suggested age for the mineralization itself. Mineralization occurs within all three of the main intrusive phases identified in the area. The composition of the mineralization, the nature and extent of associated hydrothermal alteration are similar; thus, the intrusive rocks appear to have acted as passive hosts for the mineralization.

4.4.3 Deposit-scale structure

Mineralized structures are mainly extensional veins (locally showing evidence for strike-slip reactivation and shearing) and occur in sheeted veins arrays that are typically not interlinked. Vein density appears to be the main grade-controlling feature. Auriferous vein development was dominantly controlled by the NNE-SSW striking structures parallel to the regional Penacova-Régua-Verín strike-slip fault. These observations conclude that the mineralized areas formed in a structural setting related to the main Late Variscan regional strain, coeval with lithosphere-scale strike-slip deformation and the IberoArmorican Arc.

Visible hydrothermal alteration (mica selvage) is restricted to the vein walls and is structurally controlled. A lateral zonation for the hydrothermal assemblage occurred after the opening of the joint system, which provided channels for fluid circulation. The mineral assemblage, particularly the arsenopyrite crystals, locally shows a cataclastic texture associated with regional deformation after the main sulfide deposition and corresponding to the reactivation of NNE-SSW faults. The vein style, orientation, mineralogy, and structural timing are shared with many other gold deposits in the region, such as

Limarinho, Ponte de Barca, and Penedono (Fuertes-Fuente et al., 2016; Neiva et al., 2019).

Gold mineralization at Bigorne is interpreted to be the result of two modes of gold deposition: 1) gold scavenged by bismuth melts due to local dissolution of arsenopyrite by hydrothermal fluids, which would have produced reduced conditions for the formation of bismuth melt (Pokrovski et al., 2002, 2014); and 2) a local-scale reworking of maldonite resulting from a decrease of fS_2 of ore-forming fluid, triggered by fluid-rock reactions and crystallization of sulfides, implying gold remobilization, which represents the main episode of gold deposition (coarse native Au-1).

The hydrothermal system at Bigorne evolved from an initial high temperature (> 455ºC; maximum estimated deposition temperature for Apy-1) for the oxide stage and Apy-2 with a minimum temperature of 354°C. The highest melting-T phase (371ºC) corresponds to maldonite (Au_2Bi) crystallization (Okamoto and Masaalski, 1983), followed by hedleyite (Bi_7Te_3) at 312ºC (Okamoto and Tanner, 1990). As the temperature decreased, the tellurium content in Bi-Te compounds also decreased until it reached the melting temperature of bismuth (Bi-metal at 271ºC). The upper temperature limits for the Au-Bi-Te assemblage are set by melting points: the (Bi_7Te_3 + Bi) at 266ºC, the (Au_2Bi + Bi) at 241ºC and the (Bi_7Te_3 + Bi + Au_2Bi) at 235ºC. The lower end of temperature the Au-Bi-Te assemblage and the inferred temperature deposition coarse native gold deposition (nearly less than 241ºC) latter than the latter arsenopyrite (Apy-2 with a minimum temperature of 354°C). This is in agreement with previous research on fluid inclusion data on other similar gold deposits in the Iberian Massif where the bulk fluid inclusion in quartz of the mineralized veins and gas chemistry consisted of modified fluids (P<100 MPa and T<300ºC) with the main gold deposition being relatively late (*e.g.*, Cathelineau et al., 1993; Boiron et al.,1996; Noronha et al., 2000; Fuertes-Fuente et al., 2016; Neiva et al., 2019).

4.4.4 Source of fluids

The calculated fluid oxygen and hydrogen isotope values of quartz in the Bigorne deposit overlap the metamorphic and magmatic fluids fields, suggesting that the hydrothermal fluid at Bigorne could have originated from a deep-seated metamorphic and/or magmatic source. The range of δD and $\delta^{18}O$ compositions of fluids is similar to that of many other orogenic gold deposits, ranging from +6 to +11‰ in Precambrian ores and from +7 to +13‰ in Phanerozoic ores (Goldfarb and Groves, 2015; Zhang et al., 2018). The $\delta^{18}O_{SMOW}$ values from some gold deposits in NW of Iberian Massif range from +12 to +13.7‰ (Fuertes-Fuente et al., 2016).

The $\delta^{18}O_{fluid}$ values from Bigorne quartz-sulfide veins range from +9.3 to +6.8‰. These values could reflect metamorphic fluids which were mixing with meteoric fluids during late mineralization stages. Boiron et al. (2003) reported $\delta^{18}O_{fluid}$ values from 12.5 to 0.3‰ in various Variscan gold deposits, which were interpreted to reflect fluids whose salinities decreased to shallow values during progressive dilution waters of more surficial origin in the fault system zones.

According to Bark et al. (2020), oxygen isotope compositions greater than +8‰ are interpreted to reflect surface or near-surface processes during sedimentation, diagenesis, or low-temperature hydrothermal alteration (Taylor, 1980), suggesting that the fluids could not be solely magmatic (McCuaig and Kerrich, 1998). Metamorphic fluids with $\delta^{18}O$ values greater than + 8‰ are acceptable if the source rocks contain ^{18}O-enriched rocks (Böhlke and Kistler, 1986; McCuaig and Kerrich, 1998). Few stable isotope studies have been undertaken on granitic rocks near the Bigorne area. Costa et al. (2014) reported whole-rock oxygen isotopic compositions in leucogranites of $\delta^{18}O\text{-}_{wr}$= 11.33‰ whereas related granodiorites are characterized by lower $\delta^{18}O\text{-}_{wr}$= 10.6‰. The $\delta^{18}O_{fluid}$ values from the Bigorne gold-bearing veins may suggest a metamorphic or modified fluid or a mixed fluid source with the country rocks and meteoric fluids.

$\delta^{34}S$ values of arsenopyrite in the mineralized veins (-2.8‰) point toward the possibility of a magmatic influence for the sulfur signature source (Seal, 2006; Hoefs, 2018). Due to the lack of minerals indicative of oxidizing hydrothermal conditions (*e.g.,* hematite and sulfates), a reduced state was attributed to the sulfur transport, most likely as H_2S, and the negative $\delta^{34}S$ values cannot be assigned to fractionation processes (Hoefs, 2018).

Granitoid rocks have an average $\delta^{34}S$ value of 1.0 ± 6.1‰ (Seal, 2006), but range from -11 to 14.5‰, which presumably reflects the variable assimilation or partial melting of either pyritic sedimentary rocks with low $\delta^{34}S$ values (Sasaki and Ishihara, 1979; Ishihara and Sasaki, 1989; Santosh and Masuda, 1991). Ishihara and Sasaki (1989) studies in ilmenite-series granitoids show $\delta^{34}S$ values less than 0‰, generally regarded as having formed through partial melting of dominantly sedimentary protoliths. In contrast, magnetite-series granitoids thought to originate from dominantly igneous protoliths had $\delta^{34}S$ values greater than 0‰. The geological context can also affect the isotope composition signature (Ohmoto and Goldhaber, 1997). The $\delta^{34}S$ values can be different in some gold deposits in the CIZ, but the origin of the fluids ($\delta^{18}O_{fluid}$) is well constrained (*e.g.*, Limarinho deposit: $\delta^{34}S$ values from −9.2 to −7.1‰; Penedono deposit: $\delta^{34}S$ values from −5.3 and −4.3‰). The negative values of $\delta^{34}S$ in the mineralized veins (-2.8‰) and $\delta^{18}O$ values around (12‰ to 12.3‰) could be not related to a magmatic source. Iyer

(1992) interpreted lighter values of S isotope as reflecting oxidation of reduced sulfur or influence of meteoric water, also resulting in increasing oxygen fugacity.

4.5 Conclusions

The Bigorne deposit is a “granite-hosted gold deposit” and presents some features that are more akin to the OGDs (than IRGD) elsewhere in other Phanerozoic orogenic belts.

Based on the vein textures, sulfur isotope values, composition of ore fluids, and inferred age of mineralization formation, we suggest that the granitic rocks in the Bigorne area acted only as a competent structural host for ore deposition from fault-related, metal-rich fluids that migrated up from depth. Fault zones in late Variscan deformation stages provide suitable pathways for hydrothermal fluids' leaching, transportation, and deposition processes (Pohl & Belocky, 1994, 1999).

The isotopic composition of the fluids found at Bigorne is consistent with those of OGDs elsewhere in the Variscan Belt. Hydrothermal fluids are interpreted not to be related to magmatic sources. The stable isotope data, interpreted in the context of the regional and local geology and the estimated timing of mineralization, suggest that the sulfur- and gold-bearing fluids that generated OGDs in northwestern Iberia were related to the progressive dilution and cooling of the crustal fluids by oxidizing solutions penetrating the basement from the surface, during late Carboniferous extensional tectonism (Boiron et al., 1996, 2003; Noronha et al., 2000). However, considering the other characteristics of the Bigorne deposit, the $\delta^{34}S$ can be attributed to metamorphic fluids leached metals from the country rocks or from fluid(s) that were in equilibrium with the granite. The intimate association of gold with bismuth-tellurium-bearing phases at the Bigorne deposit is assumed to be a consequence of Au scavenging by liquid bismuth-bearing phases; *e.g.*, an example of the ‘bismuth collector’ model (Douglas, 2000; Tooth et al., 2008, 2011). This gold-bearing hydrothermal event may have enhanced the gold grade in this gold deposit type, which is well represented in the Iberian Variscan belt (*e.g.*, Limarinho deposit: Fuertes-Fuente et al., 2016). This model is also thought to apply to most other granitoid-associated Au deposits in the region, considering the similarity in their structural control, paragenetic evolutions, and chemistry of the ore fluids.

Therefore, gold deposits in the western part of the CIZ were formed by the superposition of several processes and show similar timing of hydrothermal events, suggesting that large-scale late Variscan tectonic processes controlled the hydrothermal history, as consequences of crustal decompression during uplift that is commonly associated with a shift in the far-field stress regime due to a transition from compressional to transpressional settings.

CHAPTER 5 | Bigorne detrital gold

Manuscript 2: Geological Society, London, Special Publications

Characterization of heavy mineral concentrates and detrital gold particles from the Bigorne granite-hosted gold deposit in the Iberian Variscan Belt (2021)

Sara Leal[1,2]*, Alexandre Lima[1,2] and Fernando Noronha[1,2]

[1] Institute of Earth Sciences (Pole-Porto), Porto, Portugal

[2] Department of Geosciences, Environment and Spatial Planning, University of Porto, Porto, Portugal

DOI: https://doi.org/10.1144/SP516-2020-217

➢ Highlights

The Variscan belt in Portugal is characterized by the occurrence of several styles of gold-bearing veins and a small number of alluvial gold deposits, which have been exploited since ancient times (*e.g.*, Ehser et al., 2011; Fonte et al., 2017; Fig. 15-B). Alluvial gold deposits in this area typically occur in close spatial association to areas with known hypogene gold mineralization. The weathering of mineralized bedrock releases detrital gold particles, which are eventually transported and concentrated in streams.

Other workers have used several approaches to link the features of detrital gold particles to hypogene sources(s) for the development of regional exploration models. The morphology, chemistry, and inclusion mineralogy of the gold particles are potential indicators to determine the spatial variation of hypogene mineralization and the mineralization style (*e.g.*, Knight et al., 1999; Townley et al., 2003; Chapman et al., 2009; Moles et al., 2013; Chapman and Mortensen, 2016). Data available from the literature of gold detrital particles in the gold deposits of the Iberian Variscan belt are minimal. However, Barrios et al., 2015 used optical and/or environmental scanning electron microscopy to examine the differences in dimensions and morphological features in gold nuggets and particles from the Tormes Basin, Spain, in the Iberian Massif. Also, K. dos Santos Alves, in 2020, defines three different gold compositional groups (Gr1, 2, and 3) in the Fresnedoso Creek gold placer in the Moraleja Basin (Spain, western Iberian Massif). Chemical analysis of particle cores are as follows: Gr 1 = 89.4–87.4 Au wt.%; Gr 2 = 93.8–92.4 Au wt.% and Gr 3 = 89.2–98.5 Au wt.%, these being consistent with the two primary hypogene sources in the region hosted in the metasediments of the Schist Greywacke Complex.

The present research is the first approach to apply the study of the morphology, microtexture, and chemical features of gold particles from the Bigorne gold deposit to test transport/morphological models, trace the possible source(s) of gold mineralization.

A complementary study of heavy mineral concentrate samples was carried out to provide semi-quantitative data on the abundance of other heavy minerals associated with gold, to reveal particle mobility in the surficial environment, and its potential to identify mineral species linked to gold mineralization or other types of mineralization. In particular, the study provides an opportunity to examine the mineralogy of gold derived from granite-associated mineralization in a first attempt to characterize the composition of gold formed in these environments. The synthesis of gold composition and heavy mineral concentrate signature provides a platform for identifying similar deposit types elsewhere.

5.1 Deposit geology

5.1.1 Hypogene ore

In the Bigorne deposit, gold mineralization occurs as a sheet-vein array (Fig. 16-A), with an NNE-SSW trend, roughly parallel to the Penacova-Régua-Verín fault. The gold-bearing veins are localized within second-and third-order structures (Fig. 15-D). It should be noted that these are not interconnected, multidirectional quartz vein stockworks. Gold mineralization consists of quartz-sulfide veins (Fig. 16-B), oxidized fractures (Fig. 16-C), and disseminated sulfide in zones of strong sericitic (or white mica) alteration (Fig.16-D). The sericitic alteration is restricted to vein selvages and is strongly structurally controlled.

A preliminary study of the hypogene gold has shown three different modes of occurrence (Leal et al., 2019; see chapter 4 for more detailed information). The first comprises small particles of native gold or maldonite, along with native-Bi or hedleyite, infilling cavities in arsenopyrite (Fig. 16-E). The second consists of coarse native gold with high fineness infilling cracks in arsenopyrite and scorodite (Fig. 16-F). The third contains low fineness gold particles associated with later mineral assemblage composed of chalcopyrite (less common type).

5.1.2 Alluvial deposits

The alluvial gold expression of the mineralization is confined to the low-gradient Balsemão River valley, which follows an NNE-SSW lineament parallel to the regional PRVF and maybe in part of a small graben structure (Fig. 17). The alluvial deposit consists of gravel with granite and sericitically altered pebbles, sandy clay, and overlying sandy silt both in the riverbed itself and on its floodplain. In addition, there is a small eluvial deposit comprising gravel with granite and sericitically altered pebbles and sandy silt, as well as a thin soil-organic layer (Fig. 15-D).

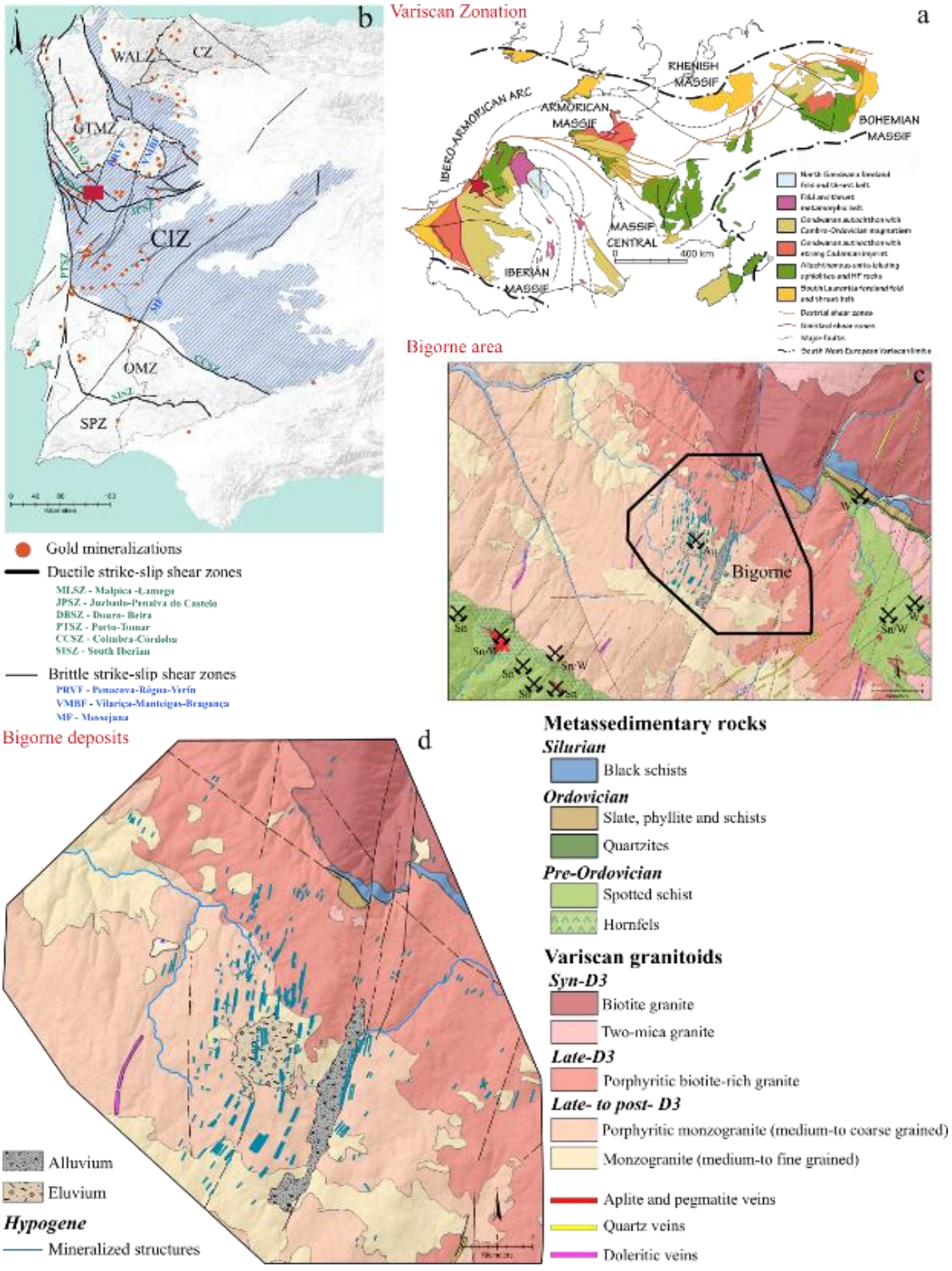

Fig. 15. (A) Schematic map of the different zones in the European Variscan belt (adapted from Pastor-Galán et al., 2012). (B) Map of the Iberian Variscan belt showing major geotectonic zones and main regional structures (adapted from Díez Fernández and Arenas, 2015). The main gold occurrences in Iberia. (C) Geological map of the Bigorne area (adapted from Teixeira et al., 1968). The polygon shows the location of the Bigorne deposit. (D) Host rocks of the Bigorne deposit showing the mineralized structures (hypogene mineralization) and the detrital deposits.

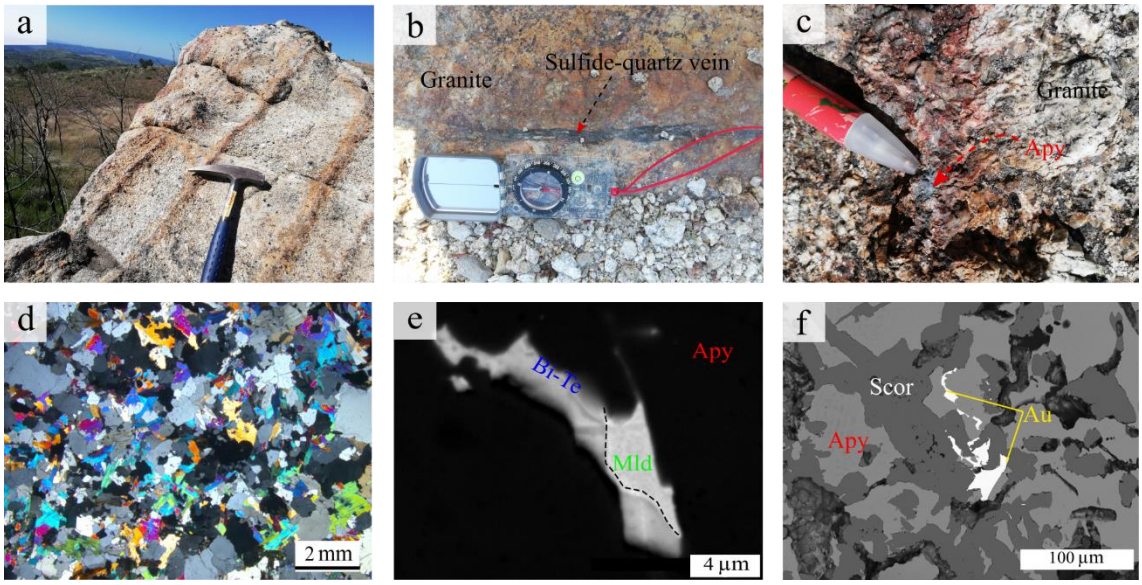

Fig. 16. (A) Representative outcrop from hypogene Bigorne gold deposit. (B) Example of a sulfide-quartz mineralized vein. (C) Oxidized fracture with disseminated arsenopyrite. (D) Mica-selvage. (E) (F) Gold assemblages in the hypogene deposit.

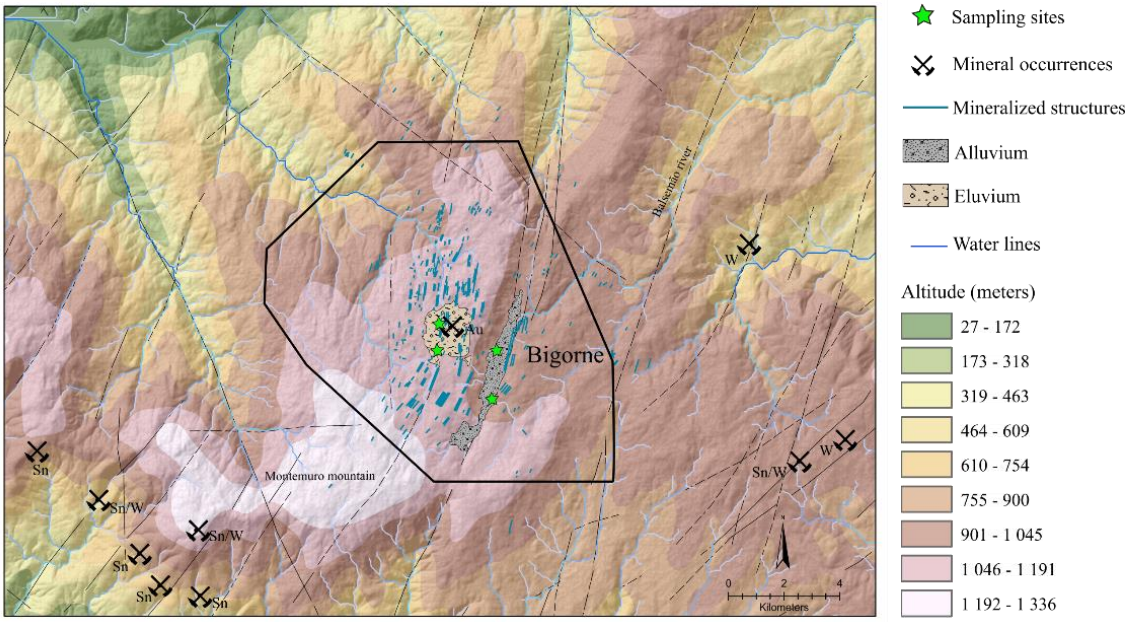

Fig. 17. Bigorne drainage network and mineral occurrences in the study area.

5.2 Sampling and analytical methods

The application of heavy mineral studies is beneficial in providing geochemical and mineralogical guides for gold exploration (Moles and Chapman, 2019). Gold particles were collected according to the field technique described by Leake et al. (1997), allowing the sampling of heavy mineral concentrates and gold particles. In most deposits in Portugal, the gold has a very fine particle size (usually less than 50µm), which is not favorable for gold detrital deposit formation by the standard hydrodynamic and

mechanical placer processes. Therefore, in the Bigorne area, time constraints in the field coupled with a low abundance of particles resulted in a smaller population size, which could be influenced the conclusions. The detrital gold abundance at sample localities was very low, with a recovery rate of one or two particles per hour or less.

Samples were collected in the Bigorne alluvial and eluvial deposits (Fig. 17). Heavy mineral concentrates were obtained by routine techniques using a sluice-box and a pan in the field. Field-panned heavy mineral concentrates were refined at the University of Porto using density separation (bromoform) to remove mineral particles with a specific gravity of less than 2.84. To simplify the picking of gold particles, the heavy mineral concentrates were manually separated into two fractions, magnetic and nonmagnetic, using an iron-neodymium magnet.

Mineralogical and geochemical studies of the heavy mineral concentrates were undertaken to provide semiquantitative data on the amount and composition of the heavy minerals. Initial characterization was made by Portable X-ray Fluorescence (p-XRF) analyzer (X-MET7500). The X-MET 7500 analyzer has a 45 kV Rh tube and a high-resolution Silicon-drift detector (SDD). Element contents were presented as an average value calculated by the analyzer based on three separate measurements at the same point. The total time of a single measurement was set as 60 seconds. Three spots of analysis were made in each sample, and between each sample, a SiO2 blank was used. Samples were analyzed for major elements (Al, Ca, Fe, K, Mg, Na, Si, Ti, P, S) and trace elements (Ag, Ba, Be, Cd, Co, Cr, Cu, Mn, Ni, Pb, Sn, Sr, V, Zn, Zr, Th, U). Only elements that showed results above 0.1wt. % were used in this research due to the detection limit of the equipment. Identification of specific mineral species in heavy mineral concentrate samples was carried out using a FlexSEM1000 scanning electron microscope (SEM) operated at 15 kV, fitted with an EDS system, at the University of Porto.

Gold particles were handpicked from the nonmagnetic fraction under a binocular microscope. The particles were photographed to record their morphological characteristics before being sorted according to size, mounted in epoxy resin blocks, and polished. The alluvial and eluvial gold particles were describe according to morphological characteristics, based on the classification scheme of Barrios et al. (2015). Quantitative analysis of gold and alloying elements (Table 11) was carried out using SEM-EDS and EPM (Cameca SX100) at the University of Oviedo (Spain). The analyses were performed on gold particles with the following operating conditions: 20 kV, 100 nA, and a beam size of 5 μm. The acquired X-ray intensities were corrected for atomic number, mass absorption, and secondary fluorescence effects using the CAMECA x-phi program. Detection limits were 0.010 wt.% for S, 0.014 wt.% for Fe, 0.027 wt.% for As, 0.173 wt.%

for Au, 0.036 wt.% for Ag, 0.023 wt.% for Cu, 0.062 wt.% for Bi, 0.038 wt.% for Se, 0.035 wt.% for Cd, 0.028 wt.% for Te, 0.018 wt.% for Ni and 0.017 wt.% for Co.

5.3 Results

5.3.1 Heavy mineral concentrates

The presence of specific indicator minerals in detrital materials provides vectors to mineralized areas, aiding detection of anomalous mineralization halos, and in some cases enabling the specific chemical composition of minerals to be correlated with the source. Both alluvial and eluvial material from the vicinity of the Bigorne deposit were characterized in this study. The p-XRF data revealed the compositional variation of the detrital material from each sampling site (Table 9; Fig. 18-19).

The magnetic fraction component of the alluvial and eluvial samples show a striking similarity in heavy mineral specimens (Fig. 18). The geochemical data of the magnetic material in both concentrates are characterized by a strong correlation between Ti, Mn, and Fe (Table 10; Fig. 18-A), which is confirmed by mineralogical examination. The alluvial material has slightly higher values of Ti and Mn, whereas the eluvial material has a high Fe content (Fig. 18). Ilmenite (Ilm) is the most abundant mineral (>95%) in both concentrates (Fig. 18-B-C). Ilmenite was usually found in pure form (Fig. 18-A), but a minor presence of manganese was noticed in some particles confirmed by SEM (Fig. 18-D-E). Some ilmenite particles show monazite inclusions. Discrete particles of wolframite were identified in the magnetic fraction in both concentrates. Other elements are recorded in trace amounts in this fraction, such as Al, K, and Si, that could be attributed to biotite and clay minerals (Fig. 18-B-C-E) as detrital mineral impurities that were mechanically trapped.

The nonmagnetic fraction can provide insights into the possible source of the detrital material (Fig. 19-A) regarding Si, P, Ca, Ti, Fe, Zr, and Ba content. The eluvial material shows higher contents of P, Zr, and Ba than the alluvial material, which could be linked to the high amounts of monazite, apatite, and zircon (Fig. 19-B). The presence of barite in both heavy mineral concentrates suggests a local or proximal source since barite is mechanically unstable during transport in the surficial environment (Moles and Chapman, 2019). Barite commonly occurs in metalliferous hydrothermal veins but also occurs in cementations and superficial environments. The contents of Ca, Ti, and Fe are generally higher in alluvial material due to the higher amount of rutile and titanite (Fig. 19-A-C) in the alluvial sample than in eluvial material. Titanite and Al_2SiO_5 polymorphs (Fig. 19-D) are also recorded in the eluvial material. The abundance of

titanite probably reflects the presence of this mineral as an accessory in the hosted granites. The Al_2SiO_5 polymorphs, probably fibrolite, may be derived from surrounding granites or the metasedimentary rocks of the SGC. Other minerals recorded in alluvial material include monazite and zircon. Vanadium commonly occurs as a substitution for titanium in Ti- and Fe-Ti-oxide minerals such as rutile. The Sn content in alluvial material is attributed to discrete cassiterite particles, which were identified by SEM analysis (Fig. 19-D).

The provenance of cassiterite particles is thought to be from regional sources, i.e., old W-Sn mines on the eastern side of the Bigorne area, which is associated with a graben structure (Fig. 17). The wolframite crystals in both concentrates could be connected with some of the composition and mineralogy of the underlying granites and mineralized quartz-sulfide veins in the Bigorne area and/or as from wolframite present in mineralized bodies from old W-Sn mines. The samples revealed similar mineralogy to the Bigorne granites, whose principal minerals are quartz, K-feldspar, plagioclase, biotite, and muscovite, with apatite, monazite, titanite, zircon, rutile as accessory minerals, whereas chlorite, calcite, epidote, and other opaque minerals are secondary minerals resulting from hydrothermal alteration and weathering. Overall, the heavy mineral concentrate composition is consistent with derivation from the local Bigorne hosted ilmenite series granites and some point sources (*e.g.*, old W-Sn mines) east of the Bigorne area, which have been dispersed within a few kilometers in the region. The gold in the Bigorne deposit is hosted in sulfides, which are not preserved in the oxidizing surficial environments. However, the sample suite provides an opportunity to correlate a specific heavy mineral concentrate signature with detrital gold particles.

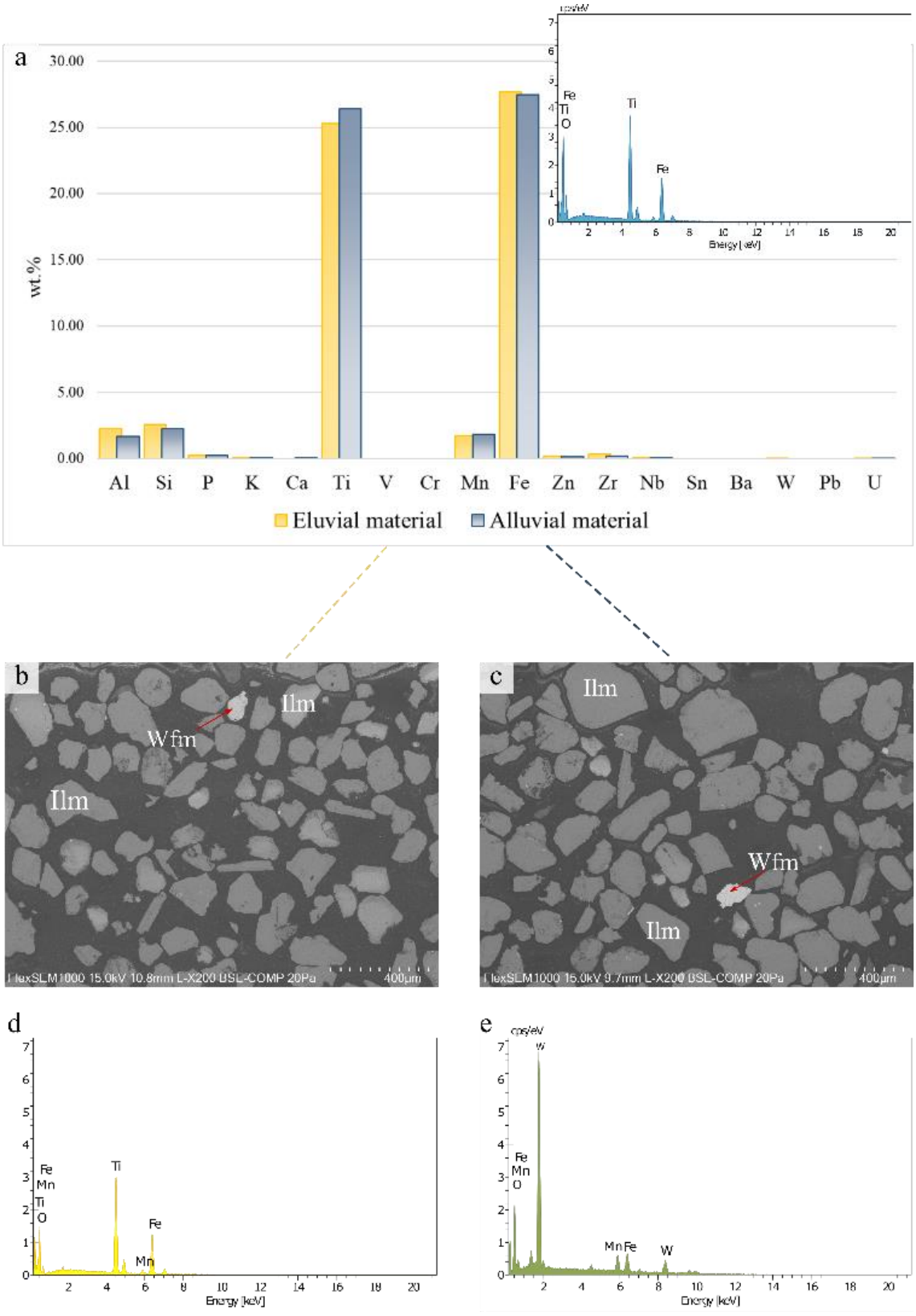

Fig. 18. (A) Semiquantitative chemical analyses from magnetic fraction from alluvial and eluvial material. SEM images of magnetic fraction from eluvial (B) and alluvial (C) material. (D) EDS spectra are showing the content of Mn in ilmenite particles. (E) EDS spectra are showing the wolframite composition.

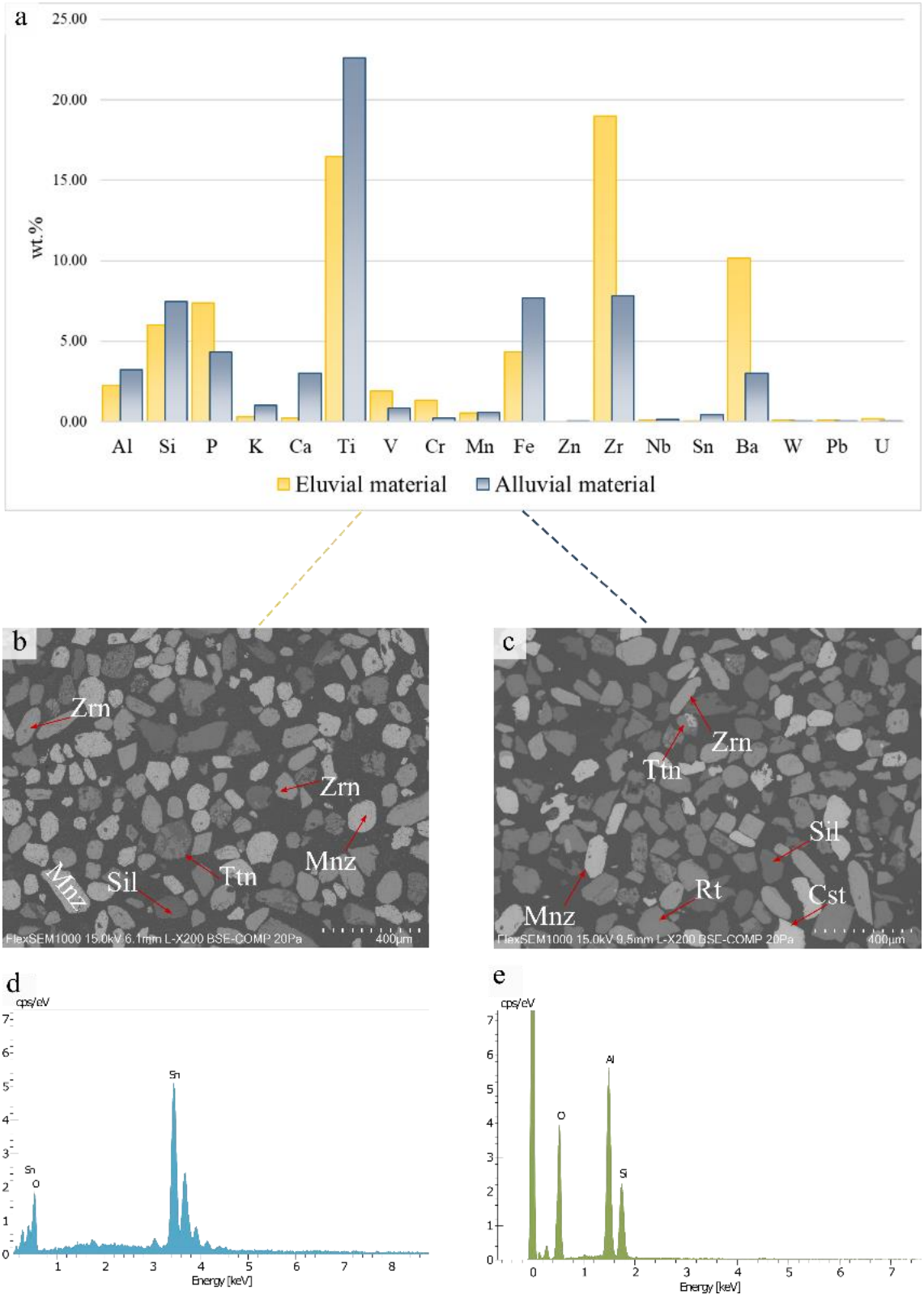

Fig. 19. (A) Semiquantitative chemical analyses from nonmagnetic fraction from alluvial and eluvial material. (B) SEM images of nonmagnetic fraction from alluvial material. (C) Cassiterite particle from alluvial samples (D) Overall SEM images from eluvial material. (E) Details from eluvial material.

Table 9. Chemical composition (wt.%) of p-XRF analysis for heavy mineral concentrate samples.

Sample type		Nº of samples	Al	Si	P	K	Ca	Ti	V	Cr	Mn	Fe	Zn	Zr	Nb	Sn	Ba	W	Pb	U
Eluvial material	Non-magnetic fraction	1	1.94	5.71	8.00	0.30	0.22	13.86	2.19	1.55	0.61	4.53	0.00	21.20	0.08	0.09	11.72	0.07	0.12	0.21
		2	1.94	5.91	7.75	0.30	0.24	14.44	2.05	1.41	0.58	4.73	0.00	20.70	0.10	0.05	11.29	0.08	0.11	0.20
		3	2.96	6.48	6.43	0.40	0.23	21.09	1.49	0.99	0.42	3.75	0.00	15.08	0.09	0.04	7.48	0.10	0.08	0.13
		$\bar{x}$	2.28	6.03	7.39	0.33	0.23	16.46	1.91	1.32	0.54	4.34	0.00	18.99	0.09	0.06	10.16	0.08	0.11	0.18
		σ	0.48	0.33	0.69	0.05	0.01	3.28	0.30	0.24	0.08	0.42	0.00	2.77	0.01	0.02	1.91	0.01	0.02	0.04
	Magnetic fraction	4	2.31	2.59	0.24	0.08	0.00	25.12	0.00	0.00	1.67	27.80	0.20	0.34	0.08	0.00	0.00	0.06	0.00	0.00
		5	2.27	2.54	0.24	0.09	0.00	25.21	0.00	0.00	1.74	27.74	0.20	0.34	0.08	0.00	0.00	0.05	0.00	0.01
		6	2.14	2.56	0.22	0.09	0.00	25.53	0.00	0.00	1.74	27.48	0.20	0.40	0.08	0.00	0.00	0.04	0.00	0.00
		$\bar{x}$	2.24	2.56	0.23	0.09	0.00	25.29	0.00	0.00	1.72	27.67	0.20	0.36	0.08	0.00	0.00	0.05	0.00	0.00
		σ	0.07	0.02	0.01	0.00	0.00	0.18	0.00	0.00	0.03	0.14	0.00	0.03	0.00	0.00	0.00	0.01	0.00	0.00
Alluvial material	Non-magnetic fraction	7	3.55	8.50	4.29	1.13	3.57	22.41	0.88	0.00	0.45	6.07	0.04	7.68	0.14	0.41	2.79	0.00	0.04	0.07
		8	3.25	7.26	4.20	1.01	2.89	22.82	0.81	0.33	0.60	7.85	0.06	7.95	0.13	0.43	2.93	0.04	0.05	0.07
		9	2.95	6.62	4.49	0.89	2.58	22.60	0.85	0.37	0.73	9.21	0.05	7.85	0.16	0.52	3.32	0.00	0.06	0.08
		$\bar{x}$	3.25	7.46	4.33	1.01	3.01	22.61	0.85	0.23	0.59	7.71	0.05	7.82	0.14	0.45	3.01	0.01	0.05	0.08
		σ	0.25	0.78	0.12	0.10	0.42	0.17	0.03	0.17	0.11	1.29	0.01	0.11	0.01	0.05	0.22	0.02	0.01	0.00
	Magnetic fraction	10	1.80	2.24	0.21	0.10	0.07	26.60	0.00	0.00	1.69	27.37	0.12	0.18	0.11	0.00	0.00	0.00	0.00	0.00
		11	1.61	2.20	0.21	0.11	0.06	26.36	0.00	0.00	1.87	27.73	0.17	0.21	0.10	0.00	0.00	0.00	0.00	0.00
		12	1.65	2.40	0.24	0.12	0.07	26.33	0.00	0.00	1.91	27.31	0.19	0.23	0.10	0.00	0.00	0.00	0.00	0.00
		$\bar{x}$	1.69	2.28	0.22	0.11	0.07	26.43	0.00	0.00	1.82	27.47	0.16	0.21	0.10	0.00	0.00	0.00	0.00	0.00
		σ	0.08	0.09	0.01	0.01	0.00	0.12	0.00	0.00	0.09	0.18	0.03	0.02	0.00	0.00	0.00	0.00	0.00	0.00

$\bar{x}$ - mean; σ – standard deviation.

Table 10. Correlation matrix for p-XRF analysis for heavy mineral concentrate samples (red values > 0.7; green values <(-0.7)).

	Al	*Si*	*P*	*K*	*Ca*	*Ti*	*V*	*Cr*	*Mn*	*Fe*	*Zn*	*Zr*	*Nb*	*Sn*	*Ba*	*W*	*Pb*	*U*
Al	1.00																	
Si	0.81	1.00																
P	0.35	0.80	1.00															
K	0.87	0.89	0.47	1.00														
Ca	0.84	0.79	0.30	0.98	1.00													
Ti	-0.08	-0.58	-0.93	-0.22	-0.07	1.00												
V	0.23	0.71	0.99	0.34	0.18	-0.97	1.00											
Cr	-0.04	0.46	0.90	0.06	-0.12	-0.95	0.95	1.00										
Mn	-0.68	-0.96	-0.92	-0.74	-0.60	0.74	-0.85	-0.67	1.00									
Fe	-0.59	-0.93	-0.96	-0.69	-0.54	0.80	-0.90	-0.74	0.99	1.00								
Zn	-0.46	-0.85	-0.95	-0.59	-0.44	0.80	-0.91	-0.78	0.95	0.96	1.00							
Zr	0.20	0.68	0.98	0.31	0.13	-0.97	1.00	0.96	-0.84	-0.89	-0.90	1.00						
Nb	0.59	0.59	0.17	0.83	0.87	0.07	0.05	-0.18	-0.42	-0.38	-0.37	0.01	1.00					
Sn	0.79	0.78	0.37	0.95	0.96	-0.14	0.24	-0.01	-0.62	-0.58	-0.48	0.20	0.90	1.00				
Ba	0.08	0.59	0.95	0.19	0.02	-0.98	0.99	0.98	-0.77	-0.83	-0.85	0.99	-0.08	0.10	1.00			
W	0.04	0.16	0.52	-0.23	-0.39	-0.59	0.57	0.68	-0.37	-0.38	-0.34	0.60	-0.61	-0.34	0.63	1.00		
Pb	0.23	0.71	0.99	0.36	0.19	-0.96	1.00	0.95	-0.86	-0.91	-0.91	1.00	0.08	0.27	0.98	0.56	1.00	
U	0.17	0.66	0.98	0.30	0.13	-0.98	1.00	0.96	-0.82	-0.87	-0.89	1.00	0.02	0.21	0.99	0.57	0.99	1.00

5.3.2 Gold particle morphology

Alluvial and eluvial gold particles from surficial materials in the vicinity of the Bigorne deposit exhibited variable sizes and shapes (Fig. 20).

The alluvial particles population ranges from 100 to 300µm in the longest dimension. These gold particles have a rounded to well-rounded shape and range from discoidal (Fig. 20-A-B) to subdiscoidal (Fig. 20-C). Their outline is relatively regular, and surface topography tends to be smooth without cavities.

The eluvial population exhibit size fractions from 232µm to 400µm and range from sub-angular to sub-rounded. Some particles display irregular surfaces due to the presence of cavities, most of which were filled with clay minerals and/or hydrothermal quartz (Fig. 20-E).

Primary imprints are absent, whereas one particle shows clear evidence of hammering. Inclusions of primary minerals in gold particles such as quartz, sulfides, and sulfosalts were not observed in the particles studied. In the absence of other studies of gold from granite-hosted mineralization, it is impossible to speculate on the likely inclusion abundance. However, it is important to note that in studies of detrital gold elsewhere, failure to identify inclusions in a small sample set does not indicate their absence (Chapman et al., 2021).

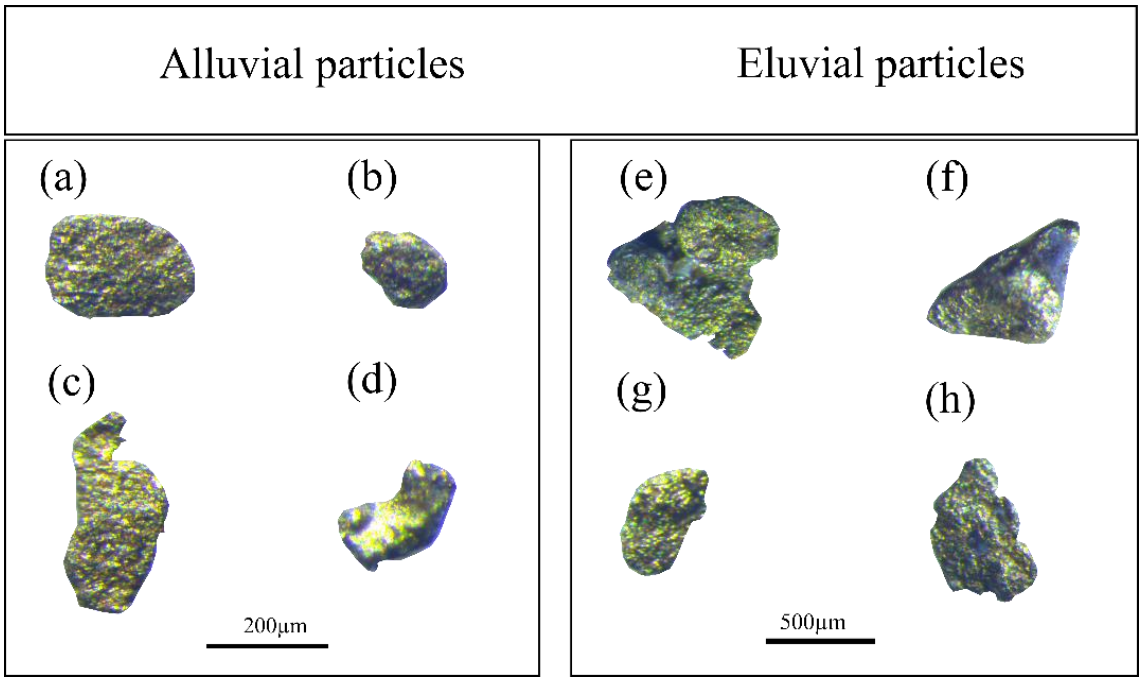

Fig. 20. Representative gold particles from eluvial and alluvial material from Bigorne deposit.

5.3.3 Gold microchemistry

Overall, the gold compositions in the hypogene gold and that from the alluvial and eluvial samples are mainly a binary Au-Ag alloy (Table 11 and Fig. 21-A-B). Trace elements occur in low quantities (below detection limits) except for a few analyses that show detectable Cu values. The electron microprobe data enables the gold particles to be categorized into two populations (alluvial and eluvial), supported by particle morphology.

As a whole, hypogene gold occurs as native gold and shows a range from 3.7 to 22.7 wt.% of Ag in the alloy, with minor Cu (0.01-0.12 wt.%) (Table 11). The eluvial gold particles show an Ag range of 0.5 to 12.4 wt.% compared to alluvial particles, which show a tight distribution around 5 wt.% Ag. Analysis of the eluvial particles revealed a relatively narrow Cu content range (0.01 to 0.07 wt.%), whereas the small number of alluvial particles exhibited Cu ranging from 0.02 to 0.25 wt.% (Fig. 21-B). Copper concentrations within individual gold particles vary (Fig. 21-C-F). Fig. 21-C shows a gold particle largely homogenous concerning Au and Ag content, but with variations in Cu content from 0.02 wt.% to 0.05 wt.%, which given the detection limit of 0.02 wt.% indicates intra-particle heterogeneity. The gold particle shown in Fig. 21-D exhibits some Au-rich areas (which may be attributed to surficial alteration: Hough et al., 2009) and Au-Ag heterogeneity within particle core areas, but here, there does not appear to be a correlation between Ag and Cu values.

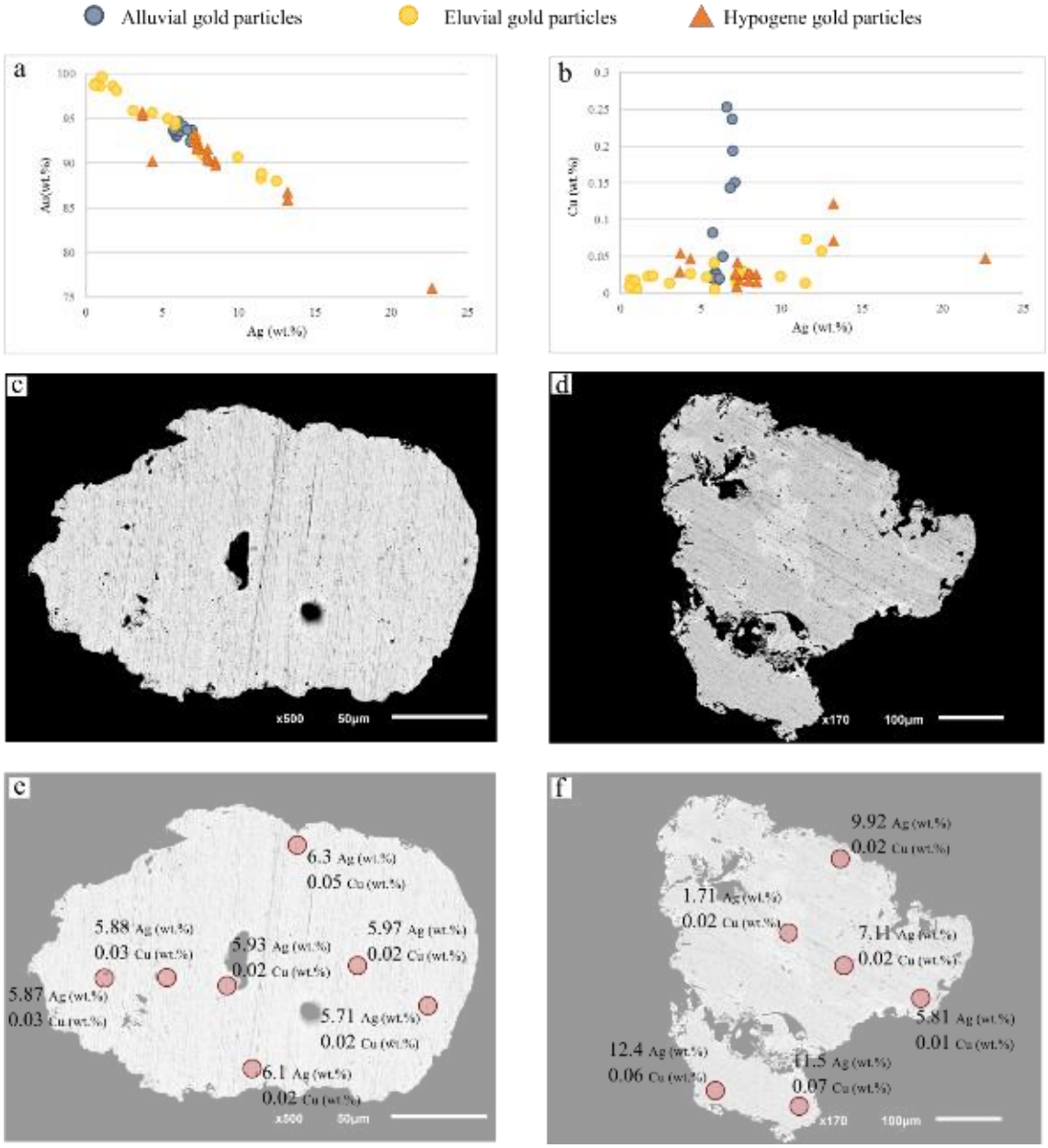

Fig 21. (A) Co-variance of Ag and Au for gold particles from Bigorne deposits. (B) Co-variance of Ag and Cu for gold particles from Bigorne deposits. (C) Representative gold particle from alluvial material. (D) Representative gold particle from eluvial material. (E) Spatial Ag and Cu content variation in alluvial gold particles. (F) Detail of zonal variation (Ag and Cu content) in particles from eluvial material. (C) (D) (E) (F) in BSE.

Table 11. Representative chemical analysis (wt.%) of gold particles from Bigorne deposits.

	Nº of particles	S	Au	Cu	Ag	Gold alloy
Eluvial	1	0.03	90.71	0.02	9.92	901.46
	2	0.04	92.95	0.02	7.11	928.94
	3	0.03	88.35	bd	11.45	885.31
	4	0.03	88.06	0.06	12.43	876.3
	5	0.03	88.93	0.07	11.47	885.76
	6	0.03	94.35	0.01	5.81	941.97
	7	0.03	98.67	0.02	1.71	982.96
	8	0.03	95.68	0.03	4.3	956.97
	9	0.04	94.74	0.04	5.79	942.42
	10	0.02	98.23	0.02	1.97	980.33
	11	0.03	99.72	bd	0.99	990.18
	12	0.04	98.98	bd	0.62	993.74
	13	0	91.06	0.03	7.58	923.18
	14	0	92.17	bd	7.2	927.54
	15	0	90.54	0.02	7.22	926.12
	16	0	92.07	0.02	7.25	927.02
	17	0	91.51	0.03	7.33	925.88
	18	0.03	95.96	bd	3.05	969.22
	19	0.03	98.67	bd	0.87	991.26
	20	0.03	95.06	0.02	5.34	946.8
	21	0.03	98.83	bd	0.52	994.78
	22	0	93.05	0.03	5.87	940.66
	23	0	93.31	0.03	5.88	940.68
	minimum	0	88.06	0.01	0.52	876.3
	maximum	0.04	99.72	0.07	12.43	994.78
	mean	0.02	93.98	0.03	5.73	942.59
Alluvial	24	0.00	93.05	0.03	5.87	940.66
	25	0.00	93.31	0.03	5.88	940.68
	26	0.00	93.18	0.02	5.94	940.09
	27	0.00	94.71	0.02	5.98	940.65
	28	0.00	93.62	0.02	5.71	942.47
	29	0.00	93.58	0.02	6.10	938.77
	30	0.00	94.17	0.05	6.33	937.03
	31	0.04	92.81	0.15	7.07	929.23
	32	0.03	93.75	0.24	6.90	931.47
	33	0.03	92.82	0.19	6.94	930.46
	34	0.02	92.46	0.14	6.78	931.65
	35	0.01	93.86	0.08	5.71	942.61
	36	0.03	93.78	0.25	6.57	934.52
	minimum	0.00	92.46	0.02	5.71	929.23
	maximum	0.04	94.71	0.25	7.07	942.61
	mean	0.01	93.47	0.10	6.29	936.95

Hypogene	1	0.07	92.01	-	7.37	926
	2	0.06	90.30	0.03	8.08	918
	3	0.05	92.37	-	7.24	927
	4	0.11	95.38	0.03	3.67	963
	5	0.11	95.73	0.05	3.71	963
	6	2.13	90.23	0.05	4.35	954
	7	0.08	90.22	0.03	8.45	914
	8	0.06	89.78	-	8.47	914
	9	0.10	90.88	0.03	7.90	920
	10	0.12	90.48	0.03	7.98	919
	11	0.10	91.61	0.02	7.97	920
	12	0.08	92.81	0.03	7.11	929
	13	0.09	91.67	0.04	7.27	927
	14	0.08	93.22	0.03	7.14	929
	15	0.02	85.89	0.07	13.20	867
	16	0.02	86.72	0.12	13.21	868
	17	0.02	75.98	0.05	22.65	770
	minimum	0.02	75.98	0.02	3.67	770
	maximum	2.13	95.73	0.12	22.65	963
	mean	0.19	90.31	0.04	8.57	913

"–" means below the detection limit.

5.4 Discussion

Leal et al., 2019 recorded that hypogene gold particles from Bigorne deposit with higher Cu content tend to be associated with lower fineness gold, linked with the late Cu-bearing mineral assemblages (Table 11). This mineral association has also been report in Limarinho and Penedono deposits (Fuertes-Fuente et al., 2016; Neiva et al., 2019).

The variation of Cu within broadly homogenous Au-Ag alloys in gold detrital particles has been reported previously (Chapman et al., 2021). It seems likely to reflect subtle changes in the mineralizing fluid and/or conditions during gold deposition. Several authors have speculated on the potential temperature control on Cu content in Au-Ag alloys (*e.g.*, Antweiler and Campbell 1977; Gas'kov et al., 2017). The relatively high values observed are associated with the hypothesis of gold derivation from a relatively high-temperature system.

Various authors have noted the presence of gold within granite-hosted mineralization (Pirajno and Bentley 1985; Cooper and Stanley 1990; Thompson et al., 1999; Cave et al., 2019). To date, there has been no systematic reporting of compositional characteristics of gold with granitic associations. Cave et al., 2019 proposed the formation of visible gold via a Bi-collector model. Hence, their analyses of gold from various stages of mineralization may not be more widely applicable. Pirajno and Bently

(1985) reported that gold from the gresenised granite cupolas of Kirwans Hill and Batemans Creek, New Zealand contained around 2.7 wt.% Ag. Ehser et al., 2010 reported Ag means ranging from 3 - 38 wt.% and Cu means of 0.0022 – 0.039 wt.% in various samples of gold from Cornwall in the vicinity of granite mineralization. However, it seems likely that the majority of these particles are associated with later stage more distal and lower temperature mineralization than that at Bigorne.

The sample set presented here is the first to document compositional characteristics of gold from a granite-hosted vein system. Despite the small sampling size, some initial observations can be made. The microfabrics observed in the gold particles do not indicate any supergene contributions. In general, the gold microchemistry from the Bigorne deposit is similar to the range values defined for Phanerozoic orogenic systems (Moles et al., 2013). However, the low Ag content and Cu high content detected in some gold particles exceed the range observed in Phanerozoic orogenic systems, better linking to that observed in gold particle studies from some specific magmatic-hydrothermal systems (Chapman et al., 2017; 2018) and in the broader consideration of gold from porphyry deposits (Morrison et al., 1991). The variations in gold composition linked with specific mineral assemblages provide the best explanation for the populations of eluvial and alluvial particles recovered here. The gold particles from eluvial material have chemical compositions consistent with coming directly from the hypogene mineralization, whereas the alluvial gold, which could be speculated coming from different sources. Understanding the auriferous vein mineralogy permits speculation on the inclusion suite, which could be expected if larger sample suites were available: e.g., chalcopyrite, arsenopyrite, and Bi- bearing minerals.

These methodologies were applied in Castromil and Numão deposits (Fig. 2-B) unsuccessfully. The detrital material in these locations has no gold particles, possibly due to the hypogene gold particles size (less than 50µm).

The synthesis of the gold compositional signature with that of the heavy mineral suite provides a holistic mineralogical template for identifying similar mineralization elsewhere. The data set will evolve into a helpful exploration tool with further study in this area and locations with similar geology.

5.5 Conclusions

The primary mineralization source of Bigorne is well known, and the presence of quartz-sulfide veins in the region provides a significant constraint to test transport/morphological models in the area. The results reported here emphasize the usefulness of p-XRF analyzers in geochemical exploration and demonstrate that they involve quick and easy

methods to collect geochemical data for tracing mineralization sources, thus providing a basis for more targeted gold-particle studies. In this case, p-XRF analyses identified resistant ore minerals such as cassiterite and wolframite, which clearly indicated local W-Sn mineralization.

The limited amount of gold compositional data generally shows low Ag contents and some particles with relatively high Cu content, consistent with derivation from the granite-hosted mineralization. The variation in Au-Ag alloy composition of the gold particles is most likely a consequence of the temporal and spatial evolution of the mineralizing system and the compositional continuum consistent with a genetic relationship. Compositional variation within and between gold particles concerning Cu may be further evidence of temperature fluctuations within the depositional environment.

In the future, it will be necessary to have an extended sampling area in the Bigorne area and test this approach in other gold deposits in the NW of Iberian Massif, taking into account the results and constraints resulting from this study. Such data sets will establish the compositional signature of articles from granite-hosted gold deposits. Characterization of gold from these deposits provides an additional indicator mineral to those commonly ascribed to granite-greisen W-Sn mineralization.

CHAPTER 6 | Numão deposit

Manuscript 3: Ore Geology reviews (*under review*)

Numão gold deposit in the Iberian Variscan belt, northern Portugal: ore features and mineralization controls. A gold deposit in a W-Sn metallogenic province. (2021)

Sara Leal[1,2]*, Alexandre Lima[1,2], John Morris [3], Miguel Pedro [3], Fernando Noronha [1,2].

[1] Institute of Earth Sciences (Pole-Porto), Porto, Portugal

[2] Department of Geosciences, Environment and Spatial Planning, University of Porto, Porto, Portugal

[3] MINAPORT - Minas de Portugal, Lda

Highlights:

Au, Au-W and W-Sn deposits are widespread in the GTMZ and CIZ of the Iberian Variscan belt (*e.g*., Corcoesto (Au), Castromil (Au), Tresminas (Au), Jales (Au), Tabuaço (W-Sn), Barruecopardo (W-Au), Panasqueira (W-Sn), El Cabaco (W-Au), Los Santos (W); Fig. 22-A-B). The association between gold and tungsten in gold deposits has long been recognized in OGD and IRGD (*e.g*., Goldfarb et al., 2005; Brugger et al., 2008; MacKenzie et al., 2017; Timón-Sánchez et al., 2019; Cheval-Garabédian et al., 2021). Furthermore, in Au-W deposits, tungstates can predate and/or are contemporaneous with gold deposition, such as in the Val-d'Or district, Canada (Beaudoin and Pitre, 2005), Macraes deposit, in New Zealand (MacKenzie et al., 2017), El Cabaco deposit, in Spain (Timón-Sánchez et al., 2019) and Bonnac deposit, in French Massif Central (Cheval-Garabédian et al., 2021).

Several gold-bearing systems in NW of the Iberian Variscan belt have minor tungsten enrichment, usually as scheelite ($CaWO_4$) and lesser as wolframite ($(Fe,Mn)WO_4$). However, no significant Au-W resource has been identified thus far in Portugal. Despite the potential economic importance of these tungsten occurrences, little work has been done to examine the relation of tungsten minerals with the gold mineralizing systems as a whole.

Numão is a gold deposit in northern Portugal's "Douro Scheelite belt" making part of the vast Iberian W-Sn metallogenic province (Goinhas, J. 1985; Martins, 2012) (Fig. 22-C). This belt incorporates a significant quantity of W deposits in calc-silicate rocks, usually skarns and quartz veins. However, most of them were known long before the belt's Au potential was yet established. Therefore, the Numão deposit is an excellent example of an Au-(W) deposit in the Iberian Variscan belt.

No published data on the local geology and mineralization type at Numão Au-(W) deposit. The main goal of this paper was the acquisition and interpretation of new petrographic, geochemical, and stable isotope data to constrain the deposit formation

conditions. The obtained results could contribute to an integrated genetic model of Phanerozoic gold deposits in the European Variscan belt. These observations are significant for interpreting relationships between gold and tungsten enrichment processes in other gold deposits in the Iberian Variscan belt. Furthermore, Numão obtained data can provide future constraints and implications for gold exploration in others Au deposits with similar metal associations and mineralization styles worldwide.

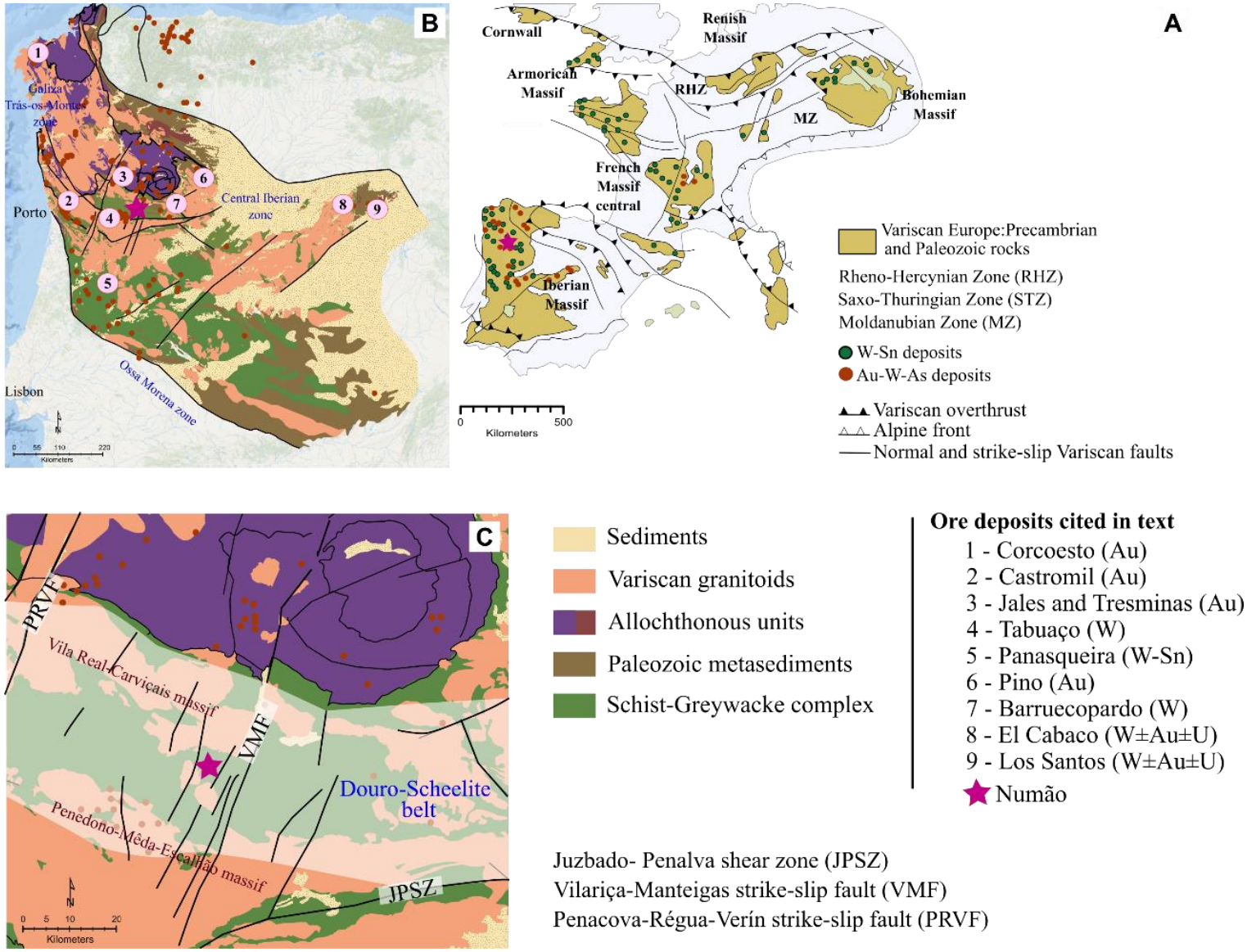

Fig. 22. (A) Map of the Variscan belt in central and western Europe (modified from Díez-Montes, 2007; Timón-Sánchez et al., 2019) and major W-Sn and Au-W-As deposits. (B) Geological sketch of the Western Variscan Europe (modified from Martínez-Catalán et al., 2007; Villaseca et al., 2014) and the Au, Au-W and W-Sn cited in the text. (C) Simplified regional geological map of the Numão area.

6.1 Local geology setting

The Numão area is located in the CIZ, in northern Portugal. The CIZ represents the autochthonous of the axial domain of the Iberian Variscan belt and contains Gondwanan affinity rocks (*e.g.*, Murphy et al., 2008; Pastor-Galán et al., 2013; Gutiérrez-Marco et al., 2017) with Barrovian and Buchan metamorphism and is intruded by igneous rocks (*e.g.*, Díez Balda, 1995; Dias et al., 1998; Gutiérrez-Alonso et al., 2018; Pereira et al., 2018). The Numão area is within the east part of a narrow W-E trending metamorphic belt (Ribeiro et al., 1990; Moreira et al., 2010). This belt is enclosed by syn-D3 two-mica granite massifs (Penedono-Mêda-Escalhão massif to the south, and by the Vila Real-Carviçais massif to the north: Ferreira da Silva et al., 1989; Pereira et al., 2018). In addition to the granites mentioned above, more two circumscribe granitic plutons intruded the metasediments from the W-E-metamorphic belt in this area (Ferreira da Silva et al., 1989): i) syn-to late-D3 Numão granite: a muscovite- biotite granite; and, ii) post-D3 Freixo de Numão granite: biotite-rich granite (Fig. 23). The W-E metamorphic belt is composed of metasediments to the Pre-Ordovician "Schist Greywacke Complex" (SGC) integrated into the so-called "Douro Group" (Sousa, 1982). From stratigraphical and palaeogeographical information, the SGC has been defined as the Super Group Dúrico–Beirão, consisting of "Douro group" and "Beiras group" (Oliveira et al., 1992). The “Douro Group” is composed of several formations Bateiras, Ervedosa do Douro, Rio Pinhão, Pinhão, and Desejosa, from the older to the younger age (Fig. 23; Sousa, 1982).

In the Numão area, there are predominantly metasedimentary rocks from two different units, Pinhão and Desejosa, of the "Douro group", characterized by metapelitic rocks interlayered metagreywacke and calc-silicate rocks. The Pinhão unit, consisting of a greenish-grey colored, thin bedding sequence, is characterized by psammitic (quartz-rich) and pelitic (mica-rich) layers with magnetite crystals and more irregularly pyrite crystals. The Desejosa unit is defined by the presence of stripped phyllites resulting from a thin inter-changing of dark with light layers and metagreywackes (Fig. 23). Calcium-rich layers in the metasedimentary sequences from the SGC are common and represented by calc-silicate rocks (Ferreira da Silva et al., 1989). The metasedimentary rocks in the northern part of the Pinhão and Desejosa Formation have been metamorphosed and range from chlorite to biotite facies, increasing grade toward the syn-kinematic two-mica granite massifs or in the (Ferreira da Silva et al., 1989).

The main Variscan deformation phase in the area is D1 and induced the formation of broad zones gently folded bounded by coeval narrow bands emphasizing more substantial deformation (Ribeiro et al., 1990; Moreira et al., 2010). The D1 folds trend WNW-ESE, with sub-horizontal fold axes and has associated an S1 cleavage. During

the D3, upright open folds with associated crenulation cleavage (S3) were formed; these folds are almost homoaxial with D1 folds.

This sequence corresponds to a succession of large amplitude anticlines and synclines, with an axial trace N100º-N150º (Fig. 22-C: Ribeiro et al., 1990; Moreira et al., 2010). This geometry shows an extensive area with intense strain partitioning with lateral continuity, interrupted by NNE-SSW faults, such as the VMF. Other regional fault systems crosscut the E-W, NNW-SSE, and NW-SE. The ca. 220 km long VMF (Fig. 22-C) shows a left-lateral offset of up to 9 km in the Variscan basement resulting from the recurrent activity. The NNE-SSW trending faults were considered primary dextral faults and later became sinistral during reactivation in the late Variscan and Alpine Orogeny (Ribeiro et al., 1990; Marques et al., 2002, Cabral, 2012). Marques et al. (2002) used K-Ar in muscovite and obtained a minimum age of ca. 312 Ma for VMF.

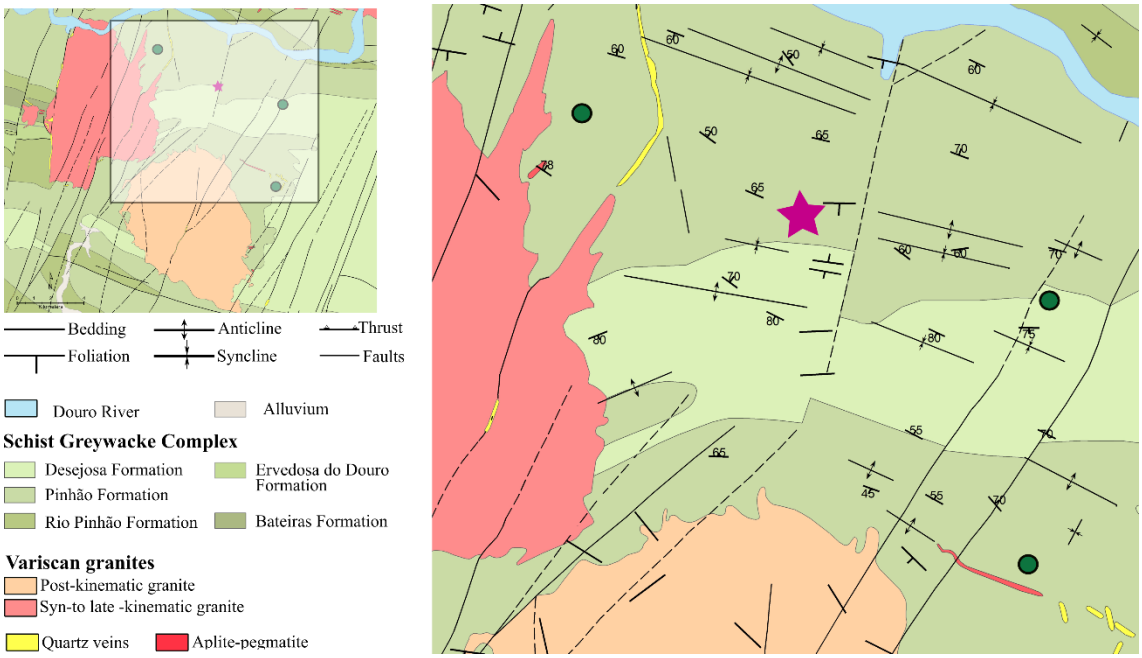

Fig. 23. Geological map of local geology at Numão area (modified from Ferreira da Silva et al., 1989).

6.2 Sampling technique and study methodology

The sampling strategy was to obtain a demonstrative set of all host rock types, mineralized structures, and hydrothermal alterations in the Numão area. This study is based on data from 41 diamond drill-cores from Numão prospect. In addition, detailed mapping of structural and lithological features was conducted in the Numão underground mining works and outcrops in surrounding areas. Twelve of the 41 drill holes were chosen for detailed logging and sampling because they allowed the observation of the different features of host rocks, hydrothermal alteration areas, and mineralized structures.

6.2.1 Petrography and mineralogy

Detailed petrography was performed in forty thin polished sections to characterize the host rock, hydrothermal alteration, and mineralized structures. These samples were carefully selected from the drill-cores at different depths and also from underground mining works. The petrographic studies were performed at the Institute of Earth Sciences (ICT-University of Porto) by transmitted and reflected light microscopy. Complementary studies for mineral characterization assemblages were done at the Materials Centre of the University of Porto (CEMUP) (equipment: FEI Quanta 400 FEG-ESEM/EDAX Genesis X4M). Abbreviations of minerals were adopted from Kretz (1983) and Whitney and Evans (2010).

6.2.2 Mineral chemistry

Chemical analyses in silicate and sulfide minerals were performed at the Faculty of Science, Masaryk University (Brno, Czech Republic) using an electron microprobe (EPMA), CAMECA SX100 model. Major elements were determined at 15 keV accelerating voltage, with a 10 nA beam current (5 μm focused beam) an acquisition time between 10 and 20 s for X-ray peak and background.

In sulfides, approximately 100 analyses of trace elements (Au, Ag, Sb, Pb, Bi, Te, Se, Cu, Zn, Co, Ni, Hg) were performed on arsenopyrite and pyrite and also in other gold mineralization-related minerals. The operating conditions for the analysis were a 15 and 25 keV accelerating voltage, with a 20 nA beam current (2 μm focused beam), and 120-180 s count time. The detection limits were determined for the individual measurement. The acquired results are present in appendices 1 and 2, showing only the measurements above the detection limit for each chemical element. Natural and synthetic sulfides, oxides, and native elements were used as reference materials.

6.2.3 Geochemistry

The geochemical analysis is based on the multi-element data from the studied drill-cores provided by MINAPORT company. The multi-element chemical analyses were acquired by ALS Global Ltd. at their laboratories in Sevilha, Spain, during 2017, 2019, and 2020. The chemical reports contain multi-element analyses, including some major and trace elements. The company only reports mineralized samples on multi-element geochemical data sets. Samples were chosen based on host rock lithology, mineralization style, and gold grade. ALS Website: https://www.alsglobal.com/en/s.ervices-and-products/geochemistry.

6.2.4 Principal Component Analysis

The principal component analysis (PCA) is a multivariate statistical technique used to reduce large dataset (Jolliffe and Cadima, 2016). PCA have been applied all over the years in order to describe geochemical/geological processes and provide a practical tool to analyze and interpret large geochemical datasets in a meaningful way (Grunsky et al., 2014; Grunsky and Caritat, 2020).

The geochemical datasets from mining companies usually revealed some issues, such as closure effect, missing values, censoring, and components not measured, merging, leveling different datasets, and inadequate geochemical data (e.g., Aitchison 1986; Van Den Boogaart et al., 2006; Grunsky et al., 2014; Grunsky and Caritat, 2020). The main problem of the Numão geochemical dataset is an inadequate sampling for the geochemical analyzes. The mining company only sent to geochemical analyzes the drill core samples with mineralized structures. So the PCA was used to discriminate the gold mineralization pathfinders, hydrothermal alteration, and intending to constrain some lithological controls if they are present.

The raw data in the Numão dataset were examined before PCA. Cd, Co, Ga, Mo, U, and Sr have been excluded because more than 40% of the data show values below or equal the detection limit (e.g., Hron et al., 2010). The remaining geochemical data contained the complete set of elements without censored data. Accordingly, to Filzmoser et al. (2009), the centered log-ratio (CRL) is a data transformation method using the ratio between each variable and the geometric mean of all values from the dataset and taking the natural logarithm to avoid the closure effect (all components sum to a constant, in our case 100%). A CLR transformation was applied to the remaining data.

PCA is a non-supervised statistical method, and there are several types of PCA (e.g., R-mode and Q-mode) (Neff, 1994; Grunsky et al., 2014) such as i) R-mode is based on variables (chemical elements) and its associations with a set of objects, and ii) Q-mode is based on objects, in our case samples. RQ-mode PCA is helpful for simultaneous interpretation of both element and sample variance on a single diagram - biplot (variables = elements; objects = samples) (Gabriel, 1971; Klovan and Imbrie, 1971; Zhou et al., 1983; Grunsky 2001). The ioGAS™ software (REFLEX 2019) was used to make the statistical calculations (RQ-mode PCA) and graphics.

6.2.5 Isotopes analysis

Isotope analyses were made on quartz and arsenopyrite once these two minerals are the main minerals associated with gold at the Numão deposit. The oxygen, hydrogen, and sulfur isotope compositions were measured in bulk samples because it was

impossible to separate the observed different generations of quartz and arsenopyrite. Six quartz bulk samples were subjected to hydrogen and oxygen isotope analysis and five arsenopyrite bulk samples to sulfur isotope analysis. One pyrite sample from the barren host rocks from Schist Greywacke Complex (SGC) was analyzed. All samples of quartz and arsenopyrite separates were hand-picked and checked under a binocular microscope to ensure the purity of > 98%. The isotope analyses were accomplished in the Stable Isotopes Laboratory of Salamanca University, Spain. The methodologies descriptions were provided by of Stable Isotopes Laboratory of Salamanca University (https://nucleus.usal.es/en/services).

Oxygen isotopes

The oxygen isotope data were acquired in quartz concentrates using a laser fluorination method. This method involves the total sample reaction with excess ClF_3 using a CO_2 laser as a heat source. The combustion resulted in a 100% release of O_2 from the silica lattice. Then, the O_2 was converted to CO_2 by the reaction with hot graphite and examined by a VG SIRA II spectrometer. Reproducibility is better than ± 0.2‰ (1σ). Results are displayed in Table 13 and reported in standard notation ($\delta^{18}O$) as per mil (‰) deviations from the Standard Mean Ocean Water (SMOW).

Hydrogen isotope

Pure quartz concentrates were heated to 150°C under a high vacuum to release unstable volatiles. Samples were gradually heated until the sample melts. The released water was then reduced to H_2 and passed slowly through a tube containing a quantity of metallic uranium inside a furnace at 800 ºC. The quantitative gas measurement was made in a Hg manometer before collecting using a Toeppler pump.

Duplicate analyses of international water standards (SMOW) gave a reproducibility of ± 2‰. Analytical results are present in Table 13, as δD notation as per mil (‰) variations from the international SMOW standard.

Sulfur isotope

Arsenopyrite and pyrite concentrates were analyzed by conventional techniques (Robinson and Kusakabe 1975). The SO_2 gas was liberated by combusting the sulfides under a vacuum with excess Cu_2O at 1075 °C. These gases were analyzed on a VG Isotech SIRA II mass spectrometer. All the analytical uncertainties were better than ±0.2‰. The $\delta^{34}S$ data are reported as per mil (‰) deviations from the VCDT standard. Table 13 summarized the analytical results.

6.3 Results

6.3.1 Host rocks

The Numão gold deposit is situated in the central segment of the W-E metamorphic belt composed of metasediments to the Pre-Ordovician "Schist Greywacke Complex" (SGC) integrated into the so-called "Douro Group" (Fig. 22-C). The rocks exposed in underground works and drilling cores are of various lithologies (Fig. 24-A-B): i) metapelites (phyllites and quartzphyllites), ii) metagreywackes, quartz-feldspathic rocks, and iii) calc-silicate rocks. In most cases, clear boundaries between these lithologies can be drawn despite being strongly interlayered on a meter-to-centimeter scale. The contacts between the different rock types are mostly gradual, striking approximately E-W bedding with a near-vertical dip that is readily visible in differential weathering profiles of more-resistant silica-rich sequences (metagreywackes, quartz-feldspathic and calc-silicate rocks) and less-resistant pelitic sequences.

Metapelites levels are fine-grained (< 100 μm) with a spaced to continuous foliation (S1) on a macroscopic and microscopic scale (Fig. 24-C) coincident with the bedding (S0) (N100º-120º). The foliation is defined by the micas (mainly muscovite and chlorite) with euhedral to subhedral dispersed sulfides, mainly pyrite (Fig. 25-A), defining a lepidoblastic to granolepidoblastic texture.

Metagreywacke levels show a massive dark aspect, fine-grained and thin-bedded (Fig. 24-D). Variable proportions of quartz and micas (biotite, muscovite) and minor potassium feldspar constitute the main mineral association (Fig.25-B). Traces of tourmaline, zircon, rutile, titanite, and ilmenite occur as accessory phases (Fig. 25-C). It displays a fine-grained granoblastic texture, with irregular quartz grain boundaries intergrown with the adjacent micas. The biotite and tourmaline blasteses are associated with a silicification episode.

Quartz-feldspathic rocks (Fig. 24-E) display a pale yellow aspect and a granoblastic texture without preferential orientation. The quartz is present in grains with irregular boundaries, and the potassium feldspar and plagioclases crystals are usually altered to white mica (sericite) (Fig. 25-E). Trace amounts of epidote and titanite aggregates are frequent (Fig. 25-D).

The calc-silicate rocks (Fig. 24-F) are granular with a mineral assemblage characterized by quartz, plagioclase, amphiboles, epidote, titanite, garnets, and minor amounts of calcite (Fig. 25-F). Scheelite (Sch-1), when present, is disseminated (0.1-0.5 mm) among these minerals, together with apatite, rutile, pyrrhotite, ilmenite, and fluorite. Garnet

occurs as massive to granular aggregates in the groundmass. Amphiboles are green to greyish green in color and form radiating fibers or acicular crystals.

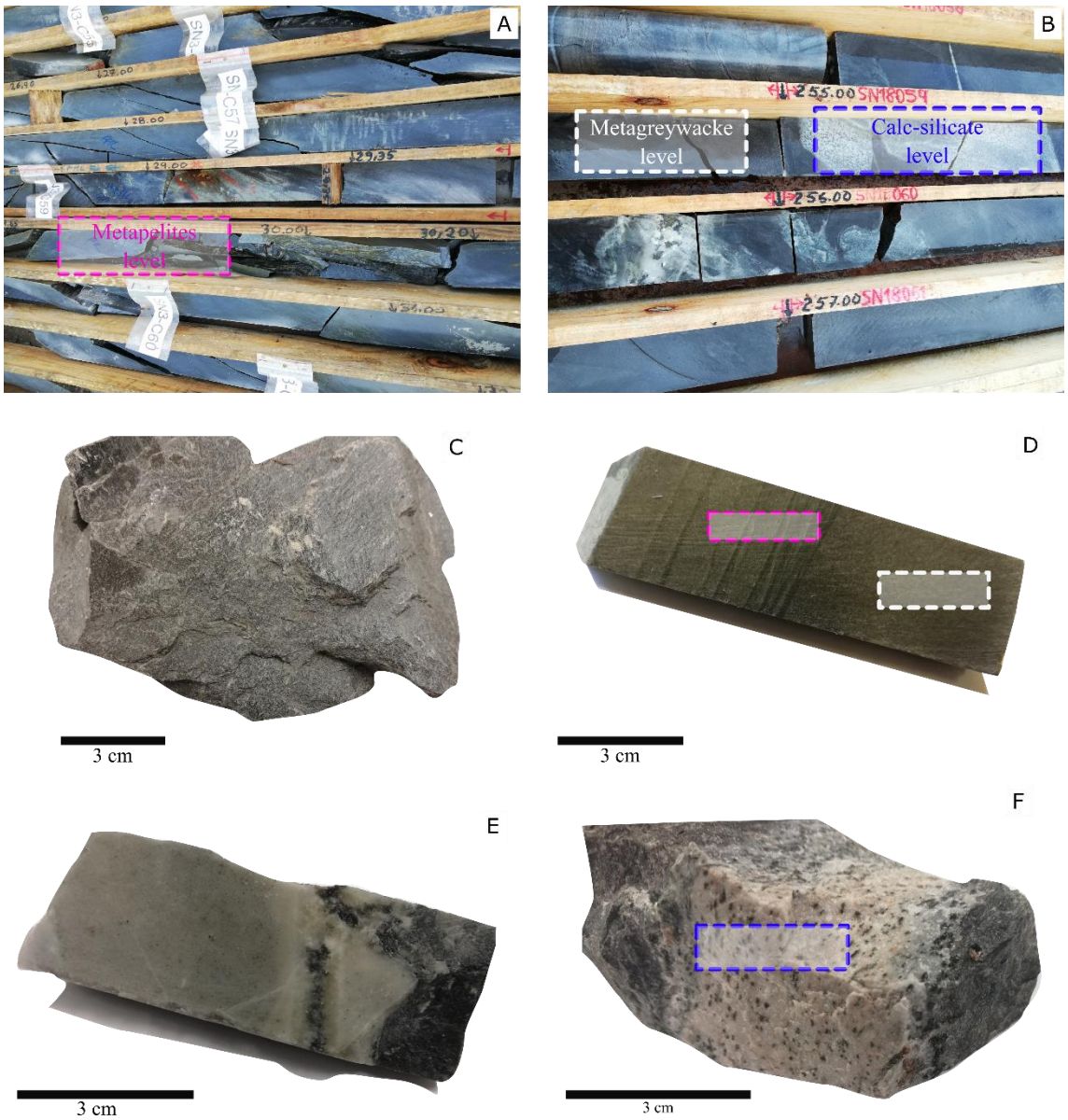

Fig. 24. Main Numão hosts rocks lithologies. (A) Drill-cores from metapelites layers. (B) Drill-cores from interlayered metagreywacke and calc-silicate rocks with no clear boundaries between them. (C) Foliation visible in metapelites. (D) Thin interlayers between phyllites and metagreywackes. (E) Quartz-feldspathic rocks with chlorite veins. (F) Calc-silicate level between metagreywackes.

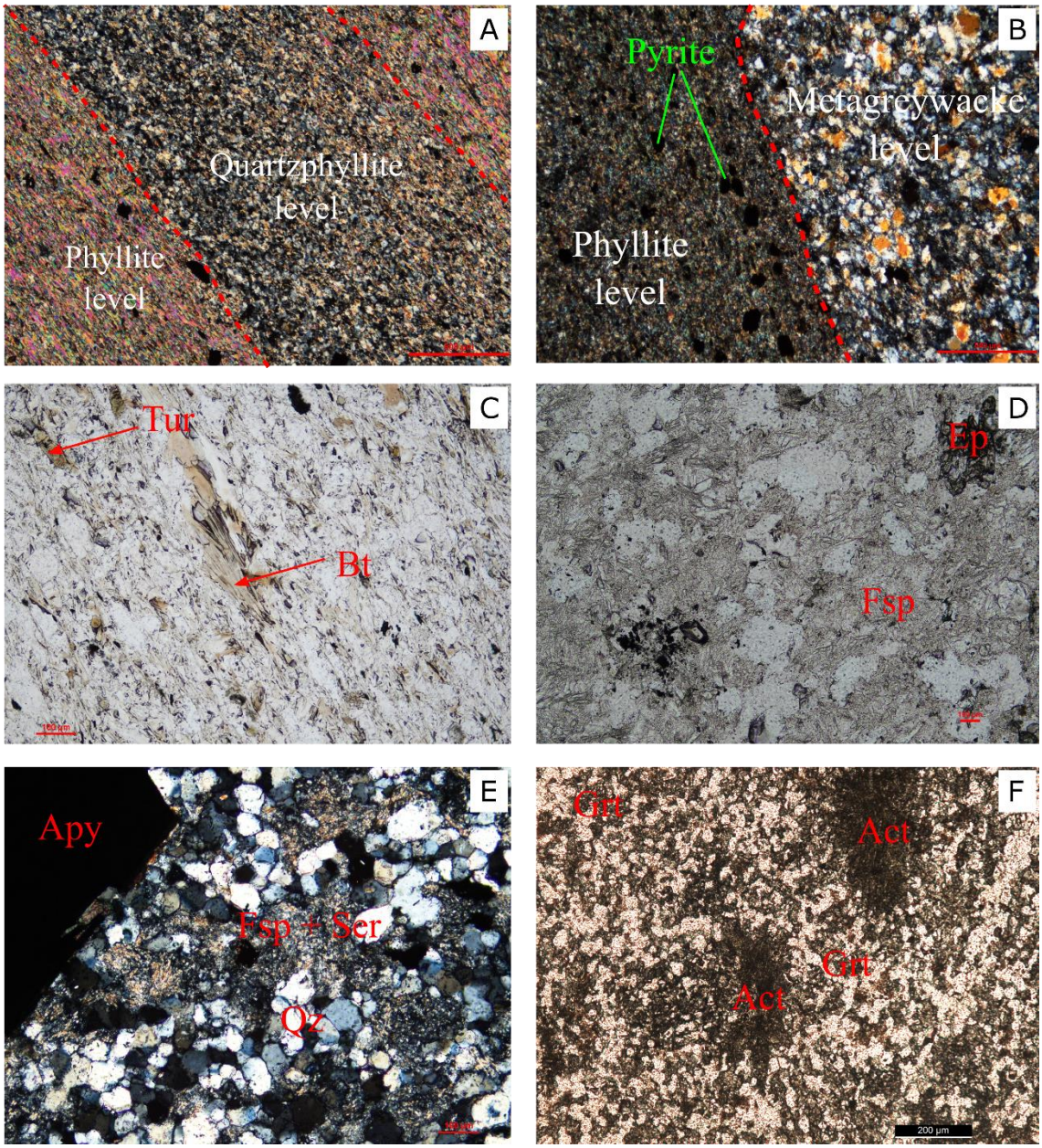

Fig. 25. Petrographic aspects from Numão host rocks types. (A) Interlayers from metapelites. (B) Metagreywacke and phyllite with dispersed pyrite crystals. (C) Tourmaline and biotite in metapelites. (D) Epidote and titanite aggregates. (E) Quartz-feldspathic rocks with altered potassium feldspars. (F) Calc-silicate levels contain garnets and amphiboles crystals. A, B, and E in CPL. C, D, and F in PPL.

6.3.2 Gold mineralized structures

The metasedimentary host rocks are strongly crosscut by the main vein system (N-S to N40º; 50ºW to sub-vertical) (Fig. 26-A-B). The vein system consists of subparallel veins with variable spacing and thickness depending on the host lithology. Within the metapelites, the mineralized veins have a small spacing (10-20 cm), less thickness, and are more scarce (<3 veins/meter). However, in more competent and chemically reactive host rocks (quartz-rich metagreywacke and/or calc-silicate rocks), the veins are locally anastomosed and have a larger thickness (> 50 cm), forming a network vein, like a

stockwork. At the macroscopic scale, the gold-bearing mineralization is characterized by conjugate vein sets of the quartz-sulfide veinlets. This type of structure only observed in the metagreywacke and calc-silicate sequences is represented by a dense network of subvertical, NNE-SSW, and E-W trending joints with a 3 to 5 meters spacing. The veins exhibit horizontal lineations (Fig. 26-G-H). In addition, the veins crosscut bedding and S1 foliation but lack any displacement.

Another mineralized vein system is sub-parallel to the calc-silicate and the metagreywacke layers (S1=S0), N100º-115º corresponding to S3. Finally, there is a barren flat vein system N80º; 20ºN older than the mineralized zones, which sometimes appear folded.

The bulk of the economic mineralization at Numão area, taking into account fieldwork, petrographic observations, and mineral chemistry (see section 4.5), includes three mineralization types (Fig. 24-C-D-E-F): Type 1 - disseminated sulfides; Type 2 - arsenopyrite-quartz veins; and Type 3 - sulfides-scheelite-quartz veins. The high-grade mineralized structures correspond to the Types 2 and 3 quartz veins, whereas Type 1 mineralization is minor.

Type 1 disseminated mineralization is mainly hosted by metagreywackes, calc-silicate rocks (Fig. 26-C), rare quartz-feldspathic rocks, and metapelites. The mineral assemblage is arsenopyrite (Apy-1) and scheelite (Sch-1), with minor pyrrhotite, pyrite, and sphalerite (Fig. 27-A-B). Arsenopyrite (Apy-1) occurs as euhedral crystals ranging in size from 0.8 to 4 mm. Scheelite (Sch-1) occurs as disseminated subhedral crystals, ranging from 2 to 5 mm in size, disseminated and occasionally forming small veinlets.

Type 2 mineralization is developed in all host lithologies. The most abundant mineral is Apy-2, which occurs in massive aggregates as small euhedral to subhedral crystals (2 to 20mm). Association of Pb-Bi-S system phases and native Bi are frequent, infilling intergranular spaces between arsenopyrite crystals and disseminated in the rock matrix.

Type 3 mineralization corresponds to sulfides-scheelite-quartz veins hosted by all host lithologies, more locally and well developed in the calc-silicate sequences. Ore minerals comprise scheelite (Sch-2), arsenopyrite (Apy-1 and Apy2), and minor chalcopyrite. Arsenopyrite forms massive coarse aggregates (2–10 mm dimensions) (Fig. 27-C). Bismuthinite as needle-like to woolly crystals are also typical and associated with native bismuth and Au-Ag phases.

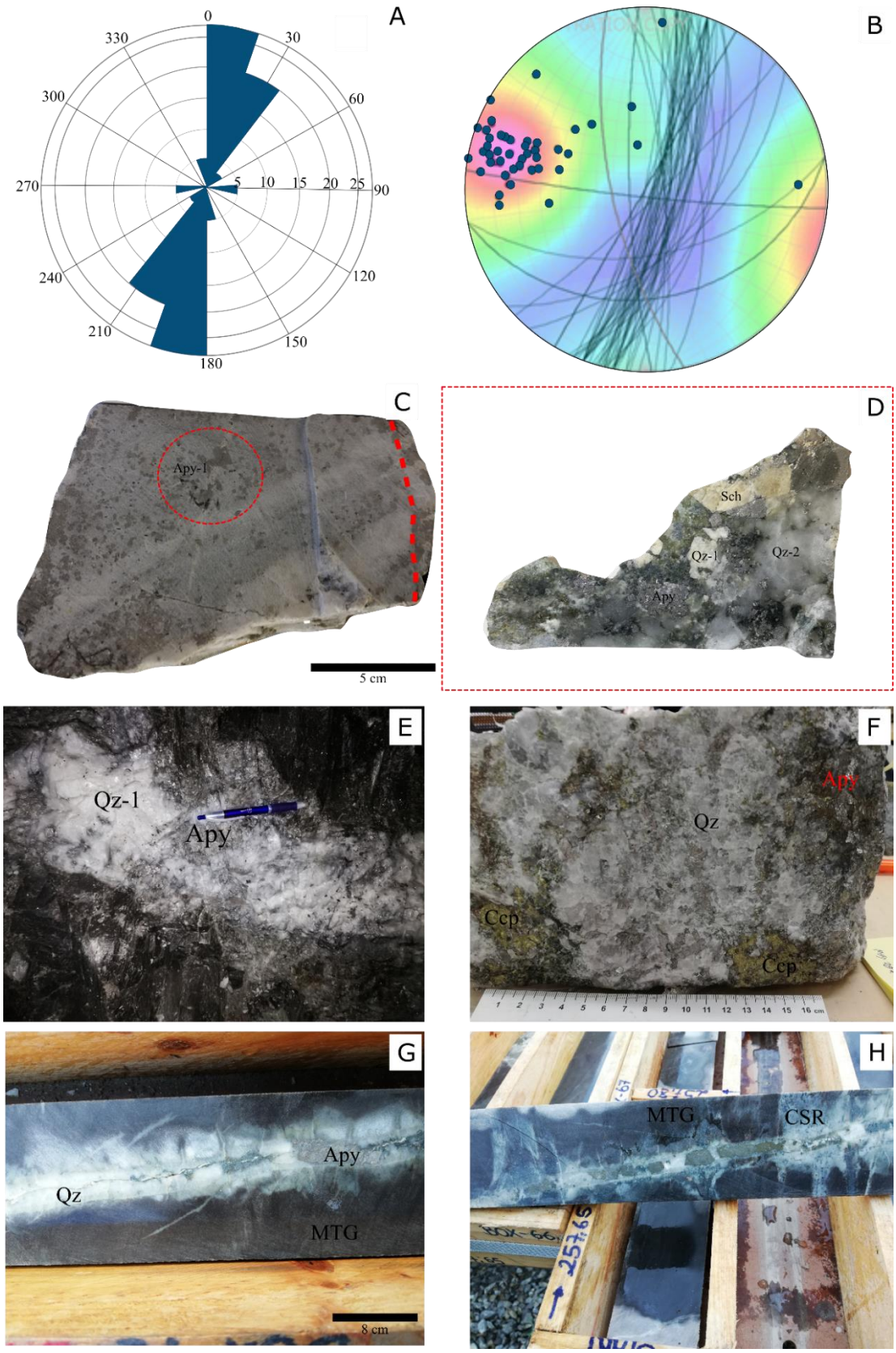

Fig. 26. Different types of mineralized bodies. (A) (B) Rose diagrams and contoured stereonet representations from the orientation of mineralized bodies ate Numão deposit. (C) Type 1- disseminated arsenopyrite in metagreywacke (MTG). (D) Type 2 - Quartz + scheelite + sulfides vein. (E) Type 3 – Quartz + sulfides vein in an underground working; (F) Type 3 – Quartz + arsenopyrite + chalcopyrite vein. (G) Type 3 -Quartz + arsenopyrite vein with chlorite. (H) Mineralized veins crosscutting metagreywacke and calc-silicate rocks (CSR).

6.3.3 Ore mineralogy

The mineral assemblages correspond to three main deposition stages. A stage-1 is represented by scheelite (Sch-1), in association with pyrrhotite, pyrite, and sphalerite with minor chalcopyrite and arsenopyrite (Apy-1) occurring disseminated in host rocks, apart from metapelites. Stage-2 corresponding to the main sulfide stage, represented by the second generation of scheelite (Sch-2) associated with sulfides and by arsenopyrite (Apy-1 and Apy-2), chalcopyrite, native bismuth, maldonite, native gold, and minor pyrite. Stage 3, characterized by bismuthinite, galena, Au-Ag alloy (low-fineness gold) and Bi-Pb-S sulfosalts.

The gold minerals occur in three different modes (Fig. 27-D-E-F): i) native-Au and maldonite (Au_2Bi), along with native-Bi as droplets in arsenopyrite and chalcopyrite; ii) electrum infilling interstitial cavities between arsenopyrite crystals and/or in its microfractures and, iii) Au-Ag minerals phases as free particles in the silicate matrix of the host rocks and grain boundaries. The size of gold particles ranges from 3 microns to 50 microns and is found in all mineralization types.

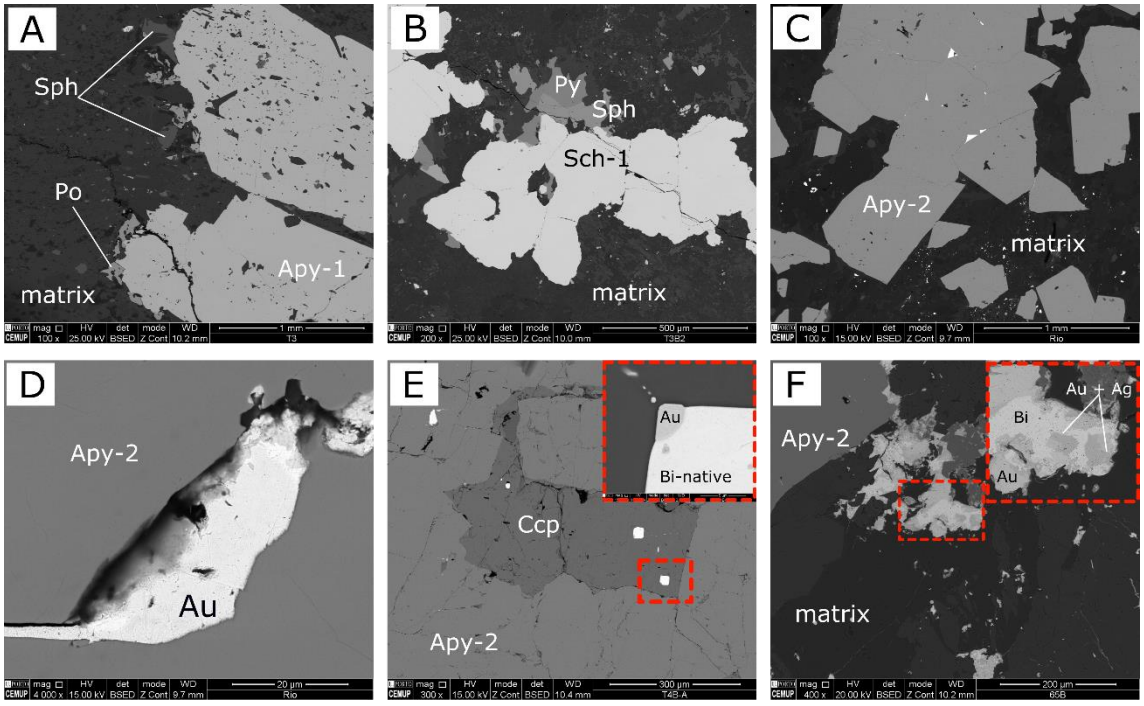

Fig. 27. BSE from petrographic features from the main ore minerals at Numão mineralized bodies. (A) Pyrrhotite and sphalerite in boundaries of Apy-1. (B) Sch-1 in association with sphalerite and pyrite disseminated in host rocks. (C) Apy-2 aggregate with bismuth in the crystal boundaries. (D) Gold in fractures with crosscutting Apy-2. (E) Gold and native bismuth in chalcopyrite. (F) Au-Ag mineral phases in association with Bi-native disperse in the matrix and Apy-2 grain limits.

6.3.4 Hydrothermal alterations

The hydrothermal alteration zones at the Numão deposit are restricted to the vicinity of the veins and comprised silicification, muscovitization, sericitization, K-feldspar alteration, chloritization, epidotization, and carbonatization (Fig. 28).

6.3.4.1 *Silicification*

Elongated stretched quartz crystals represent the early hydrothermal alteration alongside minor sulfides, sericite, and muscovite flakes. It is pervasive in all lithologies and developed in all three ore types. The effect of silicification decreases with distance from the mineralized structure. Quartz occurs as i) an early deformed coarse-grained crystals with dynamic recrystallization shown by deformation bands and subgranulation with abundant fluid inclusions planes (Fig. 28-A); ii) a fine-grained polygonal quartz associated with arsenopyrite and, iii) a later quartz associated with K-feldspar, chlorite aggregates and muscovite selvage (Fig. 28-A-B).

6.3.4.2 *Muscovitization and sericitization*

Muscovitization is commonly represented as disseminated large muscovite flakes associated with mineralized structures from Type-1 in metagreywackes, or veinlets and radial aggregates in the wall-rock of Type 3 (Fig. 28-C). Sericitization is usually represented by fine-grained white mica filling microcracks or disseminated grains coexisting with fine-grained quartz (Fig. 28-D-E). When present, biotite, K-feldspar, and plagioclase crystals were partly or replaced by sericite (Fig. 28-D-E).

6.3.4.3 *K-feldspar alteration and chloritization*

K-feldspar predominantly occurs in sulfide-quartz veins with chlorite ± sericite (Fig. 28-D-E) and is frequent in some arsenopyrite crystals' boundaries. Occasionally, chlorite crystals show anomalously blue, brown, or purple interference colors and are observed in the mineralized zones and the host rocks. It can occur, forming flakes and aggregates filling spaces between the quartz and the carbonate minerals (Fig. 28-E-F), within the veins and veinlets, and in small intergranular patches disperse in the host rock or idiomorphic shape, forming radial aggregates in veinlets and vugs associated with quartz ± K feldspar (adularia).

6.3.4.4 *Epidotization and carbonatization*

Epidote occurs preferentially when the veins cut the calc-silicate and quartz-feldspathic rocks (Fig. 28-E). It is present in minor fractures, replacing primary plagioclase, and, in most cases, forms mineral associations with quartz, chlorite, and sometimes calcite, pyrite and, pyrrhotite. Carbonatization comprises calcite as the essential alteration

mineral (Fig. 28-D-E), filling spaces between crystals or small veinlets crosscutting all structures. Titanite is frequent as an alteration product and occurs mainly due to the alteration of ferromagnesian minerals associated with chlorite, quartz, and calcite.

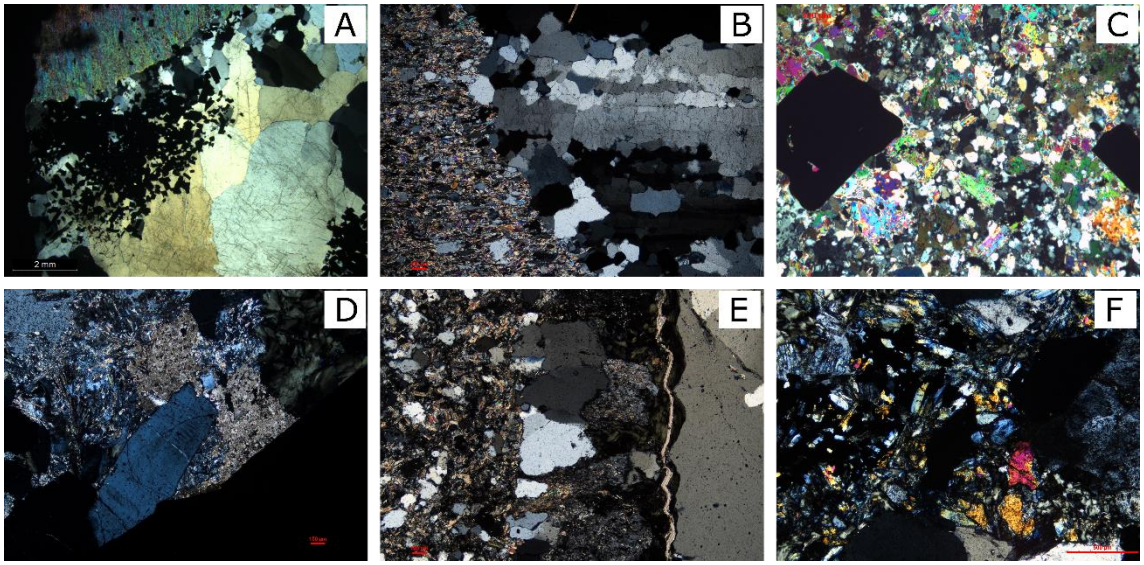

Fig. 28. Petrographic features from the hydrothermal alterations at Numão deposit. (A) (B) Silicification predates the Apy-2. (C) Muscovitization in metagreywacke with Apy-1. (D) (E) Chloritization, feldspatization, and carbonization. (F) Epidotization. All images in CPL.

6.3.5 Mineral chemistry

Mineral chemistry analysis was undertaken in several metamorphic, alteration, and ore minerals to characterize the paragenetic sequences.

6.3.5.1 *Host rocks*

Epidote, feldspar, titanite, amphiboles were analyzed by microprobe in the host rock. The EMPA data are shown in Appendix 1.

Microprobe analyses of epidote in quartz-feldspathic and calc-silicate levels indicate that these minerals are a solid solution between epidote and clinozoisite (Appendix 1-A). The contents are as follows: SiO_2 (35.60% to 40.36%), CaO (16.36% to 25.31%), Al_2O_3 (23.99% to 34.60%), and FeO_T (0.36% to 8.90%).

Potassium feldspar was recognized in most of the samples and had a similar chemical composition. Microanalyses showed Na (7.98 to 12.11 wt. % Na_2O) enrichment with a plagioclase composition of Ab_{56} and Ab_{99} (Appendix 1-B). Na-rich plagioclase is frequent in metagreywacke, while andesine is more common in calc-silicate rocks.

Titanite has a homogeneous composition without significant differences between crystals. Al_2O_3 (2.78-11.87 wt.%) and Fe_2O_3 (0.15-0.68 wt.%) contents are always low. Some positive analysis with Nb and Sn content.

The EMPA data obtained for amphiboles are shown in Appendix 1-D. The Al_2O_3 content ranges from 2.25% to 28.27%, CaO from 12.52% to 24.42%, FeO_T from 4.62% to17.82%, MgO from 0.74% to 13.81%, and Na_2O from 0.11% to 0.30%. The amphiboles from cal-silicate sequences plot in the Ca-rich dominant varieties in the field of the actinolite and ferro-sadanagaite types (Appendix 1-D).

The EPMA analysis results, calculated cations, and end-member compositions of garnet crystals are given in Appendix 1-E. Garnet crystals were mainly grossular (Gro; 37.89%–49.28%) with some spessartine (Spe; 27.17%– 30.80%) and almandine (15.59%-28.32%), mainly with small amounts of andradite.

6.3.5.2 *Ore minerals and hydrothermal alteration products*

Scheelite, gold, arsenopyrite, pyrite, chalcopyrite, pyrrhotite, galena, bismuthinite, and sphalerite are the most abundant minerals in Numão mineralized bodies. The EMPA data from these minerals are shown in Appendix 2. Chlorite, epidote, and feldspar are related to hydrothermal alteration products and their chemical composition reported in Appendix 1.

Sch-1 and Sch-2 revealed similar chemical compositions with a pure phase, without relevant trace elements (*e.g.,* Mo). Arsenopyrite is typically homogenous and shows As contents of 31.28 and 33.25 at.%, with most values clustering around 32.36 ± 0.3 at.% (Appendix 2-A). No clear correlation between As and Fe concentrations in Apy is reported. Other elements analyzed were Ag, Te, Sb, Pb, Bi, and Au. Only a few analyses showed positive values of Pb (0.07-0.15 wt.%).

According to EPMA data, pyrite, chalcopyrite, pyrrhotite, galena, bismuthinite, and sphalerite are typical stoichiometric compositions (Appendix 2-B). The microprobe analyses performed in galena crystals showed high content of Ag (up to 1.6 wt.%) and Bi (up to 3.3 wt.%), indicating a simultaneous substitution of Pb^{+2} for Bi^{+3} and Ag^{+} (Fuertes-Fuente et al., 2016). A few analyses in bismuthinite crystals revealed Pb contents upper the detection limit.

Considering the complex intergrowths between Bi-Pb sulfosalts and host minerals, the thin structure makes the EMPA analysis inaccurate.

Chemical analysis from gold minerals revealed two distinct generations (Appendix 2-C). The gold content of Au-1 varies from 75.54 to 93.85 wt.%, which is significantly higher than that of Au-2 (45.35 to 68.73 wt.% Au). The Au-1 is generally variable in Ag (6.61 to 24.37 wt.%) compared to the Au-2. According to the calculation formula for Au fineness defined by Fisher, 1945, the average fineness of Au-1 and Au-2 are 841 and 663, respectively. The high fineness of gold (Au-1) and maldonite occurs preferentially within

chalcopyrite and in arsenopyrite. The low fineness gold (Au-2) mainly occurs in fractures or grain boundaries in Apy-1 and Apy-2 and rock matrix.

The chemical classification of Numão hydrothermal chlorites is reported in Appendix 1-F, and according to Bayliss, 1975 belongs to the clinochlore and chamosite group. Epidote from hydrothermal alteration zones was Fe-poor with alumina-rich minerals and belonged to the clinozoisite subgroup (Appendix 1-F). Carbonates from all kinds of host rocks show a restricted and pure composition as calcite (CaO=56.15wt.% without any other element).

6.3.6 Multi-element geochemical drill-hole data

The statistical summary of multi-element geochemistry of the drill hole samples from the study area is given in Appendix 3. Variations in the major, minor and trace elements contents of samples from different drill holes can be identified using boxplots (Fig. 29). The major elements' content variations differ by two or three orders of magnitude (Fig. 29). These samples contain 1.44 to 12.55 wt.% of Al and 1.30 to 9.73 wt.% of Fe. The Mg, Ca, Na, K, and S contents range from thousands of ppm to 8.66 wt.% (Fig. 29), with Ti, Mn, and S contents ranging from ~40 to ~8000 ppm (Fig. 29).

Taking into account the trace elements which are not related to the metallic elements, Ba concentrations are highly variable (2-1300 ppm; Fig. 29) with other elements present at concentrations lower than ~151 ppm (Be, Co, Cr, La, Ni, Sc, and V).

Comparing samples from different drill holes indicate that Au, Ag, Cu, Pb, Zn, As, Bi, Sb, and W contents are less variable than other elements with content variations differing two or three orders of magnitude (Fig. 29). The As concentrations are highly variable, ranging from 2.5 to 82300 ppm.

From the mine and hand specimen scales, a relation between sulfides minerals and scheelite seems to exist, but as a whole, the Au-W correlation is very weak (R=0.2). Besides, there is a similar weak Au-W correlation in most drill holes at the scale of individual drill holes. Contrarily, there is a stronger correlation in someone, like in the drill hole represented in Fig. 30, representing an R=0.7, reflecting the general overlap of Au and W enrichment zones.

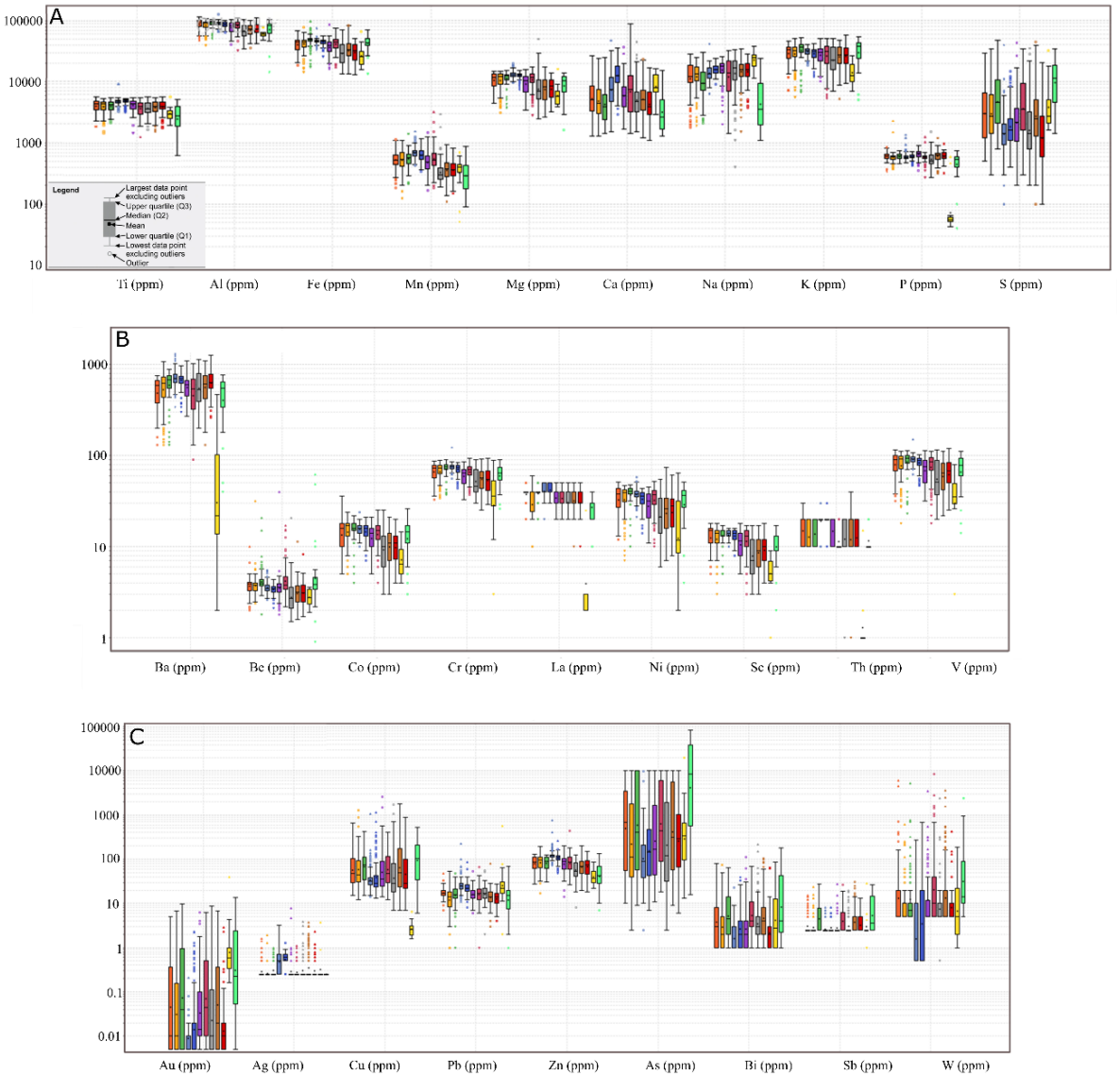

Fig. 29. (A) Major elements boxplots with a logarithmic scale for studied drill-cores from Numão area; (B) Trace element boxplots with logarithmic scale; (C) Elements associated with the mineralization.

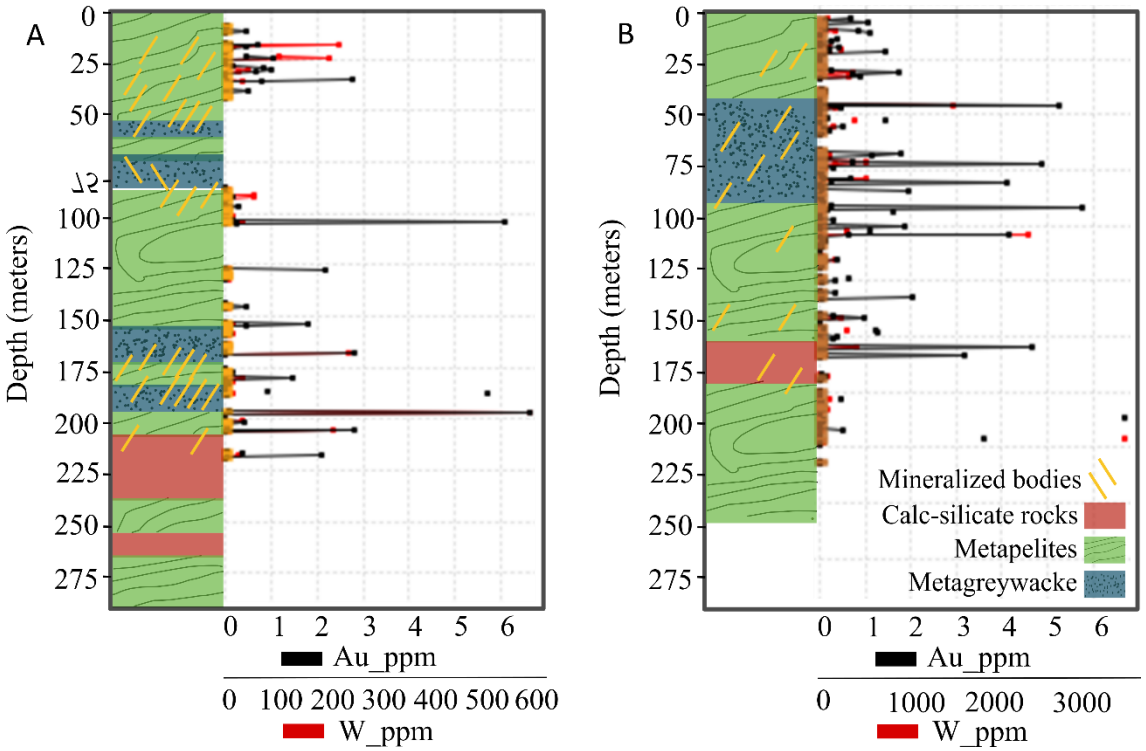

Fig. 30. Graphical logs are showing lithologic control of mineralized structures in positive drill-cores for Au and W.

6.3.7 Principal component analysis

PCA was carried out on the 29 analyzed elements for 1172 samples from 12 drill-cores from de Numão area. A scree plot of the PC (Fig. 31) shows that the first four components explain the highest variance of the data (77%) (see Table 12). Biplots of RQ1–RQ2, RQ2–RQ3, RQ3–RQ4 are shown in Fig. 31. The elements represent the degree of relative enrichment/depletion of each sample site by proximity to the position of the chemical elements.

As shown in figure 31-B, there is one major vector group in PC1-PC-2 space: W plot positively in PC1 space; two major element vectors group Au-As-Cu-Bi and Sb-S, positively attributed to both PC1 and PC2. K is positively attributed to PC2. Ni-Fe-Sc-V-Mg-Ba-Be vector group plot positively to PC2. Cr and Al-La too. All other elements plot negative in the PC1-PC2 space. Au-As-Cu-Bi and Sb-S groups have the same trend of the K in PC2-PC3 space. Ca-Na group plot in the positive PC3 space.

The Sb eigenvector has an opposite direction to the S eigenvector in PC4 space, increasing vector length in that order. Au-As-Cu-Bi group displaying smaller vector lengths. The variables associated with PC4 and PC5 have a negligible negative association.

Table 12. Eigenvalues of principal components of Numão data. Analysis carried out on centered log-ratio data.

	EIGENVALUES	PERCENT	CUMULATIVE %
PC1	14.67	54.32	54.32
PC2	3.206	11.88	66.2
PC3	1.797	6.654	72.85
PC4	1.188	4.4	77.25
PC5	1.017	3.768	81.02
PC6	0.6978	2.585	83.6
PC7	0.6535	2.42	86.02
PC8	0.5006	1.854	87.88
PC9	0.4996	1.85	89.73

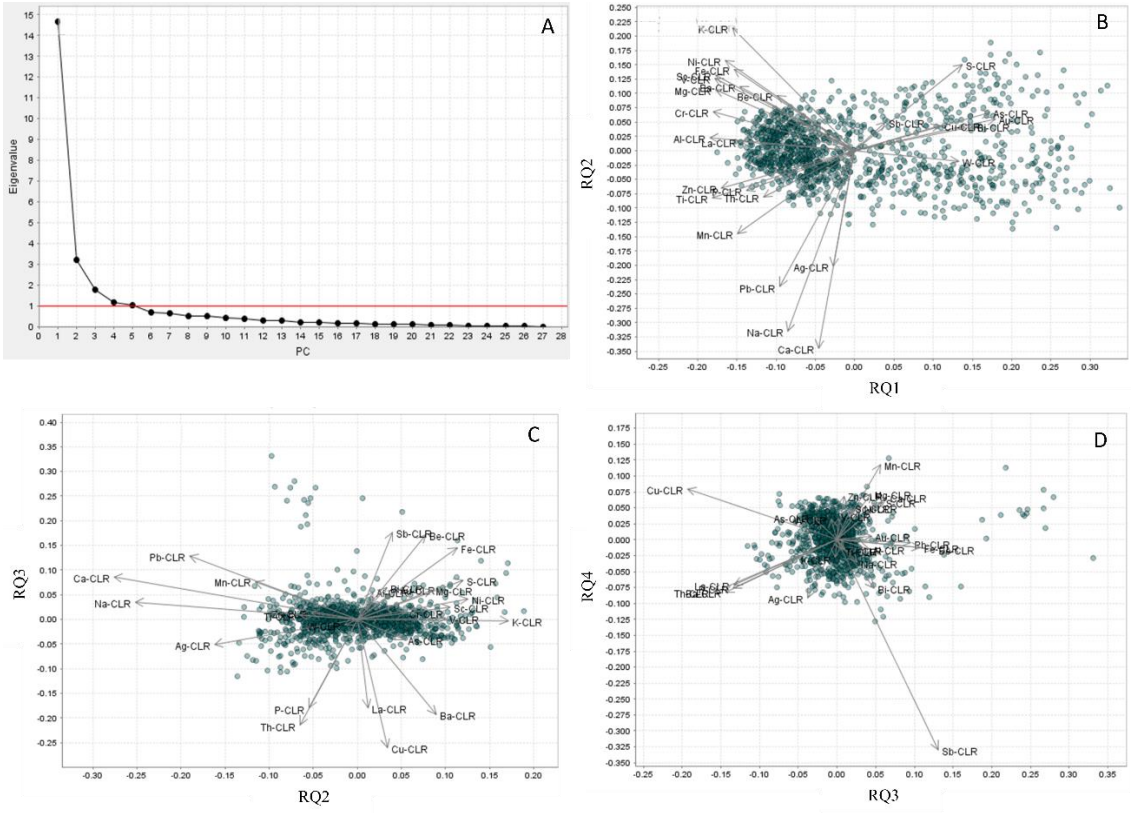

Fig. 31. Principal component analysis of CLR-transformed average Numão multi-element data. (A) Scree plot. (B) Biplot of the first two principal components, PC1 vs. PC2; (C) PC2 vs. PC3; (D) PC3 vs. PC4. A blue circle shows each drill-core sample. The element symbol plotted the corresponding scores of the elements.

6.3.8 Geothermometers

The Apy composition (Appendix 2-A) used as a geothermometer gives a temperature interval of 381º to 502 °C (Kretschmar and Scott, 1976; Sharp et al., 1985). Apy analyses

with As > 33 at.% were interpreted as late re-equilibrium with Po + fluid enriched in S and As. The majority of the analysis in arsenopyrite was below their respective detection limits for trace elements.

In addition, using the chlorite geothermometers defined by Kranidiotis and MacLean, 1987 and Cathelineau, 1988, the estimated temperature ranges between 264º to 341°C (Appendix 1-F). Thus, despite being empirical and not quantitative thermometers, chlorite and arsenopyrite geothermometry can be used to estimate the relative temperature of minerals precipitation.

6.3.9 Stable Isotope data

Oxygen, hydrogen, and sulfur isotope data are provided in Table 13. The quartz oxygen isotope compositions from the mineralized structures at Numão are clustered, ranging between +13.0 to +13.5‰. The isotopic compositions for $\delta^{18}O_{fluids}$ were calculated assuming equilibrium between fluids and minerals and based on the estimated formation temperature from chlorite and arsenopyrite geothermometers, ranging from +4.7 to +11.3‰ (Bottinga and Javoy 1973; Matsuhisa et al., 1979). The δD ranges from -72 to -83.6‰. The $\delta^{34}S$ analysis on arsenopyrite yielded values from -7.5 to -7‰. The sulfur isotope data showed clear grouped values inferring an isotopic homogeneity for the source of metals for gold mineralization (Table 13).

Table 13. Isotopes analysis of the Numão samples.

Samples	Type of mineralization	Isotopes			Estimated T (ºC)		$\delta^{18}O_{fluid}$ (‰)	
		Sulfur	Oxygen	Hydrogen	Apy	Chl		
NUM-A	Type 2	-7.4						
NUM-B	Type 2	-7.5						
NUM-C	Type 3	-7.0						
NUM-D	Type 1	-7.3						
Py-SGC	Pyrite from SGC phyllites	12.2						
NUM A	Type 2		13.4					
NUM B	Type 2		13.3					
NUM B	Type 3 -		13.3					
6C	Type 3 -		13.3					
6D	Type 3 -		13.2					
6A	Type 2		13.5	-83.6	502 -381	341 -264	11.24 – 9.04	8.04 – 5.24
6B	Type 2		13.0	-72	502 -381	341 -264	10.70 – 8.50	7.50 – 4.70

6.4 Discussion

6.4.1 Mineralization controls

The mineralized structures at Numão deposit are veins developed in extension fractures, as reflected by the growth directions of the gangue crystals orthogonal to the vein walls (Fig. 26-G-H), normally fault-controlled, crosscutting bedding and/or regional foliation, and are post-peak of regional metamorphism. The veins are normally fault-controlled, crosscutting bedding and/or regional foliation, and are post-peak of regional metamorphism. The proximity of the Numão deposit (approximately 7.5 km apart) and similar orientations of the mineralized veins with the structural corridor of NNE-trending of the Vilariça-Manteigas fault, suggest that the vein sets were formed during the same hydrothermal event. Second or third-order structures of the NNE-trending primary fault system could host the mineralized structures. The relative predominance of brittle deformation mechanisms leads to the generation of overlaid fracturing episodes and minerals precipitation, thus indicating a rapid increase of the crustal uplift rates and a notable migration of mineralizing fluids towards dilatational structures intimately related to strain accommodation within fault zones or in Numão case to strain partitioning in the metamorphic sequences with different chemical compositions and rheological features, as suggest by some authors (e.g., Mateus and Noronha, 2001). The mineralized body networks (stockwork) are well-developed into competent rock units compared to adjacent metapelites, which fractured easily and created dilatancy. These high competency sites can focus fluid flow and have negative fluid pressures, resulting in extensional veining and dilation (Ridley, 1993).

The diversity of hydrothermal alterations shows good consistency with observed host rocks mineral assemblage, reflecting differences in the protolith composition. Comparing the chemical composition of the host rocks only with metamorphic mineral assemblages, with the chemical composition of rocks from proximal alteration zones, the last ones contain more silica, Fe-Mg-K-Al minerals, and Ca-rich minerals, manifested by a higher content of quartz, chlorite, and muscovite, and clinozoisite, epidote, and calcite respectively.

6.4.2 Timing of scheelite and gold deposition

Scheelite-1 is, in fact, the early ore mineral and is present in calc-silicate rocks. Similar scheelite-bearing calc-silicate rocks are present in levels strongly folded, from the Schist-Greywacke Complex of Upper Precambrian age and also in similar Silurian sequences. In calc-silicate rocks only affected by regional metamorphism, we cannot exclude the possibility that some tungsten was already pre-concentrated in the sedimentary series

before metamorphism because scheelite is sometimes present (Noronha, 1976; Arribas, 1979; Pellitero, 1980). However, it is hard to exclude the possibility that the W is related to granite intrusions when the calc-silicate rock levels occur near the contact with granite intrusions (Derré et al., 1982). Scheelite- 2 is present in the Au-mineralized veins when they crosscut calc-silicate rocks, and it is coarser than Sch-1 and contemporaneous of arsenopyrite.

Once arsenopyrite is the main sulfide hosting the gold minerals, the arsenopyrite geothermometer is a practical method to constrains the temperature conditions for mineralization deposition. Based on the textural relationships and chemical compositions, the arsenopyrite geothermometer reached estimated temperatures ranging from 381º to 502ºC to the arsenopyrite deposition. The chlorite geothermometer gave estimated temperatures varying from 264º to 341ºC. These interval temperatures between arsenopyrite and chlorite support the textural relationships indicating both minerals are not coeval, which corroborate the paragenetic relationship (chlorite infilling fractures of arsenopyrite).

The hypogene gold at Numão was characterized by the two different types of gold occurrence representing the evolution of the same hydrothermal gold deposition event. The first one is characterized by maldonite and high fineness gold hosted in chalcopyrite and arsenopyrite (fineness 841). The second one (low-fineness gold) occurs after a decrease in temperature and sulfur fugacity, alongside sulfide deposition. A low-fineness gold (fineness 663) is associated with minerals from the Pb-Bi-S assemblages, grain boundaries, and silicate matrix of the host rocks. Several authors in northern Portugal reported these two gold assemblages (*e.g.*, Limarinho deposit (Fuertes-Fuentes et al., 2016), Penedono deposit (Neiva et al., 2019), and Bigorne deposit (Leal et al., 2021)).

6.4.3 Metal associations

The PCA from the Numão geochemical data established the major multi-element trends, gold mineralization pathfinders, insights of host rocks composition, and hydrothermal processes. The PC1 shows a positive correlation between Au-As-Cu-Bi-W, which may reflect the petrographic observations that Au mineralization is associated with sulfides, mainly arsenopyrite, chalcopyrite, and scheelite.

In terms of sample variance, mineralized samples are coupled with mainly Au-As-Cu-Bi-W vectors, while the non-mineralized samples plot against these higher-order PCs vector groups (Fig. 32).

The relative importance of Au and W decreases from PC1 to PC2, with PC1 showing a positive correlation between both and PC2 a negative one. This fact indicates that the

variations of W and Au are not regular and suggest that these elements are not related to the same mineralization process. The W is only correlated with Au when the quartz veins crosscut calc-silicate rocks with Sch-1, suggesting that Sch-2 can result from the recrystallization process of Sch-1.

The PC3 and PC4 represent a residual process in this mineralization system, such as minor Ag and Pb mineralization. Ag and Pb vectors are supported by identifying Au-Ag minerals phases and Pb sulfosalts related to the rock matrix.

Eigenvectors for Ca and Na plot negative to PC2, as Ti and Mn to a lesser degree, whereas K, Al, Mg, and Fe plot favorable. From the samples plotted in Fig. 32, we conclude that the PC1 varies as Au and /or W grades and accounted for most variation. The elements which plot positive in the PC1 space correspond to the gold mineralization pathfinders. The variation accounted for by PC2 is likely to show evidence for host rock lithology and chemical changes resulting from hydrothermal alteration. The K vector plot against Na and Ca vectors in PC2 space showing the association of muscovitization and metagreywackes and quartz-feldspathic rocks. The PCA classified the initial geochemical data according to each mineralization type and the degree of mineralization (unmineralized samples and mineralized samples for explanations, see Fig. 32). Type-1 and type-2 correspond to Au-enriched samples, and Type-3 to Au-W enriched samples. Towards the more positive side of PC1 space (Fig. 32), samples become weakly enriched and finally strongly mineralized, as represented by the green arrow.

The Numão mineralization type-1 and type-2 plot positive in PC2 space, while type-3 plot negative in PC2 space, apart from some overlap among Au-W- and Au–only-enriched samples. Observation of PC2-PC3 biplot (Fig. 32-C) showing the link between Au-only-enriched samples with K, Al, Mg, and Fe vectors, associated with metapelites and metagreywacke host rocks, in contrast with Au-W-enriched samples, which are plotted in the same field of Ca, Na and Mn, reflecting the influence of calc-silicate rocks. The Ca, Na, and Mn could reflect the mineralogy of the calc-silicate rocks, such as the presence of garnet and actinolite.

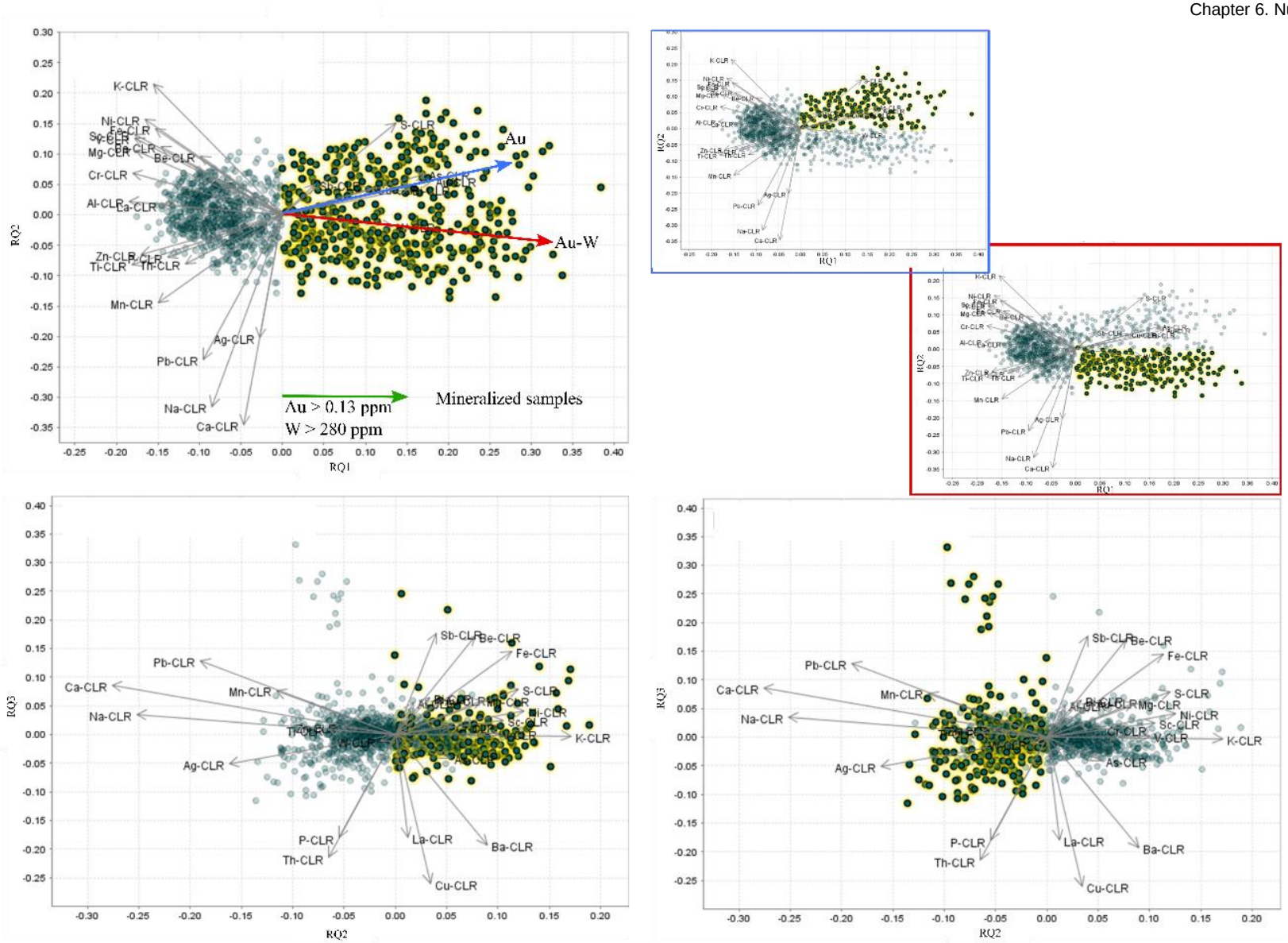

Fig. 32. Biplot of PC1 vs. PC2 and PC2 vs. PC3 for the RD dataset. Highlighted samples in the plots are the mineralized samples, plot in the positive quadrant of PC1 (green arrow). The blue arrow shows that Au has been enriched from the left to right quadrant. The red arrow shows that Au-W mineralized samples have been enriched from the left to right quadrant.

6.4.4 Fluids source

The D_{fluid} falls in metamorphic and magmatic waters fields. In Numão, the calculated $\delta^{18}O_{fluids}$ varies from +11.2 to +8.5‰ at crystallization temperatures between 502ºC and 381°C. These values show lower oxygen and hydrogen isotopic compositions than the magmatic water or metamorphic, corresponding to modify waters resulting from rock-fluid interaction (Taylor, 1974, 1979). The lighter $\delta^{18}O$ fluids values (+4.7 to +5.2‰) in equilibrium with the chlorite indicate a meteoric signature, inferred by several authors from the fluid inclusion data in other deposits (Noronha et al., 2000, Fuertes-Fuentes et al., 2016 and references therein).

Whole-rock SGC metasediments have $\delta^{18}O_{SMOW}$ values of 13.1 and 13.4‰, and δD_{SMOW} values of -67.3 and -52.6‰ (Chicharro et al., 2016). The metamorphosed sedimentary rocks for low- to medium-grade yielding similar values (Sheppard 1986; Hoefs, 2018). Recently Bark et al., 2020 interpret that oxygen isotope compositions greater than + 8‰ could result from the surface or near-surface processes related to sedimentation, diagenesis, or low-temperature hydrothermal alterations (Taylor, 1980), proposing that the fluid cannot be exclusively magmatic (McCuaig and Kerrich, 1998). The sulfur isotope results clustered around -7.3‰ may suggest a single uniform metal source. These values fall in the sedimentary and metamorphic ^{34}S-values of important geological reservoirs fields (Hoefs, 2018), discard a purely magmatic source. However, the S-data are not similar to the obtained values for SGC barren pyrites (12‰).

The isotope data from the Numão deposit may thus suggest a mixed fluid source of modified fluids and surficial fluids as described in other gold deposits in the European Variscan belt (*e.g.*, Boiron et al., 1996; Noronha et al., 2000; Mateus and Noronha, 2001; Boiron et al., 2003; Bouchot et al., 2005).

6.4.5 General Classification

The genetic classification of the Numão deposit is equivocal. The mineralized bodies display features of Orogenic Gold deposits (OGD) at a relatively deep emplacement level (mesozonal), and Reduced Intrusion-related Gold Deposit (RIGS) with a spatial-temporal link with post-D3 Variscan peraluminous intrusion emplacement.

The RIGS are the product of local-scale fluid convection likely derived from and driven by a cooling magmatic body, whereas OGD are widely considered to result from crustal-scale fluid flow likely derived from metamorphic dehydration (Groves et al., 1998; Hart, 2007). The following table presents the Numão features against each of the two classifications.

Table 14. Numão features applied to each classification (- against; + favorable).

Numão features	OGS	RIGS
Post-metamorphic timing in host sequences	+	-
Granitic intrusions in the surrounding areas	-	+
No hidden pluton in the mining levels	+	-
Magmatic differentiates of the intrusion, as dikes of pegmatite or aplite are barren.	+	-
Mineralized bodies structurally controlled by the NNE-trending fault (VMF)	+	-
Multiple stages of mineralization of the disseminated and quartz vein and veinlet/stockworks	+	+
Sulfide mineral associations of dominantly arsenopyrite and pyrite, with minor sphalerite, galena, and chalcopyrite	+	+
Base metals (Cu), without Mo	-	-
Metal association Au-As-Bi-W	+	+
Hydrothermal alteration characterized by silicic, K-feldspar, sericite, chlorite, and carbonate alterations	+	-
The fluids transformed from metamorphic/magmatic ore-forming fluids to meteoric water during fluid evolution	+	+
Possible P–T condition of Au Mineralization – lower than 381ºC (Apy-II geothermometer)	+	-
Source of the fluids are equivocal	+	+
Spatial association with W-Sn and Ag-Pb-Sb mineral occurrences	-	+

6.5 Conclusions

The Numão deposit, formed towards the end of the Variscan orogenic evolution, represents the economic products of two different hydrothermal mineralizing events, an early W-(As) and Au-Ag-Bi-(As) event with a close link with the late-variscan network of re-activated crustal-scale faults (*e.g.*, VMF). The initial ore-forming fluids were either magmatic water, possibly derived from a concealed granite body and/or “modified” or metamorphic waters, resulting from the interaction fluid-rock, directly transported via deep fractures from deeper crustal levels, and meteoric water played an increasingly important role during the fluid evolution and in particular in the late stage. In Spain, comparable W and W-Au deposits show similar features, suggesting that the hydrothermal history was controlled by large-scale Late-Variscan tectonic processes (Timón-Sánchez et al., 2019). These two hydrothermal events may have upgraded the gold grade in this type of gold deposit, which is well-represented through the European Variscan belt.

CHAPTER 7 | General conclusions

The overriding aim of this research project is to establish the deposit to regional-scale mineralization-controlling processes at the Bigorne and Numão deposits and understand how they contribute to the gold metallogenic evolution of northern Portugal. The main research findings for each case study deposit are summarized in Table 15, and additional and supportive literature information is in Table 2:

Table 15. Summary of the main characteristics of the Bigorne and Numão deposits. (1) and (6) deposit numbers in Fig. 2-B.

Deposit	Bigorne (1)	Numão (6)
Host rock	Biotite-rich granites	Metasediments
Metamorphic conditions	-	Greenschist facies
Age of host rock (Ma)	309.6 to 303±8	Lower Paleozoic
Mineralized structures geometry	N10º-40ºE	N-S – N40º N100º
Mineralization style	Quartz + oxidized veins	Quartz veins + disseminated
Ore assemblage	Wf + Sch + Apy + Py + (Ccp) + Bi + Au	Sch + Po + Py + Apy + Ccp + Au + Bi + Ag
Mineralization age	Younger than 303 Ma	<312 Ma ~VMF age
Au fineness (hypogene gold particles)	963 – 770	841 - 663
Au fineness (detrital gold particles)	994 - 876	-
Apy geothermometer (TºC)	455 - 354	502 - 381
Chl geothermometer (TºC)	-	341 - 264
Sulfur isotope (‰) in arsenopyrite and mix sulfides	-2.8	-7.5 – (-7)
Oxygen isotope (‰) in quartz	12.3 - 12	13 – 13.5
Hydrogen isotope (‰) in quartz	-64.7 – (-62.5)	-83.6 – (-72)
Sources of data	This study Leal et al., accepted Leal et al., 2021	This study Leal et al., accepted

The following sections present the conclusions of the thesis that correspond to the different aspects of the research targets and key issues outlined in section 1.2.

7.1 Timing of mineralization

In NW of the Iberian Massif, several different styles of gold mineralization of approximately the same age are present within a relatively small area. They share similar timing for hydrothermal events, suggesting a large-scale late-Variscan tectonic process, as been described by several authors (*e.g.*, Boiron et al., 2003; MacKenzie et al., 2019; Timón-Sánchez et al., 2019).

The spatial association of several significant gold deposits in the NW Iberia with their hosted granitic intrusions is evident. U-Pb dating of intrusive rocks, which cut or are cut by mineralized veins, is an excellent indirect method to indicate the age of the mineralized veins. However, the most significant examples in the studied areas (mostly Bigorne) cut the host intrusions and, therefore, their dating only indicates their maximum age. Including the analytical error, the overall range of the gold mineralization-hosted granites is from ~318 to 295 Ma. The mineralized structures cross-cut their hosted granitic intrusions and seem to be younger than them. Table 2 summarizes (section 1.5) the absolute ages of mainly igneous complexes mentioned in the text.

To help constrains the age of gold deposits, the absolute ages already published from several deposits in NW Iberia were used:

1) In the Jales district (CIZ), Ar-Ar ages on hydrothermal muscovite from the host rock and mineralized veins range from 303 ± 2.8 to 300.7±2.8 Ma, respectively (Neiva, 1992; Rosa, 2001);
2) Re-Os ages from molybdenites associated with gold mineralization in CZ and WALZ in Spain range from 292.4 ± 1.2 Ma to 293.4 ± 1.2 Ma in Salave deposit (Rodríguez-Terente et al., 2018) and around 292 Ma in Linares deposit (Gutiérrez-Alonso et al., 2011; Cepedal et al., 2013), considered as the ages of a post-orogenic magmatism developed within the inner part of the Cantabrian secondary Orocline formation (Gutiérrez-Alonso et al., 2011). These values match with the age of emplacement of the Portuguese post-tectonic granites;
3) Uraninites dating from Los Santos and El Cabaco deposits (Spanish Central System Batholith) revealed similar ages and included two events: i) an early hydrothermal event, which yields an age of 295 ± 2Ma, dating a strong-alkali mobilization and early tungsten deposition and ii) later hydrothermal processes, around 287±4Ma, associated with sulfides and late scheelite deposition and widespread silicification (Timón-Sánchez et al., 2019);

4) Although some important W-Sn-Mo deposits match with these ages, seeming to be younger than the gold mineralizations in northern Portugal: like the Carris deposit in Gêres Massif (279.4±1.2Ma; Moura et al., 2014).

The gold mineralized structures in northern Portugal appear commonly associated with strike-slip shear or fault zones, like the NNE-SSW fault zones (PRVF and VMF). K-Ar ages in muscovite indicated a minimum age of ca. 312 Ma for VMF, which sets a lower limit to the so-called late-Variscan wrench-faulting period (Marques et al., 2002). The age of these late Variscan faults is reasonably constrained by U-Pb ages for the Vila Pouca de Aguiar intrusion, which was emplaced into the PRVF fault zone, apparently late in its evolution and was dated at 299 ± 3 Ma (Martins et al., 2009).

In this research, as a whole, according to indirect ages, the gold mineralization event in northern Portugal seems to be younger than the late and late-to post-D3 granites and older than the emplacement of the post-tectonic granites, yielding a late Carboniferous age. The relative age of ca. 300 Ma for gold mineralization in northern Portugal could be reasonable, agreeing with the ages obtained for the Jales deposit (306 to 298 Ma).

The inferred age (~300 Ma) for the gold deposits in northern Portugal is coeval with other relative and absolute ages founded in the Bohemian and French Massifs (Table 2). On a metallogenic province scale, the gold mineralizations in the Iberian Variscan belt show a similar age that closely corresponds to changes in the regional stress pattern affecting Central and Western Europe. The same overall process may have controlled them. For example, 300-275 Ma mineralizations formed when Central and Western Europe underwent a crustal extension period with the shifting movement between Gondwana and Laurussia related to the end of the Rheic Ocean closure (*e.g.*, Kroner et al., 2016). Even younger reactivations of the same structural elements occurred in some mineralized regions during the opening of the Tethys and the North Atlantic (Romer and Kroner, 2016 and references therein).

Recent Bohemian and French massif studies revealed an older (~340-315 Ma) gold deposition event (*e.g.*, Zachariáš et al., 2013; Cheval-Garabédian et al., 2021). Related to these older ages, no significant gold resource has been identified thus far in Portugal.

7.2 Structural controls

Mineralized structures are mainly extensional veins (locally showing evidence for strike-slip reactivation and shearing) and occur mainly in sheeted veins arrays that are typically not interlinked. Vein density appears to be the principal ore grade-controlling feature in the study areas. Auriferous vein development was dominantly controlled by the NNE-

SSW striking structures parallel to the regional PRVF and VMF strike-slip faults. The gold mineralizations controlled by late-Variscan faults are post-regional metamorphism. These observations conclude that the mineralized areas formed in a structural setting related to the late Variscan regional strain, coeval with lithosphere-scale strike-slip deformation and the IberoArmorican Arc. Because of crustal decompression during uplift that is commonly associated with a shift in the far-field stress regime due to a transition from compressional to transpressional settings.

Geological structures observed in northern Portugal are related with (i) the main D1-D2 thrust tectonics, (ii) a first syn-collision extensional phase followed by a second post-collision extension marked by normal faults; (iii) the intense granitization marked by the development of large granite intrusions.
The development of hydrothermal activity between ~ 318-295 Ma implied changes in pre-existing structures' host rocks, which played an important role in channeling mineralizing fluids. The significant part of this evolution proceeded in ductile to brittle transition regime of deformation, originally under P-T conditions below 3 kbar and ranging from 300º to 350ºC, the foremost late-variscan (<310 Ma) reactivation events, in the brittle regime, took place under temperatures lower than 250ºC and pressures not above 2.5 kbar (Marques et al., 2002 and references therein). Consequently, this structural framework has been considered a critical factor in the formation of various ore-forming systems in Portugal, including gold (Mateus and Noronha, 2001). It is suggested that the granites acted as passive plutons on the origin of fluids and metals and only provided geometrical and rheological controls for the development or reactivation of extensional fractures (Mateus and Noronha, 2001). This is the case of the VMF and PRVF fault zones and second-or third-order structures, which acted as the main channel of As-Au fluid around 300 Ma.

The discussion above concerns the repetitive structural geometry of gold mineralization in northern Portugal. Although not dealt with specifically here, the nature of the hosting sequences plays important roles in structural and/or geochemical traps (Ca- and Fe-rich rocks units) and caps to the hydrothermal systems (*e.g*., reviews by Groves et al., 1998, 2020; Goldfarb et al., 2005; Robert et al., 2007). Due to a combination of a low mean stress, limited fault displacement, and over-pressured auriferous ore-fluid during deposit formation (*e.g*., Cox, 2005), only the most competent units in the rock sequence fail above the brittle-ductile transition, providing enhanced permeability for fluid flow and gold deposition. Several authors (*e.g.,* Goldfarb and Groves, 2015) discuss that these gold events that occur late during orogeny, typically during broad changes in far-field stresses leading to strike-slip events along with earlier compressional structures, regional uplift of

thickened crust, and seismically-induced fluid migration (Goldfarb et al., 2018), do not place ore formation into a post-orogenic scenario, as was recently proposed by de Boorder (2012). According to Groves et al., 2018, the specific rock units that fracture and are therefore gold mineralized vary in different orogenic belts because the litho-stratigraphic successions in these belts are distinct from one to the other.

7.3 Gold assemblage deposition conditions

Gold-bearing quartz veins in Bigorne and Numão deposits display similar mineralogical and textural features at the present erosion level, indicating that they have similar formation conditions. They show a relatively similar structure, described by (i) low-sulfide content, (ii) quartz-dominated gangue, (iii) lack of extensive hydrothermal alteration (restricted to the veins walls).

Despite being empirical thermometers not quantitative, chlorite and arsenopyrite geothermometry can estimate the relative temperature of minerals deposition. As a whole, an early W-As stage was identifying, with minerals deposition temperature around 500ºC or higher. The main sulfide stage, being the arsenopyrite dominant, occur at temperatures between 500º-350ºC. The late-stage is associated with base metals (Pb, Cu, Bi, Ag) and the main gold deposition episode. The lower end of inferred temperature deposition for coarse native gold is latter than the latter arsenopyrite and chlorites temperatures deposition (lower than 300ºC). This agrees with previously published data on fluid inclusion in other similar gold deposits in the Iberian Massif. These studies revealed that the bulk fluid inclusion in quartz of the mineralized veins and gas chemistry consisted of modified fluids (P<100 MPa and T<300ºC) with the main gold deposition being relatively late (*e.g.*, Cathelineau et al., 1993; Boiron et al.,1996; Noronha et al., 2000; Fuertes-Fuente et al., 2016; Neiva et al., 2019).

7.4 Source of the ore-forming fluids and metals

The composition and nature of ore-forming fluids are not only of scientific interest but also play a significant role in understanding ore-forming processes and choosing a strategy for mineral prospecting. The origin of ore-forming fluids can be distinguished by their H-O isotopic compositions (Taylor, 1997, Hoefs, 2018). Magmatic, metamorphic, and meteoric waters have been proposed as sources of metal-bearing fluids (*e.g.*, Alderton and Harmon, 1991). Fluid mixing, interaction with the country rocks, and fluid immiscibility are some of the proposed mechanisms for ore deposition (Chicharro et al., 2016).

Despite differences in host rocks (granites and metasediments) and varying metamorphic grades, ore fluid compositions from various gold deposits in northern Portugal display an excellent uniformity (see Table 2), revealing a relatively consistent ore-forming fluid. This homogeneous isotopic composition is interpreted to result from multiple mechanisms of gold deposition (*e.g.*, Au scavenging by liquid bismuth-bearing phases) from a single, ubiquitous mineralizing fluid in varying structural settings rather than from the involvement of the fluids from a different source. However, magmatic fluids from shallow-level felsic intrusions, although not completely ruled out. These results support earlier studies of fluid inclusions studies, which revealed that the mineralizing fluid is consistent with the evolution from low salinity reduced fluids (H_2O-NaCl-CO_2 ± CH_4) to H_2O-NaCl dominated fluid system.

Gold deposition took place in a narrow P-T window, below to 300ºC, after sulfide deposition. This trend also has been observed in other Variscan gold quartz veins of northwestern Iberia by Boiron et al. (1996), based on its halogen signature. In Alpine and Variscan deposits, halogen systematics based on bulk fluid extraction has been interpreted by Yardley et al. (1993) and Boiron et al. (1996) as reflecting the deep circulation of meteoric water gold ore formation.

Fluid types are similar in veins hosted by granites and metamorphic rocks. As magmatic fluids are absent, the granites thus act passively as heat engines for fluid circulation (Noronha et al., 2000). Therefore, the gold mineralizations appear to result from successive periods of fluid circulation. Without exception, these fluids have been re-equilibrated with the host rocks.

S-isotopic compositions (Table 2) from sulfides in the gold-bearing veins are inferred to have a crustal derived source. The lack or scarcity of sulfides in granitic rocks and their abundance in some lithologies of the metamorphic pile (SGC) lead us to propose that the metal source is metasedimentary rocks at deep crustal levels. There is no unique signature for the sulfur isotope. Changes in redox and other chemical parameters at the site of gold deposition can only shift sulfur compositions a few per mil, so the variability is unlikely to be due to variable sulfide deposition conditions. At least for the Phanerozoic gold deposits, $\delta^{34}S$ compositions vary with the age of the host rock. This was interpreted by Goldfarb et al. (1998) to indicate that the sulfur source was required to be disseminated syngenetic/diagenetic pyrite in the terranes being devolatilized at depth. As discussed in detail by Goldfarb and Groves (2015) and Groves et al., 2020, there are few unequivocal indications of this clear fluid or metal source from fluid inclusion, stable isotope, or radiogenic isotope data. This is because most data do not represent the original fluid and metal source, but rather the modification of that source by reactions

along the long crustal pathways traversed by the fluids as they migrate towards gold depositional sites (Ridley and Diamond, 2000; Groves et al., 2020).

7.5 General classification

Mineral deposit models are typically developed by integrating data from numerous deposit case studies to produce a unifying model representing mineral assemblage, hydrothermal alteration, and fluid characteristics typical of those deposits (McCuaig and Hronsky, 2014).

The gold mineralization in northern Portugal belongs to the gold-only group deposits and shares OGS and RIGS characteristics, as discussed in chapters 4, 5, and 6. Some characteristics are not consistent with fluid exsolution from upper crustal magmas (RIGS) (*e.g.,* Goldfarb and Santosh, 2014; Goldfarb and Groves, 2015) like i) lack of temporal association between the gold and adjacent granitic massifs, ii) the actual absence of significant vertical zoning, and iii) the relationship of the mineralized structure with major regional fault systems. A magmatic origin for ore-forming fluids is unlikely, as magmatic fluids associated with NW Iberian gold deposits are not identified in several fluid inclusions studies.

However, the evidence from RIGS shows that fluids with similar chemistry to OGDs can form from magmatism (Hart, 2007). Ascribing a solely magmatic or metamorphic origin to mineralizing fluids seems unlikely due to the potential overlap of fluids from several sources. A more probable explanation is that the mineralizing fluid originates at deeper crustal levels during the late Variscan deformation events, dominantly under mesothermal conditions, with a contribution of magmatic, metamorphic, and meteoric components.

This result highlights the need for a comprehensive review of gold-only deposit models, specifically in Phanerozoic gold deposits in small metallogenic provinces.

7.6 Exploration techniques

A mineral deposit forms because of complex geologic processes, making it challenging to effectively confirm mineralized bodies below the surface. Primary haloes are commonly utilized in mineral exploration as an indicator of the presence of blind mineralized bodies. All over the years, several methodologies have been developed and applied in gold mineralization in northern Portugal.

In this research project, the first exploration approach is a detailed deposit-scale description for the Bigorne and Numão deposits, which contribute to the characterization

and understanding of mineralization vectors, thus improving mineral exploration and locating newly available information in the area.

The persistence of gold in the surface environment and its availability makes it an ideal mineral to investigate ore-forming processes and used as a pathfinder, as tested and described in chapter 5. However, the general scarcity of gold particles in detrital material from the hypogene deposits influenced gold particles sampling approaches, as large populations are required to gain helpful research. This technique was tested in the Numão and Castromil areas without positive results due to the small size of the gold particles from hypogene veins. We recommend that a combination of classic stream-sediment geochemistry, heavy mineral analysis, and gold detrital particles studies be used more widely to provide additional insights into the location and nature of gold mineralization and regional metallogeny regions of poor exposure and complex geology. These aspects reduce the efficiency of these methods for obtaining whole-rock geochemistry data during active exploration. Thus, efforts have been devoted to implementing portable XRF as a fast, cost-effective first-stage tool in lithogeochemical exploration in gold and other mineral systems.

A fundamental concept of exploration targeting is that mineral deposits are small-scale expressions of larger, more extensive systems and the interaction of numerous ore-controlling processes (Grunsky and Caritat, 2020). In considering large-scale ore-controlling processes, in particular for structurally-controlled deposits, developing a robust multi-scale mineral deposit model is an essential first step for successful exploration (McCuaig and Hronsky, 2014). Grunsky (2010) described a systematic approach to evaluating geochemical data that involves examining geochemical data as individual elements and multivariate associations. The application of PCA proved to be of utmost importance to discriminate geochemical/ geological processes and mineralization pathfinders in the Numão area.

Determining isotope values requires detailed sample preparation and analysis, which is well beyond the scope of most exploration programs.
However, multiple ore-depositional processes at a single deposit location are potentially critical factors for large gold endowment and high gold grade. Therefore, recognizing more than one potential gold-deposition mechanism and source in a gold system is essential. Analysis of isotope values would complement structural, alteration, and fluid inclusion studies that similarly seek to identify multiple ore-forming processes.
Ultimately, the Portuguese gold occurrences are not particularly rare, including many mined historically (Roman times to 1990), which would not be economic today, mainly because of low tonnage, the difficulty of mining discrete vein-style deposits, and the lack

of detailed deposit-scale information. This recaps the importance of developing tools and techniques to detect gold mineral deposits beneath the ground surface.

7.7 Future works

- It is critical to establish absolute ages of formation for as many examples of gold mineralization in the region, as well as other types of mineralization (*e.g*., W and W-Sn) as possible;
- Realize a large and completed detailed deposit-scale study (mineral chemistry and isotope data) in other gold occurrences in northern Portugal;
- Apply the study of detrital gold particles in other gold occurrences in northern Portugal systematically to improve the Portuguese deposits' sampling technique and produce available results to the exploration companies.

"Mineral exploration is like finding a needle in a haystack."

Carranza and Sadeghi, 2012

References list

Ábalos, B.V. 1992. Cinemática y mecanismos en regimen de transpresion. Evoluvión estructural y metamorficca de la zona de cizalla dúctil de Badajoz-Córdoba.

Aitchison, J. 1986. The statistical analysis of compositional data, XII edn. Chapman and Hall, London - New York 1986, p 416.

Alcock, J.E., Martínez, J.R., Rubio, F.J., Díez, A., Díez, R., Gómez, J., Arenas, R., Dias, Í., González, E. 2015. Tectonophysics 2-D thermal modeling of HT-LP metamorphism in NW and Central Iberia: Implications for Variscan magmatism, rheology of the lithosphere and orogenic evolution. Tectonophysics 657, 21–37. https://doi.org/10.1016/j.tecto.2015.05.022.

Alderton, D.H.M., Harmon, R.S. 1991. Fluid inclusion and stable isotope evidence for the origin of mineralizing fluids in south-west England. Mineralogical Magazine, 55, 605–611. http://dx.doi.org/10.1180/minmag.1991.055.381.13.

Almeida, A. and Noronha, F. 1988. Fluids associated with Ag-Au of the Mirandela area, NE Portugal: an example of peri- granitic zoning. Bulletin Mineralogique, v. III, pp. 331-341.

Almeida, A., Leterrier, J., Noronha, F., Bertrand, J.M. 1998. U-Pb zircon and monazite geochronology of the Hercynian two-mica granite composite pluton of Cabeceiras de Basto (Northern Portugal). Comptes Rendus de l'Académie des Sciences - Series IIA - Earth and Planetary Science, 326, 11, pp. 779–785. https://doi.org/10.1016/S1251-8050(98)80243-7.

Alonso, J. L., Marcos, A., Suárez, A. 2009. Paleogeographic inversion resulting from large out of sequence breaching thrusts: The León Fault (Cantabrian zone, NW Iberia). A new picture of the external Variscan thrust belt in the Ibero-Armorican arc, Geologica Acta, 7, 451–473, https://doi.org/10.1344/105.000001449.

Antweiler, J. C. and Campbell, W. 1977. Application of gold compositional analyses to mineral exploration in the United States. Developments in Economic Geology. 8:17-29. https://doi.org/10.1016/B978-0-444-41653-7.50009-3.

Armbruster T., Bonazzi P., Akasaka M., Bermanec V., Chopin C., Giere R., Heuss-Assbichler S., Liebscher A., Menchetti S., Pan Y., Pasero M. 2006. Recommended nomenclature of epidote-group minerals. European Journal of Mineralogy 18, 551-567.

Arribas, A. 1979. Les gesiments de tungstène de la zone de Morille (Province de Salamanca, Espagne). Chronique de la Recherche Miniere, 450, 27-34.

Arthaud, F. and Matte, P.H. 1975. Les décrochements tardi hercyniens du Sud-Ouest de l'Europe. Géométrie et essai de reconstitution des conditions de la déformation. Tectonophysics, 25 (1/2): 139–171. https://doi.org/10.1016/0040-1951(75)90014-1.

Azor, A., Dias da Silva, Í., Gómez Barreiro, J., González-Clavijo, E., Martínez Catalán, J.R., Simancas, J. F, et al., 2019. Deformation and Structure. In: Quesada C, Oliveira JT, eds. The Geology of Iberia: A Geodynamic Approach: Vol. 2: The Variscan Cycle, Regional Geology Reviews. Cham: Springer International Publishing, pp. 307–348. https://doi.org/10.1007/978-3-030-10519-8_10.

Bache, J. J. 1987. World Gold Deposits, A Geological Classification, New York, Academic, 18–26.

Baker, T. 2002. Emplacement depth and carbon dioxide-rich fluid inclusions in intrusion-related gold deposits: Economic Geology, v. 97, p. 1111–1117.

Ballèvre, M., Martínez Catalán, J.R., López Carmona, A., Pitra, P., Abati, J., Díez Fernández, R., Ducassou, C., Arenas, R., Bosse, V., Castiñeiras, P., Fernández-Suárez, J., Gómez Barreiro, J., Paquette, J.L., Peucat, J.J., Poujol, M., Ruffet, G., and Sánchez Martínez, S. 2014. Correlation of the nappe stack in the Ibero-Armorican arc across the Bay of Biscay: A joint French-Spanish project: Geological Society, London, Special Publications, v. 405, p. 77–113. doi:10.1144/sp405.13.

Bark, G., Boyce, A. J., Fallick, A. E., Weihed, P. 2020. Fluid and metal sources in the Fäboliden hypozonal orogenic gold deposit, Sweden. Mineralium Deposita. https://doi.org/10.1007/s00126-020-00977-7.

Barker, S.L.L., Dipple, G.M., Hickey, K.A., Lepore, W.A., Vaughan, J.R. 2013. Applying stable isotopes to mineral exploration: teaching an old dog new tricks. Economic Geology, 108, 1, pp. 1-9. http://dx.doi.org/10.2113/econgeo.108.1.1.

Barrios, S., Merinero, R., Lozano, R., Orea, I. 2015. Morphogenesis and grain size variation of alluvial gold recovered in auriferous sediments of the Tormes Basin (Iberian Peninsula) using a simple correspondence analysis. Mineralogy and Petrology, 109, 679–691. https://doi.org/10.1007/s00710-015-0399-x.

Bayliss, P. 1975. Nomenclature for the trioctahedral chlorites. Canadian Mineralogist, 13: 178-180.

Bea F. 2004. La naturaleza del magmatismo de la Zona Centroibérica: consideraciones generales y ensayo de correlación. Libro de Geología de España (SGE-IGME), Ed J-A Vera, pp. 128-132.

Beaudoin, G., Pitre, D. 2005. Stable isotope geochemistry of the Archean Val-d'Or (Canada) orogenic gold vein field. Mineralium Deposita, 40, 59–75.

Bodnar R.J., Lecumberri-Sanchez P., Moncada D. and Steele-MacInnis M. 2014. Fluid Inclusions in Hydrothermal Ore Deposits. In: Holland H.D. and Turekian K.K. (eds.) Treatise on Geochemistry, Second Edition, vol. 13, pp. 119- 142. Oxford: Elsevier.

Böhlke, J. K, Kistler, R. W. 1986. Rb-Sr, K-Ar, and stable isotope evidence for the ages and sources of fluid components of gold-bearing quartz veins in the northern Sierra Nevada Foothills metamorphic belt, California. Economic Geology, 81, 296–322.

Böhlke, J.K. 1982. Orogenic metamorphic-hosted gold–quartz veins. U.S. Geological Survey Open-File Report 795, pp. 70–76.

Boiron, M.C., Cathelineau, M., Banks, D., Yardley, B.W.D., Noronha, F., Miller, M.F. 1996. P–T–X-Conditions of late Hercynian fluid penetration of granite-hosted Au–quartz veins in NW Iberia: a multidisciplinary study of fluid inclusions and their chemistry. Geochimica et Cosmochimica Acta, 60, 1, 43-57. https://doi.org/10.1016/0016-7037(95)00364-9.

Boiron, M.C., Cathelineau, M., Banks, D.A., Fourcade, S., Vallance, J. 2003. Mixing of metamorphic and surficial fluids during the uplift of the Hercynian upper crust: consequences for gold deposition. Chemical Geology, 194, 1-3, 119-141. https://doi.org/10.1016/S0009-2541(02)00274-7.

Boiron, M.C., Cathelineau, M., Dubessy, J., Bastoul, A.M., 1990. Fluids in Hercynian Au veins from the French Variscan belt. Mineralogical Magazine 54, 231– 243.

Boorder, H. 2012. Spatial and temporal distribution of the orogenic gold deposits in the Late Palaeozoic Variscides and Southern Tianshan: How orogenic are they? Ore Geology Reviews, 46, 1–31. doi:10.1016/j.oregeorev.2012.01.002.

Bottinga Y. and Javoy M. 1973. Comments on oxygen isotope geothermometry. Earth and Planetary Science Letters, 20, 250–265.

Bouchot, V., Ledru, P., Lerouge, C., Lescuyer, J.L., Milesi, J.P. 2005. Late Variscan mineralizing systems related to orogenic processes: the French Massif Central. Ore Geology Reviews. 27, 169-197. doi:10.1016/j.oregeorev.2005.07.017.

Boyle, R. W. 1979. The geochemistry of gold and its deposits: together with a chapter on geochemical prospecting for the element, Geological Survey of Canada Ottawa.

Boynton, W.V. 1984. Geochemistry of Rare Earth Elements: Meteorite Studies. In: Henderson, P., Ed., Rare Earth Element Geochemistry, Elsevier, New York, 63-114. http://dx.doi.org/10.1016/B978-0-444-42148-7.50008-3.

Brugger, J., Etschmann, B., Pownceby, M., Liu,W., Grundler, P., Brewe, D. 2008. Oxidation state of europiumin scheelite: tracking fluid-rock interaction in gold deposits. Chemical Geology, 257, 26-33.

Brun, J. P, Burg, J. P. 1982. Combined thrusting and wrenching in the Ibero-armorican arc - a corner effect during continental collision. Earth and Planetary Science Letters, 61, 319–332.

Cabral, J. 2012. Neotectonics of mainland Portugal: state of the art and future perspectives. Journal of Iberian Geology, 3, 1, 71–84. https://doi.org/10.5209/rev_JIGE.2012.v38.n1.39206.

Caessa, P. N. S., Oliveira, D. P. S., Barros, A. F. 1998. Bigorne: Ocorrência de ouro do tipo “sheeted vein” na zona de Castro Daire – Centro Norte de Portugal. Estudos, Notas e Trabalhos, Instituto Geológico e Mineiro, 40, 71-79. (in portuguese)

Calvo, G., Mudd, G.M., Valero, A., Valero, A. 2016. Decreasing ore grades in global metallic mining: a theoretical issue or a global reality? Resources 5, 36. https://doi.org/10.3390/resources5040036.

Carranza, E. J. M. 2012. Geochemical characteristics of mineral deposits: Implications for ore genesis. Geochemistry: Exploration, Environment, Analysis 12, 89–92. https://doi.org/10.1144/1467-7873/12-MINDEP-122.

Carrington da Costa, J. 1950. Notícia sobre uma carta geológica do Buçaco, de Nery Delgado. Publicação Especial Comunicações Serviços Geológicos Portugal, 27p. (in portuguese)

Carvalho, P.C.S., Neiva, A.M.R., Silva, M.M.V.G., Corfu, F. 2012. A unique sequential melting mechanism for the generation of anatectic granitic rocks from the Penafiel area, northern Portugal. Lithos, 155, 110–124. http://dx.doi.org/10.1016/j.lithos.2012.08.019.

Cassard, D., Bertrand, G., Billa, M., Serrano, J.J., Tourlière, B., Angel, J.M., Gaál, G. 2015. ProMine Mineral Databases: new Tools to Assess Primary and Secondary Mineral Resources in Europe. P. Weihed (Ed.), ProMine Mineral Databases: new Tools to Assess Primary and Secondary Mineral Resources in Europe., 3D, 4D and Predictive Modelling of Major Mineral Belts in Europe, pp. 9-58.

Castro A, Corretgé LG, De la Rosa J, Enrique P, Martínez FJ, Pascual E, Lago M, Arranz E, Galé C, Fernández C, Donaire T, López S. 2002. Paleozoic Magmatism. In: Gibbons W, Moreno MT (eds) The Geology of Spain, vol. Geological Society, London, London, pp 117-153.

Cathelineau M. 1988. Cation site occupancy in chlorites and illites as a function of temperature. Clay Minerals, 23, 4, 471–485.

Cathelineau M., Boiron M.C., Palomero F.G., Urbano R., Florido P., Pereira E., Noronha F., Barriga F.J.A.S., Mateus A., Yardley B., Banks D. 1993. Multidisciplinary studies of Au-vein formation. Application to the Western part of the Hesperian Massif (Spain-Portugal). Project MA2M-CT90-0033, Multi-annual R&D Programme (1990-1992) on Primary Raw Materials and Recycling of Non-ferrous Metals, CEC – Final Report: 319 pp.

Cave, B.J., Barnes, S. J, Pitcairn, I. K., Sack, P.J, Kuikka, H Johnson, S. C, Duran CJ. 2019. Multi-stage precipitation and redistribution of gold, and its collection by lead-bismuth and lead immiscible liquids in a reduced-intrusion related gold system (RIRGS); Dublin Gulch,

western Canada. Ore Geology Reviews, 106, 28-55. https://doi.org/10.1016/j.oregeorev.2019.01.010.

Cepedal, A., Fuertes-Fuente, M., Martín-Izard, A. et al., 2006. Tellurides, selenides and Bi-mineral assemblages from the Río Narcea Gold Belt, Asturias, Spain: genetic implications in Cu–Au and Au skarns. Mineralogy and Petrology, 87, 277–304. https://doi.org/10.1007/s00710-006-0127-7.

Cepedal, A., Fuertes-Fuente, M., Martin-Izard, A., García-Nieto, J., Boiron, M.C. 2013. An intrusion-related gold deposit (IRGD) in the NW of Spain, the Linares deposit: igneous rocks, veins and related alterations, ore features and fluids involved. Journal of Geochemical Exploration, 124, 101-126. http://dx.doi.org/10.1016/j.gexplo.2012.08.010.

Cepedal, A., Fuertes-Fuente, M., Martin-Izard, A., Gonzalez Nistal, S., Barrero, M. 2008. Gold-bearing As-rich pyrite and arsenopyrite from the El Valle gold deposit, Asturias, northwestern Spain. Canadian Mineralogist, 46, 233-247. DOI: 10.3749/canmin.46.1.233.

Cepedal, A., Martín-Izard, A., Reguilon, R., Rodrıguez-Pevida, L., Spiering, E., González- Nistal, S., 2000. Origin and evolution of the calcic and magnesian skarns hosting the El Valle-Boinás copper–gold deposit, Asturias (Spain). Journal of Geochemical Exploration71, 119–151. https://doi.org/10.1016/S0375-6742(00)00149-7.

Cerveira, A., 1952. Relações entre os jazigos hipogénicos portugueses de ouro e tungsténio. Boletim da Sociedade Geológica de Portugal, 10, 133–144.

Chapman, R. J, Allan, M.M., Mortensen, J. K., Wrighton, T. M., Grimshaw, M. R. 2018. A new indicator mineral methodology based on a generic Bi-Pb-Te-S mineral inclusion signature in detrital gold from porphyry and low/intermediate sulfidation epithermal environments in Yukon Territory, Canada. Mineralium Deposita, 53, 815-834. https://doi.org/10.1007/s00126-017-0782-0.

Chapman, R. J., Leake, R. C., Bond, D. P. G., Stedra, V., & Fairgrieve, B. 2009. Chemical and mineralogical signatures of gold formed in oxidizing chloride hydrothermal systems and their significance within populations of placer gold grains collected during reconnaissance. Economic Geology, 104, 563–585. https://doi.org/10.2113/gsecongeo.104.4.563.

Chapman, R. J., Mileham, T. J, Allan, M. M., Mortensen, J. K. 2017. A distinctive Pd-Hg signature in detrital gold derived from alkalic Cu-Au porphyry systems. Ore Geology Reviews, 83, 84-102. https://doi.org/10.1016/j.oregeorev.2016.12.015.

Chapman, R.J. and Mortensen, J.K. 2016. Characterization of gold mineralization in the Northern Cariboo gold district, British Columbia, Canada, through integration of compositional studies of lode and detrital gold with historical placer production: A template for evaluation of orogenic gold districts: Economic Geology, 111, 1321–1345. http://dx.doi.org/10.2113/econgeo.111.6.1321.

Chapman, R.J., Banks, D.A, Styles, M.T., Walshaw, R.D., Piazolo, S., Morgan, D.J., Grimshaw, M.R., Spence-Jones, C.P., Matthews, T.J., & Borovinskaya, O. 2021 Chemical and physical heterogeneity within native gold: implications for the design of gold particle studies. Mineralium Deposita, Feb 1, 1-26. https://doi.org/10.1007/s00126-020-01036-x.

Cheval-Garabédian F, Faure M, Marcoux E, Gouin J, Picault M. 2020. The La Bellière gold and antimony district (French Armorican Massif): a two-stage evolution model controlled by Variscan strike slip tectonic. Ore Geology Reviews, 125, 103–681.

Cheval-Garabédian, F., Faure, M., Marcoux, E., Poujol, M. 2021. The tungsten-gold veins of Bonnac (French Massif central): new constraints for a Variscan granite-related genesis. BSGF - Earth Sci. Bull. 192, 7. https://doi.org/10.1051/bsgf/2020041.

Chicharro, E., Boiron, M-C., López-García, J, A., Barfod, D, N., Villaseca, C. 2016. Origin, ore forming fluid evolution and timing of the Logrosán Sn–(W) ore deposits (Central Iberian Zone, Spain), Ore Geology Reviews, 72, 1, 896-913, https://doi.org/10.1016/j.oregeorev.2015.09.020.

Cline, J. S., Hofstra, A. H., Muntean, J. L., Tosdal, R. M. & Hickey, K. A. 2005. Carlin-type gold deposits in Nevada: Critical geologic characteristics and viable models. Economic Geology 100th anniversary volume, 100, 451-484.

Cooper, M.P and Stanley, C. J. 1990. Minerals of the English Lake District: Caldbeck Fells. The Natural History Museum. 160pp.

Costa, M., 2011. Geoquímica dos granitóides de Aguiar da Beira, Norte de Portugal. Ph.D. thesis. University of Aveiro, unpublished. (in portuguese)

Costa, M.M., Neiva, A.M.R., Azevedo, M.R., Corfuc, F. 2014. Distinct sources for syntectonic Variscan granitoids: Insights from the Aguiar da Beira region, Central Portugal. Lithos, 196-197,83–98. http://dx.doi.org/10.1016/j.lithos.2014.02.023.

Couto, H., Roger, G., Moëlo, Y., Bril, H. 1990. Le district à antimoine-or Dúrico-Beirão (Portugal): évolution paragénétique et géochimique; implications métallogéniques: Mineralium Deposita, 25, 69-81. DOI: 10.1007/BF00205252.

Cox, D. P. and Singer, D. A. 1986. Mineral deposit models, US Government Printing Office.

Cox, S.F., 2005. Coupling between Deformation, Fluid Pressures, and Fluid Flow in Ore-producing Hydrothermal Systems at Depth in the Crust. Economic Geology, 100th Anniversary Volume, pp. 39-75

Crespo, J.L., Moro, M.C., Fadón, O., Cabrera, R., Fernandez, A. 2000. The Salamón gold deposit (León, Spain). Journal of Geochemical Exploration, 71, 191-208.

Cruz, C., Noronha, F., Santos, P., Mortensen, J., & Lima, A. 2018. Supergene gold enrichment in the Castromil-Serra da Quinta gold deposit, NW Portugal. Mineralogical Magazine, 82, S1, S307-S320. doi:10.1180/minmag.2017.081.063.

Cruz, C., Sant'Ovaia, H. & Noronha, F. 2020. Magnetic mineralogy of Variscan granites from northern Portugal: an approach to their petrogenesis and metallogenic potential. Geologica Acta, 18, 5, 1-20.

Dallmeyer, R. D., Fonseca, P. E., Quesada, C., and Ribeiro, A. 1993. 40Ar=39Ar mineral age constraints for the tectonothermal evolution of a Variscan suture in southwest Iberia, Tectonophysics, 222, 177-194, https://doi.org/10.1016/0040-1951(93)90048-O.

Dallmeyer, R.D., Martinez Catalán, J.R., Arenas, R., Gil Ibarguichi, J.I., Gutiérrez-Alonso, G., Farias, P., Batisda, F., Aller, J. 1997. Diachronous Variscan tectonothermal activity in the NW Iberian Massif: evidence from 40Ar/39Ar dating of regional fabrics. Tectonophysics 277, 4, 307-337. https://doi.org/10.1016/S0040-1951(97)00035-8.

Debon, F. and Le Fort, P. 1983. A chemical–mineralogical classification of common plutonic rocks and associations. Earth and Environmental Science Transactions of The Royal Society of Edinburgh, 73, 3, 135-149. https://doi.org/10.1017/S0263593300010117.

Deng, J., Wang, Q.F., Santosh, M., Liu, X.F., Liang, Y.Y., Yang, Zhao, L.Q., Yang, R.L. 2020. Remobilization of metasomatized mantle lithosphere: a new model for the Jiaodong gold province, eastern China. Mineralium Deposita, 55, pp. 257-274. DOI: 10.1007/s00126-019-00925-0.

Derré, C., Lécolle, M. & Roger, G. 1982. Les quartzites à silicates calciques et scheelite: Préconcentrations familières ou Pièges por um Tungstène Etranger liè à L'Hydrothermalisme Périgranitique? Example du Nord-Est Transmontain (Portugal). Mineralium Deposita, 17, 363-385.

Dias da Silva, Í., Gómez-Barreiro, J., Martínez Catalán, J.R., Ayarza, P., Pohl, J., and Martínez, E., 2017, Structural and microstructural analysis of the retortillo syncline (Variscan belt, Central Iberia). Implications for the Central Iberian Orocline: Tectonophysics, v. 717, p. 99–115. doi:10.1016/j.tecto.2017.07.015.

Dias da Silva, Í., González Clavijo, E., Díez-Montes, A. 2020. The collapse of the Variscan belt: a Variscan lateral extrusion thin-skinned structure in NW Iberia, International Geology Review, 63, 6, 1–37, https://doi.org/10.1080/00206814.2020.1719544.

Dias G, Simões PP, Ferreira, N., Leterrier, J. 2002. Mantle and crustal sources in the genesis of late-hercynian granitoids (NW Portugal): geochemical and Sr-Nd isotopic constraints. Gondwana Research, 5, 2, 287–305.

Dias, G., Leterrier, J., Mendes, A., Simões, P., Bertrand, J.M. 1998. U-Pb zircon and monazite geochronology of syn- to post-tectonic Hercynian granitoids from the Central Iberian Zone

(Northern Portugal). Lithos, 45, 1-4, 349-369, https://doi.org/10.1016/S0024-4937(98)00039-5.

Dias, R. and Ribeiro, A. 1994. Constriction in a transpressive regime – an example in the Iberian branch of the Ibero-Armorican arc, Journal of Structural Geology, 16, 1543-1554.

Dias, R. and Ribeiro, A. 1995. The Ibero-Armorican Arc: a collision effect against an irregular continent? Tectonophysics, 246, 113–128. http://dx.doi.org/10.1016/0040-1951(94)00253-6.

Dias, R., Ribeiro, A. 1991. Finite strain analysis in a transpressive regime (Variscan autochthon, northeast Portugal). Tectonophysics, 191, 389-397.

Dias, R., Ribeiro, A., Coke, C., Pereira, E., Rodrigues, J., Castro, P., Moreira, N., Rebelo, J., 2013. Evolução estrutual dos sectores setentrionais do Autóctone da Zona Centro-Ibérica, in: Dias, R., Araújo, A., Terrinha, P., Kullberg, J.C. (Eds.), Geologia de Portugal, Vol. 1. Escolar Editora, pp. 74-147.

Dias, R., Ribeiro, A., Romão, J., Coke, C., Moreira, N. 2016. A review of the arcuate structures in the Iberian variscides; constraints and genetical models. Tectonophysics, 681, 170–194. http://dx.doi.org/10.1016/j.tecto.2016.04.011.

Díez Balda, M. A., Martínez Catalán, J. R., Ayarza Arribas, P. 1995. Syn-collisional extensional collapse parallel to the orogenic trend in a domain of steep tectonics: the Salamanca Detachment Zone (Central Iberian Zone, Spain), Journal of Structural Geology, 17, 2, 163–182, doi:10.1016/0191-8141(94)E0042-W, 1995.

Díez Balda, M.A., Vegas, R., González Lodeiro, F. 1990. Structure, in Dallmeyer, R.D., and Martínez García, E. eds., Pre-Mesozoic Geology of Iberia, Germany, Springer-Verlag, p. 172-188.

Díez Fernández, R. and Arenas, R. 2015. The late Devonian Variscan suture of the Iberian Massif: a correlation of high-pressure belts in NW and SW Iberia. Tectonophysics, 654, 96–100, https://doi.org/10.1016/j.tecto.2015.05.001.

Díez Fernández, R., Arenas, R., Pereira, M.F., Sánchez-Martínez, S., Albert, R., Martín Parra, L.M., Rubio Pascual, F.J., and Matas, J. 2016. Tectonic evolution of Variscan Iberia: Gondwana- Laurussia collision revisited: Earth-Science Reviews, v. 162, p. 269–292, https://doi.org/10.1016/j.earscirev.2016.08.002.

Díez Montes, A. 2007. La Geología del Dominio “Ollo de Sapo” en las comarcas de Sanabria y Terra do Bolo. A Coruña, Nova Terra 34, Instituto universitario de geología “Isidro Parga Pondal”, Área de xeoloxía e minería do seminario de estudos galegos, 494pp.

Dipple, G. M. and Ferry, J. M. 1992. Metasomatism and fluid flow in ductile fault zones. Contribution to Mineralogy and Petrology, 112, 149-164.

Douglas, N., Mavrogenes, J., Hack, A., England, R. 2000. The liquid bismuth collector model: an alternative gold deposition mechanism. AGC Abstr. vol. 59: 135.

Droop G.T.R. 1987. A general equation for estimating Fe3+ concentrations in ferromagnesian silicates and oxides from microprobe analyses using stoichiometric criteria. Mineralogical Magazine 51, 431-435.

EC, 2014. European Commission, 2014. Report on Critical Raw Materials for the EU: Critical Raw Materials Profiles. Adhoc Working Group on defining critical raw materials. European Commission.

EC, 2017. European Commission, 2017. On the 2017 list of Critical Raw Materials for the EU. Communication from the Commission to the European Parliament, the Council, the European Economic and Social Committee and the Committee of the Regions COM. 490 final. Brussels.

EDM, 2017. Empresa de Desenvolvimento Mineiro. Retrieved from: https://edm.pt/projetos/recuperacao-ambiental-da-escombreira-da-area-mineira-de-jales/.

Ehser, A., Borg G., de Oliveira D.P.S., Rosa D.R.N., Salgueiro R. 2011. Characterization of placer gold deposits from central Portugal: preliminary results. 11th SGA Biennial Meeting, Antofagasta. Proceedings Volume, p. 814-816.

Ehser, A., Borg, G., Pernicka, E. 2010. Fingerprinting of Cornish gold for provenancing prehistoric gold artefacts from Central Europe. in ‘‘IMA 2010: Bonds and Bridges’’, E. Pal-Molnar, ed., 20th General Meeting of the International Mineralogical Association, Budapest, Acta Mineral.-Petrogr., 6, 106.

Eilu, P. and Weihed, P. 2005. Fennoscandian Shield – Orogenic gold deposits, Ore Geology Reviews, 27, 326-327.

Eilu, P., Ahtola, T., Äikäs, O., Halkoaho, T., Heikura, P., Hulkki, H., Iljina, M., Juopperi, H., Karinen, T., Kärkkäinen, N., Konnunaho, J., Kontinen, A., Kontoniemi, O., Korkiakoski, E., Korsakova, M., Kuivasaari, T., Kyläkoski, M., Makkonen, H., Niiranen, T., Nikander, J., Nykänen, V., Perdahl, J.-A., Pohjolainen, E., Räsänen, J., Sorjonen-Ward, P., Tiainen, M., Tontti, M., Torppa, A. & Västi, K. 2012. Metallogenic areas in Finland. In Mineral deposits and metallogeny of Fennoscandia (P. Eilu Ed.), Geological Survey of Finland, Special Paper 53, 207–342.

Emmons, W. 1933. On the mechanism of the deposition of certain metalliferous lode systems associated with granitic batholiths. Ore deposits of the western States: New York, American Institute of Mining and Metallurgical Engineers, 327-349.

Engel, A.E.J., Clayton, R.N., and Epstein, S. 1958. Variations in isotopiccomposition of oxygen and carbon in Leadville limestone (Mississippian, Colorado) and in its hydrothermal and metamorphic phases: Journal of Geology, 66, 374–393.

Farias, P., Gallastegui, G., Gonzalez Lodeiro, F., Marquinez, J., Martin Parra, L.M., Martínez Catalan, J.R., de Pablo Maciá, J.G., Rodriguez Fernandez, L.R., 1987. Aportaciones al conocimiento de la litoestratigrafia y estructura de Galícia Central. In: IX Reunião de Geologia do Oeste Peninsular, Porto, 1985. Memórias Museu Laboratório Mineralogia Geologia da Faculdade Ciências Universidade Porto 1, 411-431. (in spanish)

Fernández-Suárez, J., Dunning, G.R., Jenner, G.A., and Gutiérrez-Alonso, G. 2000. Variscan collisional magmatism and deformation in NW Iberia: Constraints from U-Pb geochronology of granitoids: Journal of the Geological Society of London, 157, 565–576, https://doi.org/10.1144/jgs.157.3.565.

Ferreira da Silva, A. et al., 1989. Carta Geológica de Portugal na escala 1:50.000 – Notícia Explicativa da folha 11-C – Torre de Moncorvo. Serviços Geológicos de Portugal, Lisboa (in portuguese).

Ferreira, N., Iglésias, M., Noronha, F., Pereira, E., Ribeiro, A., Ribeiro, M.L., 1987. Granitóides da Zona Centro Ibérica e seu enquadramento geodinâmico. In: Bea, F., Carnicero, A., Gonzalo, J., Lopez Plaza, M., Rodriguez Alonso, M. (Ed.), Geología de los Granitoides y Rocas Asociadas del Macizo Hesperico. Editorial Rueda, Madrid. Libro de Homenaje a L.C. García de Figuerola, 37-51. (in spanish)

Filzmoser, P., Hron, K., Reimann, C. 2009. Univariate statistical analysis of environmental (compositional) data: problems and possibilities. Science of The Total Environment, 407, 6100–6108. https://doi.org/10.1016/j.scitotenv.2009.08.008.

Fisher, N.H. 1945. The fineness of gold, with special reference to the Morobe gold field, New Guinea. Economic Geology, 40, 449-495.

Fonte, J., Lima, A., Matías Rodríguez, R., Gonçalves, J.A., Leal, S. 2017. New evidence of Roman gold and tin mining in the upper Tâmega valley (Montalegre and Boticas, Northern Portugal). Estudos do Quaternário, 2017, 17, 45-55. http://www.apeq.pt/ojs/index.php/apeq.

Frimmel, H.E. 2008. Earth's continental crustal gold endowment, Earth and Planetary Science Letters, 267, (1–2), 45-55, https://doi.org/10.1016/j.epsl.2007.11.022.

Frost, B. R., Barnes, C. G., Collins, W. J., Arculus, R. J., Ellis, D. J., Frost, C. D. 2001. Geochemical Classification for Granitic Rocks. Journal of Petrology, 42, 11, 2033-2048, https://doi.org/10.1093/petrology/42.11.2033.

Fuertes-Fuente, M., Cepedal, A., Lima, A., Dória, A., Ribeiro, M.A., Guedes, A. 2016. The Au-bearing vein system of the Limarinho deposit (northern Portugal): Genetic constraints from Bi-chalcogenides and Bi–Pb–Ag sulfosalts, fluid inclusions and stable isotopes. Ore Geology Reviews, 72, 461, 213-231. https://doi.org/10.1016/j.oregeorev.2015.07.009.

Fuertes-Fuente, M., Martin-Izard, A., García-Nieto, J., Maldonado, C., Varela, A. 2000. Preliminary mineralogical and petrological study of the Ortosa Au–Bi–Te ore deposit: a reduced gold skarn in the northern part of the Rıo Narcea Gold Belt, Asturias, Spain. Journal of Geochemical Exploration, 71, 177-190.

Gabriel, K.R. 1971. The biplot graphical display of matrics with application to principal component analysis. Biometrika, 58, 453-467.

Garofalo, P. S.and Ridley, J. R. 2014. Gold-Transporting Hydrothermal Fluids in the Earth's Crust. Geological Society, London, Special Publications, 402, http://dx.doi.org/10.1144/SP402.9.

Gas'kov, IV. 2017. Major impurity elements in native gold and their association with gold mineralization settings in deposits of Asian folded areas. Russ GeolGeophys, 58, 1080-1092.

Gebre-Mariam, M., Hagemann, S.G., and Groves, D.I., 1995, A classification scheme for epigenetic Archean lode-gold deposits: Mineralium Deposita, 30, 408-410.

Goinhas, J. 1985. A prospeção mineira em Portugal. Áreas Potenciais de aplicação dos projectos. Direção Geral de Geologia e Minas. Boletim e Minas. 22 (1) (in portuguese).

Goldfarb, R. J. and Groves, D. I. 2015. Orogenic gold: Common or evolving fluid and metal sources through time. Lithos, 233, 2-26. http://dx.doi.org/10.1016/j.lithos.2015.07.011.

Goldfarb, R.J. and Santosh, M. 2014. The dilemma of the Jiaodong gold deposits: are they unique? Geoscience Frontiers, 5, 139-153.

Goldfarb, R.J., Baker, T., Dube, B., Groves, D.I., Hart, C.J., Gosselin, P. 2005. Distribution, character and genesis of gold deposits in metamorphic terranes. In: Hedenquist, J.W., Thompson, J.F.H., Goldfarb, R.J., Richards, J.P. (Eds.), Economic Geology 100th Anniversary Volume, pp. 407-450.

Goldfarb, R.J., Berger, B.R., George, M.W., and Seal, R.R., II. 2017. Tellurium, chap. R of Schulz, K.J., DeYoung, J.H., Jr., Seal, R.R., II, and Bradley, D.C., eds., Critical mineral resources of the United States—Economic and environmental geology and prospects for future supply: U.S. Geological Survey Professional Paper 1802, p. R1–R27, https://doi.org/10.3133/pp1802R.

Goldfarb, R.J., Groves, D.I., Gardoll, S. 2001. Orogenic gold and geologic time; a global synthesis. Ore Geology Reviews, 18, 1-2, 1-75. https://doi.org/10.1016/S0169-1368(01)00016-6.

Gómez-Fernández, F., Vindel, E., Martín-Crespo, T., Sánchez, V., González Clavijo, E. andMatías, R. 2012. The Llamas de Cabrera gold district, a new discovery in the Variscan basement of northwest Spain: a fluid inclusion and stable isotope study. Ore Geology Reviews, 46, 68–82, https:// doi.org/10.1016/j.oregeorev.2012.02.001.

Gonçalves, A., Sant'Ovaia, H., Noronha, F. 2020. Geochemical Signature and Magnetic Fabric of Capinha Massif (Fundão, Central Portugal): Genesis, Emplacement and Relation with W-Sn Mineralizations. Minerals 10, 6. https://doi.org/10.3390/min10060557.

González-Clavijo, E., Díez-Balda, M. A., Alvarez, F. 1993. Structural study of a semi-ductile strike-slip system in the Central Iberian Zone (Variscan fold belt, Spain): Structural controls on gold deposits. Geologische Rundschau, 82, 448-460.

Groves, D. I. and Santosh, M. 2015. Province-scale commonalities of some world-class gold deposits: Implications for mineral exploration. Geoscience Frontiers, 6, 389-399. http://dx.doi.org/10.1016/j.gsf.2014.12.007.

Groves, D. I., Goldfarb, R. J., Gebre-Mariam, M., Hagemann, S. G., and Robert, F. 1998. Orogenic gold deposits: a proposed classification in the context of their crustal distribution and relationship to other gold deposit types. Ore Geology Reviews, 13, 1–5, 7–27.

Groves, D., Santosh, M., Zhang, L. 2020. A scale-integrated exploration model for orogenic gold deposits based on a mineral system approach. Geoscience Frontiers, 11, 719–738. https://doi.org/10.1016/j.gsf.2019.12.007.

Groves, D.I. 1993. The crustal continuum model for late-Archaean lode gold deposits of the Yilgarn block, Western Australia. Mineralium Deposita, 28, 366–374.

Groves, D.I., Santosh, M., Goldfarb, R.J., Zhang, L., 2018. Structural geometry of orogenic gold deposits: implications for exploration of world-class and giant deposits. Geoscience Frontiers, 9, 1163-1177.

Grunsky, E. C. 2010.The interpretation of geochemical survey data. Geochemistry: Exploration, Environment Analysis,10, 27–74. DOI 10.1144/1467-7873/09-210.

Grunsky, E.C. 2001. A program for computing R-Q-mode principal components analysis for S-Plus and R. Computers & Geosciences, 27, 229–235.

Grunsky, E.C., Caritat, P. 2020. State-of-the-art analysis of geochemical data for mineral exploration Geochem. Explor. Environ. Anal., 20 (2), pp. 217-232. http://dx.doi.org/10.1144/geochem2019-031.

Grunsky, E.C., Mueller, U.A., & Corrigan, D. 2014. A study of the lake sediment geochemistry of the Melville Peninsular using multivariate methods: Applications for predictive geological mapping. Journal of Geochemical Exploration, 141, 15-41.

Gutiérrez-Alonso, G. 1996. Strain partitioning in the footwall of the Somiedo Nappe: Structural evolution of the Narcea Tectonic window, NW Spain, Journal of Structural Geology, 18, 1217-1229.

Gutiérrez-Alonso, G., Collins, A.S., Fernández-Suárez, J., Pastor-Galán, D., González-Clavijo, E., Jourdan, F., Weil, A.B., and Johnston, S.T. 2015. Dating of lithospheric buckling:

40Ar/39Ar ages of syn-orocline strike-slip shear zones in northwestern Iberia: Tectonophysics, 643, 44-54, https://doi.org/10.101/j.tecto.2014.12.009.

Gutiérrez-Alonso, G., Fernández-Suárez, J., and Weil, A.B. 2004, Orocline triggered lithospheric delamination, in Sussman, A.J., and Weil, A.B., eds., Orogenic curvature: Integrating paleomagnetic and structural analyses: Geological Society of America Special Paper 383, 121-130, https://doi.org /10.1130 /0 -8137-2383-3.

Gutiérrez-Alonso, G., Fernández-Suárez, J., Jeffries, T.E., Johnston, S.T., Pastor-Galán, D., Murphy, J.B., Franco, M.P., and Gonzalo, J.C., 2011, Diachronous post-orogenic magmatism within a developing orocline in Iberia, European Variscides: Tectonics, 30, 1–17, https://doi.org/10.1029/2010TC002845.

Gutiérrez-Alonso, G., Fernández-Suárez, J., López-Carmona, A. and Gärtner, A. 2018. Exhuming a cold case: The early granodiorites of the northwest Iberian Variscan belt-A Visean magmatic flare-up?, Lithosphere, 10, 2, 194-216, doi:10.1130/L706.1.

Gutiérrez-Alonso, G., Murphy, J.B., Fernández-Suárez, J., and Hamilton, M.A., 2008, Rifting along the northern Gondwana margin and the evolution of the Rheic Ocean: A Devonian age for the El Castillo volcanic rocks (Salamanca, Central Iberian Zone): Tectonophysics, 461, 157–165, https:/doi.org/10.1016/j.tecto.2008.01.013.

Gutiérrez-Marco, J. C., Piçarra, J. M., Meireles, C. A., Cózar, P., García-Bellido, D. C., Pereira, Z., Vaz, N., Pereira, S., Lopes, G., Oliveira, J. T., Quesada, C., Zamora, S., Esteve, J., Colmenar, J., Bernárdez, E., Coronado, I., Lorenzo, S., Sá, A. A., Dias da Silva, Í., González-Clavijo, E., Díez-Montes, A., and Gómez- Barreiro, J. 2019. Early Ordovician–Devonian Passive Margin Stage in the Gondwanan Units of the Iberian Massif, in: The Geology of Iberia: A Geodynamic Approach, edited by: Quesada, C. and Oliveira, J. T., 75–98, Springer International Publishing, Cham.

Gutiérrez-Marco, J. C., Sá, A. A., García-Bellido, D. C., and Rábano, I. 2017.The Bohemo-Iberian regional chronostratigraphical scale for the Ordovician System and palaeontological correlations within South Gondwana, Lethaia, 50, 258–295, https://doi.org/10.1111/let.12197.

Hart, C. J. 2007. Reduced intrusion-related gold systems. Mineral Deposits of Canada: A synthesis of Major deposit types, district metallogeny, the Evolution of geological provinces, and exploration methods: Geological Association of Canada, Mineral Deposits Division, Special Publication, 95-112.

Hart, C.J., and Goldfarb, R. 2005. Distinguishing intrusion-related from orogenic gold systems, New Zealand Minerals Conference Proceedings, pp. 125-133.

Hildenbrand, A., Marques, F.O., Quidelleur, X., Noronha, F. 2021. Exhumation history of the Variscan orogen in western Iberia as inferred from new K-Ar and 40Ar/39Ar data on

granites from Portugal. Tectonophysics 812, 28863, https://doi.org/10.1016/j.tecto.2021.228863.

Hoefs, J. 2018. Stable isotope geochemistry, 8th edition. Springer, Berlin, p 437. https://doi.org/10.1007/978-3-319-78527-1.

Hough, M, R, Charles R. M. Butt, Jörg Fischer-Bühner. 2009. The Crystallography, Metallography and Composition of Gold. Elements; 5, 5, 297–302. doi: https://doi.org/10.2113/gselements.5.5.297.

Hron, K., Templ. M., Filzmoser, P. 2010. Imputation of missing values for compositional data using classical and robust methods. Computational Statistics & Data Analysis, 54, 12, 1, 3095-3107. https://doi.org/10.1016/j.csda.2009.11.023.

IGME. Instituto Geológico y Minero de España: http://info.igme.es/catalogo/catalog.aspx?catalog=2&shim=true&shdt=false&shtb=true&shtp=false&shfp=false&shsf=false&shfo=false&master=infoigme&lang=por&intranet=false

Inverno, C. M. C. 2002. Primary gold deposits in Portugal - “mesothermal” or epithermal? Comunicações do Instituto Geológico e Mineiro. 89: 53-58.

Ishihara S, Sasaki A. 1989. Sulfur isotopic ratios of the magnetite-series and ilmenite-series granitoids of the Sierra Nevada batholith – a reconnaissance study. Geology, 17, 788-791

Iyer, S. S., 1992. Sulfur and lead isotope geochemistry of galenas from the Bambui group, mines gerais-implications for ore genesis. Economic Geology, 87, 437-443. https://doi.org/10.2113/gsecongeo.87.2.437.

Jolliffe, I. T., and Cadima, J. 2016. Principal component analysis: a review and recent developments. Philosophical transactions. Series A, Mathematical, physical, and engineering sciences, 374(2065), 20150202. https://doi.org/10.1098/rsta.2015.0202.

Julivert, M., Fontboté, J. M., Ribeiro, A., and Nabais Conde, L. E. 1974. Mapa Tectónico de la Península Ibérica y Baleares E: 1: 1.000.000 y memoria explicativa, Publ IGME, Madrid, 113, 1974.

K. dos Santos Alves, Santos Barrios Sánchez, Juan Gómez Barreiro, Raúl Merinero Palomares, José Manuel Compaña Prieto. 2020. Morphological and compositional analysis of alluvial gold: The Fresnedoso gold placer (Spain). Ore Geology Reviews, 121, 103489. https://doi.org/10.1016/j.oregeorev.2020.103489.

Kerrich, R., Goldfarb, R.J., Richards, J. 2005. Metallogenic provinces in an evolving geodynamic framework. Economic Geology 100th Anniversary, 1097–1136.

Klovan, J.E., and Imbrie, J. 1971. An algorithm and Fortran IV Program for large-scale Q–Mode Factor Analysis and Calculation of Factor Scores. Mathematical Geology. 3:61-67.

Knight, J.B., Morison, S.R., Mortensen, J.K. 1999. The relationship between placer gold particle shape, rimming, and distance of fluvial transport as exemplified by gold from the Klondike district, Yukon Territory. Canada. Economic Geology, 94, 5, 635–648. http://dx.doi.org/10.2113/gsecongeo.94.5.635.

Kolb, J., Dziggel, A., Bagas, L. 2015. Hypozonal lode gold deposits: a genetic concept based on a review of the New Consort, Hutti, Hira Buddini, Navachab, Nevoria, and The Granites deposits. Precambrian Research, 262, 20–44.

Kolb, J., Meyer, M.F., 2002. Fluid inclusion record of the hypozonal orogenic Renco gold deposit (Zimbabwe) during the retrograde P–T evolution. Contributions to Mineralogy and Petrology, 143, 495–509.

Kolb, J., Rogers, A., Meyer, F.M., 2005. Relative timing of deformation and two-stage gold mineralization at Hutti mine, Dharwar Craton, India. Mineralium Deposita, 40, 156-174.

Korolev, I., Altınkaya, P., Halli, P., Hannula, P-M., Yliniemi, K., Lundström, M. 2018. Electrochemical recovery of minor concentrations of gold from cyanide-free cupric chloride leaching solutions. Journal of Cleaner Production, 186, 840-850. https://doi.org/10.1016/j.jclepro.2018.03.177.

Kranidiotis, P., MacLean, W. 1987. Systematic of of chlorite alteration the Phelps Dodge massive sulfide deposit, Matagami, Quebec. Economic Geology, 82, 1898-1911.

Kretschmar, U. and Scott, S.D., 1976. Phase relations involving arsenopyrite in the system Fe-As-S and their application. Canadian Journal of Earth Sciences, 14, 364-386.

Kretz, R. 1983. Symbols of rock-forming minerals. American Mineralogist, 68, 277-279.

Kroner, U. and Romer, R.L., 2013. Two plates - Many subduction zones: The Variscan orogeny reconsidered. Gondwana Research, 24, 298-329. https://doi.org/10.1016/j.gr.2013.03.001.

Kroner, U., Roscher, M., Romer, R.L. 2016. Ancient plate kinematics derived from the deformation pattern of continental crust: Paleo- and Neo-Tethys opening coeval with prolonged Gondwana–Laurussia convergence. Tectonophysics, 681, 220-233 pp. https://doi.org/10.1016/j.tecto.2016.03.034.

Lang, J.R., and Baker, T. 2001. Intrusion-related gold systems: the present level of understanding: Mineralium Deposita, 36, 477-489.

Lang, J.R., Baker, T., Hart, C., and Mortensen, J.K. 2000. An exploration model for intrusion-related gold systems: Society of Economic Geologists Newsletter, 40, 1, 6-14.

Leake, R.C., Chapman, R.J., Bland, D.J., Condliffe, E., and Styles, M.T. 1997. Microchemical characterization of gold from Scotland: Transactions of the Institution of Mining and Metallurgy, Section B: Applied Earth Science, 106, 85-98.

Leal, S., Lima, A., Noronha, F. 2019. Mineralogia e temperatura de formação das mineralizações auríferas de Bigorne, Norte de Portugal. XII Congresso Ibérico de Geoquímica (CIG), Évora. 247-250pp.

Leal, S., Lima, A., Noronha, F. 2021. Characterization of heavy mineral concentrates and detrital gold particles from the Bigorne granite-hosted gold deposit in the Iberian Variscan Belt. From: Torvela, T., Lambert-Smith, J. S. and Chapman, R. J. (eds) Recent Advances in Understanding Gold Deposits: from Orogeny to Alluvium. Geological Society, London, Special Publications, 516, https://doi.org/10.1144/SP516-2020-217.

Lima, A., Leal, S., Moura, R., Pivtorak, A., Sant'Ovaia, H., Baptista, A., Santos, P. And Mortensen, J., 2018, Gold exploration. In Lahtinen, T., Pasanen, A., Turunen, K., Lima, A., Fiúza, A., Szlachta, M., Wójtowicz, P., Maftei, R., Baciu, C. and Nieminen, S. (eds.), 2018. Tools for Sustainable Gold Mining in Europe – Final report of SUSMIN project. Report /ERA-MIN – SUSMIN Final Report, Geological Survey of Finland, 22 pages.

Lindgren, W. 1933. Mineral deposits, 4th edn, McGraw-Hill, New York.

López-Carmona, A., Abati, J., Pitra, P., and Lee, J.K.W., 2014, Retrogressed lawsonite blueschists from the NW Iberian Massif: P–T–t constraints from thermodynamic modelling and 40Ar/39Ar geochronology: Contributions to Mineralogy and Petrology, 167, 987, https://doi.org/10.1007/s00410-014-0987-5.

López-Moro, F. J., López-Plaza, M., Gutiérrez-Alonso, G.,Fernández-Suárez, J., López-Carmona, A., Hofmann, M., and Romer, R. L. 2018. Crustal melting and recycling: geochronology and sources of Variscan syn-kinematic anatectic granitoids of the Tormes Dome (Central Iberian Zone). A U-Pb LA-ICP-MS study, International Journal of Earth Sciences, 107, 985-1004, https://doi.org/10.1007/s00531-017-1483-8.

López-Moro, F.J., Romer, R.L., Rhede, D. et al., 2019. Early uranium mobilization in late Variscan strike-slip shear zones affecting leucogranites of central western Spain. Journal of Iberian Geology, 45, 223–243. https://doi.org/10.1007/s41513-018-0091-1.

Lotze, F., 1945. Zur Gliederung der Varisziden der Iberischen Meseta. Geotekt Forsch 6, 78–92.

Macdonald, E. 2007. Handbook of Gold Exploration and Evaluation; Elsevier: Cambridge, UK; p. 630. ISBN 978-1-84569-175-2.

MacKenzie, D. Craw, D. Mortensen, J.K. 2019. Orogenic gold deposits in the Variscan belt in northwestern Iberia. Proceedings of the 15th SGA Biennial Meeting, 27-30 August 2019, Glasgow, Scotland, pages 736-738.

MacKenzie, D., Farmer, L., Moore, J., Craw, D. 2017. Contrasting coeval paragenesis of gold and scheelite in an orogenic hydrothermal system, Macraes mine, New Zealand. Ore Geology Reviews, 80, 645-657, https://doi.org/10.1016/j.oregeorev.2016.08.011.

Marcos, A. and Pulgar, J. A. A. 1982. An Approach to the tectonostratigraphic evolution of the Cantabrian foreland thrust and fold belt, Hercynian Cordillera of NW Spain, Neues Jahrb. Geol. P.-A., 163, 256-260.

Marignac, C., Cuney, M., 1999. Ore deposits of the French Massif Central: insight into the metallogenesis of the Variscan collision belt. Mineralium Deposita, 34, 472-504.

Marques, F.O., Mateus, A., Tassinari, C. 2002. The Late-Variscan fault network in central-northern Portugal (NW Iberia): a re-evaluation. Tectonophysics, 359 (3-4): 255-270. https://doi.org/10.1016/S0040-1951(02)00514-0.

Martínez Catalán, J. R., Gómez Barreiro, J., Dias da Silva, Í., Chichorro, M., López-Carmona, A., Castiñeiras, P., Abati, J., Andonaegui, P., Fernández-Suárez, J., González Cuadra, P., and Benítez-Pérez, J. M. 2019. Variscan Suture Zone and Suspect Terranes in the NW Iberian Massif: Allochthonous Complexes of the Galicia-Trás os Montes Zone (NW Iberia), in: The Geology of Iberia: A Geodynamic Approach, edited by: Quesada, C. and Oliveira, J. T., 99-130, Springer International Publishing, Cham.

Martínez Catalán, J. R., Rubio Pascual, F. J., Diez Montes, A., Diez Fernandez, R., Gomez Barreiro, J., Dias da Silva, I., Gonzalez Clavijo, E., Ayarza, P., and Alcock, J. E. 2014. The late VariscanHT/LP metamorphic event in NW and Central Iberia: relationships to crustal thickening, extension, orocline development and crustal evolution, Geological Society of London Special Publication, 405, 225–247, https://doi.org/10.1144/SP405.1.

Martínez Catalán, J.R., Arenas, R., Díaz García, F., González Cuadra, P., Gómez Barreiro, J., Abati, J., Castiñeiras, P., Fernández-Suárez, J., Sánchez Martínez, S., Andonaegui, P., González Clavijo, E., Díez Montes, A., Rubio Pascual, F., and Valle Aguado, B., 2007. Space and time in the tectonic evolution of the northwestern Iberian Massif: Implicationsfor the Variscan belt, in Hatcher, R.D., Jr., Carlson, M.P., McBride, J.H., and Martínez Catalán, J.R. eds., 4-D framework of continental crust, Boulder, Geologic Society of America, p. 403–423. doi:10.1130/2007.1200(21).

Martínez-Catalán, J. R. 2011. Are the oroclines of the Variscan belt related to late Variscan strike-slip tectonics? Terra Nova, 23, 4, 241-247.

Martın-Izard, A., Fuertes-Fuente, M., Cepedal, A., Moreiras, D., García-Nieto, J., Maldonado, C., Pevida, L.R., 2000. The Río Narcea Gold Belt intrusions: geology, petrology, geochemistry and timing. Journal of Geochemical Exploration, 71, 103-117.

Martins, H., Sant´Ovaia, H. Noronha, F. 2013. Late-Variscan emplacement and genesis of the Vieira do Minho composite pluton, Central Iberian Zone: Constraints from U–Pb zircon geochronology, AMS data and Sr–Nd–O isotope geochemistry. Lithos, 162-163, 221–235. https://doi.org/10.1016/j.lithos.2013.01.001.

Martins, H.C.B., Sant'Ovaia, H., Noronha, F., 2009. Genesis and emplacement of felsic Variscan plutons within a deep crustal lineation, the Penacova-Régua-Verín fault: an integrated geophysics and geochemical study (NW Iberian Peninsula). Lithos, 111 (3–4), 142–155. https://doi.org/10.1016/j.lithos.2008.10.018.

Martins, L. P. 2012. Mineral Resources of Portugal., Direcção Geral de Energia e Geologia Lisbon, 71 pp.

Mateus A. 1997. Condições de deposição hidrotermal de ligas de ouro e prata em desligamentos tardi-hercínicos: o Troço Transmontano da Falha Manteigas-Vilariça-Bragança como exemplo. X Semana de Geoquímica - IV Congresso de Geoquímica dos Países de Língua Portuguesa, Braga (Portugal): 203-206.

Mateus A. and Barriga F.J.A.S. 1991. Gold-silver mineralizations associated with the Vilariça Fault, NE Portugal. Brazil Gold'91, E.A. Ladeira (ed.), Balkema, Rotterdam: 615-622.

Mateus, A and Noronha, F. 2001. Late-variscan crustal uplift of the Iberian terrane as a response to isostatic rebound; implications for the brittle-ductile transition, fluid circulation and metallogenesis. XVI ECROFI European Current Research On Fluid Inclusions, Porto 2001. Abstracts (Eds F. Noronha, A. Dória and A. Guedes). Faculdade de Ciências do Porto, Departamento de Geologia, Memória nº 7, pp. 295-298.

Matsuhisa Y., Goldsmith J. R., Clayton R. N. 1979. Oxygen isotopic fractionation in the system quartz-albite-anorthite-water. Geochimica et Cosmochimica Acta, 43, 1131-1140.

Matte, P. 2003. The Variscan collage and orogeny (480–290 Ma) and the tectonic definition of the Armorica microplate: a review - Matt(E) 2003 - Terra Nova - Wiley Online Library. Terra Nov. 13, 122-128.

McCaig, A. M. 1988. Deep fluid circulation in fault zones. Geology, 16, 867–870.

McCoy, D., Newberry, R.J., Layer, P.W., DiMarchi, J.J., Bakke, A.A., Masterman, J.S., Minehane, D.L. 1997. Plutonic-related gold deposits of interior Alaska: Economic Geology, Monograph 9, p. 191-241.

McCuaig, T. and Kerrich, R. 1998. P-T-t-deformation-fluid characteristics of lode gold deposits: evidence from alteration systematics. Ore Geology Reviews, 12, 381–453.

McCuaig TC, Hronsky JMA .2014. The mineral system concept: the key to exploration targeting. SEG 2014: Building Exploration Capability for the 21st Century, pp 153–75

Middlemost, EAK. 1994. Naming materials in the magma/igneous rock system. Earth-Science Reviews, 37, 215-224. https://doi.org/10.1016/0012-8252(94)90029-9.

Moles, N. R., Chapman, R. J., Warner, R. B. 2013. The significance of copper concentrations in natural gold alloy for reconnaissance exploration and understanding gold-depositing

hydrothermal systems. Geochemistry: Exploration, Environment, Analysis, 13, 2, 115–130. doi: https://doi.org/10.1144/geochem2011-114.

Moles, N.R. and Chapman, R.J. 2019. Integration of Detrital Gold Microchemistry, Heavy Mineral Distribution, and Sediment Geochemistry to Clarify Regional Metallogeny in Glaciated Terrains: Application in the Caledonides of Southeast Ireland. Economic Geology, 114, 2, pp. 207–232. doi: 10.5382/econgeo.2019.4628.

Moreira, N., Búrcio, M., Dias, R., and Coke, C. 2010. Partição da deformação Varisca nos sectores de Peso da Régua e Vila Nova de Foz Côa (Autóctone da Zona Centro Ibérica): Comunicações Geológicas, 97, 147–162.

Morrison, G. W., Rose, W. J., & Jaireth, S. 1991. Geological and geochemical controls on the silver content (fineness) of gold in gold-silver deposits. Ore Geology Reviews, 6, 4, 333–364. doi:10.1016/0169-1368(91)90009-v.

Mortensen, J.K., Craw, D., MacKenzie, D., Allan, M., Chapman, R.J. 2019. Concepts and revised models for Phanerozoic orogenic gold deposits. Proceedings of the 15th SGA Biennial Meeting, 27-30 August 2019, Glasgow, Scotland, pages 731-732.

Moura, A., Dória, A., Neiva, A.M.R., Leal Gomes, C., Creaser, R.A., 2014.Metallogenesis at the Carris W-Mo-Sn deposit (Gerês, Portugal): Constraintsfrom fluid inclusions, mineral geochemistry, Re-Os and He-Ar isotopes. Ore Geology Reviews, 56:73–93.

Murphy, J. B., Gutierrez-Alonso, G., Fernandez-Suarez, J., and Braid, J. A. 2008. Probing crustal and mantle lithosphere origin through Ordovician volcanic rocks along the Iberian passive margin of Gondwana, Tectonophysics, 461, 166–180.

Murphy, J. B., Quesada, C., Gutiérrez-Alonso, G., Johnston, S. T., and Weil, A. 2016. Reconciling competing models for the tectonostratigraphic zonation of the Variscan orogen inWestern Europe, Tectonophysics, 681, 209–219.

Nance, R.D., Gutiérrez-Alonso, G., Keppie, J.D., Linnemann, U., Murphy, J.B., Quesada, C., Strachan, R.A., Woodcock, N.H. 2010. Evolution of the Rheic Ocean. Gondwana Research, 17, 194–222. https://doi.org/10.1016/j.gr.2009.08.001.

Neff, H. 1994. RQ-mode principal components analysis of ceramic compositional data. Archaeometry 36:115-130.

Neiva, A. M. R., Andráš, P., Ramos, J. M. F. 2008. Antimony quartz and antimony–gold quartz veins from northern Portugal. Ore Geology Reviews, 34: 533-546.

Neiva, A. M. R., Moura, A., Leal Gomes, C. A., Pereira, M. F., Corfu, F. 2019. The granite hosted Variscan gold deposit from Santo António mine in the Iberian Massif (Penedono, NW Portugal): constraints from mineral chemistry, fluid inclusions, sulfur and noble gases

isotopes. Journal of Iberian Geology, 45, 443-469. https://doi.org/10.1007/s41513-019-00103-1.

Neiva, A.M.R. 1992. Geochemistry and evolution of Jales granitic system, northern Portugal. Chem. Erde. 52, 225–241.

Neiva, A.M.R., Williams, I.S., Lima, S.M., Teixeira, R.J.S. 2012. U–Pb and 39Ar/40Ar data constraining the ages of the source, emplacement and recrystallization/cooling events from late- to post-D3 Variscan granites of the Gouveia area, central Portugal. Lithos, 153, 72–83.

Neiva, M.C. 1945. Alguns jazigos de ouro do alto Minho. Estudos Notas e Trabalhos, 1 (3/4), 190–265.

Newberry, R.J., McCoy, D.T., and Brew, D.A. 1995. Plutonic-hosted gold ores in Alaska: Igneous versus metamorphic origins: Resource Geology, Special Issue 18, p. 57–100.

Nogueira, P. 1997. Estudo de paleofluidos mineralizantes (Au, Ag, As) e sua migração. Aplicação a regiões auríferas do Norte de Portugal. PhD thesis, Universidade do Porto, Portugal.

Noronha, F., Cathelineau, M., Boiron, M.-C., Banks, D. A., Dória, A., Ribeiro, M. A., Nogueira, P., Guedes, A. 2000. A three stage fluid flow model for Variscan gold metallogenesis in northern Portugal. Journal of Geochemical Exploration, 71, 2, 209-224. https://doi.org/10.1016/S0375-6742(00)00153-9.

Noronha, F., Dória, A., Boiron, M.C., Cathelineau, M. 1993. Geochemical characterisation of the fluids from a gold bearing metamorphic area in north Portugal. Metamorph. Fluids Miner. Deposits 39/40, 291.

Noronha, F., Ramos, J.M.F. 1993. Mineralizações auríferas primárias do Norte de Portugal, Algumas reflexões. Cuard. Lab. Xeoloxico de Laxe. 18, 133–146.

Noronha, F., Ramos, J.M.F., Rebelo, J. A., Ribeiro, A., Ribeiro, M. L. 1978. Essai de corrélation des phases de déformation hercynienne dans le Nord-Ouest péninsulaire. Boletim da Sociedade Geológica de Portugal 21:227–237.

Noronha. F. 1976. Niveaux à scheelite dans la zone tungstifére de Borralha. Leur importance metallogénique. Publicações do Museu e Laboratório Mineralógico e Geológico. Faculdade de Ciências da Universidade do Porto, 4º Série, 87, 15 p.

Ohmoto, H. and Goldhaber, M. B. 1997. Sulfur and carbon isotopes. In: Geochemistry of Hydrothermal Ore Deposits. Barnes HL (ed) J Wiley and Sons, p 517-611.

Okamoto, K. and Masaalski, T. B. 1983. Au–Bi (gold–bismuth). In: Massalski TB et al., (eds) Binary alloy phase diagrams, vol 1: Ac–Au to Fe–Rh. Ohio, ASM International, Materials Park, Ohio, pp 238–240.

Okamoto, K. and Tanner, L.E. 1990. Bi–Te (bismuth–tellurium) TB Massalski K Ohamoto (Eds) Binary alloy phase diagrams ASM International, Materials Park Ohio 800–801

Oliveira A., Martins H., Sant'Ovaia H. 2020. Insights into the felsic vein magmatism in northern Portugal (central Iberian zone): An integrated geochemical and petrophysical study. International Multidisciplinary Scientific GeoConference Surveying Geology and Mining Ecology Management, SGEM, Issue 1.1, Pages 139-146.

Oliveira, A. 2017. Magmatismo tardi-Varisco na região do Minho. Tese de mestrado (Master thesis - unpublished). Faculdade de Ciências da Universidade do Porto. 98pp. (in portuguese).

Oliveira, J. T., Quesada, C., Pereira, Z., Matos, J. X., Solá, A. R., Rosa, D., Albardeiro, L., Díez-Montes, A., Morais, I., Inverno, C., Rosa, C., and Relvas, J. 2019. South Portuguese Terrane: A Continental Affinity Exotic Unit, in The Geology of Iberia: A Geodynamic Approach, edited by: Quesada, C. and Oliveira, J. T., 173–206, Springer International Publishing, Cham.

Oliveira. J. T., et al., 1992. O Paleozóico Inferior de Portugal: síntese da estratigrafia e da evolução paleogeográfica. In: Gutiérrez-Marco, J.C., Saavedra, J. & Rábano, I. (eds.). Paleozóico Inferior de Ibero-América, Universidad de Extremadura, Badajoz, 359-375.

Pastor-Galán, D., Gutiérrez-Alonso, G., Fernández-Suárez, J., Murphy, J. B., Nieto, F. 2013. Tectonic evolution of NW Iberia during the Paleozoic inferred from the geochemical record of detrital rocks in the Cantabrian Zone, Lithos, 182–183, 221–228, https://doi.org/10.1016/j.lithos.2013.09.007.

Pastor-Galán, D., Gutiérrez-Alonso, G., Weil, A. B. 2020.The enigmatic curvature of Central Iberia and its puzzling kinematics. Solid Earth, 11, 1247–1273. https://doi.org/10.5194/se-11-1247-2020.

Pastor-Galán, D., Gutiérrez-Alonso, G., Zulauf, G., Zanella, F. 2012. Analogue modeling of lithospheric-scale orocline buckling: Constraints on the evolution of the Iberian-Armorican Arc. GSA Bulletin, 124 (7-8): 1293–1309. doi: https://doi.org/10.1130/B30640.1.

Pawlowsky-Glahn V, Egozcue JJ, Tolosana-Delgado R. 2015. Modelling and analysis of compositional data. John Wiley & Sons, Ltd, Chichester. https://doi.org/10.1002/9781119003144.

Pellitero, E. 1980. Caracteres petrogeneticos y metalogeneticos de los yacimientos de wolframio de la provincia de Salamana. Ph.D. thesis, Facultad de Ciencias, Universidad de Salamanca.

Pereira, E., Ribeiro, A., Meireles, C., 1993. Cisalhamentos hercínicos e controlo das mineralizações de Sn-W, Au e U na Zona Centro-Ibérica, em Portugal. Cuadernos Laboratório Xeolóxico Laxe 18, 89–119. (in portuguese)

Pereira, M. F., Chichorro, M., Silva, J. B., Ordóñez-Casado, B., Lee, J. K. W. W., and Williams, I. S. 2012. Early carboniferous wrenching, exhumation of high-grade metamorphic rocks and basin instability in SW Iberia: Constraints derived from structural geology and U–Pb and 40Ar–39Ar geochronology, Tectonophysics, 558, 28–44, https://doi.org/10.1016/j.tecto.2012.06.020.

Pereira, M. F., Díez Fernández, R., Gama, C., Hofmann, M., Gärtner, A., Linnemann, U. 2018. S-type granite generation and emplacement during a regional switch from extensional to contractional deformation (Central Iberian Zone, Iberian autochthonous domain, Variscan Orogeny), International Journal of Earth Sciences, 107, 251–267. https://doi.org/10.1007/s00531-017-1488-3.

Pérez-Cáceres, I., Simancas, J. F., Martínez Poyatos, D., Azor, A., González Lodeiro, F. 2016. Oblique collision and deformation partitioning in the SW Iberian Variscides, Solid Earth, 7, 857–872, https://doi.org/10.5194/se-7-857-2016.

Pérez-Estaún, A., Bastida, F., Alonso, J. L., Marquinez, J., Aller, J., Alvarezmarron, J., Marcos, A., and Pulgar, J. A. 1988. A thinskinned tectonics model for an arcuate fold and thrust belt – the Cantabrian Zone (Variscan Ibero–Armorican Arc), Tectonics, 7, 517–537.

Phillips, G.N. and Powell, R. 2009. Formation of gold deposits review and evaluation of the continuum model. Earth-Science Reviews 94, 1-21.

Phillips, G.N. and Powell, R. 2015. A practical classification of gold deposits, with a theoretical basis. Ore Geology Reviews, 65, 568–573. http://dx.doi.org/10.1016/j.oregeorev.2014.04.006.

Pirajno, F. and Bentley, P.N. 1985. Greisen-related scheelite, gold and sulphide mineralization at Kirwans Hill and Bateman Creek, Reefton District, New Zealand, New Zealand Journal of Geology and Geophysics, 28: 97-109. https://doi.org/10.1080/00288306.1985.10422279.

Pohl, W. and Belocky, R. 1994. Alpidie Metamorphic Fluids and Metallogenesis in the Eastern Alps, Mitteilungen der Osterreichischen Geologisehen Gesellschaft 86, 141-152.

Pohl, W. and Belocky, R. 1999. Metamorphism and metallogeny in the Eastern Alps, Mineralium Deposita 34, 614-629.

Pokrovski, G. S., Akinfiev, N. N., Borisova, A. Y., Zotov, A. V., Kouzmanov, K. 2014. Gold speciation and transport in geological fluids: insights from experiments and physical-chemical modelling. In Gold-Transporting Hydrothermal Fluids in the Earth's Crust, Geological Society of London, Special Publications, (eds) Garofalo P. S., Ridley J. R. 2014, 402, http://dx.doi.org/10.1144/SP402.4.

Pokrovski, G.S., Kara, S., Roux, J. 2002. Stability and solubility of arsenopyrite, FeAsS, in crustal fluids. Geochimica et Cosmochimica Acta, 66 (13), 2361–2378. https://doi.org/10.1016/S0016-7037(02)00836-0.

Politano, A., Caputo, M., Nappini, S., Bondino, F., Magnano, E., Aliev, Z.S., Chulkov, E.V. 2014. Exploring the surface chemical reactivity of single crystals of binary and ternary bismuth chalcogenides. The Journal of Physical Chemistry C, 118, 37, 21517-21522. https://doi.org/10.1021/jp506444f.

Poulsen, K.H., Robert, F., Dubé, B. 2000. Geological classification of Canadian gold deposits: Geological Survey of Canada Bulletin 540.

Quesada, C. 2006. The Ossa-Morena Zone of the Iberian Massif: a tectonostratigraphic approach to its evolution, Z. Dtsch. Ges. Geowiss., 157, 585–595, https://doi.org/10.1127/1860-1804/2006/0157-0585.

REFLEX, 2019. ioGAS™ 7.0., IMDEX limited [computer software] https://reflexnow.com/iogas/.

Ribeiro, A., 1974. Contribution à l'Étude de Trás-os-Montes Oriental. Mem. Serv. Geol. Portug., 24, 168 pp. (in portuguese)

Ribeiro, A., Antunes, M.T., Ferreira, M.P., Rocha, R.B., Soares, A.F., Zbyzewski, G., Almeida, F.M., Carvalho, D., Monteiro, J.H. 1979. Introduction a la Géologie Génerale du Portugal Serviços Geológicos de Portugal, Lisboa.

Ribeiro, A., Munhá, J., Dias, R., Mateus, A., Pereira, E., Ribeiro, L., Fonseca, P., Araújo, A., Oliveira, T., Romão, J., Chaminé, H., Coke, C., Pedro, J. 2007. Geodynamic evolution of the SW Europe Variscides. Tectonics 26. https://doi.org/10.1029/2006TC002058.

Ribeiro, A., Pereira, E., Dias, R. 1990. Structure in the northwest of the Iberian Peninsula. In: Dallmeyer, R.D., Martínez Garcia, E. (Ed.), Pre-mesozoic Geology of Iberia. Springer-Verlag, Berlin, Heidelberg, 220-236.

Ribeiro, M. L., Castro, A., Almeida, A., Menéndez, L.G., Jesus, A., Lains, J.A., Lopes, J.C., Martins, H.C.B., Mata, J., Mateus, A., Moita, P., Neiva, A.M.R., Ribeiro, M.A., Santos, J.F., Solá, A.R., 2019. Variscan Magmatism, in: Quesada, C., Oliveira, J.T. (Eds.), The Geology of Iberia: A Geodynamic Approach: Volume 2: The Variscan Cycle. Springer, pp. 497–526. https://doi.org/10.1007/978-3-030-10519-8_13.

Ribeiro, M.A., Dória, A., Noronha, F. 1999. The role of fluid evolution in Au enrichment in Vila Pouca de Aguiar area, Portugal. In: Standley et al., (Eds.), Proceedings of the fifth Biennial SGA and the tenth quadrennial IAGOD symposium “Mineral Deposits: Processes to Processing. London. vol. 2, pp. 1029–1032.

Ridley, J. 1993. The relations between mean rock stress and fluid flow in the crust: With reference to vein- and lode-style gold deposits: Ore Geology Reviews, 8, 23–37, doi:10.1016/0169-1368(93)90026-U.

Ridley, J.R. and Diamond, L.W., 2000. Fluid chemistry of orogenic lode gold deposits and implications for genetic models. Rev. Economic Geology, 13, 141–162.

Rieder, M., Cavazzini, G., D'yakonov, Y.S., Frank-Kamenetskii, V.A., Gottardi, G., Guggenheim, S., Koval', P.V., Mueller, G., Neiva, A.M., Radoslovich, E.W., and Robert, J.L., 1998. Nomenclature of the micas: Clays, Clay Minerals, v. 46, p. 586–595. https://doi.org/10.1346/CCMN.1998.0460513.

Robert F., Brommecker R., Bourne B.T., Dobak P.J., McEwan C.J., Rowe R.R., Zhou X. 2007. Models and exploration methods for major gold deposit types. In: Milereit, B. (Ed.), Proceedings of Exploration '07: Fifth Decennial Conference on Mineral Exploration, 691–711.

Robinson, B.W., and Kusakabe, M. 1975. Quantitative preparation of sulfur dioxide for 34S/32S analyses from sulphides by combustion with cuprous oxide. Analytical Chemistry, 47, 1179-1181.

Rodríguez-Terente, L.M., Martin-Izard, A., Arias, D., Fuertes-Fuente, M., Cepedal, A. 2018. The Salave Mine, a Variscan intrusion-related gold deposit (IRGD) in the NW of Spain: Geological context, hydrothermal alterations and ore features. Journal of Geochemical Exploration, 188, 364–389. https://doi.org/10.1016/j.gexplo.2018.02.011.

Romer, R. L., and Kroner, U. 2018. Paleozoic gold in the Appalachians and Variscides. Ore Geology Reviews, 92, 475–505. https://doi.org/10.1016/j.oregeorev.2017.11.021.

Romer, R.L., Kroner, U., 2016. Phanerozoic tin and tungsten mineralization. Tectonic controls on the distribution of enriched protoliths and heat sources for crustal melting. Gondwana Research, 31, 60-95.

Rosa, D.R.N. 2001. Metallogenesis of the Jales Au District, Northern Portugal (Ph.D. dissertation), Colorado School of Mines (262 pp.).

Rubio Pascual, F. J., Arenas, R., Martínez Catalán, J. R., Rodríguez Fernández, L. R., and Wijbrans, J. R. 2013. Thickening and exhumation of the Variscan roots in the Iberian Central System: Tectonothermal processes and 40Ar=39Ar ages, Tectonophysics, 587, 207–221, https://doi.org/10.1016/j.tecto.2012.10.005.

Rubio Pascual, F. J., López-Carmona, A., Arenas, R. 2016. Thickening vs. extension in the Variscan belt: P–T modelling in the Central Iberian autochthon, Tectonophysics, 681, 144–158, https://doi.org/10.1016/j.tecto.2016.02.033.

Rudnick, R. L. and Gao S. 2014. 4.1 - Composition of the Continental Crust. In: Turekian HD, Holland KK (eds), Treatise on Geochemistry (Second Edition). Elsevier, Oxford, pp. 1-51.

Sant'Ovaia, H., Bouchez, J.L., Noronha, F., Leblanc, D. & Vigneresse, J.L. 2000. Composite laccolith emplacement of the post-tectonic Vila Pouca de Aguiar granite pluton (northern Portugal): a combined AMS and gravity study. Transactions of the Royal Society of Edinburgh Earth Sciences, 91: 123-137.

Sant'Ovaia, H., Olivier, P., Ferreira, N., Noronha, F., Leblanc, D., 2010. Magmatic structures and kinematics emplacement of the Hercynian granites from Central Portugal (Serra da Estrela and Castro Daire areas). Journal of Structural Geology, 32, 10, 1450-1465. https://doi.org/10.1016/j.jsg.2010.09.003.

Santosh, M., Masuda, H.1991. Reconnaissance oxygen and sulfur isotopic mapping of Pan-African alkali granites and syenites in the southern Indian Shield. Geochem J 25:173-185

Sasaki, A. and Ishihara, S .1979. Sulfur isotopic composition of the magnetite-series and ilmenite-series granitoids in Japan. Contributions to Mineralogy and Petrology, 68, 107-115.

Saunders, J.A., Hofstra, A.H., Goldfarb, R.J., Reed, M.H. 2014. 13.15 - Geochemistry of Hydrothermal Gold Deposits. In: Ed: Heinrich D. Holland, Karl K. Turekian, Treatise on Geochemistry (Second Edition), Elsevier, 383-424. https://doi.org/10.1016/B978-0-08-095975-7.01117-7.

Seal, R. R. 2006. Sulfur isotope geochemistry of sulfide minerals. Reviews in Mineralogy & Geochemistry, 61, 1, 633-677. https://doi.org/10.2138/rmg.2006.61.12.

Shand, S.J., 1943. Eruptive Rocks. Their genesis, composition, classification and their relation to ore-deposits with a chapter on Meteorites. New York. John Wiley & Sons.

Sharp, D., Essene, J., Kelly, C., 1985. A re-examination of the arsenopyrite geothermometer; pressure considerations and applications to natural assemblages. Canadian Mineralogist, 23, 4, 517–534.

Shelley D, Bossière G. 2000. A new model for the Hercynian Orogen of Gondwanan France and Iberia. Journal of Structural Geology, 22, 757–776. https://doi.org/10.1016/s0191-8141(00)00007-9.

Sheppard, S.M., 1986. Characterization and isotopic variations in naturalwaters. Reviews in Mineralogy & Geochemistry, 16, 1, 165–183.

Sillitoe R.H. and Thompson J.F.H. 1998. Intrusion-related vein gold deposits: types, tectonomagmatic settings and difficulties of distinction from orogenic gold deposits. Resource Geology, 48, 237–250.

Sillitoe, R., H. 2000. Gold-rich porphyry deposits: descriptive and genetic models and their role in exploration: Society of Economic Geologists Reviews in Economic Geology 13, 315-345.

Sillitoe, R.H. 1991. Intrusion-related gold deposits, in Foster, R.P., ed., Gold metallogeny and exploration: Glasgow, Blackie, p. 165-209.

Sillitoe, R.H., and Thompson, J.F.H. 2006. Changes in mineral exploration practice: consequences for discovery, in Society of Economic Geologists Special Publication 12, 193-219.

Simancas, J.F., 2019. Variscan Cycle BT - The Geology of Iberia: A Geodynamic Approach: Volume 2: The Variscan Cycle, in: Quesada, C., Oliveira, J.T. (Eds.). Springer International Publishing, Cham, pp. 1–25. https://doi.org/10.1007/978-3-030-10519-81.

Simões, P. P. 2000. Instalação, geocronologia e petrogénese de granitóides biotíticos sintectónicos associados ao cisalhamento Vigo-Régua (ZCI, Norte de Portugal). PhD Thesis (unpubl) Universidade do Minho, Braga, 351 pp.

SIORMINP. Sistema de Informação de Ocorrências e Recursos Minerais Portugueses. https://geoportal.lneg.pt/pt/bds/siorminp/#!/

Sousa, M.B. 1982. Litoestratigrafia e estrutura do “Complexo Xisto- Grauváquico” Ante-Ordovícico- Grupo do Douro (NE de Portugal). Ph.D. thesis, Univeristy of Coimbra.Teixeira, C. (1955) – Notas sobre a Geologia de Portugal: o Complexo Xisto-Grauváquico ante-Ordoviciano. Empresa Literária Fluminense, Lisboa, 50 p (in portuguese).

Taylor, H. P. 1980. The effects of assimilation of country rocks by magmas on 18O/16O and 87Sr/86Sr systematics in igneous rocks. Earth Planet Sci Lett 47:243–254.

Taylor, H.P. 1974. The application of oxygen and hydrogen isotope studies to problems of hydrothermal alteration and ore deposition. Economic Geology 69, 843–883.

Taylor, H.P. 1997. Oxygen and hydrogen isotope relationships in hydrothermal mineral deposits, in Barnes, H.L., ed., Geochemistry of hydrothermal ore deposits, 3rd edition: New York, John Wiley & Sons, p. 229–302.

Taylor, S.R. and McLennan, S.M. 1995. The geochemical evolution of the continental crust. Rev. Geophys., 33 (2): 241-265. https://doi.org/10.1029/95RG00262.

Teixeira, C., Medeiros, A. C., Fernandes, A.P., 1968. Folha 14-A Lamego da Carta Geológica de Portugal, escala 1:50.000. Direção Geral de Minas e Serviços Geológicos, Lisboa. (in portuguese)

Teixeira, R.J.S., Neiva, A.M.R., Silva, P.B., Gomes, M.E.P., Andersen, T., Ramos, J.M.F., 2017. Combined U-Pb geochronology and Lu-Hf isotope systematics by LAM-ICPMS of zircons from granites and metasedimentary rocks of Carrazeda de Ansiães and Sabugal areas, Portugal, Lithos, 125, 321–334. https://doi.org/10.1016/j.lithos.2011.02.015.

Thompson, J.F.H., and Newberry, R.J. 2000. Gold deposits related to reduced granitic intrusions: Society of Economic Geologists, Reviews 13, p. 377-400.

Thompson, J.F.H., Sillitoe, R.H., Baker, T., Lang, J.R., and Mortensen, J.K. 1999. Intrusion-related gold deposits associated with tungsten-tin provinces: Mineralium Deposita, 34, 197-217.

Timón-Sánchez, S.M., López-Moro, F.J., Romer, R.L., Rhede, D., Fernández-Fernández, A., Moro-Benito, C. 2019. Late-Variscan multistage hydrothermal processes unveiled by chemical ages coupled with compositional and textural uraninite variations in W-Au deposits in the western Spanish Central System Batholith. Geologica Acta, Vol.17.1, 1-19. DOI:10.1344/GeologicaActa2019.17.1.

Tischendorf, G., Rieder, M., Förster, H. J., Gottesmann, B., and Guidotti, Ch.V. 2004. A new graphical presentation and subdivision of potassium micas. Mineralogical Magazine, 68 (4): 649–667. https://doi.org/10.1180/0026461046840210 .

Tomkins, A.G., Grundy, C. 2009. Upper temperature limits of orogenic gold deposit formation: Constraints from the granulite-hosted Griffin's Find deposit, Yilgarn Craton. Economic Geology 104, 669-685.

Tooth, B., Brugger, J., Ciobanu, C., Liu,W.H., 2008. Modeling of gold scavenging by bismuth melts coexisting with hydrothermal fluids. Geology, 36 (10): 815–818. https://doi.org/10.1130/G25093A.1.

Tooth, B., Ciobanu, C.L., Green, L., O'Neill, B., Brugger, J. 2011. Bi-melt formation and gold scavenging from hydrothermal fluids: an experimental study. Geochimica et Cosmochimica Acta, 75 (19): 5423–5443. https://doi.org/10.1016/j.gca.2011.07.020.

Townley, B.K., Herail, G., Maksaev, V., Palacios, C., De Parseval, P., Sepuldeva, F., Orellana, R., Rivas, P., Ulloa, C. 2003. Gold grain morphology and composition as an exploration tool application to gold exploration in covered areas. Geochemistry: Exploration. Environment, Analysis 3, 29–38. http://dx.doi.org/10.1144/1467-787302-042.

Urbano, R., Toyos, M., Asensio, B. 1998. Intragranitic lode gold deposits in the Tomiño area (Pontevedra). Cuaderno Lab. Xeolóxico de Laxe Coruña. Vol. 17, pp. 341-348.

USGS, 2021. Mineral commodity summaries 2021: U.S. Geological Survey, 200 p., https://doi.org/10.3133/mcs2021.

Vaasjoki M., Sorjonen-Ward P., Lavikainen S. 1993. U-Pb age determinations and sulphide Pb-Pb characteristics from the late Archaean Hattu schist belt, Ilomantsi, eastern Finland. Geological Survey of Finland, Special Paper 17, 103–131.

Vallance, J., Cathelineau, M., Boiron, M.C., Fourcade, S., Shepherd, T.Y., Naden, J. 2003. Fluid-rock interactions and the role of late Hercynian aplite intrusion in the genesis of the Castromil gold deposit, northern Portugal. Chemical Geology, vol. 194, pp. 201–224. https://doi.org/10.1016/S0009-2541(02)00278-4.

Valle Aguado, B., Azevedo, M.R., Schaltegger, U., Martínez Catalán, J.R., Nolan, J., 2005. U-Pb zircon and monazite geochronology of Variscan magmatism related to syn-convergence extension in Central Northern Portugal. Lithos 82, 169–184. https://doi.org/10.1016/j.lithos.2004.12.012.

Valverde-Vaquero, P., and Díez Balda, M. A., Díez Montes, A., Dörr, W., Escuder Viruete, J., González Clavijo, E., Malusky, E., Rodríguez Fernández, L. R., Rubio, F. J., and Villar, P. 2007. The “hot orogen”: two separate variscan low-pressure metamorphic events in the Central Iberian Zone, in SGF, and BRGM, eds., Mechanics of Variscan Orogeny: A modern view on orogenic research, Volume 2: Orleans, Géologie de la France, p. 168.

Van Den Boogaart KG, Tolosana-Delgado R, Bren M. 2006. Concepts for handling of zeros and missing values in compositional data. In: IAMG 2006 - 11th International Congress for Mathematical Geology: Quantitative Geology from Multiple Sources. pp 1–4.

Villaseca, C, Orejana, D, Belousova, E, A. 2012. Recycled metaigneous crustal sources for S- and I-type Variscan granitoids from the Spanish Central System batholith: Constraints from Hf isotope zircon composition. Lithos 153: 84–93. https://doi.org/10.1016/j.lithos.2012.03.024.

Villaseca, C., Barbero, L., Herreros, V. 1998. A re-examination of the typology of peraluminous granite types in intracontinental orogenic belts. Earth and Environmental Science Transactions of The Royal Society of Edinburgh, 89, 2, 113-119. https://doi.org/10.1017/S0263593300007045.

Villaseca, C., Merino, E., Oyarzun, R., Orejana, D., Pérez-Soba, C., Chicharro, E. 2014. Contrasting chemical and isotopic signatures from Neoproterozoic metasedimentary rocks in the Central Iberian Zone (Spain) of pre-Variscan Europe: Implications for terrane analysis and Early Ordovician magmatic belts. Precambrian Research, 245, 131-145. http://dx.doi.org/10.1016/j.precamres.2014.02.00.

Wang, Q.F., Groves, D.I., Deng, J., Li, H.J., Yang, L., Dong, C.Y. 2020. Evolution of the Miocene Ailaoshan orogenic gold deposits, southeastern Tibet, during a complex tectonic history of lithosphere-crust interaction Mineralium Deposita, 55, pp. 1085-1104. https://doi.org/10.1007/s00126-019-00922-3.

Weihed, P., Eilu, P., Larsen, R. B., Stendal, H., Tontti, M. 2008. Metallic mineral deposits in the Nordic countries. Episodes, 31 (1), 125-132.

Whitney, D.L., and Evans, B.W. 2010. Abbreviations for Names of Rock-Forming Minerals. American Mineralogist, 95, 185-187. http://dx.doi.org/10.2138/am.2010.3371.

World Gold Council. 2021. Retrieved from: https://www.gold.org/.

Yardley, B.W.D., Banks, D.A., Bottrell, S.H., Diamond, L.W., 1993. Post-metamorphic gold – quartz veins from N.W. Italy: the composition and origin of the ore fluid. Mineralogical Magazine, 57, 407–422.

Yavuz F. and Yıldırım D.K. 2018. Periodico di Mineralogia, 87, 269-285. DOI: 10.2451/2018PM7808.

Yavuz, F., Kumral, M., Karakaya, N., Karakaya, M. Ç., Yıldırım, D. K. 2015. A Windows program for chlorite calculation and classification. Computers & Geosciences. 81, C, 101–113. DOI:https://doi.org/10.1016/j.cageo.2015.04.011.

Zachariáš, J., Žák, K., Pudilová, M., Snee, L.W., 2013. Multiple fluid sources/pathways and severe thermal gradients during formation of the Jílové orogenic gold deposit, Bohemian Massif, Czech Republic. Ore Geology Reviews, 54, 81–109.

Zemskov, V.S., Shelimova, L.E., Konstantinov, P.P., Avilov, E.S., Kretova, M.A., Nikhezina, I. Yu. 2014. Physical-chemical and thermoelectric properties of complex bismuth and lead chalcogenides and their solid solutions. Inorganic Materials: Applied Research, 5, 61–69. https://doi.org/10.1134/S2075113314010158.

Zhang, L., Yang, L.Q., Groves, D.I., Liu, Y., Sun, S.C., Qi, P., Wu, S.G., Peng, J.S. 2018. Geological and H–O–S–Pb isotopic constraints on ore genesis, Huangjindong goldfield, Jiangnan Orogen, southern China. Ore Geology Reviews, 99, 264-281. https://doi.org/10.1016/j.oregeorev.2018.06.013.

Zhao, H.S., Wang, Q.F., Groves, D.I., Deng, J. 2019. A rare Phanerozoic amphibolite-hosted gold deposit at Danba, Yangtze Craton, China: significance to fluid and metal sources for orogenic gold systems. Mineralium Deposita, 54, 133–152.

Zhou, D., Chang, T. & Davis, J.C. 1983. Dual extraction of R-mode and Q-mode factor solutions. Mathematical Geology, 15, 581–606.

Appendices

Appendix 1

- **Mineral chemistry data (EPMA) from Numão deposit.**

Minerals in host rock
Minerals from hydrothermal alteration

*below detection limit

Appendix 1-A. Epidote

Chemical compositions of epidote-supergroup minerals with calculations and classifications by WinEpclas program (Yavuz et al., 2018).

	Sample														
wt.%	**1 / 1 .**	**3 / 1 .**	**6 / 1 .**	**10 / 1 .**	**11 / 1 .**	**18 / 1 .**	**51 / 1 .**	**6 / 1 .**	**7 / 1 .**	**22 / 1 .**	**23 / 1 .**	**28 / 1 .**	**32 / 1 .**	**8 / 1 .**	**9 / 1 .**
SiO_2	39.02	38.46	37.94	35.60	37.72	37.76	39.34	46.36	37.52	39.08	39.81	35.98	39.33	38.02	38.87
TiO_2	0.21	0.15	0.00	0.16	0.00	0.00	0.00	0.00	0.00	0.00	0.00	0.00	0.00	0.00	0.26
Al_2O_3	28.14	28.72	27.49	26.60	27.45	28.80	29.68	34.60	25.62	29.28	33.42	23.99	28.64	27.07	28.03
FeO	6.46	5.88	6.54	6.26	6.99	5.54	4.05	0.00	6.62	4.92	0.36	8.90	5.75	6.47	5.29
MgO	0.15	0.07	0.04	0.18	0.09	0.05	0.05	0.00	0.12	0.05	0.00	0.14	0.00	0.00	0.00
MnO	0.50	0.60	0.41	1.38	0.52	0.06	0.17	0.03	0.57	0.37	0.12	1.27	0.07	0.34	0.46
CaO	24.43	24.29	24.25	19.45	24.22	24.50	24.35	18.39	20.87	24.52	25.31	16.36	25.06	24.09	24.86
SrO	0.00	0.00	0.00	0.00	0.00	0.24	0.29	0.00	0.00	0.00	0.00	0.00	0.00	0.00	0.00
La_2O_3	0.00	0.00	0.00	0.00	0.00	0.00	0.00	0.00	0.91	0.00	0.00	0.94	0.00	0.00	0.00
Ce_2O_3	0.00	0.00	0.00	0.35	0.00	0.00	0.00	0.00	1.95	0.00	0.00	2.04	0.00	0.00	0.00
Nd_2O_3	0.00	0.00	0.00	0.29	0.00	0.00	0.00	0.00	0.98	0.00	0.00	1.15	0.00	0.00	0.00
Y_2O_3	0.00	0.00	0.00	2.78	0.00	0.00	0.00	0.00	0.41	0.00	0.00	4.41	0.00	0.00	0.00
ThO_2	0.00	0.00	0.00	0.00	0.00	0.00	0.00	0.00	0.00	0.21	0.00	0.00	0.00	0.00	0.00
F	0.00	0.00	0.00	0.00	0.00	0.00	0.00	0.00	0.00	0.00	0.00	0.00	0.00	0.00	0.00
Cl	0.00	0.00	0.00	0.00	0.00	0.00	0.00	0.00	0.00	0.00	0.00	0.00	0.00	0.00	0.00
O=F	0.00	0.00	0.00	0.00	0.00	0.00	0.00	0.00	0.00	0.00	0.00	0.00	0.00	0.00	0.00
O=Cl	0.00	0.00	0.00	0.00	0.00	0.00	0.00	0.00	0.00	0.00	0.00	0.00	0.00	0.00	0.00
H_2O	0.00	0.00	0.00	0.00	0.00	0.00	0.00	0.00	0.00	0.00	0.00	0.00	0.00	0.00	0.00
Total	98.90	98.18	96.66	93.05	96.99	96.94	97.93	99.38	95.57	98.43	99.02	95.18	98.86	95.98	97.77
apfu															
Si	2.99	2.96	2.97	2.96	2.95	2.94	3.02	3.47	3.07	2.99	2.99	3.05	3.00	3.00	3.00
Ti	0.01	0.01	0.00	0.01	0.00	0.00	0.00	0.00	0.00	0.00	0.00	0.00	0.00	0.00	0.02
Al	2.54	2.60	2.54	2.61	2.53	2.64	2.69	3.05	2.47	2.64	2.95	2.40	2.58	2.52	2.55
Fe^{3+}	0.41	0.38	0.43	0.32	0.46	0.36	0.26	0.00	0.19	0.32	0.02	0.46	0.37	0.43	0.34
Fe^{2+}	0.00	0.00	0.00	0.12	0.00	0.00	0.00	0.00	0.27	0.00	0.00	0.18	0.00	0.00	0.00
Mg	0.02	0.01	0.01	0.02	0.01	0.01	0.01	0.00	0.01	0.01	0.00	0.02	0.00	0.00	0.00

Mn	0.03	0.04	0.03	0.10	0.04	0.00	0.01	0.00	0.04	0.02	0.01	0.09	0.01	0.02	0.03
Ca	2.00	2.00	2.03	1.73	2.03	2.04	2.00	1.48	1.83	2.01	2.03	1.49	2.05	2.04	2.06
Sr	0.00	0.00	0.00	0.00	0.00	0.01	0.01	0.00	0.00	0.00	0.00	0.00	0.00	0.00	0.00
La	0.00	0.00	0.00	0.00	0.00	0.00	0.00	0.00	0.03	0.00	0.00	0.03	0.00	0.00	0.00
Ce	0.00	0.00	0.00	0.01	0.00	0.00	0.00	0.00	0.06	0.00	0.00	0.06	0.00	0.00	0.00
Nd	0.00	0.00	0.00	0.01	0.00	0.00	0.00	0.00	0.03	0.00	0.00	0.04	0.00	0.00	0.00
Y	0.00	0.00	0.00	0.12	0.00	0.00	0.00	0.00	0.02	0.00	0.00	0.20	0.00	0.00	0.00
Th	0.00	0.00	0.00	0.00	0.00	0.00	0.00	0.00	0.00	0.00	0.00	0.00	0.00	0.00	0.00
Total	8.00	8.00	8.00	8.00	8.00	8.00	8.00	8.00	8.00	8.00	8.00	8.00	8.00	8.00	8.00
Si	2.99	2.96	2.97	2.96	2.95	2.94	3.02	3.47	3.07	2.99	2.99	3.05	3.00	3.00	3.00
$Al^{(IV)}$	0.01	0.04	0.03	0.04	0.05	0.06	0.00	0.00	0.00	0.01	0.02	0.00	0.00	0.00	0.00
$Total^{T\text{-}site}$	3.00	3.00	3.00	3.00	3.00	3.00	3.02	3.47	3.07	3.00	3.00	3.05	3.00	3.00	3.00
Ti	0.01	0.01	0.00	0.01	0.00	0.00	0.00	0.00	0.00	0.00	0.00	0.00	0.00	0.00	0.02
$Al^{(VI)}$	2.52	2.56	2.51	2.56	2.47	2.58	2.69	3.05	2.47	2.64	2.94	2.40	2.58	2.52	2.55
Fe^{3+}	0.41	0.38	0.43	0.32	0.46	0.36	0.26	0.00	0.19	0.32	0.02	0.46	0.37	0.43	0.34
Fe^{2+}	0.00	0.00	0.00	0.09	0.00	0.00	0.00	0.00	0.27	0.00	0.00	0.13	0.00	0.00	0.00
Mg	0.02	0.01	0.01	0.02	0.01	0.01	0.01	0.00	0.01	0.01	0.00	0.02	0.00	0.00	0.00
Mn^{2+}	0.03	0.04	0.03	0.00	0.04	0.00	0.01	0.00	0.04	0.02	0.01	0.00	0.01	0.02	0.03
$Total^{M\text{-}site}$	3.00	3.00	2.97	3.00	2.97	2.95	2.96	3.05	2.97	2.98	2.97	3.00	2.95	2.96	2.94
Mn^{2+}	0.00	0.00	0.00	0.10	0.00	0.00	0.00	0.00	0.00	0.00	0.00	0.09	0.00	0.00	0.00
Fe^{2+}	0.00	0.00	0.00	0.03	0.00	0.00	0.00	0.00	0.00	0.00	0.00	0.05	0.00	0.00	0.00
Ca	2.00	2.00	2.03	1.73	2.03	2.04	2.00	1.48	1.83	2.01	2.03	1.49	2.05	2.04	2.06
Sr	0.00	0.00	0.00	0.00	0.00	0.01	0.01	0.00	0.00	0.00	0.00	0.00	0.00	0.00	0.00
REE	0.00	0.00	0.00	0.14	0.00	0.00	0.00	0.00	0.13	0.00	0.00	0.33	0.00	0.00	0.00
Th	0.00	0.00	0.00	0.00	0.00	0.00	0.00	0.00	0.00	0.00	0.00	0.00	0.00	0.00	0.00
$Total^{A\text{-}site}$	2.00	2.00	2.03	2.00	2.03	2.05	2.02	1.48	1.96	2.02	2.03	1.95	2.05	2.04	2.06
Compositional parameters and end-members															
[A1]Dominant cation	Ca	Ca	Ca	Ca	Ca	Ca	Ca	Ca	Ca	Ca	Ca	Ca	Ca	Ca	Ca
[A2]Dominant cation	Ca	Ca	Ca	Ca	Ca	Ca	Ca	Ca	Ca	Ca	Ca	Ca	Ca	Ca	Ca
[M1]Dominant cation	Al	Al	Al	Al	Al	Al	Al	Al	Al	Al	Al	Al	Al	Al	Al

[M2]Dominant cation	Al	Al	Al	Al	Al	Al	Al	Al	Al	Al	Al	Al	Al	Al	Al	
[M3]Dominant cation	Al	Al	Al	Al	Al	Al	Al	Al	Al	Al	Al	Fe3+	Al	Al	Al	
[O4]Dominant anion	O	O	O	O	O	O	O	O	O	O	O	O	O	O	O	
Epidote subgroup	Clinozoisite									Clinozoisite						
Epidote name	Clinozoisite									Clinozoisite		Epidote		Clinozoisite		

Notes: The formulae were recalculated to 12.5 oxygens and total cations = 8.0; Fe^{3+} and Fe^{2+} estimations from total FeO (wt%) contents were carried out on the basis of stoichiometric constraints using Droop's (1987) method; Classification of epidote-supergroup minerals based on the dominant cations and anions at key sites (from Armbruster et al., 2006; Yavuz et al., 2018).

Appendix 1-B. Feldspar.

	Samples													
	19 / 1 .	**20 / 1 .**	**21 / 1 .**	**1 / 1 .**	**6 / 1 .**	**49 / 1 .**	**61 / 1 .**	**11 / 1 .**	**10 / 1 .**	**11 / 1 .**	**97 / 1 .**	**47 / 1 .**	**10 / 1 .**	**96 / 1 .**
SiO_2	64.07	63.99	63.84	65.33	65.06	65.34	65.85	65.58	65.38	66.20	65.65	61.88	57.46	66.74
TiO_2	0.00	0.00	0.00	0.00	0.00	0.00	0.00	0.00	0.00	0.00	0.00	0.00	0.00	0.00
Al_2O_3	18.30	18.09	18.80	18.54	18.19	17.95	18.53	17.61	18.58	18.14	18.56	25.15	27.02	19.61
FeO	0.04	0.00	0.04	0.00	0.15	0.19	0.10	0.08	0.04	0.07	0.00	0.05	0.06	0.05
CaO	0.01	0.02	0.36	0.16	0.09	0.02	0.02	0.00	0.47	0.04	0.00	6.91	9.54	0.12
Na_2O	0.41	0.36	1.23	0.43	2.82	0.27	0.21	0.38	0.37	0.17	0.27	7.98	6.91	12.11
K_2O	15.97	15.76	14.16	16.40	13.57	15.75	15.92	16.30	14.78	16.56	16.92	0.12	0.13	0.07
BaO	0.27	0.22	0.08	0.21	0.01	0.22	0.20	0.16	0.17	0.00	0.07	0.09	0.00	0.00
Compositional parameters and end-members														
Anortite	0.06	0.10	1.84	0.79	0.44	0.08	0.11	0.01	2.51	0.22	0.00	32.17	42.97	0.55
Albite	3.72	3.33	11.45	3.78	23.87	2.49	1.96	3.38	3.56	1.56	2.37	67.18	56.34	99.10
Ortoclase	96.22	96.57	86.71	95.44	75.70	97.43	97.93	96.61	93.93	98.22	97.63	0.65	0.69	0.36

Appendix 1-C. Titanite.

	Samples						
	45 / 1 .	**52 / 1 .**	**5 / 1 .**	**29 / 1 .**	**98 / 1 .**	**4 / 1 .**	**5 / 1 .**
FeO	0.52	0.21	0.24	0.52	0.15	0.28	0.68
MnO	*	0.11	0.19	0.12	*	0.13	*
TiO_2	22.47	30.03	34.74	35.73	29.46	30.80	25.12
P_2O_5	*	0.15	*	*	*	0.13	*
K_2O	*	*	*	*	0.05	*	0.04
SnO_2	*	0.59	*	*	0.40	0.38	0.19
SiO_2	32.34	31.39	31.13	31.58	30.49	30.99	31.54
Al_2O_3	11.87	6.67	3.55	2.78	7.31	6.31	10.28
Y_2O_3	0.15	*	*	*	3.05	1.42	*
CaO	30.00	29.53	29.28	29.54	27.28	28.65	29.69
Nb_2O_5	*	0.23	*	0.27	0.36	0.59	*
F	4.94	2.70	1.12	1.20	2.42	2.22	4.10
Total	102.90	102.14	101.18	102.52	103.14	102.70	102.00

Appendix 1-D. Amphiboles.

	Samples					
Analysis (wt%)	**16 / 1 .**	**17 / 1 .**	**20 / 1 .**	**21 / 1 .**	**26 / 1 .**	**27 / 1 .**
SiO_2	52.85	53.33	51.96	51.84	39.52	40.13
TiO_2	0.04	0.02	0.05	0.15	0.02	0.08
Al_2O_3	2.25	2.76	2.53	3.04	28.28	25.94
MnO	1.34	0.97	1.20	1.26	0.41	0.43
FeO	14.76	14.31	17.47	17.82	4.62	6.18
MgO	13.81	13.73	11.95	11.91	0.74	1.11
CaO	12.60	12.99	12.66	12.52	24.20	24.42
Na_2O	0.30	0.26	0.24	0.20	0.02	0.03
K_2O	0.12	0.23	0.12	0.11	0.01	0.02
F	0.69	0.74	0.57	0.51	0.23	0.20
Total	98.46	99.00	98.51	99.15	97.96	98.45
Compositional parameters and end-members						
Subgroup of (OH,F,Cl)	Ca	Ca	Ca	Ca	Ca	Ca
Species	actinolite	actinolite	actinolite	actinolite	ferro-sadanagaite	ferro-sadanagaite
T (ideally 8 apfu)						
Si	7.71	7.71	7.67	7.61	5.67	5.78
Al	0.29	0.29	0.32	0.38	2.33	2.21
T subtotal	8.00	8.00	8.00	8.00	8.00	8.00
C (ideally 5 apfu)						
Al	0.10	0.18	0.12	0.15	2.45	2.19
Mn^{2+}	0.10	0.12	0.10	0.06	0.05	0.05
Fe^{2+}	1.80	1.73	2.16	2.19	0.56	0.74
Mg	3.00	2.96	2.63	2.60	0.16	0.24
Li						

C subtotal	5.00	4.99	5.00	5.00	3.22	3.23
B (ideally 2 apfu)						
Mn^{2+}	0.07		0.05	0.10		
Ca	1.93	2.00	1.95	1.90	2.00	2.00
B subtotal	2.00	2.00	2.00	2.00	2.00	2.00
A (from 0 to 1 apfu)						
Ca	0.04	0.01	0.06	0.06	1.72	1.77
Na	0.09	0.07	0.07	0.06	0.00	0.01
K	0.02	0.04	0.02	0.02	0.00	0.00
A subtotal	0.14	0.13	0.15	0.14	1.73	1.78
O (non-W)	22.00	22.00	22.00	22.00	22.00	22.00
OH	1.68	1.66	1.73	1.76	1.90	1.91
F	0.32	0.34	0.27	0.24	0.10	0.09
W subtotal	2.00	2.00	2.00	2.00	2.00	2.00
Sum T,C,B,A	15.14	15.11	15.14	15.14	14.94	15.01
ST Sites (Si, Al)	8.00	8.00	8.00	8.00	8.00	8.00
SC Sites (Mg, Fe etc)	5.04	4.99	5.00	5.04	3.22	3.23
SB Sites (Ca, Na)	2.00	2.00	2.00	2.00	2.00	2.00
SA Sites (Na, K)	0.07	0.13	0.09	0.04	1.73	1.78
$Mg/(Mg+Fe^{2+})$	0.64	0.63	0.57	0.57	0.22	0.24
$Fe^{3+}/(Fe^{3+}+[6]Al)$	0.61	0.00	0.68	0.69	0.00	0.00

Appendix 1-E. Garnets.

	Samples					
	14 / 1 .	**15 / 1 .**	**18 / 1 .**	**19 / 1 .**	**24 / 1 .**	**25 / 1 .**
SiO_2	38.483	38.634	38.565	38.145	38.385	38.784
Al_2O_3	20.059	20.907	19.953	20.369	20.099	20.191
MgO	0.109	0.28	0.158	0.339	0.286	0.183
TiO_2	0.569	0.092	0.534	0.238	0.301	0.181
CaO	20.149	17.792	20.485	14.946	16.515	19.913
FeO	8.658	11.277	8.612	12.698	14.106	10.631
MnO	12.291	12.4	12.046	13.802	11.083	10.92
F	0.207	0.395	0.208	0.091	0.096	0.118

Compositional parameters and end-members

Spessartine	30.8%	24.6%	24.1%	26.6%	27.2%	27.2%
Pyrope			0.7%		1.1%	0.4%
Almandine	26.0%	28.3%	19.5%	15.7%	21.7%	15.6%
Grossular	37.9%	40.0%	48.3%	49.3%	44.9%	49.0%
Andradite	1.7%	2.4%	2.9%	1.8%	1.6%	1.3%

Appendix 1-F. Chlorites.

Chorite analyses (wt%) with their structural formulae (apfu), atomic site partition,site fractions,and empirical chlorite geothermometers(°C) estimated by WinCcac program (Yavuz et al., 2015).

	Samples												
wt.%	**4 / 1 .**	**12 / 1 .**	**17 / 1 .**	**46 / 1 .**	**48 / 1 .**	**53 / 1 .**	**55 / 1 .**	**56 / 1 .**	**57 / 1 .**	**59 / 1 .**	**3 / 1 .**	**35 / 1 .**	**94 / 1 .**
SiO_2	28.446	26.19	25.533	26.105	25.784	26.11	29.296	29.446	26.399	26.801	25.544	31.565	25.818
TiO_2	0.027	0.039	0.006	0.052	0.02	0.022	0.003	0.004	0.042	0.007	0.055	1.575	0.021
Al_2O_3	20.176	20.514	21.6	21.087	22.028	21.558	19.124	18.923	21.03	20.936	20.948	21.473	21.803
FeO	19.115	20.484	27.244	25.365	26.209	25.764	18.801	18.754	25.329	24.235	30.014	20.153	23.691
MnO	0.634	1.149	0.623	0.6	0.625	0.539	0.321	0.301	0.502	0.463	0.961	0.457	0.592
MgO	20.715	18.384	14.722	15.344	15.028	15.391	21.442	21.772	15.818	16.313	11.808	9.964	15.26
CaO	0.024	0.298	0.024	0.041	0.026	0.063	0.004	0.047	0.067	0.046	0.049	4.627	0.044
Na_2O	0.014	0.027	0.021	0.005	0.001	0.008	0	0.001	0.013	0.04	0.038	1.044	0.047
K2O	0	0.038	0.001	0	0.027	0	0.019	0	0.025	0.03	0	0.018	0.028
F	0.279	0.172	0.195	0.19	0.204	0.178	0.323	0.352	0.137	0.196	0.013	0.234	0.085
O=F	0.1175	0.0724	0.0821	0.08	0.0859	0.075	0.136	0.1482	0.0577	0.0825	0.0055	0.0985	0.0358
O=Cl	0	0	0	0	0	0	0	0	0	0	0	0	0
Total	89.3125	87.2226	89.8869	88.709	89.8661	89.558	89.197	89.4518	89.3043	88.9845	89.4245	91.0115	87.3532
apfu													
Si	2.8437	2.7244	2.6527	2.7231	2.6653	2.7	2.9216	2.9279	2.731	2.7648	2.7131	3.1222	2.7098
Ti	0.002	0.0031	0.0005	0.0041	0.0016	0.0017	0.0002	0.0003	0.0033	0.0005	0.0044	0.1172	0.0017
Al	2.3771	2.515	2.6448	2.5925	2.6836	2.6273	2.2478	2.2176	2.5641	2.5455	2.6223	2.5033	2.6971
Fe^{3+}	0	0	0.0392	0	0	0	0	0	0	0	0	0	0
Fe^{2+}	1.5981	1.782	2.3279	2.2127	2.2657	2.228	1.568	1.5595	2.1914	2.0908	2.666	1.6671	2.0795
Mn	0.0537	0.1012	0.0548	0.053	0.0547	0.0472	0.0271	0.0254	0.044	0.0405	0.0865	0.0383	0.0526
Mg	3.0871	2.8509	2.2801	2.3861	2.3158	2.3726	3.1878	3.2273	2.4395	2.5088	1.8697	1.4693	2.3877
Ca	0.0026	0.0332	0.0027	0.0046	0.0029	0.007	0.0004	0.005	0.0074	0.0051	0.0056	0.4904	0.0049
Na	0.0027	0.0054	0.0042	0.001	0.0002	0.0016	0	0.0002	0.0026	0.008	0.0078	0.2002	0.0096
K	0	0.005	0.0001	0	0.0036	0	0.0024	0	0.0033	0.0039	0	0.0023	0.0037
F	0.0885	0.0565	0.064	0.0628	0.0667	0.0583	0.1023	0.1111	0.0449	0.0642	0.0044	0.0762	0.0284

Cl	0	0	0	0	0	0	0	0	0	0	0	0	0
OH	7.9115	7.9435	7.936	7.9372	7.9333	7.9417	7.8977	7.8889	7.9551	7.9358	7.9956	7.9238	7.9716
Si	2.8437	2.7244	2.6527	2.7231	2.6653	2.7	2.9216	2.9279	2.731	2.7648	2.7131	3.1222	2.7098
$Al^{(IV)}$	1.1563	1.2756	1.3473	1.2769	1.3347	1.3	1.0784	1.0721	1.269	1.2352	1.2869	0.8778	1.2902
Total - Tetrahedral	4	4	4	4	4	4	4	4	4	4	4	4	4
$Al^{(VI)}$	1.2208	1.2394	1.2975	1.3156	1.3489	1.3273	1.1694	1.1455	1.2951	1.3103	1.3354	1.6255	1.4069
Ti	0.002	0.0031	0.0005	0.0041	0.0016	0.0017	0.0002	0.0003	0.0033	0.0005	0.0044	0.1172	0.0017
Fe^{3+}	0	0	0.0392	0	0	0	0	0	0	0	0	0	0
Fe^{2+}	1.5981	1.782	2.3279	2.2127	2.2657	2.228	1.568	1.5595	2.1914	2.0908	2.666	1.6671	2.0795
Mn	0.0537	0.1012	0.0548	0.053	0.0547	0.0472	0.0271	0.0254	0.044	0.0405	0.0865	0.0383	0.0526
Mg	3.0871	2.8509	2.2801	2.3861	2.3158	2.3726	3.1878	3.2273	2.4395	2.5088	1.8697	1.4693	2.3877
Ca	0.0026	0.0332	0.0027	0.0046	0.0029	0.007	0.0004	0.005	0.0074	0.0051	0.0056	0.4904	0.0049
Na	0.0027	0.0054	0.0042	0.001	0.0002	0.0016	0	0.0002	0.0026	0.008	0.0078	0.2002	0.0096
K	0	0.005	0.0001	0	0.0036	0	0.0024	0	0.0033	0.0039	0	0.0023	0.0037
Total	0.0053	0.0437	0.007	0.0056	0.0066	0.0086	0.0028	0.0052	0.0133	0.017	0.0134	0.6929	0.0183
OH	7.9115	7.9435	7.936	7.9372	7.9333	7.9417	7.8977	7.8889	7.9551	7.9358	7.9956	7.9238	7.9716
F	0.0885	0.0565	0.064	0.0628	0.0667	0.0583	0.1023	0.1111	0.0449	0.0642	0.0044	0.0762	0.0284
Total	8	8	8	8	8	8	8	8	8	8	8	8	8
$Si_{(T1)}$	1.6874	1.4488	1.3054	1.4462	1.3305	1.3999	1.8433	1.8558	1.4621	1.5296	1.4262	n.c.	1.4197
$Al_{(T1)}$	1.1563	1.2756	1.3473	1.2769	1.3347	1.3	1.0784	1.0721	1.269	1.2352	1.2869	n.c.	1.2902
$Si_{(T2)}$	1.1563	1.2756	1.3473	1.2769	1.3347	1.3	1.0784	1.0721	1.269	1.2352	1.2869	n.c.	1.2902
$Al_{(T2)}$	1.2208	1.2394	1.2975	1.3156	1.3489	1.3273	1.1694	1.1455	1.2951	1.3103	1.3354	n.c.	1.4069
$Mg_{(M1+M4)}$	1.7906	1.609	1.2866	1.3584	1.3084	1.3482	1.8777	1.9036	1.3928	1.4384	1.0552	n.c.	1.3499
$Fe_{(M1+M4)}$	0.9269	1.0058	1.3357	1.2597	1.2801	1.2661	0.9236	0.9199	1.2511	1.1987	1.5047	n.c.	1.1757
$Al_{(M1+M4)}$	1.1563	1.2756	1.3473	1.2769	1.3347	1.3	1.0784	1.0721	1.269	1.2352	1.2869	n.c.	1.2902
$Vacancy_{(M1+M4)}$	0.0323	0	0	0.0193	0.0071	0.0136	0.0455	0.0367	0.0131	0.0376	0.0242	n.c.	0.0584
$Mg_{(M2+M3)}$	1.2966	1.2419	0.9935	1.0277	1.0074	1.0244	1.3101	1.3237	1.0467	1.0704	0.8144	n.c.	1.0378
$Fe_{(M2+M3)}$	0.6712	0.7762	1.0314	0.953	0.9856	0.962	0.6444	0.6396	0.9402	0.8921	1.1613	n.c.	0.9038
$Al_{(M2+M3)}$	0.0323	0	0	0.0193	0.0071	0.0136	0.0455	0.0367	0.0131	0.0376	0.0242	n.c.	0.0584
XSi,tet	0.4219	0.3622	0.3263	0.3616	0.3326	0.35	0.4608	0.464	0.3655	0.3824	0.3566	n.c.	0.3549
XAl,tet	0.5781	0.6378	0.6737	0.6384	0.6674	0.65	0.5392	0.536	0.6345	0.6176	0.6434	n.c.	0.6451

XTotal,tet	1	1	1	1	1	1	1	1	1	1	1	n.c.	1
XAl,oct	0.2035	0.2067	0.2163	0.2194	0.2249	0.2213	0.1949	0.1909	0.216	0.2184	0.2227	n.c.	0.2345
XMg,oct	0.5236	0.4923	0.3892	0.4068	0.3952	0.4034	0.5358	0.5421	0.4141	0.4249	0.3263	n.c.	0.4068
XFe,oct	0.2664	0.2971	0.3945	0.369	0.3777	0.3714	0.2613	0.2599	0.3654	0.3485	0.4447	n.c.	0.3467
XVacancy,oct	0.0064	0.0039	0	0.0048	0.0022	0.0039	0.0079	0.007	0.0045	0.0082	0.0064	n.c.	0.0119
XTotal,oct	1	1	1	1	1	1	1	1	1	1	1	n.c.	1
XSi(T2)	0.4215	0.3788	0.3314	0.3631	0.3315	0.35	0.4597	0.464	0.3642	0.3767	0.3548	n.c.	0.3491
XAl(T2)	0.5785	0.6212	0.6686	0.6369	0.6685	0.65	0.5403	0.536	0.6358	0.6233	0.6452	n.c.	0.6509
XFe(M2M3)	0.3355	0.3846	0.5052	0.4756	0.4929	0.4808	0.3224	0.3198	0.47	0.4473	0.5805	n.c.	0.4531
XMg(M2M3)	0.6481	0.6154	0.4948	0.5129	0.5038	0.512	0.6554	0.6618	0.5233	0.5367	0.4071	n.c.	0.5202
XAl(M2M3)	0.0165	0	0	0.0115	0.0034	0.0073	0.0223	0.0184	0.0067	0.0161	0.0124	n.c.	0.0267
XFe(M1)	0.2763	0.2914	0.3349	0.3384	0.3246	0.332	0.2885	0.2903	0.3383	0.3279	0.4026	n.c.	0.3002
XMg(M1)	0.5338	0.4662	0.328	0.3649	0.3317	0.3535	0.5864	0.6008	0.3767	0.3934	0.2823	n.c.	0.3447
XAl(M1)	0.157	0.2425	0.3371	0.2738	0.3369	0.2999	0.0805	0.072	0.2716	0.2466	0.2903	n.c.	0.3018
XVacancy(M1)	0.0329	0	0	0.0229	0.0067	0.0145	0.0445	0.0369	0.0134	0.0321	0.0247	n.c.	0.0534
Si	2.8437	2.7244	2.6527	2.7231	2.6653	2.7	2.9216	2.9279	2.731	2.7648	2.7131	3.1222	2.7098
Fe/(Fe+Mg)	0.3411	0.3846	0.5094	0.4812	0.4945	0.4843	0.3297	0.3258	0.4732	0.4546	0.5878	0.5315	0.4655
Fe(total)	1.5981	1.782	2.3671	2.2127	2.2657	2.228	1.568	1.5595	2.1914	2.0908	2.666	1.6671	2.0795
(Al+Mg+Fe)	7.0623	7.1479	7.292	7.1913	7.2651	7.228	7.0036	7.0043	7.195	7.145	7.1579	5.6396	7.1643
(XMg+XFe)	4.6852	4.6329	4.6472	4.5988	4.5815	4.6006	4.7558	4.7868	4.6309	4.5996	4.5357	3.1364	4.4672
Octahedral occupancy	5.9618	5.9766	6	5.9715	5.9866	5.9769	5.9526	5.9579	5.9733	5.9508	5.9619	4.9173	5.9284
Vacancy	0.0382	0.0234	0	0.0285	0.0134	0.0231	0.0474	0.0421	0.0267	0.0492	0.0381	1.0827	0.0716
(XAl+XVacancy)	2.4154	2.5384	2.6448	2.621	2.697	2.6505	2.2952	2.2597	2.5908	2.5946	2.6604	3.5859	2.7687
(Fe2+Mg)	4.6852	4.6329	4.608	4.5988	4.5815	4.6006	4.7558	4.7868	4.6309	4.5996	4.5357	3.1364	4.4672
R^{2+}	4.7389	4.7341	4.6629	4.6519	4.6362	4.6479	4.783	4.8121	4.6749	4.64	4.6221	3.1747	4.5198
R^{3+}	1.2229	1.2425	1.3371	1.3196	1.3504	1.329	1.1696	1.1458	1.2984	1.3108	1.3398	1.7427	1.4085
$Al/(Al+Mg+Fe^{2+})$	0.3366	0.3519	0.3647	0.3605	0.3694	0.3635	0.3209	0.3166	0.3564	0.3563	0.3663	0.4439	0.3765
$Mg/(Mg+Fe^{2+})$	0.6589	0.6154	0.4948	0.5188	0.5055	0.5157	0.6703	0.6742	0.5268	0.5454	0.4122	0.4685	0.5345
Na+K+2Ca	0.0079	0.0769	0.0097	0.0102	0.0095	0.0156	0.0033	0.0102	0.0208	0.0221	0.019	1.1832	0.0232
$AlVI+Fe^{2+}$	2.8189	3.0214	3.6254	3.5283	3.6145	3.5553	2.7375	2.705	3.4865	3.4011	4.0014	3.2926	3.4864
AlVI+Mg+Fe2+	5.9061	5.8723	5.9055	5.9144	5.9303	5.928	5.9253	5.9323	5.926	5.9098	5.871	4.7619	5.8741

AlVI/(Si+AlIV)]	0.2891	0.3189	0.3368	0.3192	0.3337	0.325	0.2696	0.268	0.3172	0.3088	0.3217	0.2194	0.3225
%[Al-chl	20.1246	21.4142	22.3926	21.9165	22.6262	22.1606	18.9677	18.6908	21.6343	21.5357	22.3323	26.2845	22.9572
Fe-chl	27.6045	30.0374	38.9974	37.7397	38.3239	37.8152	27.232	26.9068	37.1997	36.0138	45.8222	42.8606	36.3946
Mg-chl]	52.2709	48.5483	38.61	40.3438	39.0499	40.0242	53.8003	54.4024	41.166	42.4504	31.8456	30.8549	40.6482
% Clinochlore	65.1449	60.2202	48.8998	51.2934	49.9504	51.0475	66.6493	67.0658	52.1835	54.0677	40.4505	46.2816	52.8274
% Chamosite	33.7223	37.6413	49.9244	47.567	48.8693	47.9368	32.7838	32.4074	46.8756	45.0604	57.6791	52.5124	46.0082
% Pennantite	1.1328	2.1385	1.1757	1.1396	1.1803	1.0157	0.5669	0.5268	0.9409	0.8719	1.8705	1.2061	1.1644
Subgroup (R) a	tri-tri	tri-tri	tri-tri	tri-tri	tri-tri	tri-tri	tri-tri	tri-tri	tri-tri	tri-tri	tri-tri	di-tri, tri-di	tri-tri
Subgroup (Vacancy) a	tri-tri	tri-tri	tri-tri	tri-tri	tri-tri	tri-tri	tri-tri	tri-tri	tri-tri	tri-tri	tri-tri	di-tri, tri-di	tri-tri
Type b	Type-I	Type-I	Type-I	Type-I	Type-I	Type-I	Type-I	Type-I	Type-I	Type-I	Type-I	Type-II	Type-I
Species (This study) d	Clinochlore	Clinochlore	Chamosite	Clinochlore	Clinochlore	Clinochlore	Clinochlore	Clinochlore	Clinochlore	Clinochlore	Chamosite	Sudoite	Clinochlore
TCN $_{85\text{-}Al^{IV}}$(ºC)	259	284	299	284	297	289	242	241	283	276	287	287	287
TCN $_{85\text{-}OctahedralVacancy}$ (ºC)	272	276	281	275	278	276	270	271	275	270	272	272	264
TKML $_{87\text{-}Al^{IV}}$(ºC)	288	317	341	324	338	330	271	269	322	314	334	334	326
TC $_{88\text{-}Al^{IV}}$(ºC)	310	349	372	349	368	357	285	283	347	336	352	352	353
TK $_{90\text{-}Si}$(ºC)	216	274	314	274	306	287	185	183	270	253	280	280	281
TJ $_{91\text{-}Al^{IV}}$(ºC)	311	350	377	354	373	361	286	283	351	340	360	360	357
THV $_{91\text{-}Al^{IV}}$(ºC)	252	311	347	312	341	324	213	210	308	291	317	317	319
TC $_{93\text{-}OctahedralOccupancy}$(ºC)	303	314	331	310	321	314	296	300	311	295	303	303	278
TC $_{93\text{-}Si^{IV}}$(ºC)	293	383	437	384	428	402	519	514	378	353	392	n.c.	394
TZF $_{95\text{-}Al^{IV}}$(ºC)	263	284	288	276	287	280	248	247	275	269	268	268	280
TX $_{97\text{-}Al^{IV}}$(ºC)	297	317	287	276	289	282	277	277	277	274	233	233	287
TES $_{00\text{-}Al^{IV}}$(ºC)	245	266	268	256	267	261	230	229	255	250	248	248	261

Notes: H_2O[c]=calculated H_2O (wt%) content based on stoichiometry; Fe_2O_3[c] and FeO[c]=calculated Fe_2O^3 (wt%) and FeO (wt%) contents from electron- microprobe chlorite analysis based on stoichiometry.Chlorite geothermometers of TCN85-AlIV (from Cathelineau and Nieva(1985); TCN85-Octahedral vacancy from Cathelineau and Nieva (1985);**TKML87-AlIV from Kranidiotis and MacLean (1987);** TC88-AlIV from Cathelineau (1988); TK90-Si from Kavalierisetal.(1990); TJ91-AlIV from Jowett (1991); THV91-AlIV from Hiller and Velde (1991); TC93-Octahedral occupancy from De Caritat et al.(1993); TC93-SiIV from De Caritat et al.(1993); TZF95-AlIV from Zang and Fyfe (1995); TX97-AlIV from Xie et al.(1997); TES00-AlIV from El-Sharkawy (2000); n.c.¼notcalculated. a-Subgroup from Zane and Weiss (1998). b-Type from Zane andWeiss (1998). d-Species by WinCcacprogram.

Appendix 2

Appendix 2-A. Representative chemical analysis (wt.%) of arsenopyrite from Numão deposit.

	wt.%					at.%			
	Fe	**As**	**S**	**Pb**	**Total**	**Fe**	**As**	**S**	**Pb**
23 / 1 .	34.79	45.43	19.73	*	100.14	33.75	32.85	33.34	0.02
24 / 1 .	34.99	45.16	20.03	0.11	100.34	33.77	32.49	33.68	0.03
25 / 1 .	34.97	45.11	20.16	0.11	100.39	33.70	32.41	33.84	0.03
28 / 1 .	35.06	44.24	20.34	0.12	99.98	33.84	31.83	34.20	0.03
29 / 1 .	34.82	45.19	20.19	0.11	100.39	33.56	32.47	33.89	0.03
34 / 1 .	34.72	44.66	19.96	0.10	99.48	33.77	32.37	33.81	0.03
40 / 1 .	34.59	43.99	20.11	0.11	98.93	33.74	31.98	34.17	0.03
42 / 1 .	34.90	44.93	20.13	*	100.20	33.70	32.34	33.87	0.02
43 / 1 .	34.83	44.39	20.29	0.11	99.68	33.70	32.02	34.21	0.03
44 / 1 .	34.72	44.74	19.85	0.12	99.47	33.81	32.48	33.67	0.03
67 / 1 .	34.78	45.17	19.98	0.15	100.24	33.64	32.57	33.66	0.04
68 / 1 .	34.60	44.79	20.11	0.15	99.77	33.56	32.38	33.98	0.04
69 / 1 .	34.85	45.05	20.27	0.13	100.31	33.58	32.36	34.03	0.03
72 / 1 .	34.61	45.03	20.15	0.10	99.95	33.49	32.48	33.97	0.03
73 / 1 .	34.63	45.14	20.04	0.12	100.06	33.52	32.57	33.80	0.03
74 / 1 .	34.79	45.05	20.17	0.11	100.15	33.60	32.43	33.93	0.03
75 / 1 .	34.53	45.01	19.90	*	99.61	33.58	32.63	33.71	0.02
76 / 1 .	34.80	44.20	20.53	*	99.70	33.60	31.80	34.52	0.02
77 / 1 .	34.73	44.80	20.30	*	100.02	33.53	32.25	34.14	0.03
78 / 1 .	34.69	45.35	20.14	0.12	100.34	33.47	32.62	33.85	0.03
79 / 1 .	34.70	44.93	20.19	*	99.96	33.55	32.38	34.01	0.02
86 / 1 .	35.08	44.21	20.60	0.13	100.27	33.70	31.66	34.47	0.04
87 / 1 .	34.78	44.48	20.30	*	99.81	33.63	32.07	34.19	0.02
88 / 1 .	34.81	45.01	20.11	*	100.09	33.64	32.43	33.85	0.02
89 / 1 .	34.79	45.15	20.21	0.15	100.42	33.53	32.43	33.93	0.04
95 / 1 .	33.93	44.72	20.23	0.10	99.04	33.08	32.50	34.36	0.03
96 / 1 .	34.47	44.91	19.95	0.13	99.51	33.54	32.58	33.81	0.03
97 / 1 .	34.58	44.23	20.11	0.11	99.06	33.69	32.12	34.13	0.03
100 / 1 .	34.94	44.32	20.17	*	99.61	33.87	32.02	34.05	0.02
101 / 1 .	34.19	44.84	20.19	0.15	99.42	33.24	32.50	34.19	0.04
102 / 1 .	34.25	44.57	20.10	*	99.08	33.40	32.40	34.14	0.02
104 / 1 .	34.25	45.21	20.01	*	99.62	33.30	32.76	33.88	0.00
105 / 1 .	35.13	44.89	20.28	0.12	100.48	33.79	32.18	33.98	0.03
106 / 1 .	35.00	44.67	20.41	0.15	100.35	33.67	32.03	34.20	0.04
122 / 1 .	34.67	45.08	20.09	0.11	100.05	33.54	32.51	33.85	0.03
48 / 1 .	34.02	45.69	19.69	*	99.56	33.21	33.25	33.48	0.00
49 / 1 .	34.20	45.48	19.72	*	99.59	33.36	33.07	33.50	0.00
86 / 1 .	35.31	43.75	20.84	0.11	100.00	33.87	31.28	34.82	0.03
105 / 1 .	34.55	45.22	20.25	0.10	100.37	33.32	32.50	34.02	0.03
12 / 1 .	34.54	45.34	20.24	0.14	100.34	33.31	32.59	34.00	0.04

20 / 1 .	34.42	45.23	20.23	0.12	100.06	33.27	32.60	34.06	0.03
23 / 1 .	34.75	44.98	20.54	0.11	100.42	33.38	32.20	34.37	0.03
28 / 1 .	34.84	44.92	20.45	0.08	100.32	33.50	32.20	34.25	0.02
31 / 1 .	34.42	44.80	20.25	0.15	99.72	33.36	32.37	34.18	0.04
38 / 1 .	34.73	44.99	20.45	0.11	100.39	33.40	32.25	34.26	0.03
42 / 1 .	34.40	44.96	20.43	0.12	100.02	33.20	32.35	34.36	0.03
15/1.	34.11	44.60	19.93	*	98.65	33.41	32.57	34.01	0.00
Minimum	33.93	43.75	19.69	0.08	98.65	33.08	31.28	33.34	0.00
Maximum	35.31	45.69	20.84	0.15	100.48	33.87	33.25	34.82	0.04
Mean	34.66	44.86	20.18	0.12	99.90	33.55	32.36	34.01	0.03
Stard_desv	0.29	0.40	0.23	0.02	0.45	0.19	0.33	0.28	0.01

Appendix 2-B. Representative chemical analysis (wt.%) of sulfides from Numão deposit.

			wt.%								at.%						
			Cu	Fe	Ag	S	Pb	Bi	Total	Zn	Cu	Fe	Ag	S	Pb	Bi
Bi-Pb-S																	
	35 / 1 .		0.157	0.693	0.603	16.306	32.319	49.081	99.926	*	0.266	1.338	0.603	54.838	16.818	25.323
galena																	
	70 / 1 .	*	*	0.727	0.243	13.423	83.277	0.642	98.414	*	*	1.548	0.268	49.827	47.831	0.365
	18 / 1 .	*	*	0.272	1.658	13.84	80.452	3.369	99.626	*	*	0.569	1.794	50.383	45.318	1.881
	19 / 1 .	*	*	0.365	1.606	13.885	81.192	3.527	100.6	*	*	0.757	1.724	50.149	45.374	1.954
	39 / 1 .	*	*	0.172	*	13.551	85.561	*	100.082	*	*	0.364	*	49.927	48.778	*
chalcopyrite																	
	41 / 1 .	*	33.779	29.708	*	34.05	*	*	97.624	*	24.997	25.015	*	49.945	*	*
	67 / 1 .	*	34.729	30.268	*	34.754	*	*	99.801	*	25.147	24.938	*	49.879	*	*
	68 / 1 .	*	34.273	30.087	*	34.342	*	*	98.774	*	25.084	25.056	*	49.82	*	*
	75 / 1 .	*	34.596	30.267	*	34.637	*	*	99.642	*	25.104	24.991	*	49.819	*	*
	79 / 1 .	*	34.627	30.024	*	34.99	*	*	99.822	*	25.041	24.705	*	50.154	*	*
	109 / 1 .	*	34.137	29.564	*	34.563	*	*	98.346	*	25.037	24.672	*	50.245	*	*
	38 / 1 .	*	33.983	30.574	*	35.2	0.163	*	99.949	*	24.516	25.097	*	50.332	0.036	*
	108 / 1 .	*	33.796	30.099	*	35.147	0.137	*	99.369	*	24.517	24.844	*	50.536	0.031	*
bismuthinite																	
	98 / 1 .	*	*	*	*	19.15	*	78.855	98.93407	*	*	*	*	60.249	*	38.06
	126 / 1 .	*	*	*	*	10.991	*	89.01	100.636	*	*	*	*	43.896	*	54.538
	128 / 1 .	*	*	*	*	18.548	*	80.354	99.56158	*	*	*	*	59.261	*	39.385
	113 / 1 .	*	*	*	*	18.825	0.877	78.354		*	*	*	*	59.776	0.431	38.169
	114 / 1 .	*	*	*	*	18.617	5.968	74.525		*	*	*	*	59.314	2.942	36.426
pyrrhotite																	
	39 / 1 .	*	0.055	59.312	*	39.146	0.152	*	98.836	*	0.038	46.451	*	53.404	0.032	*
	40 / 1 .	*	*	59.023	*	40.096	0.136	*	99.367	*	*	45.762	*	54.152	0.028	*
pyrite																	
	107 / 1 .	*	*	46.388	*	53.622	0.16	*	100.332	*	*	33.142	*	66.734	0.031	*
Sphalerite																	
	80 / 1 .	55.014	0.658	9.538		33.791			100.953	40.178	0.494	8.155	*	50.326	*	*
	17 / 1 .	59.061	0.009	5.857		32.365			98.232	44.577	0.007	5.175	*	49.815	*	*

Appendix 2-C. Representative chemical analysis (wt.%) of Au-Ag minerals from Numão deposit.

	Bismuth					Au-Ag phases				
	Au		Ag	Bi	Total	Au	Ag	Bi	Total	
30 / 1 .	*		*	98.931	99.25323	**31 / 1 .**	81.78555	18.04685	*	100.1184	native gold
33 / 1 .	*		*	97.248	98.01148	**32 / 1 .**	81.58282	17.75585	*	99.49366	native gold
37 / 1 .	*		*	98.917	99.86259	**66 / 1 .**	75.53875	24.37319	*	100.0529	electrum
65 / 1 .	*		*	98.46	99.9771	**83 / 1 .**	90.35647	8.60196	*	99.0867	native gold
92 / 1 .		0.2134	*	99.424	100.0852	**84 / 1 .**	88.39998	11.19671	*	99.66669	native gold
93 / 1 .	*		*	98.9	99.46614	**111 / 1 .**	91.77655	8.71351	*	100.6941	native gold
94 / 1 .	*		*	99.845	100.4398	**112 / 1 .**	86.6016	12.93398	*	99.836	native gold
99 / 1 .	*		*	99.216	99.93779	**41 / 1 .**	85.88477	12.86996	*	99.29847	native gold
103 / 1 .	*		*	98.861	99.45549	**52 / 1 .**	87.11182	11.77192	*	99.61037	native gold
115 / 1 .	*		*	98.833	99.198	**56 / 1 .**	86.80142	12.74774	*	99.90216	native gold
116 / 1 .	*		*	98.18	99.35228	**57 / 1 .**	86.22621	12.41212	*	99.51	native gold
117 / 1 .	*		*	98.976	99.34639	**82 / 1 .**	59.4416	37.19077	0.194	98.78959	Au-Ag phases
123 / 1 .	*		*	98.175	98.55713	**84 / 1 .**	54.6595	44.09426	*	99.196	Au-Ag phases
124 / 1 .	*		*	98.173	98.73337	**88 / 1 .**	68.73323	31.55313	*	100.5124	Au-Ag phases
51 / 1 .	*		*	98.971	99.678	**89 / 1 .**	68.71965	31.83346	*	100.6931	Au-Ag phases
55 / 1 .	*		*	98.215	98.90121	**16 / 1 .**	93.847	6.609	*	100.6874	native gold
65 / 1 .	*		*	97.828	98.98492	**35 / 1 .**	45.35138	53.75546	*	100.5383	Au-Ag phases
77 / 1 .		0.19885	*	97.063	98.59463						
78 / 1 .	*		*	97.407	99.21986						
81 / 1 .		0.50731	*	99.092	100.2418						
83 / 1 .	*		*	97.526	99.12016						
15 / 1 .	*		*	99.3	100.0325						

Appendix 3

Appendix 3. Univariate statistics from the multi-element analysis (ppm) of the Numão deposit.

	Au	Ag	Cu	Pb	Zn	Al	As	Ba	Be	Bi	Ca	Co	Cr
Minimum	0.0	0.3	1.6	1.0	7.0	14400.0	2.5	2.0	0.9	1.0	1100.0	3.0	3.0
Maximum	39.6	7.9	2610.0	575.0	753.0	125500.0	82300.0	1370.0	61.9	218.0	86600.0	36.0	123.0
Mean	0.4	0.4	92.3	19.0	87.5	80261.3	2309.7	604.5	3.7	7.6	7582.7	13.3	64.6
Median	0.0	0.3	36.0	17.0	90.0	83600.0	172.0	640.0	3.5	3.0	5700.0	14.0	69.0
Range	39.5	7.7	2608.4	574.0	746.0	111100.0	82297.5	1368.0	61.0	217.0	85500.0	33.0	120.0
Interquartile Range	0.1	0.3	67.0	9.0	54.0	22800.0	1529.0	270.0	0.9	4.0	6400.0	7.0	23.0
Standard Deviation	1.6	0.4	177.7	19.7	41.6	15747.1	6148.3	210.3	2.9	16.5	6325.5	4.4	15.3
1 percentile	0.0	0.3	2.7	3.0	22.0	42372.0	7.0	36.6	1.7	1.0	1400.0	4.0	30.0
5 percentile	0.0	0.3	13.6	7.0	34.0	51080.0	15.6	216.0	2.1	1.0	1900.0	5.0	37.0
10 percentile	0.0	0.3	18.0	9.0	39.0	56520.0	23.0	310.0	2.3	1.0	2400.0	6.0	40.0
25 percentile	0.0	0.3	25.0	13.0	59.0	69400.0	51.0	470.0	3.0	1.0	3400.0	10.0	54.0
75 percentile	0.1	0.5	92.0	22.0	113.0	92200.0	1580.0	740.0	3.9	5.0	9800.0	17.0	77.0
90 percentile	1.0	0.7	189.0	27.0	122.0	98000.0	10001.0	840.0	4.5	18.0	15000.0	18.0	80.0
95 percentile	2.3	0.9	355.8	31.0	131.0	100500.0	10001.0	910.0	5.0	33.0	19840.0	19.0	83.0
99 percentile	5.8	2.1	940.6	60.3	188.1	106140.0	16320.0	1090.0	11.9	85.3	29836.0	22.0	89.0

Appendix 3 (Cont.). Univariate statistics from the multi-element analysis (ppm) of the Numão deposit.

	Fe	K	La	Mg	Mn	Mo	Na	Ni	P	S	Sb	Sc	Th	Ti	V	W
Minimum	13000.0	5100.0	0.5	1600.0	51.0	0.5	400.0	2.0	40.0	100.0	1.0	1.0	1.0	600.0	3.0	0.5
Maximum	97300.0	57300.0	60.0	49700.0	3220.0	3.0	41100.0	74.0	2270.0	47000.0	31.0	18.0	40.0	8900.0	151.0	8480.0
Mean	39639.2	29119.3	35.4	10394.9	521.1	0.8	14625.3	31.7	593.4	4341.3	3.9	11.5	14.9	4013.3	76.1	76.3
Median	42400.0	30600.0	40.0	11300.0	493.0	0.5	14600.0	34.0	600.0	2100.0	2.5	13.0	20.0	4200.0	84.0	5.0
Range	84300.0	52200.0	59.5	48100.0	3169.0	2.5	40700.0	72.0	2230.0	46900.0	30.0	17.0	39.0	8300.0	148.0	8479.5
Interquartile Range	14700.0	13400.0	10.0	5200.0	290.0	0.5	7200.0	16.0	110.0	3400.0	0.0	5.0	10.0	1300.0	34.0	5.0
Standard Deviation	11259.7	9768.8	9.4	3609.2	240.9	0.3	5925.0	11.1	136.7	6073.3	3.5	3.7	5.5	913.3	23.7	440.4
1 percentile	15200.0	7072.0	3.0	3072.0	159.7	0.5	1800.0	8.0	56.0	100.0	2.5	3.7	1.0	1500.0	23.0	0.5
5 percentile	18600.0	11760.0	20.0	4000.0	222.0	0.5	3660.0	11.0	410.0	460.0	2.5	5.0	10.0	2300.0	32.0	0.5
10 percentile	21740.0	14320.0	20.0	4920.0	259.0	0.5	6600.0	14.0	470.0	700.0	2.5	6.0	10.0	2700.0	37.0	0.5
25 percentile	32400.0	22300.0	30.0	7800.0	361.0	0.5	11200.0	24.0	540.0	1100.0	2.5	9.0	10.0	3400.0	60.0	5.0
75 percentile	47100.0	35700.0	40.0	13000.0	651.0	1.0	18400.0	40.0	650.0	4500.0	2.5	14.0	20.0	4700.0	94.0	10.0
90 percentile	49700.0	41000.0	50.0	13800.0	778.4	1.0	22100.0	44.0	710.0	11100.0	7.0	15.0	20.0	5000.0	100.0	90.0
95 percentile	52700.0	43900.0	50.0	14400.0	846.0	1.0	24000.0	45.0	750.0	16700.0	10.0	16.0	20.0	5100.0	104.0	250.0
99 percentile	70556.0	49628.0	50.0	16300.0	1186.0	2.0	28428.0	50.3	965.6	32296.0	21.3	17.0	20.0	5400.0	112.0	1815.6